Design and characterisation of novel peptide-based hydrogel for controlled delivery of therapeutics

A thesis submitted to The University of Manchester for the degree of

Doctor of Philosophy

in the Faculty of Science and Engineering

2022

Siyuan Dong

School of Engineering

Contents

Chapter 5 Control release of macromolecules in self-assembled peptide hydrogel system

Chapter 6 Encapsulation of recombinant human interleukin 2/21 (rhIL-2/21) cytokine in peptide hydrogel for the activity assessment

List of Tables

List of Figures

Abstract

Peptide-based hydrogels are widely applied in biomedical applications because they possess good biocompatibility, biodegradability, injectability, and non-toxicity. Peptides with short chains ($\leq$ 20 amino acids) can self-assembled into nano fibrous hydrogels with secondary structures including α-helices, beta-sheets and coiled-coils. Chemically cross-linked peptide hydrogels may be harmful to the human body because their toxic cross-linkers are difficult to degrade, which poses limitations in biomedical applications. To overcome these issues, physically cross-linked hydrogels have been designed with adjustable properties to suit different purposes.

In this PhD project, peptide KFEFKFEFK and EFKFEFKFE were designed with beta-sheet structures and self-assembled into hydrogels at pH 7. KFEFKFEFK carried +1 net charge and EFKFEFKFE carried -1 net charge. The mechanical properties of these two hydrogels depended on the concentration of peptides. Both of them exhibited injectability according to the shear thinning/recovery test. Besides, hydrogels with different charges exhibited apparently different 3D cell culture abilities according to the mechanical properties test over 14 days. The biocompatibility of hydrogels depended on the type of cell lines according to the cell viability. In addition, large molecular weight polymeric probes with different charges (fluorescein-dextran, FITC-Poly-L-Lysine) were encapsulated into these two peptide hydrogels to study how electrostatic interactions can be exploited for controlled release kinetics. Based on the diffusion coefficient D_E, it has been revealed that the large diffusivities of probes were induced by electrostatic repulsion in hydrogel system. Furthermore, recombinant human interleukine-2/21 (rhIL-2/21) were selected as large drug molecules to encapsulate into peptide hydrogels for the assessment of drug delivery application. The long-term (21days) controlled release of

rhIL-21 in EFKFEFKFE hydrogel demonstrated that EFKFEFKFE was a promising drug delivery system for cancer immunotherapy.

Declaration

I declare that no portion of the work in the thesis has been submitted in support of an application

for another degree or qualification of this or any other university or other institute of learning.

Copyright

(i) The author of this thesis (including any appendices and/or schedules to this thesis) owns certain copyright or related rights in it (the "Copyright") and she has given The University of Manchester certain rights to use such Copyright, including for administrative purposes.

(ii) Copies of this thesis, either in full or in extracts and whether in hard or electronic copy, may be made only in accordance with the Copyright, Designs and Patents Act 1988 (as amended) and regulations issued under it or, where appropriate, in accordance with licensing agreements which the University has from time to time. This page must form part of any such copies made.

(iii) The ownership of certain Copyright, patents, designs, trade marks and other intellectual property (the "Intellectual Property") and any reproductions of copyright works in the thesis, for example graphs and tables ("Reproductions"), which may be described in this thesis, may not be owned by the author and may be owned by third parties. Such Intellectual Property and Reproductions cannot and must not be made available for use without the prior written permission of the owner(s) of the relevant Intellectual Property and/or Reproductions.

(iv) Further information on the conditions under which disclosure, publication and commercialisation of this thesis, the Copyright and any Intellectual Property and/or Reproductions described in it may take place is available in the University IP Policy (see http://documents.manchester.ac.uk/Docuinfo.aspx?DocID=24420), in any relevant thesis restriction declarations deposited in the University Library, The University Library's regulations (see http://www.library.manchester.ac.uk/about/regulations/) and in The University's policy on Presentation of Theses.

Acknowledgements

Chapter 1. General introduction

In this chapter, the background of hydrogels, their classification, self – assembled peptide hydrogels and their drug delivery applications for the treatment of cancer are introduced. In Fig. 1.1, the structure of this introduction chapter, which includes the PhD aim and objectives, is shown schematically.
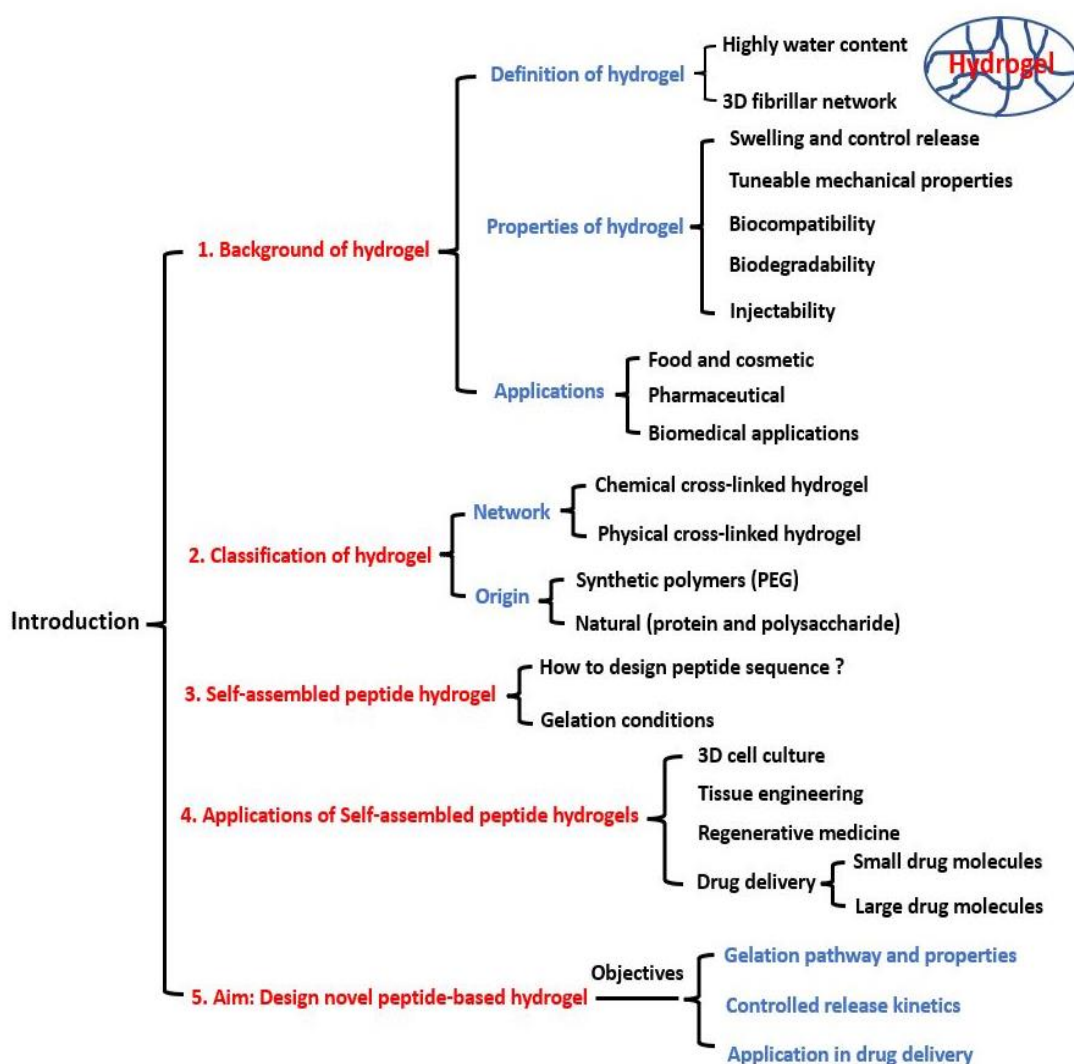
Figure 1.1 General structure of the introduction about hydrogel and the aim of PhD project.

1.1 Background of hydrogel

Hydrogel is a type of material that contains a high water content (typically around 95%) and has a three-dimensional (3D) fibrillar network. These materials exhibit swelling behavior in aqueous solutions and are able to retain most of the water molecules within the network, resulting in a stable hydrogel system [1].

The properties of hydrogels depend on various factors, including the type of cross-linking, the compounds used, charge, pH, hydrophobicity, concentration of monomers, and mechanical properties. The storage modulus G' of hydrogels can range from 100 to 10000 kPa, providing a range of conditions for different purposes [2][3]. For example, a relatively high G' can lead to a stiffer scaffold for bone tissue engineering [4]. In addition, hydrogels, as a type of soft material, can be used to encapsulate drug molecules and cells for drug delivery, regenerative medicine, 3D cell culture, and tissue engineering [5][6]. Hydrogels consist of hydrophilic polymers that can absorb water, and the porous network allows for molecules to diffuse in and out of the hydrogel system. Furthermore, hydrogels can be made to be biocompatible and biodegradable, mimicking the internal environment of the human body, which is important for designing smart biomaterials to avoid toxicity in biomedical applications. Hydrogels can also be designed to be injectable, allowing for localized delivery of therapeutics and targeted treatment.

Due to these properties, hydrogels have been applied in a wide range of areas, including cosmetics, contact lenses, food, pharmaceuticals, biosensors, wound healing, and biomedical applications [7][8][9][10]. Hydrogels have also been designed as drug delivery systems to achieve controlled release kinetics, and the pore size of the network is controllable, making hydrogels suitable for different sized drugs and cells used in the treatment of various diseases [11][12]. Overall, this versatile material is a potential candidate in biomedical applications.

1.2 Classification of hydrogel

Hydrogels can be classified into two main categories based on the nature of the network: chemical cross-linked and physical cross-linked hydrogels. Chemical cross-linked hydrogels are formed through covalent bonds between polymer chains, resulting in an irreversible hydrogel with a stable 3D network and relatively high mechanical properties. These hydrogels can be used for 3D cell culture and tissue engineering, and the chemical reaction can be initiated by UV, electron beam, enzymatic reaction, and photopolymerization [13][14]. The initiators used in chemical reactions, such as redox and thermal polymerization, can also enable hydrogels to be designed with good biocompatibility and biodegradability [15][16]. However, chemical cross-linked hydrogels used in biomedical applications may pose safety risks. For example, photopolymerization hydrogels used as drug carriers have limitations due to the penetration of light into the human body, which may cause side effects [18].

In contrast, physically cross-linked hydrogels can overcome these limitations. These hydrogels are formed under physical conditions (pH, temperature, ionic strength, hydrogen bonding, hydrophobic interaction, π-π stacking) without any chemical reactions, making them reversible. For example, thermosensitive hydrogels undergo a sol-gel transition based on hydrophobic interactions. They will be in a gel-like state at higher temperatures and return to a liquid-like state when the temperature decreases [14]. Based on thermosensitive materials, physical cross-linked hydrogels can be designed for injectability, as the gelation process occurs during the injection process under human body temperature. Additionally, physical hydrogels have been used for drug release depending on charge interactions. The cross-linking process can be triggered by pH, through the deprotonation/protonation of ionic functional groups, forming a gel state at a specific pH. The mechanical properties and degradability of hydrogels are based on the pH value, enabling controlled drug release. The physical cross-linked hydrogels avoid

the toxicity from chemical initiators, and their application areas relate to the properties and source of materials.

Supramolecular hydrogels are a type of physical hydrogels that have been attracting a lot of interest in biomedical applications [19]. They are formed through non-covalent intermolecular interactions, resulting in reversible hydrogels. The dynamic nature of supramolecular interactions endows them with shear thinning/recovery properties, making them potential materials for drug/cell delivery [19][20]. Supramolecular hydrogels also provide an excellent environment for protein drug delivery [20]. For example, Shuguang Zhang and co-workers designed a two-layered self-assembled peptide to form a supramolecular hydrogel for the controlled release of human immunoglobulin (IgG) [21]. This injectable hydrogel, consisting of ac-(RADA)4-CONH2 and ac-(KLDL)3-CONH2, was able to maintain the binding activity of the antibody after encapsulation. The density of the network and mechanical properties could be modulated by the ratio of ac-(KLDL)3-CONH2. The long-term controlled release kinetics make this hydrogel a potential drug delivery system for antibody therapeutics.

Hydrogels can be formulated using synthetic polymers (such as polyethylene glycol, polyethylene oxide, poly hydroxyethyl methacrylate) or natural materials (such as protein and polysaccharides). Synthetic polymers can be used to form hydrogels with tunable properties for different purposes. For example, the mechanical properties can be controlled by adjusting the ratio of polymer components. Polyethylene glycol (PEG) is a popular polymer for synthetic hydrogels. PEG is biocompatible and does not cause any immunogenicity, making it a potential candidate for use in tissue engineering and drug delivery [22].

Natural hydrogels are formulated according to their intended application. For example, in biomedical applications, good biocompatibility, biodegradability, and non-toxicity are required. For this purpose, natural materials such as alginate, dextran, gelatin, and peptides can be used

to form hydrogels. Alginate and dextran are polysaccharide-based materials that can be used to encapsulate drugs, bioactive agents, and living cells. Gelatin and peptides are protein-based building blocks that can be functionalized under physical or chemical conditions. As a result, hydrogels have attracted much research attention and have led to the development of commercialized products in the pharmaceutical industry.

1.3 Self – assembled peptide hydrogel

One type of hydrogel that has attracted attention is peptide hydrogel. Peptides are composed of amino acid monomers (typically 20 or fewer) that can bind together via peptide bonds (-CONH) to form short peptide chains. Peptides can form secondary structures, such as beta sheets, beta hairpins, alpha helices, and coiled-coils, through non-covalent bonds (hydrogen bonds, π–π stacking, electrostatic interactions, van der Waals forces). Hydrogen bonds play a key role in causing peptide chains to self-assemble into nanostructures, such as fibers, nanotubes, or ribbons, in aqueous environments and create a stable network. Additionally, π–π stacking in peptide chains containing aromatic residues, and the hydrophobic force between two chains, contribute to the hydrophobic core inside the structure. As a result, hydrophilic surfaces are exposed in water, promoting the formation of peptide nanostructures. Electrostatic interactions also play a role in the self-assembly process. For example, strong electrostatic interactions promote the self-assembly process and form a more elastic hydrogel. On the other hand, polar interactions in peptides can induce a relatively weak hydrogel [23]. These factors are all taken into account when designing peptide sequences for hydrogel formation.

In this project, KFEFKFEFK and EFKFEFKFE were designed with beta-sheet structures based on the FEFKFEFK (F8) in Saiani's group [24]. These two sequences consist of natural amino acids, designed by alternating hydrophobic residues and hydrophilic residues, which induce self-assembly process through hydrophobic force. The ionic complementary amino acids in

sequence cause electrostatic interactions that promote self-assembly into nanofiber network. Besides, these short sequences are easy to synthesize that save time for preparation. In aqueous, F8 would form the gel state at very acid or very basic environment which might limit the applications into human body. KFEFKFEFK carried +1 net charge and EFKFEFKFE carried -1 net charge at pH 7, that can form peptide hydrogels at physiological environment. This property makes these two hydrogels more suitable for biomedical applications. In addition, charge interactions in hydrogel enabled to control the network, which provide a smart system to encapsulate different sizes of drugs/cells for release. The release kinetics could be controlled through electrostatic interactions between hydrogel and drugs/cells, in the case, achieve the long-term release profile. Therefore, this type of peptide-based hydrogel is a promising material in drug delivery application.

1.4 Applications of self-assembled peptide hydrogels

Self-assembled peptide hydrogels are novel biological materials that have been widely applied in the field of 3D cell culture, regenerative medicine, tissue engineering and drug delivery. The gelation process can be controlled by chemical and physical conditions, leading to a multifunctional hydrogel. For tissue engineering, the stiffness and stability of peptide hydrogels can be enhanced by chemical cross-linkers [25]. Claudia Tomasini and co-workers have employed physical self-assembled peptide-based hydrogels for 3D cell culture, which presents a potential application in regenerative medicine according to cell seeding and cell viability tests [26]. As peptide-based hydrogels can be designed with nanostructures, high water content, adjustable network, non-toxicity, injectability and good biocompatibility, they can encapsulate different sizes of drugs and achieve localized deliver. For example, RADA16 peptide self-assembled into hydrogel under physical conditions, improving the delivery of chemotherapeutics for cancer treatment [27]. RADA16 hydrogel presented sustained release of antitumour drugs, prolonging the retention of drug, which increased drug efficacy and

avoided side effects. Cancer is a high mortality disease, self-assembled peptide hydrogels have been used to deliver small molecule therapeutics (doxorubicin, curcumin, paclitaxel, bioactive reagents) to synergic the defence against cancer recurrency. Apart from small drug molecules, large molecule therapeutics (protein drugs, antibodies) for cancer have caused a vast of interest in pharmaceuticals and clinical applications in recent years. Encapsulating large molecule drugs into self-assembled peptide hydrogels has been considered for the immune related diseases. However, some large molecule drugs for immune therapy have short half-life and are easily degraded in vivo, which causes high-frequency dosage and may be toxic to the human body. Therefore, in this project, we will design and explore novel peptide-based hydrogels to control release of large molecule therapeutics for the optimisation of drug efficacy.

1.5 Aim and objectives of the PhD

The overall aim of PhD is to design and characterise novel peptide-based hydrogels to achieve controlled release through electrostatic interactions and deliver large molecule therapeutics for immunotherapy. There are three main objectives of the PhD as follows: (i) Design and characterise novel positive and negative charge peptides to study their gelation pathway and properties. (ii) Investigate the release of large molecular weight polymeric probes and study how electrostatic interactions can be exploited for controlled release kinetics. (iii) Apply novel peptide-based hydrogels for recombinant human interleukin 2/21(rhIL2/21) delivery in cancer immunotherapeutic.

1.6 References

[1]   K. Deligkaris, T. S. Tadele, W. Olthuis, and A. van den Berg, "Hydrogel-based devices for biomedical applications," Sensors Actuators, B Chem., vol. 147, no. 2, pp. 765–774, 2010, doi: 10.1016/j.snb.2010.03.083.

[2]   N. E. Mushi, J. Kochumalayil, N. T. Cervin, Q. Zhou, and L. A. Berglund, "Nanostructurally Controlled Hydrogel Based on Small-Diameter Native Chitin Nanofibers: Preparation, Structure, and Properties," ChemSusChem, vol. 9, no. 9, pp. 989–995, 2016, doi: 10.1002/cssc.201501697.

[3]   F. L. C. Morgan, J. Fernández-Pérez, L. Moroni, and M. B. Baker, "Tuning Hydrogels by Mixing Dynamic Cross-Linkers: Enabling Cell-Instructive Hydrogels and Advanced Bioinks," Adv. Healthc. Mater., vol. 11, no. 1, pp. 1–15, 2022, doi: 10.1002/adhm.202101576.

[4]   J. L. Vanderhooft, M. Alcoutlabi, J. J. Magda, and G. D. Prestwich, "Rheological properties of cross-linked hyaluronan-gelatin hydrogels for tissue engineering," Macromol. Biosci., vol. 9, no. 1, pp. 20–28, 2009, doi: 10.1002/mabi.200800141.

[5]   A. Vashist, A. Vashist, Y. K. Gupta, and S. Ahmad, "Recent advances in hydrogel based drug delivery systems for the human body," J. Mater. Chem. B, vol. 2, no. 2, pp. 147–166, 2014, doi: 10.1039/c3tb21016b.

[6]   K. Y. Lee and D. J. Mooney, "Hydrogels for tissue engineering," Chem. Rev., vol. 101, no. 7, pp. 1869–1879, 2001, doi: 10.1021/cr000108x.

[7]   X. Chen, B. D. Martin, T. K. Neubauer, R. J. Linhardt, J. S. Dordick, and D. G. Rethwisch, "Enzymatic and chemoenzymatic approaches to synthesis of sugar-based polymer and hydrogels," Carbohydr. Polym., vol. 28, no. 1, pp. 15–21, 1995, doi: 10.1016/0144-8617(95)00082-8.

[8]   S. R. Van Tomme, G. Storm, and W. E. Hennink, "In situ gelling hydrogels for pharmaceutical and biomedical applications," Int. J. Pharm., vol. 355, no. 1–2, pp. 1–18, 2008, doi: 10.1016/j.ijpharm.2008.01.057.

[9]   P. Krsko, T. E. McCann, T. T. Thach, T. L. Laabs, H. M. Geller, and M. R. Libera, "Length-scale mediated adhesion and directed growth of neural cells by surface-patterned poly(ethylene glycol) hydrogels," Biomaterials, vol. 30, no. 5, pp. 721–729, 2009, doi: 10.1016/j.biomaterials.2008.10.011.

[10]   P. Sikareepaisan, U. Ruktanonchai, and P. Supaphol, "Preparation and characterization of asiaticoside-loaded alginate films and their potential for use as effectual wound dressings," Carbohydr. Polym., vol. 83, no. 4, pp. 1457–1469, 2011, doi: 10.1016/j.carbpol.2010.09.048.

[11]   W. E. Rudzinski, A. M. Dave, U. H. Vaishnav, S. G. Kumbar, A. R. Kulkarni, and T. M. Aminabhavi, "Hydrogels as controlled release devices in agriculture," Des. Monomers Polym., vol. 5, no. 1, pp. 39–65, 2002, doi: 10.1163/156855502760151580.

[12]   N. A. Peppas and A. R. Khare, "Preparation, structure and diffusional behavior of hydrogels in controlled release," Adv. Drug Deliv. Rev., vol. 11, no. 1–2, pp. 1–35, 1993, doi: 10.1016/0169-409X(93)90025-Y.

[13]   J. Maitra and V. K. Shukla, "Cross-linking in Hydrogels - A Review," Am. J. Polym. Sci., vol. 4, no. 2, pp. 25–31, 2014, doi: 10.5923/j.ajps.20140402.01.

[14]   R. parhi, "Cross-Linked Hydrogel for Pharmaceutical Applications: A Review," Adv. Pharm. Bull., 2017, doi: 10.15171/apb.2017.064.

[15]   A. S. Sawhney, C. P. Pathak, and J. A. Hubbell, "Photopolymerized Polyethylene glycol)-co-poly(-hydroxy," Macromolecules, vol. 26, pp. 581–587, 1993.

[16] B. Wang, W. Zhu, Y. Zhang, Z. Yang, and J. Ding, "Synthesis of a chemically-crosslinked thermo-sensitive hydrogel film and in situ encapsulation of model protein drugs," React. Funct. Polym., vol. 66, no. 5, pp. 509–518, 2006, doi: 10.1016/j.reactfunctpolym.2005.10.003.

[17] E. Mueller, I. Poulin, W. J. Bodnaryk, and T. Hoare, "Click Chemistry Hydrogels for Extrusion Bioprinting: Progress, Challenges, and Opportunities," Biomacromolecules, vol. 23, no. 3, pp. 619–640, 2022, doi: 10.1021/acs.biomac.1c01105.

[18] L. Yu and J. Ding, "Injectable hydrogels as unique biomedical materials," Chem. Soc. Rev., vol. 37, no. 8, pp. 1473–1481, 2008, doi: 10.1039/b713009k.

[19] X. Yan et al., "Advances in the Application of Supramolecular Hydrogels for Stem Cell Delivery and Cartilage Tissue Engineering," Front. Bioeng. Biotechnol., vol. 8, no. July, pp. 1–13, 2020, doi: 10.3389/fbioe.2020.00847.

[20] Y. Lyu and H. S. Azevedo, "Supramolecular hydrogels for protein delivery in tissue engineering," Molecules, vol. 26, no. 4, 2021, doi: 10.3390/molecules26040873.

[21] S. Koutsopoulos and S. Zhang, "Two-layered injectable self-assembling peptide scaffold hydrogels for long-term sustained release of human antibodies," J. Control. Release, 2012, doi: 10.1016/j.jconrel.2012.03.014.

[22] D. A. Gyles, L. D. Castro, J. O. C. Silva, and R. M. Ribeiro-Costa, "A review of the designs and prominent biomedical advances of natural and synthetic hydrogel formulations," Eur. Polym. J., vol. 88, no. 01, pp. 373–392, 2017, doi: 10.1016/j.eurpolymj.2017.01.027.

[23] K. Joyner, M. B. Taraban, Y. Feng, and Y. B. Yu, "An interplay between electrostatic and polar interactions in peptide hydrogels," Biopolymers, vol. 100, no. 2, pp. 174–183, 2013, doi: 10.1002/bip.22194.

[24]   M. A. Elsawy, J. K. Wychowaniec, L. A. Castillo Díaz, A. M. Smith, A. F. Miller, and A. Saiani, "Controlling Doxorubicin Release from a Peptide Hydrogel through Fine-Tuning of Drug-Peptide Fiber Interactions," Biomacromolecules, vol. 23, no. 6, pp. 2624–2634, 2022, doi: 10.1021/acs.biomac.2c00356.

[25]   J. Li, R. Xing, S. Bai, and X. Yan, "Recent advances of self-assembling peptide-based hydrogels for biomedical applications," Soft Matter, vol. 15, no. 8, pp. 1704–1715, 2019, doi: 10.1039/C8SM02573H.

[26]   N. Zanna et al., "Thixotropic Peptide-Based Physical Hydrogels Applied to Three-Dimensional Cell Culture," ACS Omega, vol. 2, no. 5, pp. 2374–2381, 2017, doi: 10.1021/acsomega.7b00322.

[27]   C. Karavasili, E. Panteris, I. S. Vizirianakis, S. Koutsopoulos, and D. G. Fatouros, "Chemotherapeutic Delivery from a Self-Assembling Peptide Nanofiber Hydrogel for the Management of Glioblastoma," Pharm. Res., 2018, doi: 10.1007/s11095-018-2442-1.

Chapter 2 Literature review

Hydrogels consist of hydrophilic molecules that form a three-dimensional (3D) network. The high water content of hydrogels makes them excellent candidates for biomedical applications [1]. Water is a key component of the human body, and therefore, the biocompatibility and biodegradability of hydrogels provide a suitable condition to mimic extracellular matrix (ECM) for cell culture and can serve as a smart delivery system for controlled drug release [2][3][4].

Hydrogels can be made of natural or synthetic components, leading to further classification based on the different formation mechanisms. The subsequent versatility of these materials has led to extensive research regarding their design and applications. Natural components such as proteins and peptides are common components in drug delivery systems due to their ideal biocompatibility and low toxicity. Peptides are composed of amino acid monomers that form different lengths of chains via peptide bonds, defined as the primary structure. This is a linear sequence that generally starts from the N-terminal (amino group) to the C-terminal (carboxyl group). Peptides can be designed to undergo a self-assembling process to form hydrogels with secondary structures, under the conditions of specific pH, temperature, light, or enzyme [5][6][7]. Several configurations of the secondary structure of peptides have currently been identified, including alpha helix, beta sheet, beta hairpin, and random coil. The self-assembling procedure can result in the formation of nanostructures, including nanofibers, nanotubes, and nanoparticles; these occur through hydrogen bonding, $\pi - \pi$ stacking, ionic strength, or hydrophobic force [8][9][10][11]. These non-covalently bonded peptide hydrogels maintain dynamic networks known as physical cross-linked hydrogels. Meanwhile, synthetic hydrogels are constructed from synthetic polymers that can form a chemical cross-linked network with relatively high mechanical properties compared to their natural counterparts. These hydrogels have been considered for use as a scaffold in tissue engineering. However, the mechanical

properties of physical hydrogels are more easily adjustable compared with chemical cross-linked hydrogels, as well as having more flexible pore sizes based on the desired biomedical application [12].

The properties and adaptability of hydrogels have led to their potential application in tissue engineering, 3D cell culture, and drug delivery. This review focuses on the various types of hydrogels for the development of drug delivery systems. By analysing existing literature, the available methods to design hydrogels as part of a drug delivery system are determined and current challenges in this field are identified. Hydrogels can be designed with different properties based on the size, pH, charge, and hydrophobicity of drugs to stabilize the drugs and maintain drug efficacy after encapsulation. [13][14][15]. In the case, maintain the drug efficacy after encapsulating into hydrogels. Hydrogels can also be designed and modified as a controllable release system, enabling sustainable release of drugs, which would enhance drug efficiency and minimise adverse effects. In addition, injectable hydrogels are a type of smart delivery system for localised therapy. The structure of this review is divided into sections, as presented in Fig. 2.1.
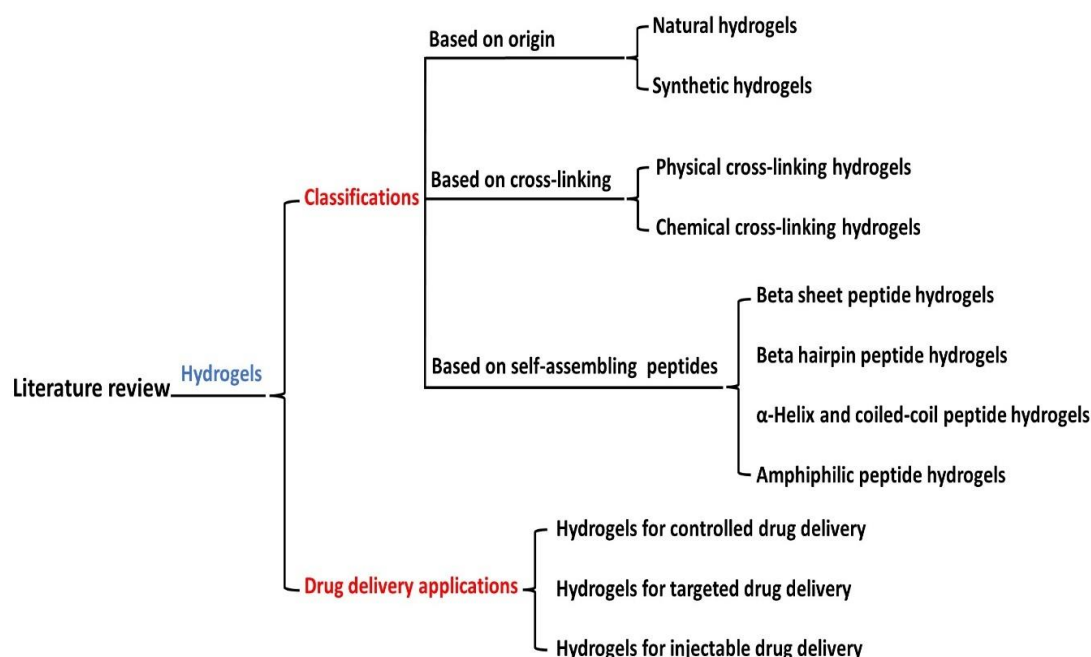
Figure 2.1 A schematic of the structure of literature review.

2.1 Classification of hydrogels

2.1.1 Based on origin

2.1.1.1 Natural hydrogels

Hydrogels derive from natural polymers, such as proteins, peptides, and polysaccharides [16]. This kind of hydrogels mean they are highly valuable for biomedical research, preclinical testing, and clinical trials.

Alginate is a common polysaccharide that can be isolated from brown seaweed or bacteria. It consists of homopolymer blocks ($1 \rightarrow 4$ linked $\beta - D -$ mannuronate, M and $1 \rightarrow 4$ linked $\alpha - L -$ guluronate, G), which form a backbone based on varying sequences. The M region is named M $-$ block and the G region is named G $-$ block, it is the ratio of these blocks that controls the properties of alginate. In addition, alginate dissolves in water to produce a highly viscous gel, whereby water molecules become physically trapped inside the gel providing suitable

conditions for cell encapsulation [17]. In an aqueous solution containing bivalent counter ions (Ca^{2+}, Mg^{2+}, Cu^{2+}), alginate can form ionotropic hydrogels following the interaction between ions and carboxylic acid residues [17][18]. Further, the mechanical properties of alginate hydrogel are related to the affinity of bivalent ions. Spencer et al. studied the swelling state of different M/G ratios of calcium alginate gels in potassium chloride (KCl) electrolyte. The results of this study showed that when the M/G ratio (ratio of M-block residues to G – block residues) in alginate was low, the swelling volume was smaller. This indicated that Ca^{2+} has a greater binding affinity for G – block residues than M – block residues. The binding ability of Ca^{2+} in alginate was reduced due to competition between K^+ in the electrolyte and Ca^{2+}. However, G – block residues were highly bound with Ca^{2+}, leading to a more stable gel. On the other hand, the binding ability of Ca^{2+} to bind to M – block residues was lower, making it easier to exchange with K^+, resulting in an extensive swelling of the gel. These results suggested that calcium alginate hydrogels can be easily disrupted in salt solution without Ca^{2+} [19]. Alginate hydrogel can also be designed as a novel system through the use of chitosan or a short peptide sequence in drug delivery and tissue engineering [20][21].

Hydrogels made from peptides are composed of amino acid monomers that form different chain lengths via peptide bonds. This primary structure is a linear sequence and starts from the N-terminal (amino group) to the C-terminal (carboxyl group) (Fig. 2.2). Polypeptide hydrogels are extracted from natural protein sources and are commonly used in the pharmaceutical and food industries. A well-known example is gelatin, which derives from animal collagen under acidic or basic conditions. Gelatin can form a thermos-physical gel when the concentration is higher than the critical gelation concentration [22]. Furthermore, this gel is reversible based on temperature control, whilst the proline, hydroxyproline, and glycine amino acids of gelatin determine the thermal stability of the gel [23]. The acidic or basic nature of gelation also determines the different isoelectric points (IEPs) of the gelatin hydrogels; consequently, gelatin

carries different charges, which makes it valuable in drug transport and drug release studies. Ikada et al. studied the release kinetics of basic fibroblast growth factor (bFGF) in acidic gelatin with 5.0 IEP and basic gelatin with 9.0 IEP [24]. bFGF performed a fast release kinetics from basic gelatin in the initial, however, it remained a large amount of bFGF in acidic gelatin which is significant due to the positive effect on neovascularisation. These findings could be a result of the ionic complexation between bFGF and gelatin. The basic growth factor interacts ionically with acidic gelatin, and the subsequent release is proceeded by the degradation of gelatin. The initial small amount of bFGF would have diffused out in the acidic gelatin due to the uncomplexed bFGF in the hydrogel system. In this *in vitr*o setting, the release kinetics of bFGF were controlled by charge interactions.
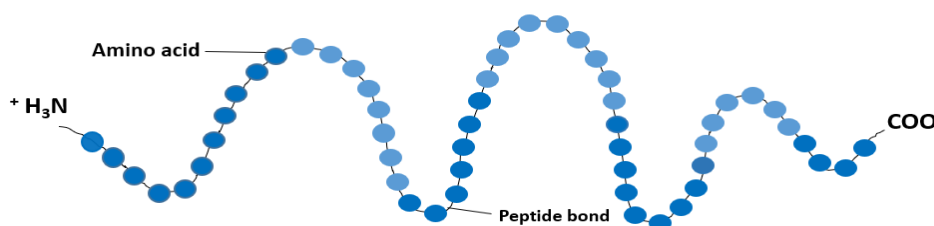
Figure 2.2 The primary structure of peptides shows a linear sequence from N terminal to C terminal linked with peptide bonds.

2.1.1.2 Synthetic hydrogels

Synthetic polymers can also be used to produce synthetic hydrogels, synthesised by chemical reactions. The mechanical properties of these synthetic hydrogels are stronger than their natural counterparts; therefore, they are regarded as promising scaffold biomaterials in the repair and regeneration of tissues [25][26].

Polyethylene glycol (PEG), also known as polyethylene oxide (PEO) and polyoxyethylene (POE) dependent on molecular weight, can be used to make a synthetic hydrogel. The molecular weight of PEG is generally less than 100,000. PEGs are amphiphilic and are soluble in water and organic solvents (benzene, chloroform, ethanol, acetone). Moreover, they are deemed ideal for hydrogel synthesis due to properties such as non-toxicity, high solubility, and biocompatibility. Following specific chemical reactions, PEG hydrogels form a network of crosslink fibres, which can be used as stable scaffolding in tissue engineering and drug delivery.

The properties of PEG-based hydrogels can be adjusted to form different structures of hydrogels. Marra et al. designed injectable PEG-based hydrogels for tissue engineering by adjusting the number of arms at the amino terminus [27]. The researchers then crosslinked these PEG hydrogels with varying concentrations of genipin, a natural crosslinking agent (Fig. 2.3). The resultant structures of four-arm amino–terminated PEG hydrogels and eight-arm amino-terminated PEG hydrogels were characterised by scanning electron microscopy (SEM), whereby porous structures were identified in the four-arm PEG hydrogels, compared with a compact structure in eight-arm PEG hydrogels. Under the lower concentration of an eight-arm PEG hydrogel, a layered structure was observed, which could be due to the lesser crosslinking with genipin. Additionally, human adipose-derived stem cells (human ASCs) were encapsulated in 35.2 mM of PEG hydrogels and the subsequent analysis found that cell adhesivity was higher in the four-arm PEG hydrogel after 6h incubation; this can be explained by the morphologies of hydrogel. In particular, the porous structure of four-arm PEG hydrogel deems it more suitable for cell attachment, which means it could serve as a potential carrier for cell therapy.
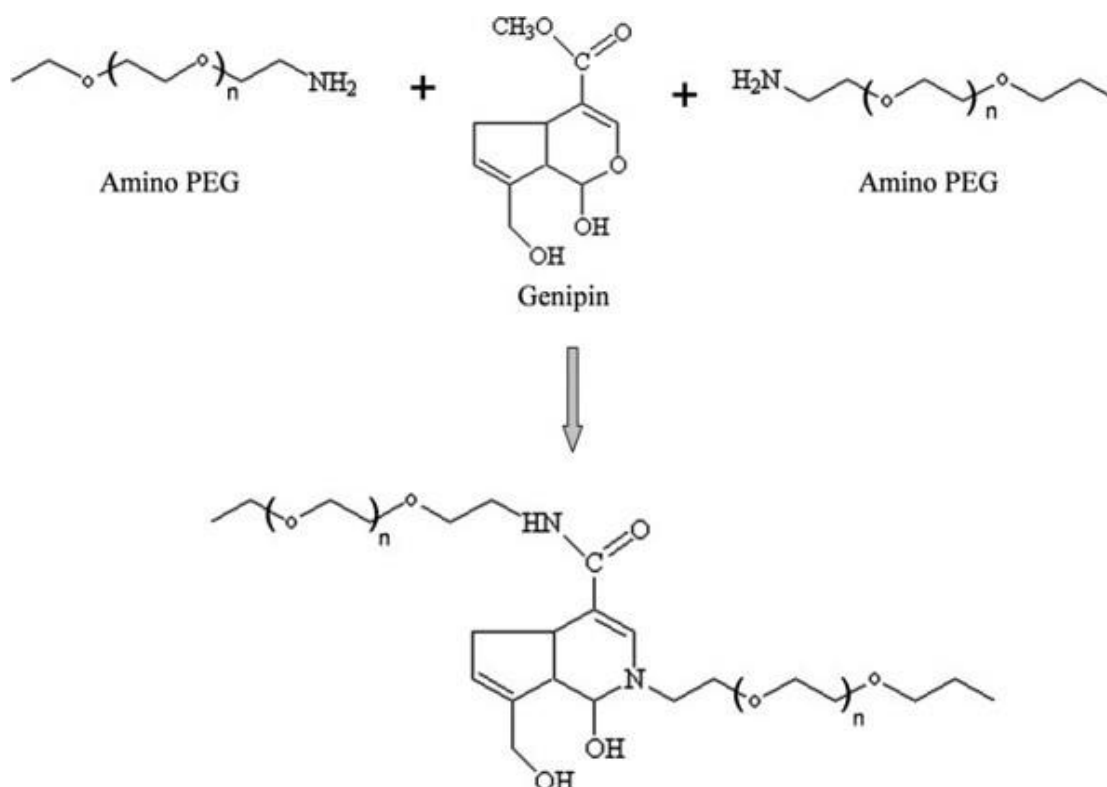
Figure 2.3 Scheme of chemical reaction process of PEG – genipin hydrogel [27].

Poly(2-hydroxyethyl methacrylate) (pHEMA) hydrogels are another commonly used type of synthetic hydrogel, first introduced by Wichterle and Lim in 1960 [28]. As smart materials, pHEMA hydrogels are used in medical and biological contexts due to their excellent biocompatibility and high water absorption. The swelling property of pHEMA hydrogel also makes it a viable tool in drug delivery systems, as the swelling ratio is proportional to the efficiency of drug delivery [25].

Gil et al. assessed the effects of pH on the properties of pHEMA crosslinked with tripropyleneglycol diacrylate (TPGDA) hydrogel, in order to determine its potential as a controlled release drug delivery system [29]. Different concentrations of TPGDA were crosslinked with pHEMA and tested with different pH values to evaluate the resultant swelling behaviour. It was found that the equilibrium swelling degree and dynamic swelling degree were related to the concentration of TPGDA and pH values. Further, the crosslinked TPGDA

influenced the mechanical properties of the pHEMA hydrogel, as a higher concentration of TPGDA induced an increased density of crosslinking. Meanwhile, pH was found to be an external factor affecting swelling behaviour; as the pH value increased, so did the swelling degree. A lower swelling degree results in a more stable hydrogel system. In another study, salicylic acid (SA) was loaded into the hydrogel and release kinetics were performed to compare the diffusion coefficients of SA under different conditions. SA was encapsulated into hydrogel and the loading capacity was dependent on the pH of the hydrogel - a higher pH induced a larger loading capacity. However, the study found that release of SA was slower in an acidic or neutral pHEMA hydrogel. Therefore, pHEMA-based hydrogel can be viewed as an ideal material for a controlled release drug delivery system by changing the pH and density of crosslinking of the hydrogel.

2.1.2 Based on cross – linking

2.1.2.1 Chemical cross – linking hydrogels

Chemical crosslinked hydrogels form as a result of covalent bonding between polymer chains; this results in stronger linkage, and thus, a permanent or irreversible gel is produced [30][31]. Chemical crosslinking occurs with a crosslinker that binds with the functional group (- NH_2, - COOH, - OH, - NCO) of polymers. Some common crosslinkers are formaldehyde, *N*, *N*-(3-dimethylaminopropyl)-*N*-ethyl carbodiimide (EDC) and epoxy compounds. Several methods can be used for this reaction to induce a gel state, including an enzymatic reaction, radical reaction (gamma, UV, electron beam), and photopolymerisation. In comparison to physical crosslinked hydrogels, chemical crosslinked hydrogels possess superior mechanical properties, have better durability for application purposes, and are more stable [32].

Enzymatic crosslinked hydrogels form a stable network that can be used for 3D cell seeding. For example, Griffith and Sperinde synthesised a PEG-based hydrogel through an enzymatic

reaction, which resulted in a feasible cell-laden hydrogel that could potentially be useful in tissue engineering [33]. The authors used transglutaminase (TG) as a crosslinker between PEG and polypeptide containing lysine (poly (KF)) to form a network. The mechanism of such reactions is based on the specific substrate used, as shown in Fig. 2.4. The study results found that TG activity was unaffected by the incorporation of long chain PEG, and therefore, the increased half-life of the enzyme deemed it suitable for therapy *in vivo* [34]. In addition, swelling and gelation behaviours were examined when hydrogels were made with different ratios of PEG-Q_a/poly (KF)·HBr. It was established that the ratio of gel composition influenced the appearance, mechanical properties, and swelling ratio of the hydrogel. Therefore, the ratio could be manipulated to produce an optimal condition for cell scaffolding.
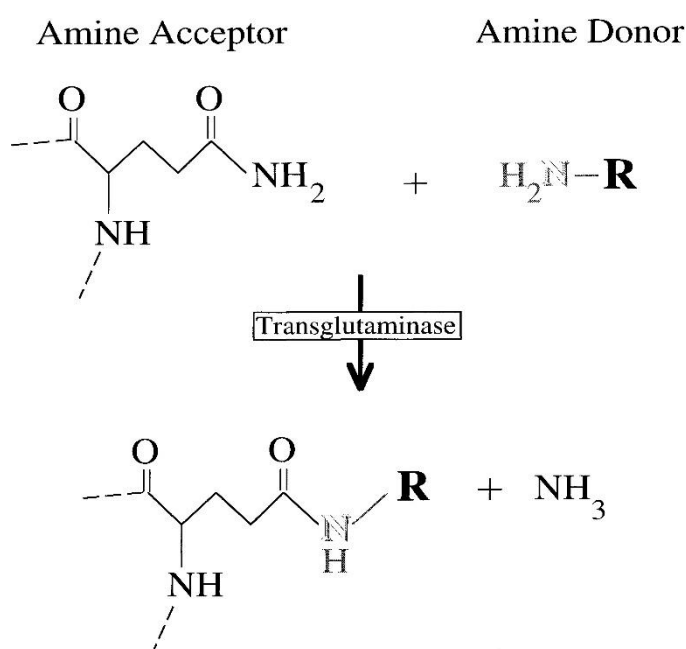
Figure 2.4 Chemical cross – linking process based on transglutaminase reaction [33].

Photo crosslinking hydrogels can also be functionalised under light, causing photopolymerisation. This form of hydrogel is popular in biomedical applications [35]. For

example, gelatin methacryloyl (GelMA) hydrogels are used in tissue engineering, drug delivery systems, and bio-sensing due to their biocompatibility, biodegradability, and bioactivity [36][37][38][39]. Tezcaner et al. prepared a photo crosslinked pectin/gelatin hydrogel for curcumin release as part of a wound dressing [40]. Different ratios of methacrylated pectin (PeMA) and methacrylated gelatin (GelMA) were exposed to UV light to form the photo crosslinked hydrogels. SEM was used to determine the pore size of the resultant hydrogels, whereby it was found that a higher concentration of PeMA induced a larger pore size (43.58 $\pm$ 5.60 um). In contrast, a higher concentration of GelMA resulted in a decreased pore size (26.78 $\pm$ 4.80 um), which facilitated photo crosslinking. Overall, it was established that the network density of photo crosslinked hydrogels depends on the ratio of PeMA/GelMA. The study also found that the release kinetics of curcumin and the swelling ratio of the hydrogels were reliant on the pH value, thereby illustrating the potential of this hydrogel as a wound healing material for chronic wounds on basic skin [41], as curcumin release was highest at pH 7.4 after 14 days. In addition, this type of photo crosslinked hydrogel demonstrates strong compatibility, antibacterial activities, micron pore size, and pH sensitivity release kinetics, deeming it a smart biomaterial for wound dressing.

Bertassoni et al. prepared photopolymerised GelMA hydrogels under two conditions: dental curing light (DL) and UV light [37]. The polymerisation time of GelMA by DL was faster than UV (20 seconds vs. 50 seconds), but resulted in a larger pore size than UV photopolymerisation following SEM analysis. It was also demonstrated that the exposure time of DL could influence the porosity, degradability, cell viability, and elasticity of GelMA hydrogel. Compared with the more familiar UV method, a DL method for the polymerisation of hydrogel showed impressive bioactivities and mechanical properties, thus implying its potential use in dental care.

2.1.2.2 Physical cross – linking hydrogels

Physical crosslinked hydrogels form through molecular entanglements, hydrogen bonding, hydrophobic interactions, charge interactions, and supramolecular chemistry (intermolecular forces) [30]. These hydrogels mimic natural soft tissue due to their high water content and are insoluble due to their 3D network structure. They are also highly biocompatible as there are no chemical reactions that result in toxicity. However, the hydrogels are reversible as the crosslinking occurs under pure physical conditions [42]. Moreover, they are flexible due to the easy transition between gel and solution, thus supporting their use in injectable pharmaceuticals.

Charge interaction is the most common method of hydrogel formation. For example, physical crosslinking occurs through a positively charged polymer with a negatively charged molecule or polymer [43]. Langer et al. designed an injectable polymer-nanoparticle (PNP) hydrogel based on electrostatic interaction, whereby PEG-b-PLA was prepared as the nanoparticles (NPs) and negatively charged biopolymers, carboxymethylcellulose (CBMC) and hyaluronic acid (HA), were used for hydrogel formation [44]. A cationic molecule, cetyltrimethylammonium bromide (CTAB), was applied as a surfactant to ascertain the effect of electrostatic interaction on the mechanical properties of the hydrogel. According to the oscillatory shear modulus G', a higher concentration of CTAB (0.5%) with CBMC-NPs produced a more robust hydrogel. However, the shear modulus G' of HA-NPs was not dependent on the concentration of CTAB. Meanwhile, the HA-NPs formed a gel state. These results occurred due to the charges of CBMC and HA, as HA has a lower negative charge (-7.8 $\pm$ 1.2 mV) compared with CBMC (-29.7 $\pm$ 2.0 mV). Thus, a stronger charge interaction resulted between CMBC and CTAB, and induced a higher G'. The recovery properties of the hydrogels were also contingent on the charge interaction. A higher concentration of CTAB (0.5%) resulted in a more rapid recovery rate of the CBMC-NPs hydrogel. The variable mechanical properties of PNP hydrogels make them universally applicable for a range of pharmaceutical purposes.

As mentioned, hydrogen bonding also contributes to the creation of hydrogels. Wang et al. studied the mechanical properties of physical crosslinked hydrogel that had been formed by hydrogen bonding and entanglements of polymer chains [45][46]. Specifically, cooperative hydrogen bonding occurred between poly (N – vinylpyrrolidone) (PVP) and aqueous acrylamide (AAm), as well as non-cooperative hydrogen bonding between PAAm chains, resulting in PVP–*in situ*–PAAm hydrogel (Fig. 2.5). To study the effects of hydrogen bonding on the mechanical properties of hydrogels, different monomer ratios of AAm and PVP (C_{AAm}/C_{VP}) were used at a moderate temperature. Rheology testing measured the viscoelastic behaviour of the resultant PVP–*in situ*–PAAm hydrogels, the results of which showed that the storage modulus G' was mainly dependent on the ratio of C_{AAm}/C_{VP}. When the C_{AAm}/C_{VP} ration increased, a solid elastic-like material was produced. The excess PAAm chains that involved non-cooperative hydrogen bonding underwent entanglement together to increase the G' of the hydrogel.
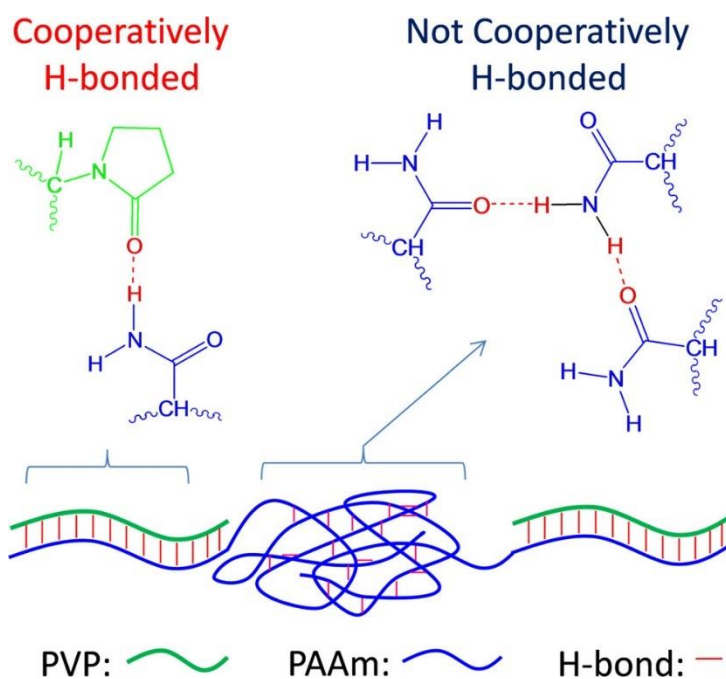
Figure 2.5 A schematic of PVP – in situ – PAAm hydrogel formed through cooperative hydrogen bonding between PVP and PAAm, and non-cooperative hydrogen bonding between PAAm chains [45].

The study further explored the effect of hydrogen bonding on hydrogel behaviour by implementing urea to compete at the hydrogen bonding site in PVP–*in situ*–PAAm hydrogel. This gel presented a relatively low G' compared with the control gel; this likely occurred due to the NH_2 groups in urea molecules replacing the hydrogen bonds between PVP and PAAm. Thus, urea is able to influence the effectivity of the cross–linking network by disrupting the formation of hydrogen bonds. The authors concluded that the concentration of hydrogen bonding is a driving force of the mechanical properties of hydrogel. A higher C_{AAm}/C_{VP} ratio contained more hydrogen bonding and polymer entanglements, and therefore, contributed to a higher G'. However, under the condition of greater stress than the strength of the hydrogen bonding, this hydrogel can undergo deformation to become a viscous liquid. This physical crosslinked hydrogel was also found to be reversible, with the recovery rate relying on its composition (C_{AAm}/C_{VP}), temperature, and strain [45].

Polymers that contain hydrophobic segments can be crosslinked through hydrophobic interactions at a specific temperature. Fig. 2.6. illustrates the mechanism of gelation [47]. The hydrophobic segments couple with hydrophilic segments to create an amphiphilic polymer that is soluble in water at a low temperature. However, at higher temperatures, the hydrophobic domains aggregate internally to prevent the hydrophobic surface from reaching bulk water. Hence, the ordered water molecules are reduced and the entropy of the solvent is increased. The gelation process is intricately linked to temperature, length of the hydrophobic segment, and the concentration and chemical structure of the polymers [43].
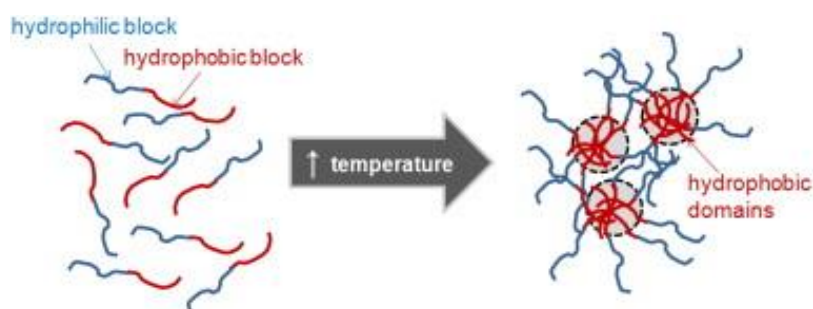
Figure 2.6 A schematic of the mechanism of physical cross – linking network through hydrophobic interactions [47].

Hennink et al. worked to characterise the mechanical properties of thermosensitive triblock copolymer hydrogels under different conditions [48]. The triblock copolymer (ABA) consisted of poly (N-(2-hydroxypropyl) methacrylamide lactate), referred to as A–block (pHPMAm – lactate), hydrophilic poly (ethylene glycol), referred to as B–block, and another A-block. The rheological properties of the hydrogel varied with the concentration of the polymers, the temperature, and the length of the A-block. In particular, an increase in the temperature and concentration of the polymers resulted in a higher G'. However, as the length of the A-block chains increased, the gel became weaker. Thus, the shorter the chains of the polymers, the

greater the density of the physical crosslinked network. The optimal temperature of gelation for this thermosensitive hydrogel was 37℃, thus demonstrating its potential as an injectable formulation for drug delivery applications.

2.1.3 Based on self-assembling peptides

2.1.3.1 Beta sheet peptide hydrogels

Beta sheets are a typical structure of proteins and peptides and can include parallel and anti-parallel configurations, as identified by Pauling and Corey in the 1950s [49]. The beta sheet structure is based on hydrogen bonding between the carbonyl oxygen of one peptide chain and the amide hydrogen of another peptide chain. When adjacent peptide chains present the same orientation, a parallel beta sheet is produced via hydrogen bonds. Fig. 2.7A shows the parallel orientation of the beta sheet when all the chains start from the N terminus to the C terminus, whilst Fig. 2.7B displays the orientation of the beta sheet when the N terminus and C terminus run in opposing directions, subsequently referred to as an anti-parallel beta sheet.

Beta sheets
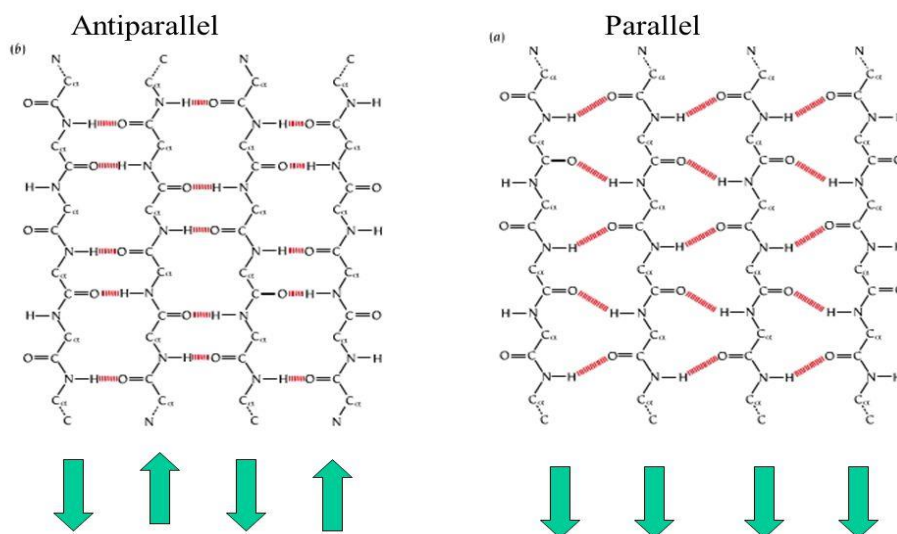
Figure 2.7 A diagram that demonstrate the formation of parallel beta sheet and anti-parallel beta sheet (http://slideplayer.com/slide/4918741/).

The beta sheet structure can additionally be formed through the actions of hydrophobic and hydrophilic residues in peptide chains. These residues establish a hydrophobic face and a hydrophilic face during the process of self-assembly of the beta sheet configurations. The hydrophobic faces can potentially overlap inside the structure, which accounts for the hydrophilic property of peptides (Fig. 2.8). Peptides self-assemble into different hierarchical structures based on the number of folded beta sheets; such structures include tapes, tubes, ribbons, spheres, fibrils, and fibres. Then, further adjustments can be made to the structure by altering the amino acids, peptide concentration, or ionic environment, thereby enabling the generation of a range of peptide materials for biomedical applications [50].
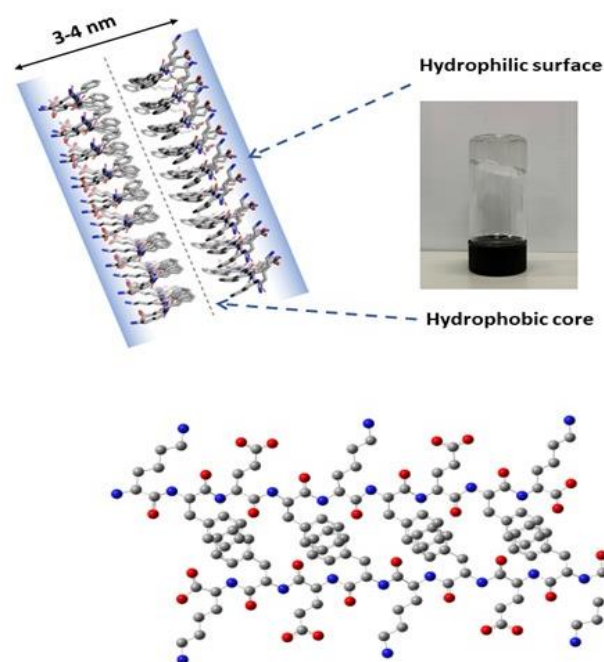
Figure 2. 8 The formation of antiparallel beta sheet structure, the peptide illustrated here is KFEFKFEFK. The hydrophobic faces formed by the benzene rings of phenylalanine that buried inside the structure.

Self-assembled peptides are created by alternating the charge residues of amino acids $(+ -)$ or by interchanging the hydrophobic and hydrophilic residues of the amino acids. Zhang et al. identified a representative peptide which was subsequently known as the EAK16 family, also known as an ionic complementary peptide [51]. This peptide has a hydrophilic surface based on the alternating positively charged amino acid residue K (lysine) and the negatively charged amino acid residue E (glutamic acid). The sequence can be transformed by changing the charge modulus. For example, EAK16–I consists of the following charge arrangement: AEAKAEAKAEAKAEAK $(- + - + - + - +)$; meanwhile, EAK16–II has the charge arrangement of AEAEAKAKAEAEAKAK $(- - + + - - + +)$. Overall, this peptide forms a

52

self-assembled beta sheet for a hydrogel that can be employed for 3D cell culture, tissue engineering, and drug delivery [52].

EAK16–II was initially identified in zuotin, a Z-DNA binding protein, and was shown to be able to self-assemble into a maintained stable beta sheet structure at a lower concentration in water. Zhang et al. also demonstrated the relation between the stability of the beta sheet structure and the chirality of the amino acids of EAK16 peptides. Furthermore, adjusting the pH value or increasing the temperature did not disrupt D-EAK16 hydrogel [53][54]. Therefore, this hydrogel is well-structured and consequently provides a solid 3D environment for cell scaffolds [55].

Zheng et al. compared the structures, morphologies, mechanical properties, and biological activities of D-EAK16-II hydrogel and l–EAK16–II hydrogel [56]. The results highlighted the greater sensitivity of the secondary structure of D-EAK16-II in phosphate-buffered saline (PBS), whereby stronger variation was observed according to the circular dichroism spectra. The study incubated the two hydrogels with Na^+ and K^+ and subsequently measured their mechanical properties. At a concentration of 1 mg/mL, the G' of D-EAK16-II hydrogel showed an increase in salt solution (0.01 M PBS, Na^+/K^+). However, at a higher concentration (20 mg/mL), the D-EAK16-II hydrogel in salt solution presented similar mechanical properties to that of the lower concentration hydrogel. The process of self-assembly was controlled by the ions in salt, which affected the rigidity of the hydrogels; this is an important factor for 3D cell culture. The study also found that the D-EAK16-II hydrogel could resist protease digestion based on its morphology, as shown under atomic force microscopy (AFM). In the context of the 3D cell culture SMMC7721, EAK16-I hydrogel presented good biocompatibility. However, the D-EAK16-II hydrogel had higher cell viability, less cell apoptosis, and faster haemostasis, thus providing an ideal microenvironment for the design of advanced biomaterials for wound healing.

The study of the EAK16-II hydrogel also identified its ability to self-assemble into a network of nanofibrils when a pH of 11 is reached from pH 4. Another member of the EAK16 family that can self-assemble into various nanostructures is EAK16-IV (AEAEAEAEAKAKAKAK) [57]. A change of configuration was observed when the pH of EAK16-IV became ~ 6.71 [58]. At a neutral pH, EAK16-IV presented a globular structure, whilst a fibrillar structure was distinguished when the pH was lower than 6.5 or higher than 7.5. An explanation of this is the charge distribution of EAK16-IV, as at ~ pH 7, there would be a strong electrostatic attraction between negatively charged glutamine (E) and positively charged lysine (K), thereby causing a bending of the molecules. Resultantly, the intramolecular charge attraction of the hydrophilic E and K amino acid produces a hydrophilic core, whilst the hydrophobic alanine (A) remains exposed externally, establishing the overall globular structure. Additionally, when the pH is above or below 7, the charge of E or K is neutralised, which diminishes the electrostatic attraction. As this force is not strong enough to bend the molecules, EAK16-IV assembles as a straight fibrillar structure. Thus, the design of self-assembled peptide hydrogels can be regulated by altering the amino acid composition and the pH value.

Another common self-assembled beta sheet peptide hydrogel is FEFKFEFK (F8), which involves alternating hydrophobic and hydrophilic amino acids. The critical gelation concentration of F8 is ~ 5 mg/mL at pH 4, at which point it self-assembles into a transparent hydrogel that can be used as an injectable formulation for tissue engineering [59]. As found by Wychowaniec, F8 maintains a clear gel state in an acidic (~ pH 4) or basic (~ pH 9) environment [9]. In another study, Ligorio prepared F8 hydrogels at pH 4 and pH 9 to encapsulate nucleus pulposus (NP) cells. At both pH values, the hydrogels produced a similar level of cell viability and gene expression. Therefore, F8 in an acidic or basic environment shows potential as a platform for cell screening and survival [60].

2.1.3.2 Beta hairpin peptide hydrogels

The beta hairpin is another key structure with similarities to beta sheets, comprising two beta strands linked by a loop sequence. These two strands are stabilised through hydrogen bonds to maintain the folded structure. Schneider et al. designed the first MAX peptide, MAX1 (H_2N-VKVKVKVK-V^{D}PPT-KVKVKVKV-NH_2), consisting of a basic beta hairpin structure, to investigate intramolecular folding [61][62]. MAX1 contains 20 amino acids and is made up of two beta sheet strands with alternating hydrophobic valine (V) and hydrophilic lysine (K) residues. These amphiphilic strands are linked by a type II′ β-turn sequence -V^{D}PPT-, resulting in a tight hairpin motif following hydrogen bonding between residues (Fig. 2.9). However, the peptide can fold in different conditions (Fig. 2.10) [63]. In an acidic environment or lower ionic strength, K is protonated, leading to disorder of the MAX1 peptide or a monomeric state due to electrostatic repulsion in K residues. However, when the pH increases to ~ 9 or a higher ionic state, the peptide folds into a hairpin structure and then self-assembles into beta sheet fibrils. The hairpin arrangement occurs as a result of intramolecular folding via van der Waals forces and hydrogen bonding, whilst the subsequent beta sheet layer formation occurs through hydrophobic interaction, hydrogen bonding, and van der Waals forces. Specifically, the hydrophobic faces of amino acid V collapse together to form a beta sheet bilayer. Therefore, MAX1 peptide self-assembles into a hydrogel with nano fibrils (3 nm) through non-covalent bonds, which makes it viable for tissue engineering and drug delivery systems [64][65][66].
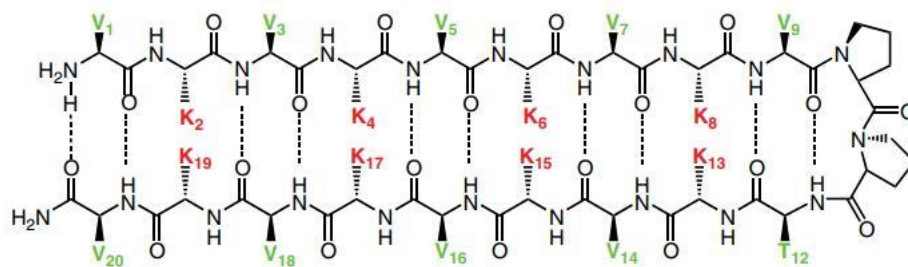
Figure 2. 9 Characterization of MAX1 peptide with beta – hairpin structure, Valine amino acid residues are labelled with green colour, Lysine amino acid residues are labelled with red colour, the dash lines present the formation of hydrogel bonding between two strands. These two strands are linked by a type II′ β-turn sequence [63].
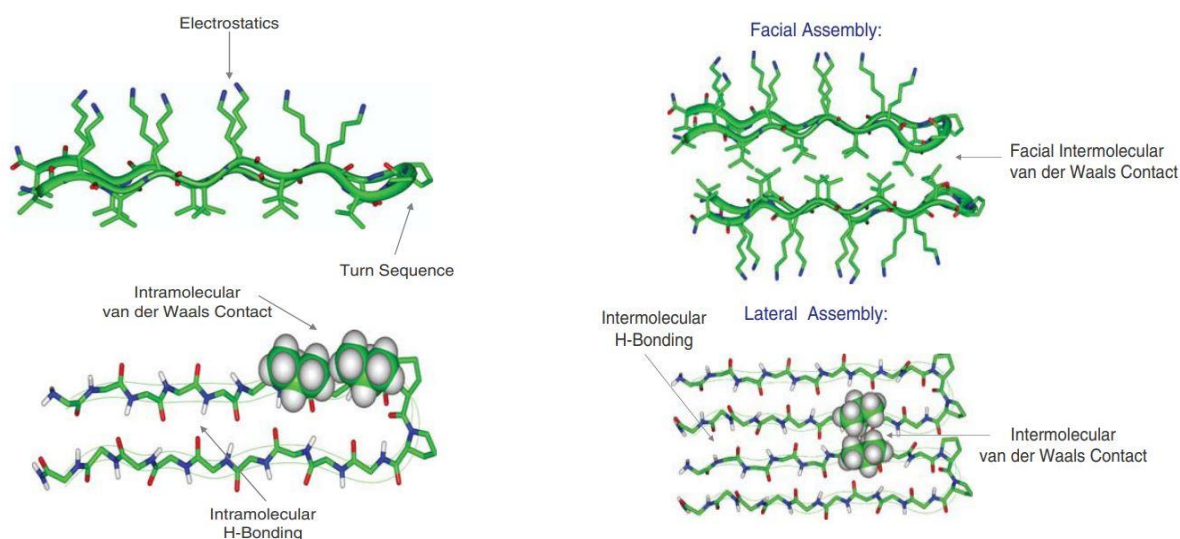
Figure 2.10 Model of beta – hairpin peptide undergoes folding and self – assembling process through intramolecular and intermolecular factors [63].

The mechanical properties of self-assembled MAX1 hydrogel vary based on pH, ionic strength, and temperature [67][68]. However, its rigidity and cytocompatibility have led to its application in tissue scaffolding, whereby the folding and assembly of MAX1 into a hydrogel

is stimulated by the addition of Dulbecco's Modified Eagle's Medium (DMEM) containing a high salt content and pH 7.4. DMEM can also screen the charge of each lysine residue, thereby facilitating the beta hairpin folding, self-assembly, and hydrogel formation [69]. It has been found that MAX1 hydrogel possesses antibacterial properties based on the inhibition of both Gram-negative and Gram–positive bacteria. Research has also indicated that MAX1 is nonhaemolytic as the surface of the hydrogel did not result in the lysis of human red blood cells (hRBC's) according to the haemoglobin measurements. Nonetheless, it has been established as a multi-functional hydrogel that can inhibit bacterial growth and induce cell adhesion and cell proliferation [70].

Several derivatives of MAX1 have been modified for specific applications. For example, the fifteenth amino acid K was replaced by the negative residue glutamic acid (E) to produce MAX8 (H_2N-VKVKVKVK-V^DPPT-KVKEKVKV-NH_2). As the overall positive charges had been altered by this replacement, charge screening would take longer. In a comparison of MAX8 and MAX1, MAX8 performed a more rapid gelation kinetic at pH 7.4, and also had a more homogenous network after self-assembly into a hydrogel. As a result, MAX8 presented a stiffer gel state even at a low concentration (0.5 wt%). It was concluded that MAX8 is more suitable for cell encapsulation due to the greater homogenous distribution [71]. However, both MAX1 and MAX8 would be useful materials for injection therapy based on their shear thinning/recovery properties. In an *in vitro* study, neither hydrogel caused inflammation, as depicted by macrophage viability. Therefore, MAX1 and MAX8 could potentially prevent or limit the inflammatory immune response in an *in vivo* implant, which could advance regenerative tissue engineering [72].

2.1.3.3 α – helix and coiled – coil peptide hydrogels

Peptides that self-assemble into coiled-coils consist of several α – helices. These α – helical structures are found in parallel or antiparallel orientation to form super helical bundles under specific conditions, as initially determined by Pauling, Corey, and Crick [50].

Heptad repeats are a typical motif of the coiled-coil structure and are presented as a helical wheel containing seven amino acids, denoted as a to g in Fig. 2.10. The coiled-coil structure is stable as a result of the hydrophobic interactions between the first residue "a" and the fourth residue "d", as well as electrostatic attraction between the fifth residue "e" and the seventh residue "g". The hydrophobic residues unite to form a hydrophobic core, contributing to the stable interface. Additionally, the coiled-coil orientation can be controlled based on the specific charge pattern: charge attraction contributes to a parallel orientation, whilst charge repulsion contributes to an antiparallel orientation that destabilises the coiled-coil formation. Further, the "b", "c", and "f" residues should be hydrophilic amino acids so as to induce a helical structure when exposed to solvent [73][74].
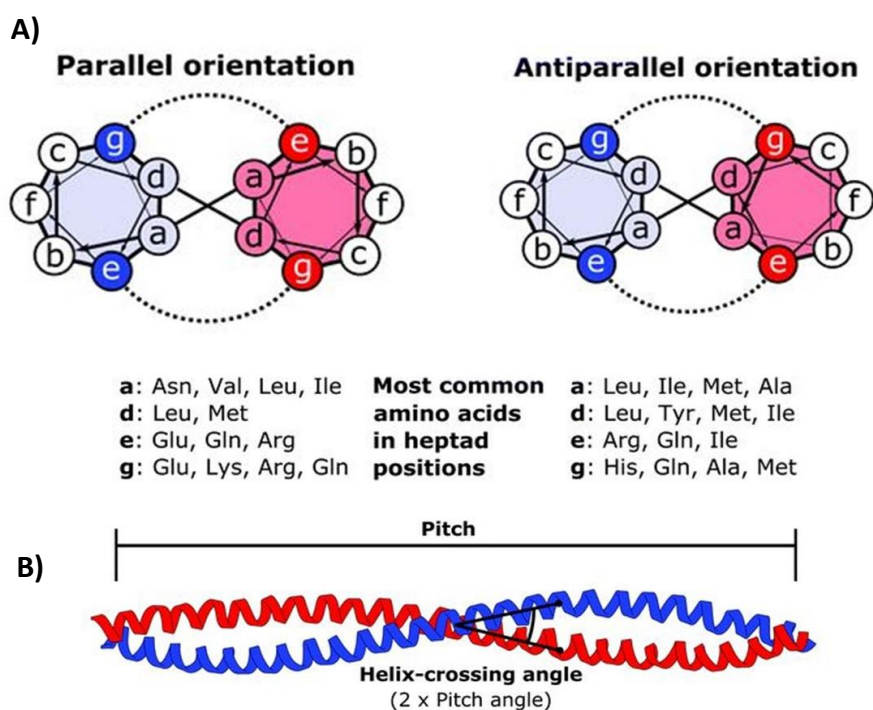
Figure 2.11 A) A representation of heptad wheels as parallel orientation and antiparallel orientation. B) The diagram of coiled coil chains [75].

Dexter et al. designed a coiled-coil peptide hydrogel based on the classic heptad structure (abcdefg) [76]. This 21 residue peptide was named AFD19 (Ac-LKELAKV LHELAKL VSEALHA-CONH$_2$, FW 2354); it could form a single helical peptide and could self-assemble into long fibres depending on the pH value. Leucine (L), valine (V), and alanine (A) are hydrophobic residues that are located at positions "a" and "d". However, Dexter et al. expanded the hydrophobic core to position "e" and "g", which resulted in increased oligomerisation of the coiled-coil structure and subsequently formed a thermally stable, self-assembled peptide hydrogel. The charged residues were now located at positions "b", "c", and "f". It was also found that the distribution of variously charged residues controlled the molecular charge of the peptide, which then determined the gelation pH. According to the phase diagram of AFD19, a

clear gel state occurs at pH 6 and pH 10.7, which corresponds to a molecular charge of +1 and -1, respectively. The ability of a coiled-coil peptide to self-assemble into a hydrogel depends on the pH, and therefore there has been an interest in the potential biological applications of such a hydrogel.

Conventionally, the coiled-coil structure was designed based on the creation of specific charge interactions between positions "b" and "c", resulting in fibres with a highly ordered thickness [77]. However, Woolfson et al. altered the specific interactions between "b", "c", and "f", to create a flexible network with comparatively thinner fibres. From their study, the authors had constructed a biocompatible peptide suitable for cell culture [8]. This hydrogel self-assembled into an α–helical structure that was referred to as hydrogelating self–assembling fibres (hSAFs). Positions "b", "c", and "f" consisted of glutamine (Q) or alanine (A) residues. The role of Q residues was to induce the formation of hydrogen bonds, whilst the A residues were used to induce hydrophobic interactions. The hSAF$_{AAA}$ peptide with A residues at positions "b", "c", and "f" produced a weak gel at lower temperatures, but heating was found to increase the gel strength. Whilst this gel could not be melted at 95 ℃, the hSAF$_{QQQ}$ peptide with Q residues at positions "b", "c", and "f" did show a gel-liquid transition based on temperature. Specifically, it formed a gel state at low temperatures, but a liquid-like state at ~ 16 to 19 ℃, before returning to a gel state at a higher temperature. Both of these hSAF peptide hydrogels contained an α-helical structure that was characterised by circular dichroism (CD) and X-ray fibre diffraction (XRD). However, X-ray results illustrated a cross-β structure also in the hSAF$_{QQQ}$ hydrogel, thus indicating that a high content of glutamine residues promotes assembly into the β-sheet structure.

In addition, the hSAF$_{AAA}$ hydrogel was shown to be stable in PBS and cell culture media during the cell culture process. To further increase the stability of the hydrogel for cell culture, the A residue was replaced with tryptophan (W) due to its greater hydrophobicity; the subsequent

product was named hSAF$_{AAA-W}$. Further testing showed that this hydrogel supported cell growth and cell differentiation, suggesting its viability as a scaffold for cell culture and tissue engineering.

The outer surface distribution of the coiled-coil structure determines the properties of peptide hydrogels. For example, the glutamine residues at the outer surface ("b" "c" "f") induced the creation of a hydrogen bonding crosslinked network that was easily breakable by warming. It has also been found that the alanine residues at the outer surface contribute to a hydrophobic crosslinked network, which forms a comparatively stronger gel that maintains stability at 95 ℃. Yet, the structure is unable to form a gel state when the chemical uniformity at the outer surface is disrupted at the outer surface.

2.1.3.4 Amphiphilic peptide hydrogels

Peptide amphiphiles (PA) are a class of peptides composed of alternating hydrophobic and hydrophilic residues to form self-assembled nanostructures [78]. Normally, the structure begins with a hydrophobic chain containing 12 to 16 carbons, referred to as the alkyl tail, followed by a sequence that can form a beta sheet with other peptide fragments, a charge sequence, and then finally a hydrophilic sequence. For example, a bioactive peptide sequence may be at the end of the chain, resulting in a PA that has functional therapeutic use (Fig. 2.12). This type of peptide has the potential to self-assemble into nanofibers when in a suitable environment. The typical geometry of this structure is a cylinder with a hydrophobic core and an alkyl tail, whereby the peptide is embedded into the core and can subsequently form the beta sheet structure (Fig. 2.12). The diameter of the nanofibers can be adjusted by altering the length of the alkyl tail, whilst the solubility of PAs can be increased through the charged amino acids [79].
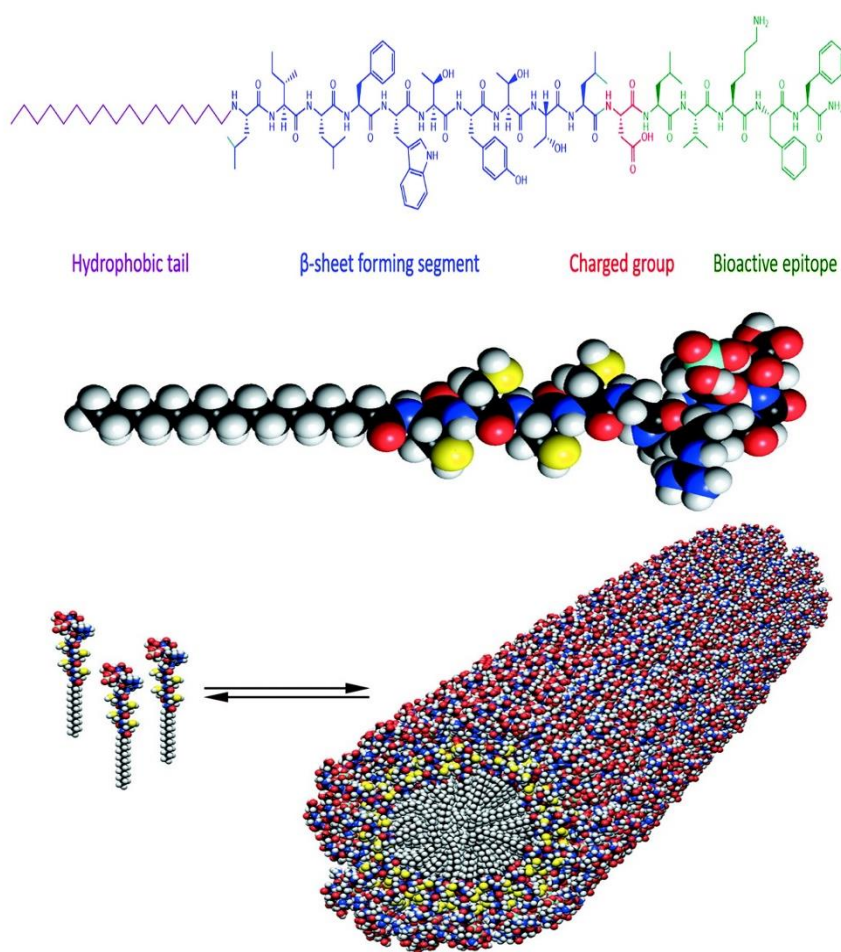
Figure 2.12 A typical scheme for the interpretation of the structure of amphiphilic peptides and the formation of cylindrical micelle [80][81].

The modifiable properties of PAs deem them promising candidates for drug delivery systems as they could facilitate the encapsulation of drugs and control drug release at the target site. Jo et al. studied a peptide containing a cell-adhesive sequence GTAGLIGQRGDS (MMP-2) and synthesised a PA $(CH_3(CH_2)_{14}CONH\text{-}GTAGLIGQRGDS\text{-}COOH)$ with the intention of developing a bio-responsive cisplatin (cis-diamminedichlo-platinum, CDDP) delivery system [82]. This CDDP-PA self-assembled into a hydrogel through the formation of a physical crosslinked network with nanofibers, as observed by transmission electron microscopy. The hydrophobic alkyl tail in the PA promoted the self-assembly process, whilst hydrogen bonding

of the G, A, and L residues stabilised the cylindrical nanofibers, thus forming the nanofiber network. CDDP was subsequently complexed with the carboxylic groups of PA, creating a nanofiber hydrogel. Relative to a calcium induced PA gel, the storage modulus G' of the CDDP-PA hydrogel was greater, thereby demonstrating that the interaction between CDDP and carboxylic groups contributed to a more stable network [83].

A major finding of the study was that the release of the CDDP-peptide complex was achieved by the MMP-2 sequence. The proteolysis of MMP-2 triggered the degradation of the nanofiber network, resulting in the CDDP-PA complexes diffusing out; as they contained integrin-binding RGDS, they were recognised by cancer cells. An advantage of CDDP-PA is its lower cytotoxicity compared with other current therapies in clinical trials. Therefore, PA should be viewed as a prospective biomimetic material to develop the anticancer drug delivery system.

RADA16 ($[COCH_3]$-RADARADARADARADA-$[CONH_2]$) is another common PA that can self-assemble into beta sheet hydrogels for controlled release drug delivery or to be used as scaffolds for tissue engineering [52][84]. This PA comprises 16 amino acids with alternating hydrophobic and hydrophilic residues. The dye-binding assays of Congo red and thioflavin T were used to study the self-assembly process, and consequently elucidated the beta sheet structure of the peptide [85]. The helical structure in RADA16 decreased in environments of pH 3 and pH4 in a solution state. At pH 5, the structure remained stable for 120 days. At pH 7 or less, the physiological salt self–assembled into the beta sheet structure with a pore size network of 5 – 200 nm, and presented in a gel state. The stability of the secondary structure of RADA16 was found to be dependent on the pH and temperature [86].

Muraoka et al. studied the effect of glycine substitution on the mechanical properties and cell adhesivity of RADA16 PA hydrogels [87]. In particular, glycine replacement of alanine (A) at positions 4, 8, 12, and 16 was performed to generate four distinct gels: A4G, A8G, A12G,

andA16G, respectively. Compared with RADA16, the position of substitution was shown to affect the gelation properties. When glycine was added at the acentric (A4G) or end position (A16G), a weaker gel was formed, whilst glycine at position 12 (A12G) inhibited gel formation. In contrast, glycine added at the centre of the peptide sequence (A8G) resulted in the creation of a stiffer gel. The A8G gel depicted a twisted beta sheet structure and was shown to form bundles of nanofibers under the CD, ATR–IR spectra, and TEM observations. Moreover, the A8G hydrogel had strong cell adhesivity and was a thermally reversible hydrogel. Overall, the structures, mechanical properties, and gelation properties of PA hydrogels can be altered by the substitution of a single amino acid. This should be considered a novel method in the construction of diverse materials for future biological applications [88].

2.2 Drug delivery applications

Drugs administrated without carriers can cause adverse effects in patients due to issues such as incorrect dosage, short half-life, narrow therapy window or drug accumulation due to repeated administration. In the case, resulting in relatively low drug efficacy. Hydrogels, as an alternative method, form a 3D network with high water content (70% - 99%) which can encapsulate drug molecules to ensure sustained drug release or localised delivery. This can prolong the half-life of drugs and improve drug efficiency [3].

The mesh size of the hydrogel network can be amended to correspond with the size of the target drug, meaning the desired controlled release kinetics can be achieved. For example, the concentration of hydrogels can be increased to reduce the mesh size, leading to a greater density network. This is important as different sizes of drugs have different rates of diffusion [14]. Moreover, hydrogels can be designed with good biocompatibility and biodegradability, which enables them to avoid the toxicity in the human body. Hydrogels that have been formed in an aqueous environment prevent drug denaturation and aggregation in organic solvents. The

crosslinked networks of hydrogels can also restrict the early degradation of bioactive molecules by enzymes, thereby stabilising drug activity and achieving the target therapy [89]. This is especially so for macromolecule drugs, such as antibodies, proteins, and cytokines.

The changeable structures, pore sizes, and mechanical properties of hydrogels make them ideal for use in drug delivery systems, especially as they can be designed to suit various routes of drug administration. Some of the more common hydrogel drug delivery systems will be discussed in the following section, along with an overview of the advantages of hydrogels for this therapeutic purpose.

2.2.1 Hydrogels for controlled drug delivery

A controlled release delivery system can be designed based on different mechanisms, including diffusion controlled, swelling controlled, and chemically controlled [90]. Diffusion controlled involves the most common form of drug release kinetics in the hydrogel drug delivery system. Zhang et al. focused on the controlled release of model drug molecules in ionic complementary peptide hydrogel [91]. The authors calculated the diffusion coefficients of the drug molecules using Fick's second law. Their protocol involved adding a drug-loading gel into a cylinder vial to form a thin film, described as thickness H (Fig. 2.13). The diffusion coefficient D_E can be obtained as shown in Eq. 2.1:

$$\frac{M_t}{M_\infty} = \left(\frac{16 D_E t}{\pi H^2}\right)^{0.5} \tag{2.1}$$

where t is the release time, and M_t and M_∞ are the mass of fraction drug release. Specifically, M_t refers to the molecular mass at a specific time point, while M_∞ is the saturated molecular mass diffused out of the hydrogels. Eq. 2.1 was used for the early time release of mass $< 60\%$, *i.e.* $0 < M_t/M_\infty < 0.6$ [92][93]. Meanwhile, Eq. 2.2 was used for the late time release of mass, *i.e.* $M_t/M_\infty > 0.6$.

$$\frac{M_t}{M_\infty} = 1 - \left(\frac{8}{\pi^2}\right) exp\left[-\frac{(\pi^2 D_L t)}{H^2}\right] \tag{2.2}$$
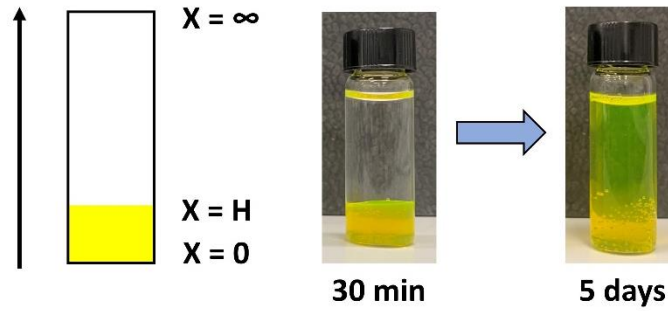
Figure 2. 13 A model of release experiment performed in 5 days, the pictures were the fluorescein – dextran in peptide hydrogel. The diffusion coefficient was calculated at 30 min and day 5 based on the definition sketch on the left picture [91].

Mathematical models have also been employed to analyse the transport mechanisms of drugs to be able to predict release kinetics and formulate an optimal drug delivery system. Such models include Higuchi, Ritger–Peppas, Peppas–Sahlin, and zero-order kinetics.

The Higuchi model can be used to predict drug release kinetics from semisolid and solid matrix systems. The corresponding equation is based on Fickian diffusion, and is shown in Eq. 2.3:

$$\frac{M_t}{M_\infty} = k_H \times t^{0.5} \tag{2.3}$$

where k_H is the release constant of Higuchi [94]. and the cumulative mass of drug is proportional to the square root of time, t. The following hypotheses apply when this model is used: 1) The loading drug concentration is higher than the drug solubility; 2) The diffusion coefficient of drugs should be calculated in one direction, for example, from matrix to supernatant; 3) Diffusivity remains constant without consideration of the swelling of polymers in water; 4) The dissolution of matrix and edge effects should be neglected; and 5) The systems

should maintain an optimal sink condition during the release process [95]. The Higuchi model is especially important as it can be expanded into other mathematical models to classify release profiles.

Ritger-Peppas models can also be used to describe the drug release from a polymeric system, as shown in Eq. 2.4:

$$\frac{M_t}{M_\infty} = k_1 t^n \tag{2.4}$$

where k_1 is the rate constant, t is the release time, and n is the release exponent. This is a useful model due to the release exponent being variable, thereby enabling the model's use to interpret a mass transport mechanism. When n=0.5, a thin hydrogel film follows the Fickian diffusion mechanism, whereby the release kinetics can be described by the diffusion coefficient. However, when n=1, Case II transport occurs, subsequently resulting in zero-order release kinetics, caused by swelling of the system or the relaxation of the polymeric chains. When 0.5 < n< 1, non-Fickian diffusion is followed, whereby release occurs through diffusion and swelling factors. Of note, the model is only applicable when mass $\leq 60\%$ [96][97].

Peppas–Sahlin model of drug release is also valuable to explain diffusion and relaxation in a polymeric system [98]. The model equation is presented in Eq. 2.5:

$$\frac{M_t}{M_\infty} = k_1 t^m + k_2 t^{2m} \tag{2.5}$$

where k_1, k_2, and m are constant; $k_1 t^m$ represents the mechanism of Fickian diffusion, $k_2 t^{2m}$ represents the Case II transport related to the relaxation of the polymer chains. m is the Fickian exponent used to describe the release kinetics in controlled release systems, including thin film, cylinder, and sphere [94].

In regard to zero–order kinetics, drug concentration is independent of the release rate. The equation is depicted in Eq. 2.6:

$$C_t = C_0 + K_0 t \qquad\qquad (2.6)$$

where C_0 is the initial concentration of drug released from the system, whereby C_0 normally equals 0. C_t is the concentration of drugs released as a function of time, t. K_0 is the zero-order constant. This mechanism can be applied to drug release systems that prolong the drug release profile [94].

Additionally, zero-order kinetics can outline controlled drug release from a hydrogel system. Ratner et al. explored the sustained release of norfloxacin from pHEMA gels on the basis of a zero-order release mechanism over a 72h period [99]. This was achieved by adding hydrophobic octadecyl isocyanate to the pHEMA gel. Consequently, the hydrophobic residues prevented an initial burst release of hydrophilic norfloxacin from the hydrogel. Although hydrogel has received validation as a mediator of the zero-order release of drugs, it remains critical to further explore methods to prolong the time of zero-order kinetics in a hydrogel system [100].

Swelling control refers to the swelling rate of the hydrogel being lower than the drug diffusion, thereby enabling the controlled release of trapped drugs. Swelling control release kinetics can be achieved in hydrogel by adjusting the density of the crosslinked network. Muhamad and Hezaveh modified the structure of a carrageenan-based hydrogel through the addition of varying concentrations of genipin [101]. Genipin was selected as it serves as a natural crosslinker to develop hydrogel as a controlled release drug delivery system. The swelling behaviours were then observed in different pH buffer solutions. The swelling experiment was continued until the hydrogel reached equilibrium. The swelling ratio is depicted in Eq. 2.7:

$$Swelling\ ratio\ (\%) = \left[\frac{W_t - W_0}{W_0}\right] \times 100 \qquad\qquad (2.7)$$

where W_t is the weight of the swelling hydrogel at time t, and W_0 is the initial weight of the hydrogel.

Following the addition of different concentrations of genipin to the hydrogel, a higher swelling ratio was found as the concentration increased in neutral buffer. Yet in basic buffer, the swelling ratio of the hydrogel decreased as the concentration of genipin increased. Hence, the genipin-modified hydrogel was a pH-sensitive system suitable for drug release. Furthermore, the addition of genipin caused relaxation of the hydrogel polymer chains, as shown by the results of the swelling kinetics study. In light of this, the release of β-carotene could be controlled by altering the concentration of genipin and the pH of buffer.

In another study, Sakurai et al. determined the swelling control mechanism in thermo–responsive poly(N-isopropylacrylamide–co–butyl methacrylate) hydrogel (poly(IPAAm – co – BMA) [102]. The swelling-deswelling transition of the poly(IPAAm – co – BMA) gel indicated that the lower critical solution temperature (LCST) was 25 ℃. The authors discovered that the swelling behaviour of the hydrogel was guided by the diffusion of water molecules when the temperature exceeded the LCST. However, when the temperature was less than the LCST, the swelling ratio increased as the temperature decreased, due to the relaxation of the polymer chains. Hence, it was established that the swelling mechanism was dependent on temperature changes. Based on this finding, adjustments can be made to the release of indomethacin from hydrogel to suit specific therapeutic purposes, such as by introducing a crosslinker or modifying the temperature to manipulate swelling control of the hydrogel.

Chemically controlled drug release occurs through chemical reactions in the hydrogel system, such as cleavage of polymer chains under hydrolytic or enzymatic degradation. Moreover, such reactions can ensue between the drug and the network of the hydrogel, causing the release of the drug from the hydrogel. Mooney et al. studied the release of anticancer drugs from hydrogel through different mechanisms [103]. Their results highlighted that the release kinetics of doxorubicin were controlled by the concentration of the crosslinker adipic dihydrazide, which was responsible for covalent bonding between doxorubicin and the hydrogel [104]. It was

found that the release profile could be extended by using a higher concentration of adipic dihydrazide (150 mM). Additionally, poly(aldehyde guluronate) hydrogel was used to control the release of daunomycin via the hydrolytic reaction of linkage between the drug and polymer. This biodegradable hydrogel presented sustained release of the drug *in vivo* [104].

2.2.2 Hydrogels for targeted drug delivery

The ability of hydrogels to control the release of drugs enables them to increase the efficacy of drugs. Furthermore, sustained release of drugs by hydrogels over longer periods of time means repeated administration can be avoided, thus limiting the likelihood of adverse effects. Another advantage is that hydrogels can be modified to establish the target drug delivery system. Specifically, drug molecules can be released at a distinct site to improve the therapeutic effectiveness in the treatment of many diseases, whilst also reducing the toxicity of drugs in the surrounding environment.

The high water content and adjustable pore size of hydrogels mean they have the ability to encapsulate different sizes of hydrophobic drugs and achieve the targeted therapy. Zhang et al. designed a negatively charged hydrogel to encapsulate hydrophobic anti-inflammatory drugs, and then performed targeted release on the positively charged surface of an inflamed colon [105]. This was established to be a promising system for the treatment of chronic diseases, such as inflammatory bowel disease. Dexamethasone was one of the anti-inflammatory drugs that were loaded into an ascorbyl palmitate (AP) amphiphilic hydrogel, whereby it was found that the drug was released from the AP hydrogel through enzymatic digestion. This negatively charged hydrogel preferred to bind to the inflamed surface of the colon through charge attraction, and therefore the target drug delivery was achieved. Further testing was conducted on a murine model through enema administration, by which it was found that the AP hydrogel

provided less drug exposure to the untargeted position compared with free drug control. Thus, the AP hydrogel system would avoid toxicity at other sites.

DNA-hydrogel is another system involving complementary strands of DNA. The strands can hybridise to form a crosslinked network and demonstrate swelling behaviour in aqueous conditions [106]. The DNA-hydrogel can also bind to a fluorophore so as to trace the target delivery *in vivo*. Zhang et al. designed a self-assembling quantum dot DNA hydrogel (QDH) to deliver doxorubicin (Dox), an anticancer drug that targets DNA, to cancer cells [107]. The mechanical properties of QDH were measured through rheological characterisation, whereby it was found that the diameter and swelling ratio of QDHs could be modulated based on the concentration of DNA-functionalised QD. This hydrogel could also be modified to localise drug release at target cells, whilst smaller QDHs resulted in a higher cellular uptake of drug. Additionally, the QDH was employed for gene or siRNA delivery to target intracellular nucleic acids to modulate or include new proteins, making it valuable for cancer therapies. QDHs with Dox presented a controlled release mechanism, which resulted in increased target cellular uptake. This has been applied to an animal model to further study drug efficacy in QDHs; the results indicated biocompatible QDHs as being a promising drug carrier for targeted cancer therapy.

The biocompatibility, biodegradability, and ability to immunomodulate make DNA-based hydrogels highly suitable for cancer immunotherapy. For instance, cytosine-phosphate-guanine (CPG)-DNA hydrogel can stimulate innate immunity through the CpG-DNA receptor (Toll-like receptor 9), thereby deeming this DNA hydrogel an efficient system for antigen delivery [108]. Takakura et al. assessed the immune activity of ovalbumin (OVA) using CpG-DNA hydrogel. OVA is a model antigen, and was loaded into the hydrogel, which subsequently demonstrated sustained release and was found to promote an OVA-specific immune response. Compared with OVA with alum or other adjuvants, the OVA-loaded CpG-DNA hydrogel

showed a decrease in adverse effects [106]. Thus, DNA hydrogels should be regarded as versatile systems that can be modified with different <u>oligodeoxynucleotides</u> to create specific immunomodulatory antigen delivery systems.

Overall, the literature shows that hydrogels can efficiently perform targeted drug delivery due to their adjustable properties, such as charge, hydrophobicity, and mechanical properties. Furthermore, hydrogels can be used with a crosslinker or can be modified by a specific DNA sequence for localised therapy [109]. These characteristics constitute these hydrogels as being a smart platform for the treatment of a wide range of human diseases.

2.2.3 Hydrogels for injectable drug delivery

In accordance with the desired form of drug administration, hydrogel has the potential to be formulated into various delivery systems. Injectable hydrogels have caught the attention of numerous researchers for biomedical applications, as this administration minimises invasive delivery, reduces recovery time and wound area, and prevents inflammation of the skin and subsequent infections [110]. Injectable hydrogels have been favoured as a drug delivery system due to their sustainable release profile and localised injection site. This results in drug release of the required concentration at the target site whilst reducing the risk of adverse effects.

As noted, hydrogels form a 3D network through physical or chemical crosslinking, but in order to become injectable, processes involving the temperature, pH, ionic strength, enzymes, or photoirradiation must be applied. Hartgerink et al. used an injectable self-assembled MultiDomain Peptide (MDP) hydrogel to control the release of cyclic dinucleotides (CDNs) for immune cancer therapy [111]. CDNs trigger the stimulation of interferon genes (STING) and have been validated as small molecule immunotherapy drugs in clinic trials [112]. Hartgerink et al. used hydrogel as a vehicle with the aim of improving the efficacy of CDNs. The MDP was a positive hydrogel comprising a $K_2(SL)_6K_2$ sequence, which is able to self-

assemble into an antiparallel beta sheet through ionic strength; as a result, a robust hydrogel with a nanofibrous network was constructed. The electrostatic interaction between positively charged lysine residues of the MDP and negatively charged thiophosphate linkages of CDNs meant that this hydrogel presented a viable potential to control the release of the immunotherapy drug. Following injection of the MDP + CDNs in *in vivo* murine animal models, it was found that 60% of the mice survived. Moreover, the single injection of MDP + CDNs achieved successful anti-tumour activity and immune responses in the mice. Therefore, the authors concluded that the injectable hydrogel had localised CDNs at the target site in the *in vivo* animal model and had prolonged the effective concentration of CDNs through controllable drug release. The injection process is highly valuable as it can prevent repeated drug administration, thereby decreasing toxicity and drug resistance.

In a study by Burdick et al., hyaluronic acid (HA) hydrogel was modified to sustain the release of doxorubicin and doxycycline, both small drug molecules [113]. The addition of β – cyclodextrin (CD) to the HA led to the formation of a tuneable hydrogel (HA-CD) that could enhance the affinity between drugs and hydrogel. This produced an ideal system for loading different drugs and variable release kinetics. According to the results of the shear thinning/recovery assay by rheometer, the injectability of the modified hydrogel was not affected by drug loading. Furthermore, the HA-CD hydrogel recovered to a gel-like state after receiving a high strain (500%). These findings indicated the potential of the HA-CD system as a modifiable hydrogen through host-guest chemistry, which could be made to suit various forms of drug delivery. In particular, it was deemed viable as an injectable formulation for many diseases based on its shear thinning and self-healing potential.

In addition, modified hydrogels can encapsulate macromolecule drugs for targeted cancer therapy. For example, Ding et al. used injectable hydrogel to control the release of human epidermal growth factor receptor 2 (HER2)-targeted antibody following surgical intervention

for breast cancer, as this treatment prevents the local recurrence of HER2+ breast cancer [114]. In the study, the hydrogel was created with different proportions of PEG/PLGA over increasing temperature. It then encapsulated the antibody (Herceptin) and performed sustained release following hypodermal injection in the *in vivo* murine animal model. It was found that the release kinetics of Herceptin could be adjusted by mixing differing proportions of PEG/PLGA; this also meant the release time could be regulated to extend drug activity. At the tumour site, the sustained release of Herceptin resulted in a higher concentration, which subsequently enhanced the antitumour activity. Moreover, the sustainable properties of the hydrogel meant there was lower risk of cardiotoxicity induced by repeated dosage.

2.3 The structure of the PhD project

Existing literature shows that distinct types of hydrogels have been considered for tissue engineering and drug delivery. However, chemical crosslinked hydrogels contain organic components that could affect the intracellular environment [12]. Therefore, to avoid toxicity *in vivo*, physical crosslinked hydrogels have been the main focus of research for clinical applications.

Self-assembled peptide hydrogels offer a modifiable network and suitable mechanical properties under various conditions, and therefore, have been regarded as a smart biomaterial for drug delivery systems. Based on the biocompatibility and reversible gel state of physical crosslinked hydrogels, two ionic complementary peptide hydrogels were designed with opposite charges to test the controlled release of model drug molecules (macromolecules) and protein drugs. This aligns with the hypothesis of this research that the release kinetics of macromolecules can be controlled in a peptide hydrogel through electrostatic interactions and the density of the network, whereby the shear thinning/recovery properties of the hydrogel will support its potential to deliver protein drugs for cancer immunotherapy.

In this PhD project, Chapter 4 described two peptide hydrogels, EFKFEFKFE and KFEFKFEFK. At pH 7, the hydrogels presented a clear gel state, with EFKFEFKFE carrying -1 charge and KFEFKFEFK carrying +1 charge from the theoretical curves. The secondary structures of these hydrogels were characterised by CD, ThT binding assay, and attenuated total reflectance Fourier transform infrared spectroscopy (ATR-FTIR). A transmission electron microscope (TEM) was used to determine the morphology of the hydrogels, whilst the fibre size was measured by ImageJ software and subsequently confirmed by small-angle X-ray scattering (SAXS). The gel stiffness was ascertained through dynamic strain sweeps using a rheometer, which confirmed the optimal hydrogel concentration according to the initial storage modulus G'. In addition, the shear thinning/recovery properties were obtained from a rheometer for the injectable assessment of hydrogels. The biocompatibility of the hydrogels was determined by measuring their stability in cell culture media through a rheometer; these measurements were repeated on days 3, 7, and 14. Mesenchymal stem cells (MSCs) and 3T3 fibroblast cells were then used for 3D seeding to evaluate the biocompatibility and capability for 3D scaffolding. Cell viability was determined through LIVE/DEAD assays and PicoGreen staining.

In Chapter 5, the potential role of the EFKFEFKFE and KFEFKFEFK hydrogels as a drug delivery system to encapsulate macromolecules was explored. Fluorescein–dextran with different negative charges and FITC-Poly–L-Lysine (positively charged) were selected as the protein drug models to study the release kinetics in different hydrogels. The value of zeta potential was used to determine the charges of these macromolecules. The hydrodynamic radius of the macromolecules and the diffusion coefficient D_0 in water were determined through fluorescence correlational spectroscopy (FCS). The study protocol involved mixing 0.8 mg/mL of macromolecule with 12 mg/mL of hydrogel. To determine whether the encapsulation of differently charged macromolecules affected the hydrogel system, the results

of ATR-FTIR, TEM, SAXS, and rheology were analysed to characterise the structure of the macromolecule-loaded hydrogels. Swelling experiments were also conducted to assess the tunability of the crosslinked network. Different charges and sizes of the macromolecules were mixed with each of the hydrogels, followed by measurement of the release mass from a UV-Vis spectrophotometer. This was repeated five days subsequently. The diffusion coefficients D_E and D_L were calculated based on Fick's second law, and were then compared with D_0.

Chapter 6 focused on the encapsulation of recombinant human interleukin-2 (rhIL-2) and interleukin-21 (rhIL-21) in differently charged hydrogels. These two proteins derive from the same family, whilst their short half-life limits their drug efficacy and increases the risk of toxicity. Therefore, an injectable peptide hydrogel could be an ideal delivery system to overcome these issues. The proteins were reconstituted according to the protocol provided by R&D Systems (Bio–Techne). Protein activity in the hydrogels was measured by enzyme-linked immunosorbent assay (ELISA). A range of concentrations of bovine serum album (BSA) were used as the supernatants to determine the optimal concentration for this release study. Human peripheral blood mononuclear cells (PBMCs) were used to assess the activity of rhIL-21, whilst fluorescence-activated cell sorting (FACS) was used to evaluate cell marker expression.

Chapter 7 presented the results of this study, whereby the physical crosslinked peptide hydrogel appears as a promising material for controlled release drug delivery. However, restrictions caused by the COVID-19 pandemic from 2020 to 2021 meant that measuring cell marker expression after loading the hydrogels could not be completed in this study. Nonetheless, the potential of these hydrogels to sustainably release protein drugs, such as antibodies and cytokines, and achieve localised therapy should be recognised, especially through injectable administration. This could advance immunotherapy and achieve the ultimate goal of improving treatment efficiency and efficacy of a wide range of human diseases; therefore, this is an important area of research that should be developed further.

2.4 References

[1]   E. Caló and V. V. Khutoryanskiy, "Biomedical applications of hydrogels: A review of patents and commercial products," *European Polymer Journal*. 2015. doi: 10.1016/j.eurpolymj.2014.11.024.

[2]   M. W. Tibbitt and K. S. Anseth, "Hydrogels as extracellular matrix mimics for 3D cell culture," *Biotechnol. Bioeng.*, vol. 103, no. 4, pp. 655–663, 2009, doi: 10.1002/bit.22361.

[3]   J. Li and D. J. Mooney, "Designing hydrogels for controlled drug delivery," *Nature Reviews Materials*. 2016. doi: 10.1038/natrevmats.2016.71.

[4]   C. Yan, A. Altunbas, T. Yucel, R. P. Nagarkar, J. P. Schneider, and D. J. Pochan, "Injectable solid hydrogel: Mechanism of shear-thinning and immediate recovery of injectable β-hairpin peptide hydrogels," *Soft Matter*, vol. 6, no. 20, pp. 5143–5156, 2010, doi: 10.1039/c0sm00642d.

[5]   M. C. Branco, D. J. Pochan, N. J. Wagner, and J. P. Schneider, "The effect of protein structure on their controlled release from an injectable peptide hydrogel," *Biomaterials*, 2010, doi: 10.1016/j.biomaterials.2010.08.047.

[6]   J. H. Collier *et al.*, "Thermally and photochemically triggered self-assembly of peptide hydrogels [11]," *J. Am. Chem. Soc.*, vol. 123, no. 38, pp. 9463–9464, 2001, doi: 10.1021/ja011535a.

[7]   R. J. Williams and R. V. Ulijn, "Enzyme-triggered self-assembly of peptide hydrogels via reversed hydrolysis," *8th World Biomater. Congr. 2008*, vol. 3, p. 1420, 2008.

[8]   E. F. Banwell *et al.*, "Rational design and application of responsive α-helical peptide hydrogels," *Nat. Mater.*, vol. 8, no. 7, pp. 596–600, 2009, doi: 10.1038/nmat2479.

[9]   J. K. Wychowaniec, A. M. Smith, C. Ligorio, O. O. Mykhaylyk, A. F. Miller, and A.

Saiani, "Role of Sheet-Edge Interactions in β-sheet Self-Assembling Peptide Hydrogels," *Biomacromolecules*, vol. 21, no. 6, pp. 2285–2297, 2020, doi: 10.1021/acs.biomac.0c00229.

[10]   P. Worthington, S. Langhans, and D. Pochan, "B-Hairpin Peptide Hydrogels for Package Delivery," *Adv. Drug Deliv. Rev.*, vol. 110–111, pp. 127–136, 2017, doi: 10.1016/j.addr.2017.02.002.

[11]   M. Abbas, Q. Zou, S. Li, and X. Yan, "Self-Assembled Peptide- and Protein-Based Nanomaterials for Antitumor Photodynamic and Photothermal Therapy," *Adv. Mater.*, vol. 29, no. 12, 2017, doi: 10.1002/adma.201605021.

[12]   D. M. Ryan and B. L. Nilsson, "Self-assembled amino acids and dipeptides as noncovalent hydrogels for tissue engineering," *Polym. Chem.*, vol. 3, no. 1, pp. 18–33, 2012, doi: 10.1039/c1py00335f.

[13]   Z. Sun, C. Song, C. Wang, Y. Hu, and J. Wu, "Hydrogel-Based Controlled Drug Delivery for Cancer Treatment: A Review," *Mol. Pharm.*, vol. 17, no. 2, pp. 373–391, 2020, doi: 10.1021/acs.molpharmaceut.9b01020.

[14]   A. Bertz *et al.*, "Encapsulation of proteins in hydrogel carrier systems for controlled drug delivery: Influence of network structure and drug size on release rate," *J. Biotechnol.*, vol. 163, no. 2, pp. 243–249, 2013, doi: 10.1016/j.jbiotec.2012.06.036.

[15]   P. Gupta, K. Vermani, and S. Garg, "Hydrogels: From controlled release to pH-responsive drug delivery," *Drug Discov. Today*, vol. 7, no. 10, pp. 569–579, 2002, doi: 10.1016/S1359-6446(02)02255-9.

[16]   M. K. T. Vijay Kumar Thakur, *Hydrogels: Recent Advancess*. 2018.

[17]   H. H. Tønnesen and J. Karlsen, "Alginate in drug delivery systems," *Drug Dev. Ind.*

Pharm., vol. 28, no. 6, pp. 621–630, 2002, doi: 10.1081/DDC-120003853.

[18] T. Coviello, P. Matricardi, C. Marianecci, and F. Alhaique, "Polysaccharide hydrogels for modified release formulations," *J. Control. Release*, vol. 119, no. 1, pp. 5–24, 2007, doi: 10.1016/j.jconrel.2007.01.004.

[19] X. Wang and H. G. Spencer, "Calcium alginate gels: Formation and stability in the presence of an inert electrolyte," *Polymer (Guildf).*, vol. 39, no. 13, pp. 2759–2764, 1998, doi: 10.1016/S0032-3861(97)00597-1.

[20] S. C. Chen, Y. C. Wu, F. L. Mi, Y. H. Lin, L. C. Yu, and H. W. Sung, "A novel pH-sensitive hydrogel composed of N,O-carboxymethyl chitosan and alginate cross-linked by genipin for protein drug delivery," *J. Control. Release*, vol. 96, no. 2, pp. 285–300, 2004, doi: 10.1016/j.jconrel.2004.02.002.

[21] E. Alsberg, K. W. Anderson, A. Albeiruti, R. T. Franceschi, and D. J. Mooney, "Cell-interactive alginate hydrogels for bone tissue engineering," *J. Dent. Res.*, vol. 80, no. 11, pp. 2025–2029, 2001, doi: 10.1177/00220345010800111501.

[22] C. Yan and D. J. Pochan, "Rheological properties of peptide-based hydrogels for biomedical and other applications," *Chemical Society Reviews*. 2010. doi: 10.1039/b919449p.

[23] A. Veis, "The science and technology of gelatin," *J. Colloid Interface Sci.*, vol. 66, no. 2, pp. 373–374, 1978, doi: 10.1016/0021-9797(78)90323-5.

[24] Y. Tabata and Y. Ikada, "Vascularization effect of basic fibroblast growth factor released from gelatin hydrogels with different biodegradabilities," *Biomaterials*, vol. 20, no. 22, pp. 2169–2175, 1999, doi: 10.1016/S0142-9612(99)00121-0.

[25] D. A. Gyles, L. D. Castro, J. O. C. Silva, and R. M. Ribeiro-Costa, "A review of the

designs and prominent biomedical advances of natural and synthetic hydrogel formulations," *Eur. Polym. J.*, vol. 88, no. 01, pp. 373–392, 2017, doi: 10.1016/j.eurpolymj.2017.01.027.

[26]   I. M. Garnica-Palafox and F. M. Sánchez-Arévalo, "Influence of natural and synthetic crosslinking reagents on the structural and mechanical properties of chitosan-based hybrid hydrogels," *Carbohydr. Polym.*, vol. 151, pp. 1073–1081, 2016, doi: 10.1016/j.carbpol.2016.06.036.

[27]   H. Tan, A. J. DeFail, J. P. Rubin, C. R. Chu, and K. G. Marra, "Novel multiarm PEG-based hydrogels for tissue engineering," *J. Biomed. Mater. Res. - Part A*, vol. 92, no. 3, pp. 979–987, 2010, doi: 10.1002/jbm.a.32438.

[28]   F. Islands and D. Survey, "Industrial Research Associations: Some Taxation Problems," *Nature*, vol. 185, no. 4706, pp. 63–64, 1960, doi: 10.1038/185063a0.

[29]   L. Ferreira, M. M. Vidal, and M. H. Gil, "Evaluation of poly(2-hydroxyethyl methacrylate) gels as drug delivery systems at different pH values," *Int. J. Pharm.*, vol. 194, no. 2, pp. 169–180, 2000, doi: 10.1016/S0378-5173(99)00375-0.

[30]   J. Maitra and V. K. Shukla, "Cross-linking in Hydrogels - A Review," *Am. J. Polym. Sci.*, vol. 4, no. 2, pp. 25–31, 2014, doi: 10.5923/j.ajps.20140402.01.

[31]   W. Hu, Z. Wang, Y. Xiao, S. Zhang, and J. Wang, "Advances in crosslinking strategies of biomedical hydrogels," *Biomater. Sci.*, vol. 7, no. 3, pp. 843–855, 2019, doi: 10.1039/c8bm01246f.

[32]   M. Ermis *et al.*, *Hydrogels as a new platform to recapitulate the tumor microenvironment*. Elsevier Inc., 2018. doi: 10.1016/B978-0-12-813339-2.00015-3.

[33]   J. J. Sperinde and L. G. Griffith, "Synthesis and Characterization of Enzymatically-

Cross-Linked Poly (ethylene glycol) Hydrogels," vol. 9297, no. 97, pp. 5255–5264, 1997.

[34] J. M. Harris, "Introducdon to Blotechnlcal and Biomedical Appllcadons of Poly (Ethylene Glycol)," no. 1, pp. 1–2.

[35] D. M. Djordjevic, S. T. Cirkovic, and D. S. Mandic, "Biomedical applications," *Magn. Ferroelectr. Multiferroic Met. Oxides*, pp. 411–430, 2018, doi: 10.1016/B978-0-12-811180-2.00020-7.

[36] W. Schuurman *et al.*, "Gelatin-methacrylamide hydrogels as potential biomaterials for fabrication of tissue-engineered cartilage constructs," *Macromol. Biosci.*, vol. 13, no. 5, pp. 551–561, 2013, doi: 10.1002/mabi.201200471.

[37] N. Monteiro *et al.*, "Photopolymerization of cell-laden gelatin methacryloyl hydrogels using a dental curing light for regenerative dentistry," *Dent. Mater.*, vol. 34, no. 3, pp. 389–399, 2018, doi: 10.1016/j.dental.2017.11.020.

[38] T. C. Lai, J. Yu, and W. B. Tsai, "Gelatin methacrylate/carboxybetaine methacrylate hydrogels with tunable crosslinking for controlled drug release," *J. Mater. Chem. B*, vol. 4, no. 13, pp. 2304–2313, 2016, doi: 10.1039/c5tb02518d.

[39] S. Darvishi, M. Souissi, M. Kharaziha, F. Karimzadeh, R. Sahara, and S. Ahadian, "Gelatin methacryloyl hydrogel for glucose biosensing using Ni nanoparticles-reduced graphene oxide: An experimental and modeling study," *Electrochim. Acta*, vol. 261, pp. 275–283, 2018, doi: 10.1016/j.electacta.2017.12.126.

[40] N. S. Bostancı, S. Büyüksungur, N. Hasirci, and A. Tezcaner, "pH responsive release of curcumin from photocrosslinked pectin/gelatin hydrogel wound dressings," *Biomater. Adv.*, vol. 134, no. December 2021, p. 112717, 2022, doi: 10.1016/j.msec.2022.112717.

[41]   M. Abrigo, S. L. McArthur, and P. Kingshott, "Electrospun nanofibers as dressings for chronic wound care: Advances, challenges, and future prospects," *Macromol. Biosci.*, vol. 14, no. 6, pp. 772–792, 2014, doi: 10.1002/mabi.201300561.

[42]   G. Fletes-vargas, H. Espinosa-andrews, and M. L. Pita-l, "Physically cross-linked chitosan-based hydrogels for tissue engineering applications : A state-of-the-art review," vol. 145, no. November 2020, 2021, doi: 10.1016/j.eurpolymj.2020.110176.

[43]   R. parhi, "Cross-Linked Hydrogel for Pharmaceutical Applications: A Review," *Adv. Pharm. Bull.*, 2017, doi: 10.15171/apb.2017.064.

[44]   E. A. Appel *et al.*, "Exploiting Electrostatic Interactions in Polymer-Nanoparticle Hydrogels," *ACS Macro Lett.*, vol. 4, no. 8, pp. 848–852, 2015, doi: 10.1021/acsmacrolett.5b00416.

[45]   G. Song, Z. Zhao, X. Peng, C. He, R. A. Weiss, and H. Wang, "Rheological Behavior of Tough PVP-in Situ-PAAm Hydrogels Physically Cross-Linked by Cooperative Hydrogen Bonding," *Macromolecules*, vol. 49, no. 21, pp. 8265–8273, 2016, doi: 10.1021/acs.macromol.6b01448.

[46]   G. Song, L. Zhang, C. He, D. Fang, P. G. Whitten, and H. Wang, "Facile Fabrication of Tough Hydrogels Physically Cross-Linked by Strong Cooperative Hydrogen Bonding," 2013.

[47]   T. R. Hoare and D. S. Kohane, "Hydrogels in drug delivery : Progress and challenges *," *Polym. with aligned carbon Nanotub. Act. Compos. Mater.*, vol. 49, no. 8, pp. 1993–2007, 2008, doi: 10.1016/j.polymer.2008.01.027.

[48]   T. Vermonden, N. A. M. Besseling, and M. J. Van Steenbergen, "Rheological Studies of Thermosensitive Triblock Copolymer Hydrogels," no. 15, pp. 10180–10184, 2006.

[49] L. PAULING and R. B. COREY, "The pleated sheet, a new layer configuration of polypeptide chains.," *Proc. Natl. Acad. Sci. U. S. A.*, vol. 37, no. 5, pp. 251–256, 1951, doi: 10.1073/pnas.37.5.251.

[50] R. V. Ulijn and A. M. Smith, "Designing peptide based nanomaterials," *Chem. Soc. Rev.*, 2008, doi: 10.1039/b609047h.

[51] S. Zhang, "Discovery and design of self-assembling peptides," *Interface Focus*, vol. 7, no. 6, 2017, doi: 10.1098/rsfs.2017.0028.

[52] F. Gelain, Z. Luo, and S. Zhang, "Self-Assembling Peptide EAK16 and RADA16 Nanofiber Scaffold Hydrogel," *Chem. Rev.*, vol. 120, no. 24, pp. 13434–13460, 2020, doi: 10.1021/acs.chemrev.0c00690.

[53] X. Ding *et al.*, "Synthetic peptide hydrogels as 3D scaffolds for tissue engineering," *Adv. Drug Deliv. Rev.*, vol. 160, pp. 78–104, 2020, doi: 10.1016/j.addr.2020.10.005.

[54] Z. Luo, X. Zhao, and S. Zhang, "Structural dynamic of a self-assembling peptide d-EAK16 made of only D-amino acids," *PLoS One*, vol. 3, no. 5, 2008, doi: 10.1371/journal.pone.0002364.

[55] Z. Luo, X. Zhao, and S. Zhang, "Self-organization of a chiral D-EAK16 designer peptide into a 3D nanofiber scaffold," *Macromol. Biosci.*, vol. 8, no. 8, pp. 785–791, 2008, doi: 10.1002/mabi.200800003.

[56] Z. Luo *et al.*, "Designer D-form self-assembling peptide nanofiber scaffolds for 3-dimensional cell cultures," *Biomaterials*, vol. 34, no. 21, pp. 4902–4913, 2013, doi: 10.1016/j.biomaterials.2013.03.081.

[57] L. Sun and X. Zhao, "[Effect of amino acid sequence and time on nanofiber formation of self-assembly peptides].," *Sheng Wu Yi Xue Gong Cheng Xue Za Zhi*, vol. 26, no. 6,

pp. 1276–1280, 2009.

[58]   S. Zhang, C. Lockshin, R. Cook, and A. Rich, "Unusually stable β-sheet formation in an
ionic self-complementary oligopeptide," *Biopolymers*, vol. 34, no. 5, pp. 663–672, 1994,
doi: 10.1002/bip.360340508.

[59]   C. Ligorio *et al.*, "TGF-β3-loaded graphene oxide - self-assembling peptide hybrid
hydrogels as functional 3D scaffolds for the regeneration of the nucleus pulposus," *Acta
Biomater.*, vol. 127, pp. 116–130, 2021, doi: 10.1016/j.actbio.2021.03.077.

[60]   C. Ligorio, A. Vijayaraghavan, J. A. Hoyland, and A. Saiani, "Acidic and basic self-
assembling peptide and peptide-graphene oxide hydrogels: characterisation and effect
on encapsulated nucleus pulposus cells," *Acta Biomater.*, vol. 143, pp. 145–158, 2022,
doi: 10.1016/j.actbio.2022.02.022.

[61]   J. P. Schneider, D. J. Pochan, B. Ozbas, K. Rajagopal, L. Pakstis, and J. Kretsinger,
"Responsive hydrogels from the intramolecular folding and self-assembly of a designed
peptide," *J. Am. Chem. Soc.*, vol. 124, no. 50, pp. 15030–15037, 2002, doi:
10.1021/ja027993g.

[62]   C. J. Bowerman and B. L. Nilsson, "Self-assembly of amphipathic β-sheet peptides:
insights and applications.," *Biopolymers*, vol. 98, no. 3, pp. 169–184, 2012, doi:
10.1002/bip.22058.

[63]   R. V. Rughani and J. R. Schneider, "Molecular design of β-hairpin peptides for material
construction," *MRS Bull.*, vol. 33, no. 5, pp. 530–535, 2008, doi: 10.1557/mrs2008.106.

[64]   M. S. Lamm, K. Rajagopal, J. P. Schneider, and D. J. Pochan, "Laminated morphology
of nontwisting β-sheet fibrils constructed via peptide self-assembly," *J. Am. Chem. Soc.*,
vol. 127, no. 47, pp. 16692–16700, 2005, doi: 10.1021/ja054721f.

[65] "Self Assembled Bi-functional Peptide Hydrogels withBiomineralization-Directing Peptides.pdf."

[66] A. Altunbas, S. J. Lee, S. A. Rajasekaran, J. P. Schneider, and D. J. Pochan, "Encapsulation of curcumin in self-assembling peptide hydrogels as injectable drug delivery vehicles," *Biomaterials*, 2011, doi: 10.1016/j.biomaterials.2011.04.069.

[67] B. Ozbas, J. Kretsinger, K. Rajagopal, J. P. Schneider, and D. J. Pochan, "Salt-triggered peptide folding and consequent self-assembly into hydrogels with tunable modulus," *Macromolecules*, vol. 37, no. 19, pp. 7331–7337, 2004, doi: 10.1021/ma0491762.

[68] D. J. Pochan, J. P. Schneider, J. Kretsinger, B. Ozbas, K. Rajagopal, and L. Haines, "Thermally reversible hydrogels via intramolecular folding and consequent self-assembly of a de novo designed peptide," *J. Am. Chem. Soc.*, vol. 125, no. 39, pp. 11802–11803, 2003, doi: 10.1021/ja0353154.

[69] J. K. Kretsinger, L. A. Haines, B. Ozbas, D. J. Pochan, and J. P. Schneider, "Cytocompatibility of self-assembled β-hairpin peptide hydrogel surfaces," *Biomaterials*, vol. 26, no. 25, pp. 5177–5186, 2005, doi: 10.1016/j.biomaterials.2005.01.029.

[70] D. A. Salick, J. K. Kretsinger, D. J. Pochan, and J. P. Schneider, "Inherent antibacterial activity of a peptide-based β-hairpin hydrogel," *J. Am. Chem. Soc.*, vol. 129, no. 47, pp. 14793–14799, 2007, doi: 10.1021/ja076300z.

[71] L. Haines-Butterick *et al.*, "Controlling hydrogelation kinetics by peptide design for three-dimensional encapsulation and injectable delivery of cells," *Proc. Natl. Acad. Sci. U. S. A.*, vol. 104, no. 19, pp. 7791–7796, 2007, doi: 10.1073/pnas.0701980104.

[72] L. A. Haines-Butterick, D. A. Salick, D. J. Pochan, and J. P. Schneider, "In vitro

assessment of the pro-inflammatory potential of β-hairpin peptide hydrogels," *Biomaterials*, vol. 29, no. 31, pp. 4164–4169, 2008, doi: 10.1016/j.biomaterials.2008.07.009.

[73] J. M. Mason and K. M. Arndt, "Coiled coil domains: Stability, specificity, and biological implications," *ChemBioChem*, vol. 5, no. 2, pp. 170–176, 2004, doi: 10.1002/cbic.200300781.

[74] W. D. Kohn, C. M. Kay, and R. S. Hodges, "Protein destabilization by electrostatic repulsions in the two-stranded α-helical coiled-coil/leucine zipper," *Protein Sci.*, vol. 4, no. 2, pp. 237–250, 1995, doi: 10.1002/pro.5560040210.

[75] F. Lapenta, J. Aupič, Ž. Strmšek, and R. Jerala, "Coiled coil protein origami: From modular design principles towards biotechnological applications," *Chem. Soc. Rev.*, vol. 47, no. 10, pp. 3530–3542, 2018, doi: 10.1039/c7cs00822h.

[76] N. L. Fletcher, C. V. Lockett, and A. F. Dexter, "A pH-responsive coiled-coil peptide hydrogel," *Soft Matter*, vol. 7, no. 21, pp. 10210–10218, 2011, doi: 10.1039/c1sm06261a.

[77] D. Papapostolou *et al.*, "Engineering nanoscale order into a designed protein fiber," *Proc. Natl. Acad. Sci. U. S. A.*, vol. 104, no. 26, pp. 10853–10858, 2007, doi: 10.1073/pnas.0700801104.

[78] C. J. Bowerman and B. L. Nilsson, "Self-assembly of amphipathic β-sheet peptides: insights and applications.," *Biopolymers*. 2012. doi: 10.1002/bip.22058.

[79] T. Kobori, S. Iwamoto, K. Takeyasu, and T. Ohtani, "Biopolymers Volume 85 / Number 4 295," *Biopolymers*, vol. 85, no. 4, pp. 392–406, 2007, doi: 10.1002/bip.

[80] C. J. C. Edwards-Gayle and I. W. Hamley, "Self-assembly of bioactive peptides, peptide

conjugates, and peptide mimetic materials," *Org. Biomol. Chem.*, vol. 15, no. 28, pp. 5867–5876, 2017, doi: 10.1039/c7ob01092c.

[81] T. J. Mitchison *et al.*, "Self-Assembly and Mineralization of Peptide-Amphiphile Nanofibers," vol. 294, no. November, pp. 1684–1689, 2001.

[82] J. K. Kim, J. Anderson, H. W. Jun, M. A. Repka, and S. Jo, "Self-assembling peptide amphiphile-based nanofiber gel for bioresponsive cisplatin delivery," *Mol. Pharm.*, 2009, doi: 10.1021/mp900009n.

[83] H. W. Jun, V. Yuwono, S. E. Paramonov, and J. D. Hartgerink, "Enzyme-mediated degradation of peptide-amphiphile nanofiber networks," *Adv. Mater.*, vol. 17, no. 21, pp. 2612–2617, 2005, doi: 10.1002/adma.200500855.

[84] J. Liu, L. Zhang, Z. Yang, and X. Zhao, "Controlled release of paclitaxel from a self-assembling peptide hydrogel formed in situ and antitumor study in vitro.," *Int. J. Nanomedicine*, vol. 6, pp. 2143–2153, 2011, doi: 10.2147/ijn.s24038.

[85] Y. Chen *et al.*, "Amyloid-like staining property of RADA16-I nanofibers and its potential application in detecting and imaging the nanomaterial," *Int. J. Nanomedicine*, vol. 13, pp. 2477–2489, 2018, doi: 10.2147/IJN.S159785.

[86] D. Ho *et al.*, "The effects of concentration-dependent morphology of self-assembling RADA16 nanoscaffolds on mixed retinal cultures," *Nanoscale*, vol. 3, no. 3, pp. 907–910, 2011, doi: 10.1039/c0nr00666a.

[87] A. Ishida, G. Watanabe, M. Oshikawa, I. Ajioka, and T. Muraoka, "Glycine Substitution Effects on the Supramolecular Morphology and Rigidity of Cell-Adhesive Amphiphilic Peptides," *Chem. - A Eur. J.*, pp. 13523–13530, 2019, doi: 10.1002/chem.201902083.

[88] C. Nilsberth *et al.*, "The 'Arctic' APP mutation (E693G) causes Alzheimer's disease by

enhanced Aβ protofibril formation," *Nat. Neurosci.*, vol. 4, no. 9, pp. 887–893, 2001, doi: 10.1038/nn0901-887.

[89]   J. Su, B. H. Hu, W. L. Lowe, D. B. Kaufman, and P. B. Messersmith, "Anti-inflammatory peptide-functionalized hydrogels for insulin-secreting cell encapsulation," *Biomaterials*, vol. 31, no. 2, pp. 308–314, 2010, doi: 10.1016/j.biomaterials.2009.09.045.

[90]   C. C. Lin and A. T. Metters, "Hydrogels in controlled release formulations: Network design and mathematical modeling," *Adv. Drug Deliv. Rev.*, vol. 58, no. 12–13, pp. 1379–1408, 2006, doi: 10.1016/j.addr.2006.09.004.

[91]   Y. Nagai, L. D. Unsworth, S. Koutsopoulos, and S. Zhang, "Slow release of molecules in self-assembling peptide nanofiber scaffold," *J. Control. Release*, 2006, doi: 10.1016/j.jconrel.2006.06.031.

[92]   Y. Fu and W. J. Kao, "Drug release kinetics and transport mechanisms of non-degradable and degradable polymeric delivery systems," *Expert Opinion on Drug Delivery*. 2010. doi: 10.1517/17425241003602259.

[93]   S. Koutsopoulos, L. D. Unsworth, Y. Nagai, and S. Zhang, "Controlled release of functional proteins through designer self-assembling peptide nanofiber hydrogel scaffold," *Proc. Natl. Acad. Sci. U. S. A.*, 2009, doi: 10.1073/pnas.0807506106.

[94]   "Mathematical models of drug release," in *Strategies to Modify the Drug Release from Pharmaceutical Systems*, 2015. doi: 10.1016/b978-0-08-100092-2.00005-9.

[95]   A. D. Nurhan, "Dash, Murthy," *Polish Pharm. Soc.*, vol. 67, no. 3, pp. 217–223, 2010.

[96]   N. A. Peppas and J. J. Sahlin, "A simple equation for the description of solute release. III. Coupling of diffusion and relaxation," *Int. J. Pharm.*, 1989, doi: 10.1016/0378-5173(89)90306-2.

[97] L. Serra, J. Doménech, and N. A. Peppas, "Drug transport mechanisms and release kinetics from molecularly designed poly(acrylic acid-g-ethylene glycol) hydrogels," *Biomaterials*, 2006, doi: 10.1016/j.biomaterials.2006.06.011.

[98] N. A. Peppas and J. J. Sahlin, "A simple equation for the description of solute release. III. Coupling of diffusion and relaxation," *Int. J. Pharm.*, vol. 57, no. 2, pp. 169–172, 1989, doi: 10.1016/0378-5173(89)90306-2.

[99] E. M. Anderson *et al.*, "Sustained release of antibiotic from poly(2-hydroxyethyl methacrylate) to prevent blinding infections after cataract surgery," *Biomaterials*, vol. 30, no. 29, pp. 5675–5681, 2009, doi: 10.1016/j.biomaterials.2009.06.047.

[100] M. L. Laracuente, M. H. Yu, and K. J. McHugh, "Zero-order drug delivery: State of the art and future prospects," *J. Control. Release*, vol. 327, no. September, pp. 834–856, 2020, doi: 10.1016/j.jconrel.2020.09.020.

[101] H. Hezaveh and I. I. Muhamad, "Modification and swelling kinetic study of kappa-carrageenan-based hydrogel for controlled release study," *J. Taiwan Inst. Chem. Eng.*, vol. 44, no. 2, pp. 182–191, 2013, doi: 10.1016/j.jtice.2012.10.011.

[102] Y. Okuyama, R. Yoshida, K. Sakai, T. Okano, and Y. Sakurai, "Swelling controlled zero order and sigmoidal drug release from thermo-responsive poly(N-isopropylacrylamide-co-butyl methacrylate) hydrogel," *J. Biomater. Sci. Polym. Ed.*, vol. 4, no. 5, pp. 545–556, 1993, doi: 10.1163/156856293X00195.

[103] K. H. Bouhadir, E. Alsberg, and D. J. Mooney, "Hydrogels for combination delivery of antineoplastic agents," *Biomaterials*, vol. 22, no. 19, pp. 2625–2633, 2001, doi: 10.1016/S0142-9612(01)00003-5.

[104] K. H. Bouhadir, G. M. Kruger, K. Y. Lee, and D. J. Mooney, "Sustained and controlled

release of daunomycin from cross-linked poly(aldehyde guluronate) hydrogels," *J. Pharm. Sci.*, vol. 89, no. 7, pp. 910–919, 2000, doi: 10.1002/1520-6017(200007)89:7<910::aid-jps8>3.0.co;2-%23.

[105] S. Zhang *et al.*, "An inflammation-targeting hydrogel for local drug delivery in inflammatory bowel disease," *Sci. Transl. Med.*, vol. 7, no. 300, pp. 1–11, 2015, doi: 10.1126/scitranslmed.aaa5657.

[106] R. Narayanaswamy and V. P. Torchilin, "Hydrogels and their applications in targeted drug delivery," *Molecules*, vol. 24, no. 3, 2019, doi: 10.3390/molecules24030603.

[107] L. Zhang *et al.*, "Multifunctional quantum dot DNA hydrogels," *Nat. Commun.*, vol. 8, no. 1, 2017, doi: 10.1038/s41467-017-00298-w.

[108] M. Nishikawa *et al.*, "Injectable, self-gelling, biodegradable, and immunomodulatory DNA hydrogel for antigen delivery," *J. Control. Release*, vol. 180, no. 1, pp. 25–32, 2014, doi: 10.1016/j.jconrel.2014.02.001.

[109] M. A. Shahbazi, T. Bauleth-Ramos, and H. A. Santos, "DNA Hydrogel Assemblies: Bridging Synthesis Principles to Biomedical Applications," *Adv. Ther.*, vol. 1, no. 4, pp. 1–22, 2018, doi: 10.1002/adtp.201800042.

[110] D. J. Overstreet, D. Dutta, S. E. Stabenfeldt, and B. L. Vernon, "Injectable hydrogels," *J. Polym. Sci. Part B Polym. Phys.*, vol. 50, no. 13, pp. 881–903, 2012, doi: 10.1002/polb.23081.

[111] D. G. Leach *et al.*, "STINGel: Controlled release of a cyclic dinucleotide for enhanced cancer immunotherapy," *Biomaterials*, vol. 163, pp. 67–75, 2018, doi: 10.1016/j.biomaterials.2018.01.035.

[112] H. Weinmann, "Cancer Immunotherapy: Selected Targets and Small-Molecule

Modulators," *ChemMedChem*, vol. 11, no. 5, pp. 450–466, 2016, doi: 10.1002/cmdc.201500566.

[113] J. E. Mealy, C. B. Rodell, and J. A. Burdick, "Sustained small molecule delivery from injectable hyaluronic acid hydrogels through host-guest mediated retention," *J. Mater. Chem. B*, vol. 3, no. 40, pp. 8010–8019, 2015, doi: 10.1039/c5tb00981b.

[114] X. Chen *et al.*, "Injectable hydrogels for the sustained delivery of a HER2-targeted antibody for preventing local relapse of HER2+ breast cancer after breast-conserving surgery," *Theranostics*, vol. 9, no. 21, pp. 6080–6098, 2019, doi: 10.7150/thno.36514.

Chapter 3 Principles of techniques

3.1 Introduction

In this chapter, the principles of techniques used in the PhD project will be concluded. The techniques include Reverse Phase High Performance Liquid Chromatography (RP-HPLC), Attenuated Total Reflectance Fourier Transform Infrared Spectroscopy (ATR-FTIR), Transmission Electron Microscope (TEM), Small-Angle X-ray Scattering (SAXS), Zeta potential, UV-Vis Spectrophotometer, Enzyme-linked Immunosorbent Assay (ELISA), LIVE/DEAD Cell Viability Assay, Confocal Laser Scanning Microscopy (CLSM) and Pico-Green Assay. The fundamental theory and reaction mechanisms of each technique are described in the corresponding section.

3.2 Reverse Phase High Performance Liquid Chromatography (RP-HPLC)

Reverse-phase high-performance liquid chromatography (RP-HPLC) is a common variant of chromatography used for purification, separation and quantification of proteins and peptides. It is also widely used in analytical chemistry to identify compounds in a mixture. The technique requires a non-polar stationary phase and a polar mobile phase. A common choice of stationary phase is a modified silica surface covalently bonded to an octadecyl hydrocarbon group (C18). This forms a bonded-phase column, and changing the length of the bonded alkyl chain both modulates the hydrophobicity of the sorbent phase and controls the retention time [1]. The mobile phase is one or more solvents that carry eluents through the column; common choices include acetonitrile (ACN), isopropanol (IPA) or tetrahydrofuran (THF) mixed with water.

Components of the RP-HPLC instrument include solvent reservoirs, a solvent degasser, the pump, the column and a UV detector. The stationary phase used for this experiment was a C12 column, with a mixture of ACN + 0.1% trifluoroacetic acid (TFA) and HPLC water + 0.1%

TFA. When samples are injected into a chromatography column, polar molecules are typically quickly eluted because they have stronger interactions with the polar mobile phase. In contrast, non-polar molecules interact with the hydrocarbon chains (C12 column) via hydrophobic force in the stationary phase. They also have poor solubility in the polar mobile phase, as they cannot form dipole-dipole interactions or hydrogen bonds like the solvent molecules form with each other. Therefore, they move slowly through the column and have a large retention time. The most-polar molecules are the first to elute, followed by less-polar and non-polar molecules [2].

Elution time also depends on the choice of solvents. A solvent's acidity or basicity influences the ionization state of compounds, which changes their interaction with the column and therefore affects their retention time. Furthermore, it is possible to alter the solvent/water ratio for method optimization. For example, increasing the amount of water in the mobile phase can increase the affinity of hydrophobic eluents to the hydrophobic alkyl chain in the stationary phase, increasing the retention time of non-polar compounds. Similarly, retention time could be decreased by adding more organic solvents for elution.

3.3 Attenuated Total Reflectance Fourier Transform Infrared Spectroscopy (ATR-FTIR)

Fourier transform infrared spectroscopy (FTIR) is an analytical technique employed to characterise protein structure, and elucidate the results of reactions by analysing their products. It is commonly-used in biomedical research, including for cancer diagnoses, microorganism differentiation and investigation of cellular composition [3][4][5].

Radiation in the infra-red (IR) region of the electromagnetic spectrum has wavelengths of 0.78-1000 µm, divided into three ranges: near-IR (0.78-2.5 µm), mid-IR (2.5-25 µm) and far-IR (25-1000 µm). In this study, samples were irradiated by mid-IR radiation with wavelengths from 2.5-25 µm (4000-400 cm^{-1}). The mechanism of FTIR is displayed in Fig. 3.1. It uses an

interferometer, consisting of a fixed mirror and a movable mirror, to split an incident IR light source. Around 50% of the incident light is reflected toward the fixed mirror and back to the beam splitter, where it is transmitted to samples. The remaining light intensity is transmitted to the movable mirror and reflected to the samples via the beam splitter; giving rise to an optical path difference (OPD) d between the two split beams, which depends on the position of the movable mirror. This path difference allows the waves to interfere either constructively or destructively upon recombination at the beam splitter, generating an interferogram with movement of the mirror. This interferogram is Fourier transformed and deconvoluted to yield the sample's infra-red spectrum.
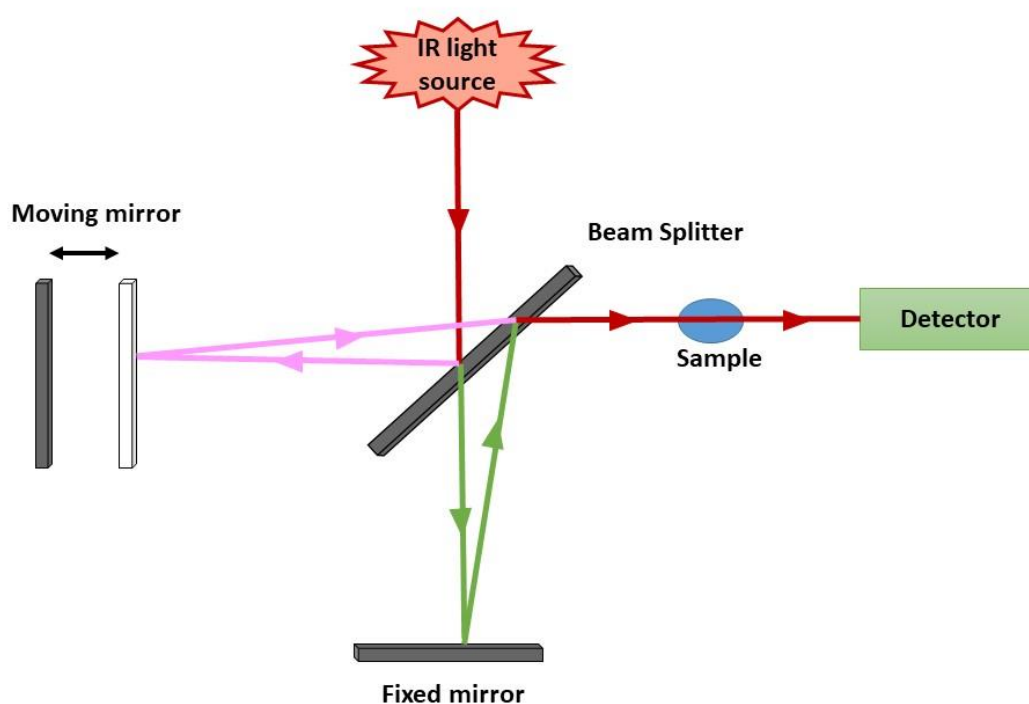
Figure 3. 1 The scheme of interferometer in FTIR.

Attenuated total reflectance (ATR) is a modification applied to the method of FTIR spectroscopy to directly test solid and liquid samples. The incident IR light passes through the

ATR crystal, which is in contact with the sample. This IR light reflects off the interface between the crystal and the sample, generating an evanescent wave that penetrates into the sample itself. At this interface, the sample absorbs specific regions of the incident IR radiation, attenuating the reflected light which is collected by the detector (Fig. 3.2), allowing the absorbed radiation to be measured. The penetration depth of light into the sample depends on multiple factors, including the incident radiation wavelength, the indices of refraction of the ATR crystal and the sample, and the radiation's angle of incidence. ATR-FTIR is widely employed since it only requires a small amount of sample on the crystal's surface, and can be used to investigate samples that otherwise would absorb IR too strongly to be measured [5][6].
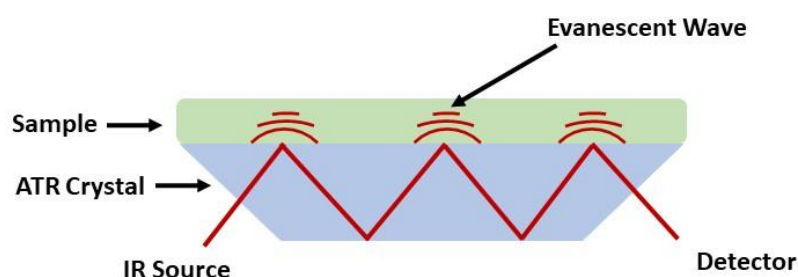
Figure 3. 2 The scheme of ATR-FTIR.

A spectrum can be obtained by means of absorbance or transmittance. For a homogeneous sample, the Beer-Lambert law can be used to describe the relationship between absorbance and sample concentration Eq. 3.1:

$$A = \log{(I_0/I)} = \varepsilon c l \qquad (3.1)$$

where A is the absorbance, I_0 is the incident intensity (W m^{-2}), I is the transmitted intensity (W m^{-2}), ε is the molar absorptivity of sample (L mol^{-1} cm^{-1}), c is the molar concentration of sample (mol L^{-1}), and l is the path length of the light passing through the sample (cm).

The transmittance can correspondingly be obtained via Eq. 3.2:

$$T = \frac{I}{I_0} = e^{-\varepsilon c l} \tag{3.2}$$

3.4 Transmission Electron Microscope (TEM)

Transmission electron microscopy (TEM) is an advanced microscopy technique used to examine the internal structure of samples in an ultra-thin film. An electron beam is passed through and scatters off the specimen, and the amount of scattering by a sample region reduces the amount of electrons collected, leading to contrasts of dark areas (high-density regions with large scattering angles) and bright areas (low-density, narrow scattering angle) where more electrons have been collected. The sample can then be imaged two-dimensionally, allowing the collection of sample information such as structure, shape, and diameter [7]. TEM has a higher magnification and resolution than a conventional optical microscope, which allows researchers to resolve structures on the nanoscale, including atomic alignment within samples, which is impossible with a light microscope.

A schematic of a TEM microscope is illustrated in Fig. 3.3. Its key components include an electron gun at the top, which emits an electron beam via a tungsten filament or a lanthanum hexaboride (LaB$_6$) crystal. The electrons are accelerated by a high voltage (80-300 kV) from a cathode to an anode, emitting a beam into a vacuum tube at a constant voltage. The beam then is focused by the condenser lenses, forming a fine beam through the condenser aperture which is then transmitted into the specimen. After passing through the specimen, the objective lenses,

intermediate lenses and projector lenses are used to focus the beam on to a fluorescent screen, which generates a 2D image captured by a digital camera [8].

Image resolution can be modified by adjusting the accelerating voltage of the electrons, which alters their wavelength. A higher accelerating voltage leads to a faster beam velocity and shorter wavelength, which affords a better resolution. However, the choice of voltage used for TEM must also take into account the specimen composition. High voltage (e.g. 200-300 kV) might destroy or damage the specimen, particularly if it includes light elements (such as hydrogen, carbon, nitrogen, oxygen, fluorine, sodium). Additionally, an increased beam velocity can lead to wider scattering angles upon specimen interaction, which could lower image quality; therefore it is vital to adjust the accelerating voltage according to the needs of the specimen.
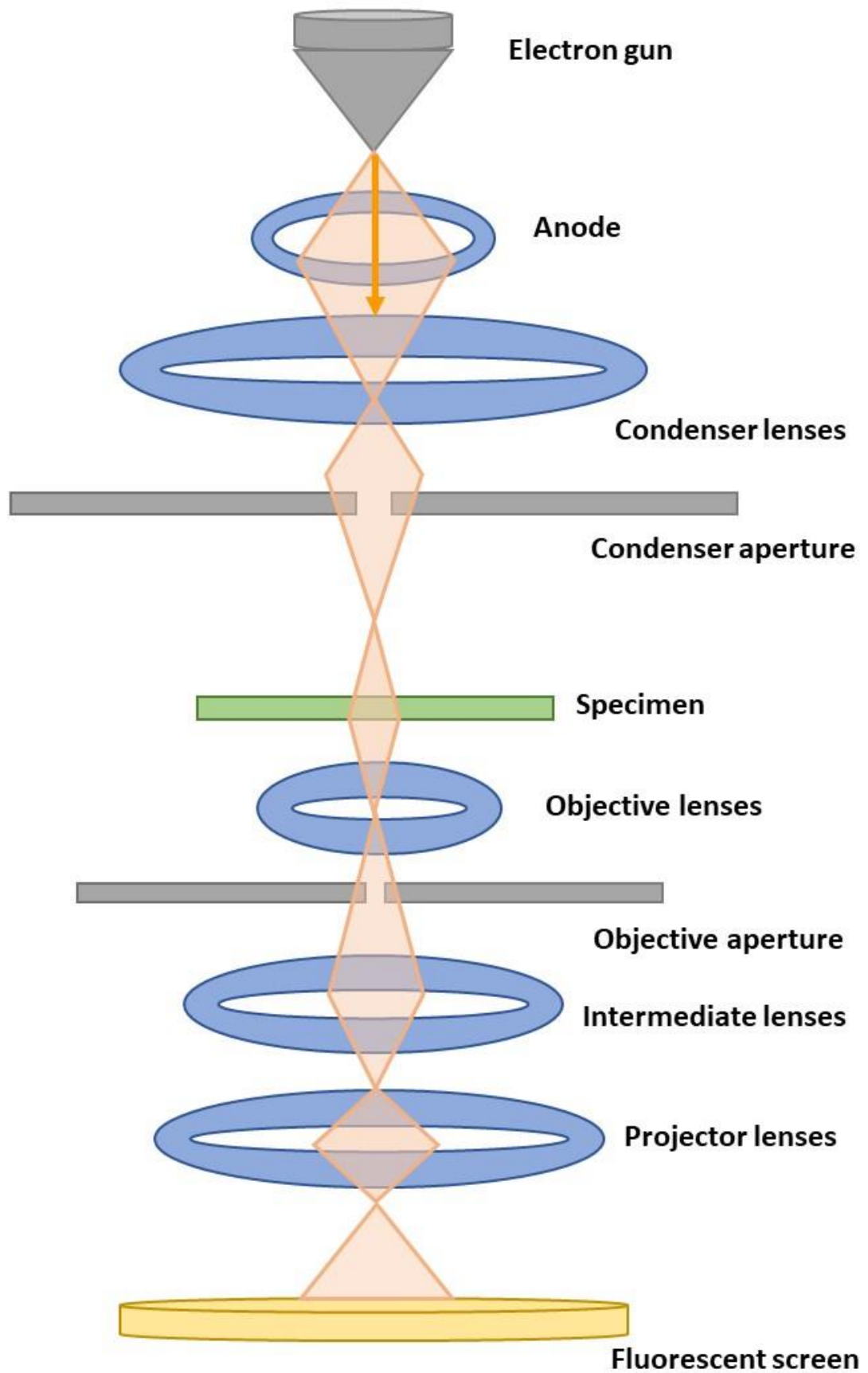
Figure 3. 3 A simplified diagram of the mechanism of TEM.

98

As the specimens examined with TEM in this study are polymer and peptide hydrogels consisting of light elements (C, H, N), the accelerating voltage of the electrons should be kept below 100 kV to minimise specimen damage [8]. The samples were dispersed on copper grids (400 mesh) with a supporting carbon film to allow for imaging. Heavy metal salt (eg. uranyl acetate) used as a stain to improve image contrast. The heavy metal stains the copper grids, increasing the scattering of incident electrons and producing relatively dark areas, in contrast to the bright areas of the specimen, which are caused by low scattering off the lighter constituent elements. This technique is termed heavy metal negative staining, and it has been commonly employed to investigate polymer and peptide materials via TEM [9]. The increased contrast produced by this technique in turn increases image clarity.

3.5 Small-Angle X-ray Scattering (SAXS)

SAXS technique has been widely used for analysing the structure of polymers and peptides. Compared with the microscopes, SAXS will give more specific information of fibre size, shape, distribution and aggregation. For example, self-assembled peptide hydrogels need to be prepared by diluting, staining or drying before microscope study, which might influence their structural characterizations. However, SAXS can directly measure peptide hydrogels, making it a useful tool to complement the results obtained from other characterisation techniques such as microscopy [10].

In a SAXS experiment, the X-ray wavelength used is around 0.07-0.2 nm, and the angle of scattering is typically from 0.1 to 10°. As shown in Fig. 3.4, an incident X-ray beam scatters at an angle of 2θ. As the scattering process is elastic, the incident $|k_i|$ and scattered $|k_s|$ wavevectors have the same magnitude, therefore $|k_i| = |k_s| = 2\pi/\lambda$. The momentum transfer vector q is given in Eq. 3.3:

$$q = \frac{4\pi \sin\theta}{\lambda} \qquad (3.3)$$
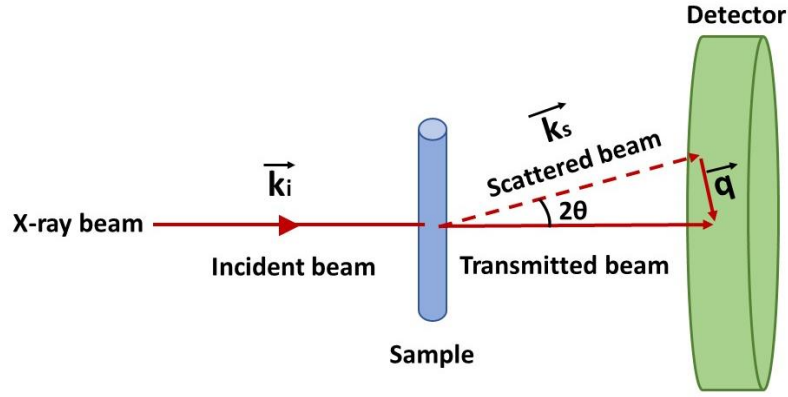
Figure 3. 4 A diagram of SAXS experiment. q is the definition of momentum transfer vector, $\overrightarrow{k_i}$ is the incident waves vector, $\overrightarrow{k_s}$ is the scattered waves vector, 2θ is the scattering angle.

In self-assembled peptide hydrogels with a complex 3D network, the fibres distribute randomly, forming an inhomogeneous system. In SAXS patterns, the peaks come out when the X-ray beam scatters on different phases of hydrogel. Therefore, the scattering intensity depends on both the structure and the phase composition of the hydrogel [10][11]. Bragg's law can be combined with Eq. 3.3 to predict the pore size, d, as in Eq. 3.4:

$$d = \frac{2\pi}{q} \tag{3.4}$$

In this isotropic system, the scattering intensity from a peptide hydrogel contains contributions from coherent and incoherent scattering, which can be explained by Eq. 3.5:

$$I(q) = BT_S\delta_S[S^{coh}(q) + S^{inc}] \tag{3.5}$$

where B is a constant, T_S is the transmission of sample, δ_S is the thickness of sample, S^{coh} is the coherent scattering and S^{inc} is the incoherent scattering. S^{inc} does not contain information about the structure of sample, therefore, it needs to be subtracted from the total scattering

intensity in order to obtain the accurate scattering intensity of the sample. The coherent scattering contains all the structure information of sample that can be explained by Eq. 3.6:

$$S^{coh}(q) = P(q) + Q(q) \qquad (3.6)$$

where $P(q)$ represents intra-scattering events, i.e., between the same scattering objects in the hydrogel, and $Q(q)$ represents inter-scattering events – between different scattering objects in the hydrogel.

Here, the $P(q)$ term describes the size and shape of the fibres, and the $Q(q)$ term reveals the interaction between different scattering objects, so here yields information on the self-assembling state. $P(q)$ is linked to the concentration, so a series of dilutions could be performed to examine how hydrogel concentration affects scattering. The coherent normalized scattering intensity from a peptide hydrogel, $I_N(q)$, can be written as in Eq. 3.7 [12]:

$$I_N(q) = \frac{1}{K} \left[I_A(q) - (1 - C_P)I_S(q) - I_b \right] \qquad (3.7)$$

where $I_A(q)$ is the normalised peptide scattering intensity, $I_s(q)$ is the normalised scattering intensity from the solvent (in this study we used HPLC water), C_P is the peptide concentration in g cm^{-3}, I_b is the incoherent scattering intensity, and K is a contrast factor, given by Eq. 3.8 [10][13]:

$$K = \frac{N_A}{m_p{}^2} \left(A - \frac{v_p}{v_S} B \right)^2 \qquad (3.8)$$

where N_A is Avogadro's number, A and B are the scattering amplitudes of the peptide and water, v_p and v_S are the molar volumes of the peptide and water, and m_p is the molecular weight of the peptide.

With increasing q range, a power law was used to describe the shape of the sample, as given by Eq. 3.9 [10]:

101

$$I_N(q) \propto q^{-\alpha} \tag{3.9}$$

This equation can be manipulated into $\log I_N(q)$ vs $\log q^{-\alpha}$ form to plot a slope. At intermediate values of q, the value of the exponent α represents the sample shape: when $\alpha = -1$, the sample is thin and rod-like, when $\alpha = -2$, it has a thin disk-like shape, and when $\alpha = -4$, it is spherical.

For thin rod-like structures such as peptide hydrogels, the Guinier law was employed to estimating the fibre diameters, given in Eq. 3.10:

$$I_N(q) = I_0 \exp\left(-\frac{1}{3} q^2 R_g^2\right) \tag{3.10}$$

where I_0 is the absolute intensity, linked to the molecular weight of the peptide, and R_g is the radius of gyration, which defines the overall size of the peptide hydrogel at a small q range.

A Guinier plot ($l_n q I_N(q)$ $vs.$ q^2) can be obtained from Eq. 3.10. In monodisperse systems, the slope of a line of best fit can be calculated, which corresponds to the radius of gyration, R_g. However, without monodispersity, the sample structure cannot be considered as a thin rod-like shape. For the long thin fibres, a modified Guinier law can be used by Eq. 3.11:

$$qI_N(q) = KCL_M \exp\left(-\frac{1}{2} q^2 R_{gc}^2\right) \tag{3.11}$$

where L_M is the fibres/cylinder mass per unit length, and R_{gc} is the cross-sectional radius of gyration of the fibres/cylinder. If the observed scattering is of the form given by Eq. 3.11, then at low q, a line of best fit should be calculated for a plot of $l_N [q\, I_N(q)]$ vs q^2. R_{gc} can then be determined, and related to the fibre diameter d_f by Eq. 3.12 [14]:

$$R_{gc} = \sqrt{\frac{d_f^2}{8}} \tag{3.12}$$

3.6 Oscillatory Rheology

Rheology is the study of the behaviour of liquids, solids and soft solid matters under an applied force, deflection or velocity, leading to their flow (for liquids) or deformation (solids). It is also possible to analyse the behaviour of viscoelastic materials in the same manner, demonstrating that they behave both as a liquid and a solid.

The two-plate model (Fig. 3.6) is used to illustrate the process of oscillatory tests in rheometers [15]. The upper plate is acted on by a shear force to give it a velocity v, and the lower plate remains stationary. A sample is loaded on the lower plate, with a gap, h, to the upper plate. The sample is sheared in this gap and will undergo flow or deformation behaviour, depending on the shear force. A range of parameters can be used to describe rheological properties of materials. Shear stress τ arises from a shear force F, in the case the rectangle changes the shape into parallelogram (Fig. 3.5), and is given by Eq. 3.13:

$$\tau = \frac{F \, (Force)}{A \, (Area)} \qquad\qquad (3.13)$$
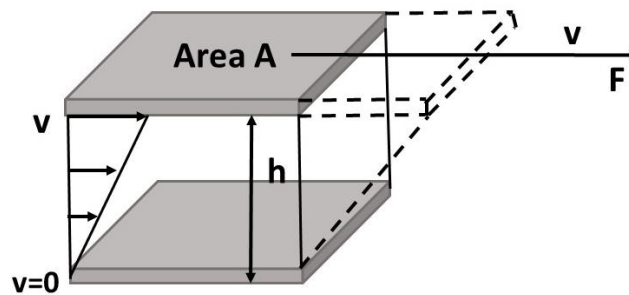
Figure 3. 5 A diagram of Two-Plates-Model illustrates the oscillatory test in rheometer.

For soft materials, the shear causes a related strain, which can be used to describe viscoelasticity and fracture properties. The shear stress is related to pure shear strain by Eq 3.14:

$$\tau = \gamma G \tag{3.14}$$

where γ is the shear strain and G is the shear modulus.

The shear rate is linked to the velocity of rotation of the upper plate. If a fluid is considered to exist between the plates, with the material deforming according to the shear rate, as in Eq. 3.15:

$$\dot{\gamma} = \frac{V}{h} \tag{3.15}$$

where $\dot{\gamma}$ is the shear rate, v is the velocity (m/s) and h is the gap between the two plates.

In materials that flow, the molecules undergo relative motion between each other due to the shear force, and this produces internal friction, acting against the flow to deform the materials. Materials have the flow property that is so called fluids. The flow resistance in material deformation can be described by viscosity, which is measured under the ideal temperature and a reasonable shear rate. In most fluids, the relationship between shear rate and shear strain is linear and obeys Newton's law, as in Eq. 3.16:

$$\tau = \eta\gamma \tag{3.16}$$

where η is the viscosity. These fluids are termed "Newtonian fluids".

Oscillatory rheology is used to investigate viscous liquids, polymers, gels, dispersions, elastomers, melts and rigid solids. In a dynamic oscillatory test, a stress or strain is applied to the sample at a fixed frequency, and the quantity varies with the harmonic waveforms of stress and strain as a function of time. A viscoelastic sample possesses a linear viscoelastic region (LVR), where the sinusoidal strain waveform is delayed behind the sinusoidal stress waveform

at a specific angular frequency, as shown in Fig. 3.6A. The phase of the delay is the phase shift angle δ. The angular frequency is given in Eq. 3.17:

$$\omega = 2\pi f \tag{3.17}$$

where ω is the angular frequency in rad/s or in s^{-1}, and f is the frequency in Hz.

If the sample is a pure viscous liquid, it is unable to return to its original shape following a stress or strain. The stress and strain waveforms therefore display a phase shift angle δ equal to $\pi/2$ (Fig. 3.6B). However, if the sample is a pure elastic material, the stress and strain waveforms have the same phase, i.e., the phase shift angle δ is equal to 0 rad/s (Fig. 3.6C).

A)   B)   C)
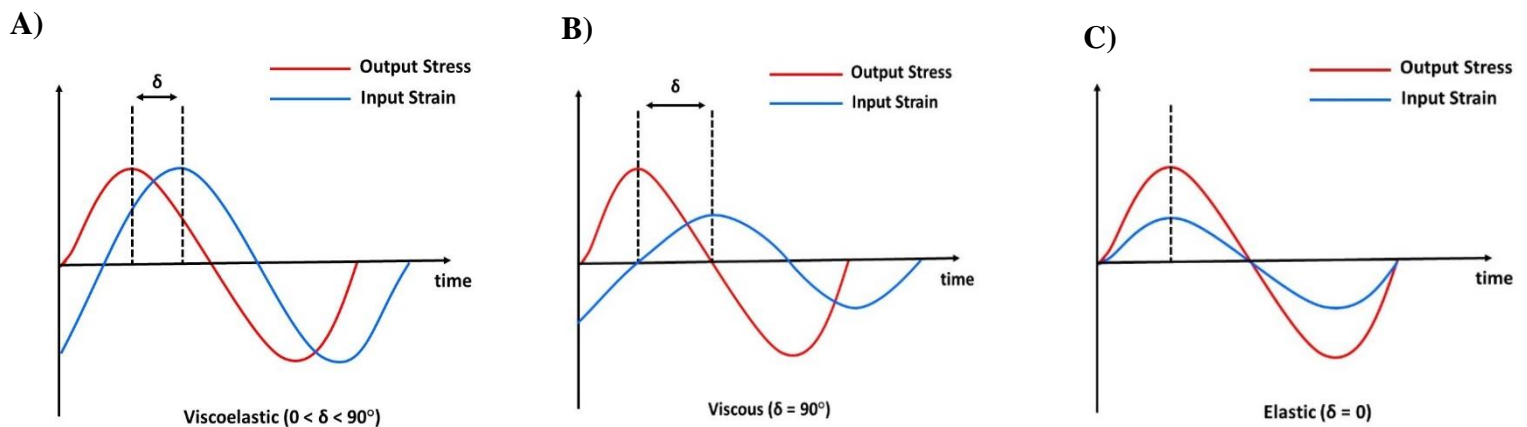
Figure 3. 6 The relationships between stress and strain waves. A) represents the viscoelastic material B) represents the viscous material C) represents the elastic material.

Amplitude oscillatory shear measurements are commonly used to investigate viscoelastic hydrogels [16]. It involves the use of a rotational rheometer to test a loaded hydrogel in an equilibrium state (ideal gap and temperature). The amplitude of oscillation is equal to the maximum stress or strain, and the angular frequency is the number of oscillations per second. The hydrogel is loaded on the stationary plate and the upper plate is lowered to a gap, h. The

105

upper plate then rotates to produce an oscillatory stress or strain relative to the stationary plate (Fig. 3.7).
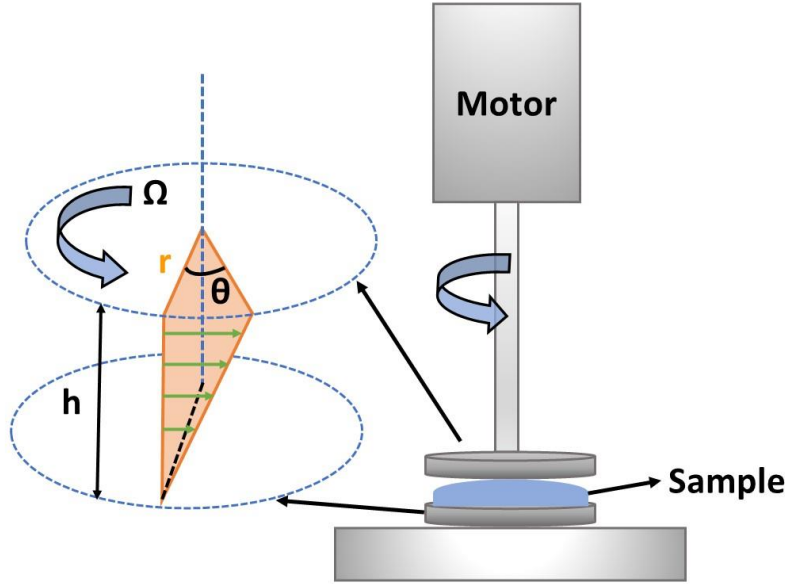
Figure 3. 7 A schematic diagram of oscillatory rheometer.

The rheometer motor controls the angular displacement and angular speed, so stress can be calculated from the torque of upper plate of the motor, as shown in Fig. 3.8 and given by Eq. 3.18:

$$\sigma = M \times K_\sigma = M \times \frac{2}{\pi r^3} \tag{3.18}$$

where M is the torque in N/m or gm^{-cm}, K_σ is a stress constant representing the geometry-dependent factor, and r is the plate radius.

The strain is given in Eq. 3.19:

$$\gamma = K_\gamma \times \theta = \frac{r}{h} \times \theta \tag{3.19}$$

where θ is the angular motor deflection, K_γ is strain constant representing the geometry-dependent factor, and h is the gap between the plates.

The shear rate can be written as in Eq. 3.20:

$$\dot{\gamma} = \Omega \times \frac{r}{h} \tag{3.20}$$

Where Ω is the motor angular velocity in rad/s.

The oscillation of the upper plate varies as a function of time, and is related to the stress or strain. The relationship between the applied stress/strain and corresponding measured strain/stress is given by Hooke's law, as in Eq. 3.21:

$$G^* = \frac{\sigma(t)}{\gamma(t)} \tag{3.21}$$

where G^* is the complex modulus, representing material stiffness (i.e. resistance to deformation), and t is time. The sinusoidal shear strain can be written as in Eq. 3.22:

$$\gamma(t) = \gamma \times \sin(\omega t + \delta) \tag{3.22}$$

The vector diagram in Fig. 3.8 illustrates the relationships between G* and $\frac{G''}{G'}$, and demonstrates how it is possible to use trigonometry to investigate material behaviour:
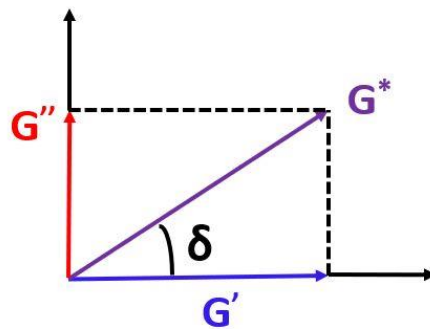
Figure 3. 8 A vector diagram to show the relationships between G* and $\frac{G''}{G'}$.

where $G' = G^* \cos \delta$, $G'' = G^* \sin \delta$, so $\tan \delta = \frac{G''}{G'}$ represents the loss factor.

The rheometer measures a storage modulus G' and a loss modulus G'' at a given oscillatory amplitude or frequency. In a hydrogel, G' represents the energy remaining within the gel after shear, and G'' represents the energy lost during shear. This means that G' is the stiffness of the gel, and G'' is the viscosity of gel. If tan δ > 1 (i.e., $G'' > G'$), the gel behaves like a viscous liquid, while if tan δ < 1 ($G' > G''$), the gel is in an elastic solid-like state.

The storage modulus G' and loss modulus G'' can be written as sine and cosine functions:

$$G' = \frac{\sigma(stress)}{\gamma(strain)} \times \cos(\omega t + \delta) \tag{3.23}$$

$$G'' = \frac{\sigma(stress)}{\gamma(strain)} \times \sin(wt + \delta) \tag{3.24}$$

The measurements require determination of the linear viscoelastic region (LVR) of the examined materials, in which stress is proportional to strain. In LVR, the G' should be parallel with G''. If $G' > G''$, this means the sample is in the viscoelastic state. Within the LVR, the applied stress is insufficient to break down the samples, so they retain their structure, and various material properties such as shear thinning and recovery can be examined. The shear stress/strain is maintained in the LVR for a set time period, then a strong stress/strain is briefly applied to temporarily destroy the material's structure, before another stress/strain measurement is repeated in the LVR, allowing the injectability of a hydrogel to be confirmed. The range of the LVR can be determined by a stress or strain sweep experiment.

3.7 Zeta Potential

The zeta potential represents the electric potential in a material's slipping plane, and indicates the stability of a colloidal dispersion. It has been widely used in formulation research, allowing

insights into a material's dispersion, aggregation and flocculation, which can be used to improve pharmaceutical formulations and benefit patients.

In a colloidal system, the dispersed particles have a charged surface (-) which attracts counter ions (+), to form an electrical double layer (Fig. 3.9). The first layer is called the Stern layer, and features counter ions (+) that are strongly-bound to the surface; the second layer is named the diffuse layer, and has ions (+) more weakly-bound to the surface. This difference arises because the force between the ions is dependent on both charge and distance. Fig. 3.9 shows how some anions in the diffuse layer are repelled by the negatively-charged particles, but are simultaneously attracted by the cations in the Stern layer. The particles and ions therefore form a stable diffuse layer with a boundary called the slipping plane (shear plane) [17]. When the particle moves, ions within the slipping plane follow it due to electrical attraction, but ions outside the slipping plane do not move. Therefore, the zeta potential of the particle is measured as the voltage (V or mV) at this plane.
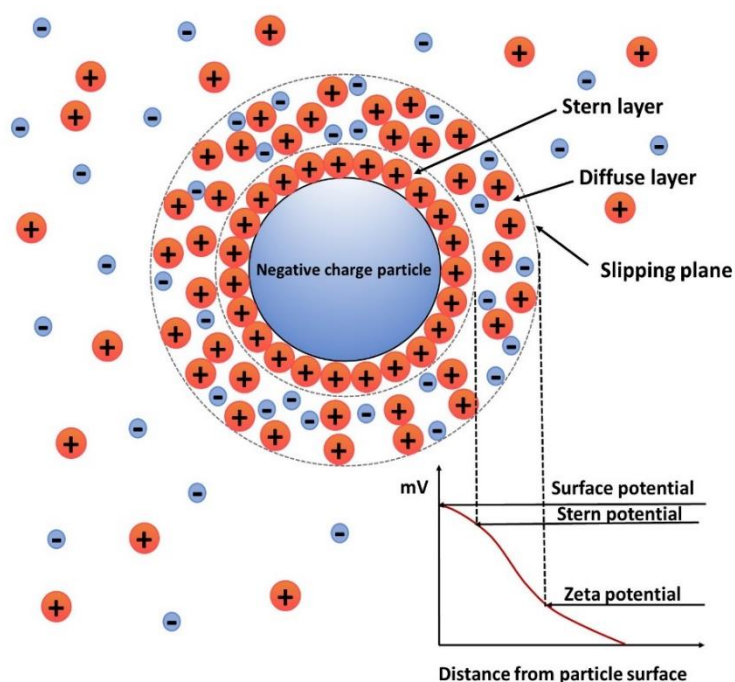
Figure 3. 9 A schematic diagram of double layer and zeta potential in a colloidal system.

The zeta potential represents the magnitude of the interactions between particles. For a small dispersed particle, a higher absolute value of the zeta potential represents a more stable colloidal system. The stability of particles in a system depends on electrostatic repulsion between them. Strong repulsion forces the particles to distribute individually, preventing aggregation or flocculation. This is known as the DLVO theory (Derjaguin-Landau-Berwey-Overbeek theory) that describes the stability of suspensions in terms of the balance of attractive and repulsive forces between particles. However, low zeta potential values indicate that the system is unstable, as the magnitude of the attractive forces between particles increase which induce them to come together to aggregate or flocculate. The relationship between zeta potential and colloidal stability is displayed in Table 3.1.

Table 3. 1 The relationships between zeta potential and stability of colloid [18].

Magnitude of zeta potential (mV)	Colloidal stability
0-5	Flocculates/coagulates rapidly
10-30	Becomes unstable
30-40	General stability
40-60	Better stability
> 61	Extremely stable state

Methods of measuring the zeta potential of a colloid include electrophoresis, electro-osmosis, steaming potential and ultrasound. In the method of electrophoresis, particles move under an applied electric field, with a velocity defined as the electrophoretic mobility. The Henry equation illustrates the relationship between zeta potential and electrophoretic mobility:

$$U = \frac{2\varepsilon\zeta f(\kappa a)}{3\eta} \tag{3.25}$$

where U is the electrophoretic mobility ($m^2 \cdot s^{-1} \cdot V^{-1}$), ε is the dielectric constant ($kg \cdot mV^{-2} \cdot s^{-2}$), ζ is the zeta potential (mV), η is the viscosity ($kg \cdot m^{-1} \cdot s^{-1}$), and $f(\kappa a)$ is Henry's function. The parameter κ is the Debye length, and its reciprocal κ^{-1} is defined as the thickness of the electrical double layer; a is the particle radius, so κa represents the ratio of particle radius to double layer thickness. The value of $f\kappa a$ is linked to the medium, e.g., for smaller particles in a non-polar medium, $f\kappa a = 1$, and the Huckel approximation is used to measure the zeta potential. For a measurement in polar media, $f\kappa a = 1.5$ and the Smoluchowski approximation will be applied into calculation.

In this study, Malvern's Zetasizer Nano was used to measure electrophoretic mobility to obtain the zeta potential and the surface charge of macromolecules and peptides. The instrument is

based on the mechanism of Doppler electrophoresis, or electrophoretic light scattering, and consists of a laser, a beam splitter, an attenuator, a capillary, a set of compensation optics, a set of combining optics, a detector and a digital signal processor (correlator) (Fig. 3.10). The laser emits a light source that is subsequently split into two to yield an incident beam and a reference beam. The incident beam is passed through the centre of the sample to be investigated, which is loaded into a capillary with electrodes attached. The sample particles move under an applied electric field, with positively charged ions moving towards the negative electrode and vice versa. The speed at which the particles move causes changes in the amount of light scattering, resulting in a variation of light intensity proportional to the particle speed. The digital signal processor is used to collect these signals and display them on a computer. In this process, scattered light after passing through the sample should be in a specific range to confirm the detection. Therefore, an attenuator is used to modulate the intensity of the incident light and allow the measurement of scattered intensity. The thickness of the capillary can vary with the type of sample being measured, so a set of optics is required to correct for these variations.
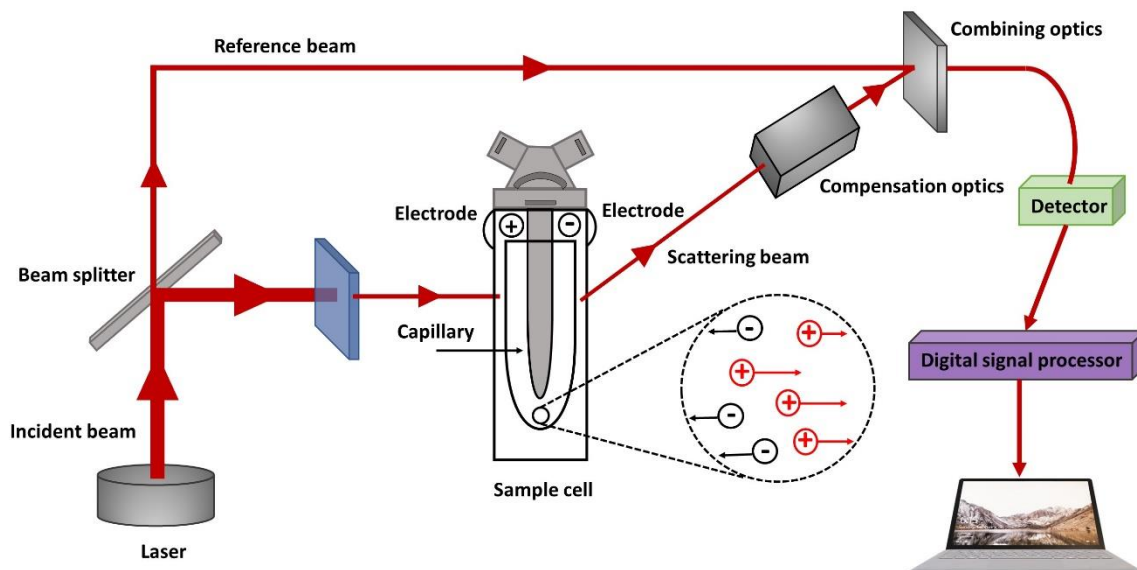
Figure 3. 10 A schematic representation of Malvern's Zetasizer Nano.

3.8 UV-Vis Spectrophotometer

Ultraviolet-visible spectroscopy (UV-vis) is a simple technique that allows accurate measurement of chemical structure. It uses light radiation in the ultraviolet (100-400 nm wavelength) and visible (400-800 nm wavelength) ranges of the electromagnetic spectrum.

These wavelengths are able to cause electronic transitions within atoms or molecules after absorption of the incident radiation, and measurement of when these transitions occur allows determination of the nature of the electronic energy levels present. These electronic transitions could take the form of bonding and non-bonding electrons being excited to a antibonding orbital that is higher in energy. Three types of orbitals contribute to the transitions seen on a UV-vis spectrum: σ orbitals, which form single covalent bonds, π orbitals, which form double bonds, and non-bonding orbitals, represented by n. Electrons in these orbitals can absorb energy from an incident photon and transition from their ground state to an excited state.

There are four main types of transitions observed in UV-vis: $\sigma\to\sigma^*$, $n\to\sigma^*$, $\pi\to\pi^*$ and $n\to\pi^*$, where the * represents an antibonding orbital. The energies of the transitions follow the order $\sigma\to\sigma^* > n\to\sigma^* > \pi\to\pi^* > n\to\pi^*$. The energy of a photon is inversely proportional to its wavelength, i.e., a shorter wavelength corresponds to a higher energy. For example, the C-H bonds in methane display a $\sigma\to\sigma^*$ transition with $\lambda_{max} = 125$ nm. This transition requires a larger amount of energy, so the wavelength of the incident photon is in the far-UV region with $\lambda < 200$ nm. However, the energy of an $n\to\sigma^*$ transition is lower and could occur at a wavelength of $\lambda_{max} = 200$ nm, as is often seen in saturated alcohols, ethers or amines. Most compounds that display $\pi\to\pi^*$ and $n\to\pi^*$ transitions can be measured via UV-Vis spectroscopy as their absorbance peaks are in the range of 200-700 nm. These compounds include unsaturated hydrocarbons and saturated ketones.

This study used a Jenway temperature controlled 6715 UV/Vis spectrophotometer for measurements. It functions across wavelengths of 190 to 1100 nm, with an ultra-narrow bandwidth of 1.5 nm. Fig, 3.11 is a schematic of the machine's operation. A pulsed xenon laser was used as a light source, which passes through a monochromator to obtain the desired wavelength of light, before passing through the sample in a cuvette. A reference sample (e.g HPLC water) was first collected as a background. After the sample, a detector is used to convert the light into an electric signal and record a spectrum as a plot of absorbance/transmittance against wavelength. The intensity of a peak on the spectrum is related to its corresponding electronic transition and can be used to determine the nature of the sample.
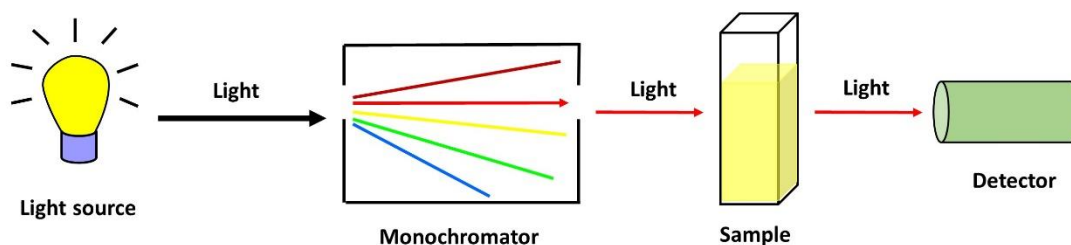
Figure 3. 11 A simplified scheme of UV/Vis spectrophotometer.

3.9 Enzyme-linked Immunosorbent Assay (ELISA)

The enzyme-linked immunosorbent assay (ELISA) is commonly employed to test antigens, antibodies, and proteins in serums, liquid samples and cell lysates. The principle of ELISA is that the enzyme-linked antibody specifically binds to the antigen on the surface of the solid phase, allowing the enzyme to oxidise the substrate and cause a colour change via the redox reaction of a hydrogen donor. It is a useful tool for analyte quantification, for diagnosing diseases in medical research and for quality control of drugs prior to marketing [19].

ELISA is commonly broken down into different types: direct, indirect, sandwich and competitive. The mechanisms of these types are shown in Fig. 3.12.

(A) Direct ELISA
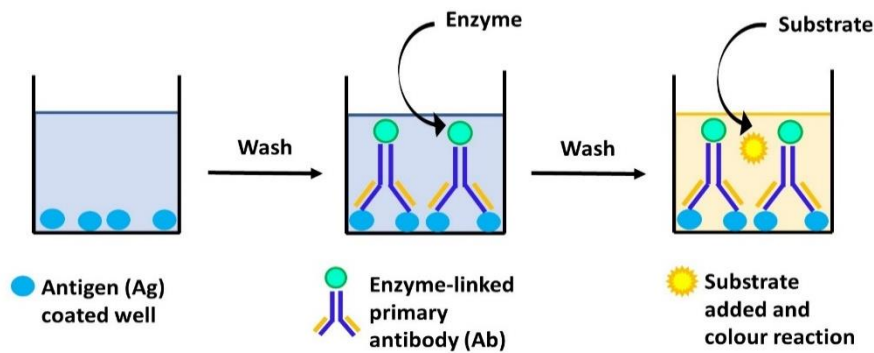
(B) Indirect ELISA
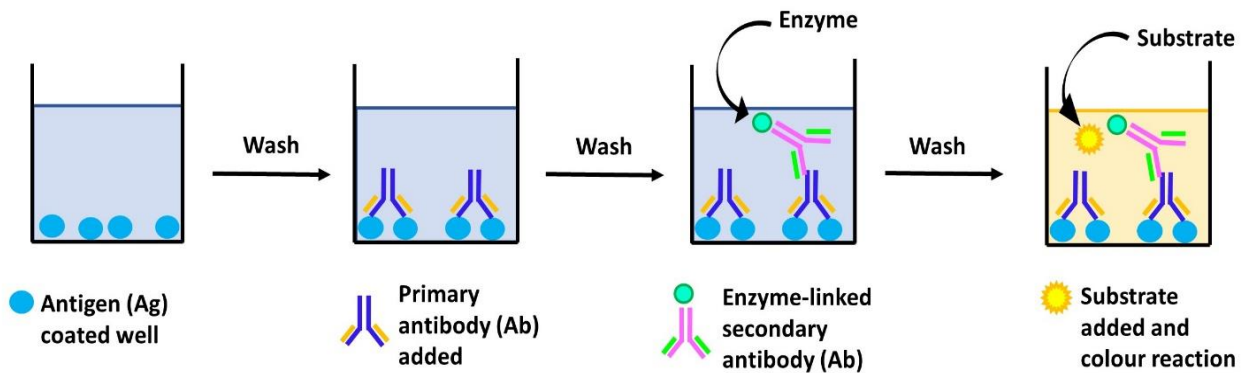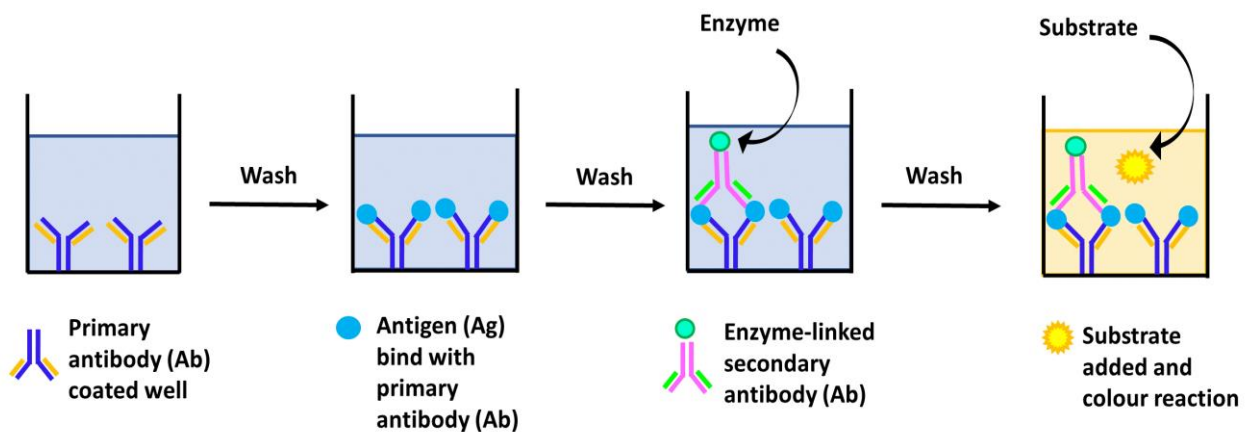
(C) Sandwich ELISA

(D) Competitive ELISA
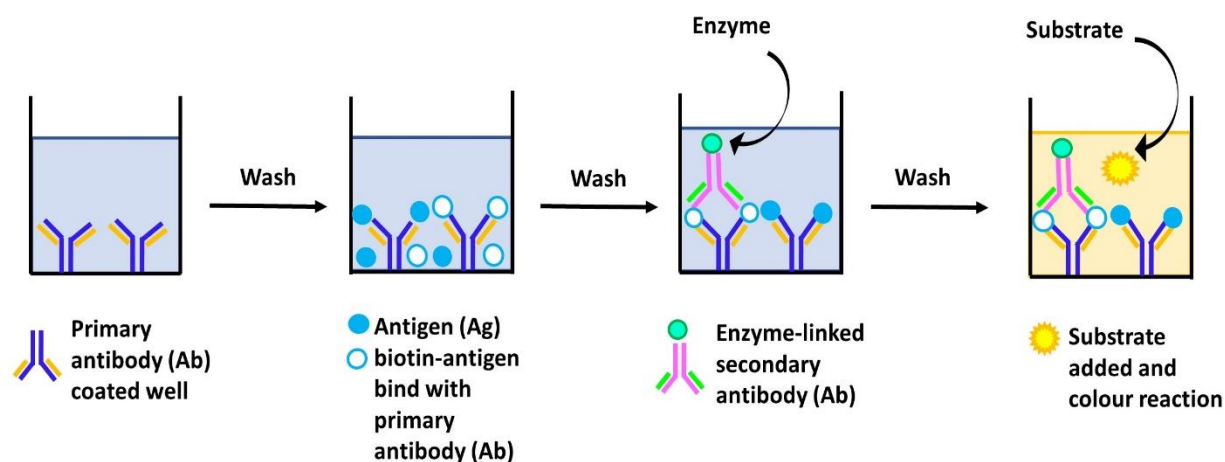
Figure 3. 12 The scheme of different types of ELISA. A) Direct ELISA B) Indirect ELISA C) Sandwich ELISA D) Competitive ELISA.

In direct ELISA, the antigen is directly coated on to the solid phase support (a polystyrene microtiter plate), and the primary antibody is able to specifically bind to the antigen. Horseradish peroxidase (HPR) or alkaline phosphatase (PA) is added to conjugate to the primary antibody bound to the antigen. After the addition of the substrate, a reaction will proceed with a colour change dependent on analyte concentration. Analyte quantity can therefore be determined from a standard curve of known concentrations (Fig. 3.12A) [20]. Direct ELISA is often used to investigate the affinity and specificity of a given antibody.

Indirect ELISA differs in that there are two processes for detection. The antigen is coated onto the microtiter plate and first bound to the antigen-specific antibody. After the non-binding complex is removed by washing with a buffer, an enzyme-linked secondary antibody binds to the primary antibody [21]. Analyte concentration can again be obtained from a standard curve (Fig. 3.12B). Indirect ELISA is used to measure endogenous antibodies.

The sandwich variant of ELISA uses two antibodies to form matched antibody pairs that are specific to a target antigen in the analyte. A primary antibody, dubbed a 'capture antibody', is coated onto the microtiter plate. The analyte is added to the plate surface, allowing the target antigen to bind to the capture antibody. Following this, an enzyme-linked antibody can bind to the antigen, creating a sandwich form (see Fig. 3.12C). A substrate is then added, fluorescence occurs upon reaction and the target antigen concentration can be calculated from a standard curve. The sandwich ELISA technique is therefore commonly used to measure analyte concentration [22][23].

In competitive ELISA, a specific antibody called a capture antibody is precoated onto the microtiter plate. A biotin-labelled antigen is added as a reference, to compete with the target antigen in the analyte to bind with the capture antibody. HPR-streptavidin is then added, to bind with the biotin-labelled antigen-antibody complex via a non-covalent interaction to form an avidin-biotin complex. Following the addition of a substrate, fluorescence intensity is negatively correlated to target antigen concentration (Fig. 3.12D); i.e., a weaker signal occurs if the target analyte concentration is higher than the reference antigen concentration. Also known as inhibition ELISA, the competitive ELISA technique is often used for small molecule antigens, haptens and viruses [24].

Table 3. 2 The advantages and disadvantages of these four types of ELISA are in detail.

	Advantages	Disadvantages
Direct ELISA	• Quick test with short protocols • Saves on reagents • No cross-reaction with a secondary antibody.	• The coated antigen is non-specific and causes a high background • Labelling a primary antibody is expensive and time-consuming • Less flexible as the primary antibody must be conjugated • No signal amplification.
Indirect ELISA	• Many commercially-available secondary antibodies for labelling • Cheaper as less labelled primary antibody is required • Highly sensitive, as many primary epitopes can be bound by the secondary antibody • Flexible, as one secondary antibody can be used to test many primary antibodies.	• Takes much longer than direct ELISA • Secondary antibody cross-reactions may occur, leading to a non-specific signal.
Sandwich ELISA	• More sensitive than direct	• Difficult to find matched

		antibody pairs that can both bind to a target antigen.
	• and indirect ELISA • Flexible, as direct and indirect sandwiches can be used • Highly specific, as two antibodies detect epitopes on the same antigen • More suitable for complex analytes • No sample purification needed.	
Competitive ELISA	• Suitable for small molecule antigens, haptens and viruses • No purification required.	• Lower specificity and sensitivity

To validate ELISA results and ensure precision, control groups are required. These can be classified into two groups: negative and positive controls. For the sandwich ELISA in our study, a standard curve was used as a positive control group. A series of titrations can be performed to obtain the standard curve, reference to which allows determination of unknown analyte concentrations. Furthermore, the standard curve can be used to test equipment functionality. A negative control group is required to exclude any non-specific binding or false positive results.

The most common negative control group is a "blank control", but this is sometimes uncertainly defined. Here, "blank" means empty wells that contain no reagents or only the ELISA buffer. This control is used to exclude any effects on the signal from the plastic plate and buffer. A chromogen blank can also be used, which adds substrate and stop solution into a

well to examine the influence of substrate on the results, but this blank is only needed for old substrates.

A wavelength correction can be used as a control in many forms of ELISA to correct the signal. The signals are first read at a specific wavelength, and then again off-wavelength, to remove any undesirable background effects, such as those from a plastic well, dust or bubbles. The signals are subtracted from one another to obtain results with reduced errors.

The S0 control contains zero standard, leading to a minimum colour background in the absence of analytes. This can be used to correct all the signals in a plate.

3.10 LIVE/DEAD Cell Viability Assay

The LIVE/DEAD cell viability assay uses a mixture of two fluorescent dyes to stain cells, allowing recognition and differentiation of live and dead cells from their binding to different fluorophores.

The technique is based on using a calcein-AM probe to permeate into the live cell membrane. Calcein-AM is not a fluorophore, and the attached acetoxymethyl ester (AM) group increases its hydrophobicity, to allow simple insertion into cells. This attached group can be subsequently removed via hydrolysis to yield the green fluorophore calcein within an intact cell membrane. This process requires intracellular esterase to function (Fig. 3.13), and dead cells do not have active intracellular esterase enzymes, therefore they cannot absorb calcein and fluoresce green. In comparison to other probes, calcein-AM is an ideal dye, as it has low cytotoxicity and is not very sensitive to pH. The excitation and emission wavelengths of calcein-AM are around 494 nm and 517 nm respectively.
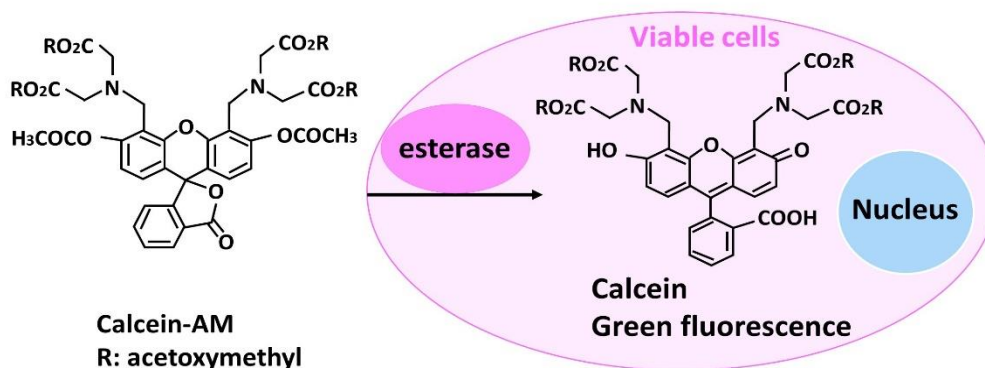
Figure 3. 13 A schematic representations of live cell staining. Calcein-AM inserts into the cells and hydrolysed to green fluorescence calcein by the activity of esterase.

Ethidium homodimer I is commonly used to stain dead cells, as it has a high binding affinity for ssDNA, dsDNA, RNA and oligonucleotide molecules (Fig. 3.14). Its binding to DNA enhances the intensity of its fluorescence, producing a bright red colour. The maximum excitation and emission wavelengths are around 528 nm and 617 nm respectively. As the molecule has a strong positive charge, it is unable to permeate into an intact plasma membrane and is thus a good probe for the evaluation of cell viability. Used in conjunction with calcein-AM, the two molecules together form a prevalent kit to test viability or cytotoxicity in mammalian cells, via study of intracellular esterase activity and plasma membrane integrity.
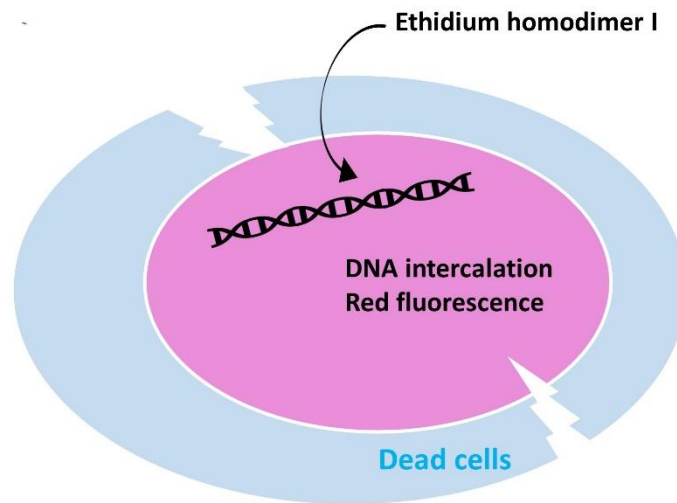
Figure 3. 14 A schematic representations of dead cell staining. Ethidium homodimer I enters into the damage cell membrane and binds to dsDNA.

3.11 Confocal Laser Scanning Microscopy (CLSM)

Confocal laser scanning microscopy (CLSM) is an advanced imaging technique used in biomedical research. In contrast to conventional microscopy techniques, CLSM uses a laser scanning device to focus a light source on a specimen, exciting fluorophores that are present to display an image. The technique yields a high resolution and degree of contrast, with high sensitivity and optical sectioning, allowing for the digital visualisation and construction of three-dimensional structures via the variation of specimen depth.

CLSM uses a laser as a beam source for scanning, as shown in Fig. 3.15. The experimental setup consists of a laser, an illumination pinhole (light source aperture), a beam splitter (dichroic mirror), a scanner, an objective lens, a confocal pinhole and a photomultiplier detector. The laser light first passes through the illumination pinhole into the beam splitter,

where it is reflected. The light then passes through the scanner, which has sets of mirrors aligned in X and Y directions to facilitate quick and precise scanning, before it travels through the objective lens and is focused on the specimen. The laser light induces fluorescence in the sample, and the emitted photons travel back to the beam splitter and are focused on the confocal pinhole aperture, where they are transmitted to the photomultiplier. The photomultiplier detector captures and amplifies the signals, which are converted by a computer into an image.
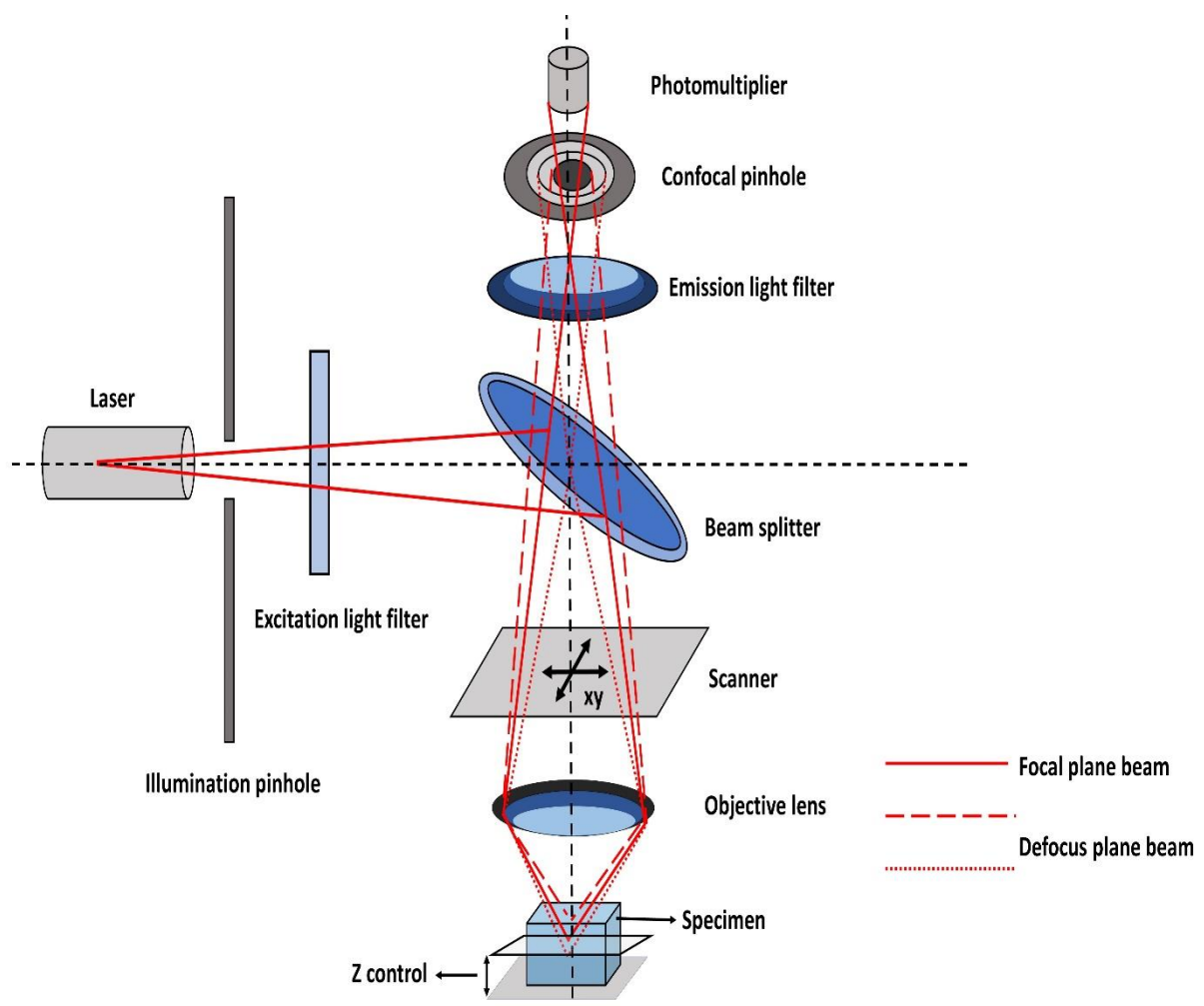
Figure 3. 15 A simplified scheme of Confocal Laser Scanning Microscopy.

In the CLSM microscope, the illumination pinhole and the confocal pinhole lie in the focal plane of the objective lens, so only light in the focal plane can pass through the pinhole and be

detected. Out-of-focus light does not arrive at the photomultiplier, presenting dark areas on the image and yielding a high amount of image contrast [25]. A z-stepper is also used to vary sample depth in the observation of 3D specimens, for example in the study of cell encapsulation in peptide hydrogels. This variation allows the total amount of cells in the hydrogel to be measured as a function of depth. Overall, CLSM is a high-resolution technique that produces a large amount of image contrast, which are essential attributes for an imaging technique.

CLSM is therefore an ideal technique to analyse cells, as it is non-destructive and easily allows the study of cellular structure and activity, especially in combination with immunofluorescence labelling or ion fluorescence labelling. CLSM was therefore employed in this study to investigate the results of LIVE/DEAD cell staining.

3.12 Pico-Green Assay

Pico-Green is a highly sensitive fluorescence probe used to quantify amounts of dsDNA, as it binds to the dsDNA to yield a luminescent complex. The intensity of the fluorescence is dependent on dsDNA concentration in the sample. Pico-Green can be used to rapidly and specifically detect dsDNA in the presence of ssDNA, RNA and monomeric nucleotides, even if the concentration of dsDNA is as low as 25 pg/mL.

In this study, a Pico-Green dsDNA kit was used to count the number of cells in a peptide hydrogel. The enzymatic mixture Pronase E was used to digest the peptide hydrogel for this purpose. Pronase E is isolated from the extracellular fluid of *Streptomyces griseus*, which contains proteases and peptidases for the hydrolysis of proteins and peptides into individual amino acids [26][27]. Pronase E can cleave peptide bonds at either the C-terminus or N-terminus, as displayed in Fig. 3.16, and the hydrolysis procedure is dependent on conditions such as time, temperature, concentration, and the ratio of volumes of Pronase E and the sample.

For a Pico-Green assay to be performed, the peptide hydrogel must be degraded into solution to allow the constituent cells to be exposed for detection, hence the necessity of Pronase E.
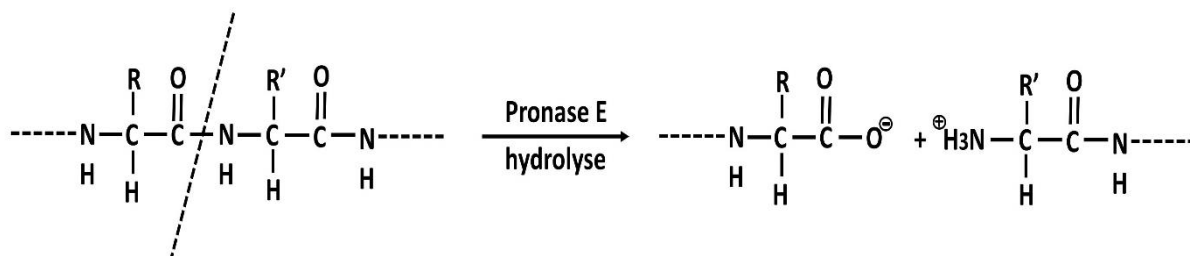
Figure 3. 16 A scheme illustrates the cleavage of peptide bond by pronase E.

In comparison to traditional methods, a Pico-Green dsDNA assay has many advantages. For example, it is orders of magnitude more sensitive than UV absorbance, which allows the use of much lower amounts of sample; the assay is specific to dsDNA even in the presence of the RNA molecules at similar concentrations; it is simple to run the assay on fluorescence-based microplate readers with Ex/Em = 480/520nm; and it can be applied to many different studies, including in PCR analysis, the study of chip samples, DNA damage analysis, analysis of enzymatic activity, quantification of genomic DNA and viral DNA, and identification of dsDNA in a complex.

3.13 References

[1]   C.-H. Shen, "Quantification and Analysis of Proteins," in Diagnostic Molecular Biology, 2019. doi: 10.1016/b978-0-12-802823-0.00008-0.

[2]   S. D. Sarker and L. Nahar, "Applications of High Performance Liquid Chromatography in the Analysis of Herbal Products," in Evidence-Based Validation of Herbal Medicine, 2015. doi: 10.1016/B978-0-12-800874-4.00019-2.

[3]   S. Y. Lin, M. J. Li, and W. T. Cheng, "FT-IR and Raman vibrational microspectroscopies used for spectral biodiagnosis of human tissues," Spectroscopy. 2007. doi: 10.1155/2007/278765.

[4]   D. Naumann, "FT-infrared and FT-Raman spectroscopy in biomedical research," Applied Spectroscopy Reviews. 2001. doi: 10.1081/ASR-100106157.

[5]   A. Barth, "Infrared spectroscopy of proteins," Biochimica et Biophysica Acta - Bioenergetics. 2007. doi: 10.1016/j.bbabio.2007.06.004.

[6]   S. G. Kazarian and K. L. A. Chan, "Applications of ATR-FTIR spectroscopic imaging to biomedical samples," Biochimica et Biophysica Acta - Biomembranes. 2006. doi: 10.1016/j.bbamem.2006.02.011.

[7]   P. anka, "Uses of Transmission Electron Microscope in Microscopy and its Advantages and Disadvantages," Int. J. Curr. Microbiol. Appl. Sci., 2018, doi: 10.20546/ijcmas.2018.705.090.

[8]   B. J. Inkson, "Scanning Electron Microscopy (SEM) and Transmission Electron Microscopy (TEM) for Materials Characterization," in Materials Characterization Using Nondestructive Evaluation (NDE) Methods, 2016. doi: 10.1016/B978-0-08-100040-3.00002-X.

[9]   W. Baschong and U. Aebi, "Chapter 23 - Negative Staining," in Cell Biology (Third Edition), 2006.

[10]   J. B. Guilbaud and A. Saiani, "Using small angle scattering (SAS) to structurally characterise peptide and protein self-assembled materials," Chemical Society Reviews. 2011. doi: 10.1039/c0cs00105h.

[11]   L. Barré, "Contribution of small-angle X-ray and neutron scattering (SAXS and SANS) to the characterization of natural nanomaterials," in X-ray and Neutron Techniques for Nanomaterials Characterization, 2016. doi: 10.1007/978-3-662-48606-1_12.

[12]   "Role of Sheet-Edge Interactions in β-sheet Self-Assembling Peptide Hydrogels".

[13]   N. P. Balsara, "Polymers and neutron scattering by J. Higgins and H. Benoit, Clarendon Press, Oxford, UK, 1994.," J. Polym. Sci. Part A Polym. Chem., 1996, doi: 10.1002/pola.1996.834.

[14]   D. Roberts, C. Rochas, A. Saiani, and A. F. Miller, "Effect of peptide and guest charge on the structural, mechanical and release properties of β-sheet forming peptides," Langmuir, 2012, doi: 10.1021/la303328p.

[15]   T. Mezger, The Rheology Handbook. 2020. doi: 10.1515/9783748603702.

[16]   Malvern Instruments Limited, "A Basic Introduction to Rheology," Whitepaper, 2016.

[17]   M. Instruments, "Zeta potential: An Introduction in 30 minutes," Zetasizer Nano Serles Tech. Note. MRK654-01, 2011.

[18]   A. Kumar and C. K. Dixit, "Methods for characterization of nanoparticles," Adv. Nanomedicine Deliv. Ther. Nucleic Acids, pp. 44–58, 2017, doi: 10.1016/B978-0-08-100557-6.00003-1.

[19]   R. Hidayat and Patricia Wulandari, "Enzyme Linked Immunosorbent Assay (ELISA) Technique Guideline," Biosci. Med.   J. Biomed. Transl. Res., 2021, doi: 10.32539/bsm.v5i2.228.

[20]   A. V. Lin, "Direct ELISA," Methods Mol. Biol., 2015, doi: 10.1007/978-1-4939-2742-5_6.

[21]   A. V. Lin, "Indirect ELISA," Methods Mol. Biol., 2015, doi: 10.1007/978-1-4939-2742-5_5.

[22]   L. Zhu, J. He, X. Cao, K. Huang, Y. Luo, and W. Xu, "Development of a double-antibody sandwich ELISA for rapid detection of Bacillus Cereus in food," Sci. Rep., 2016, doi: 10.1038/srep16092.

[23]   O. Stephan and S. Vieths, "Development of a real-time PCR and a sandwich ELISA for detection of potentially allergenic trace amounts of peanut (Arachis hypogaea) in processed foods," J. Agric. Food Chem., 2004, doi: 10.1021/jf035178u.

[24]   A. Moreno et al., "MAb-based competitive ELISA for the detection of antibodies against influenza D virus," Transbound. Emerg. Dis., 2019, doi: 10.1111/tbed.13012.

[25]   A. Mauko, T. Muck, B. Mirtič, A. Mladenovič, and M. Kreft, "Use of confocal laser scanning microscopy (CLSM) for the characterization of porosity in marble," Mater. Charact., 2009, doi: 10.1016/j.matchar.2009.01.008.

[26]   P. Bermejo-Barrera, S. Fernândez-Nocelo, A. Moreda-Pineiro, and A. Bermejo-Barrera, "Usefulness of enzymatic hydrolysis procedures based on the use of pronase E as sample pre-treatment for multi-element determination in biological materials," J. Anal. At. Spectrom., 1999, doi: 10.1039/a903924d.

[27]   K. D. Vosbeck, B. D. Greenberg, and W. M. Awad, "The proteolytic enzymes of the K 1 strain of Streptomyces griseus obtained from a commercial preparation (Pronase). Specificity and immobilization of aminopeptidase," J. Biol. Chem., 1975, doi: 10.1016/s0021-9258(19)41494-4.

Chapter 4 Determination of beta-sheet self-assembling peptide hydrogel and the properties assessment

4.1 Introduction

Self-assembled peptides that form hydrogels are excellent candidates for a range of biomedical applications due to their biocompatibility, biodegradability and injectability. For example, they are able to mimic the extracellular matrix (ECM) for applications in tissue engineering, drug screening and drug delivery [1][2][3][4][5].

Peptide self-assembly is driven by specific physical or chemical conditions, and results in formation of hydrogels with complex network structures [5][6]. One of the classic types of self-assembling peptides was devised by Zhang's group, and consists of patterned hydrophilic and hydrophobic amino acids in sequences that are typically 8–20 amino acids long. These peptides can form antiparallel beta sheet structures through the ionic forces of complementarily charged amino acids in water, and thus, they convert to nanofibrillar hydrogels in solution [6][7][8]. In this case, the charged residues are displayed on the outside whereas the hydrophobic side chains overlap together inside the structure (Fig. 4.1C). This kind of peptide hydrogel consists only of natural amino acids, without any chemical cross linkers, to minimise their toxicity in a biological environment. Furthermore, their stable β-sheet structures and high water content allow for applications to be developed in cell culture, drug delivery and tissue regeneration, among others [9][10][11].

Peptide self-assembly process can be initiated by a variety of triggers including temperature, UV light, time, pH, concentration or enzymes [2][12][13]. Above the critical gelation concentration (CGC), this results in formation of hydrogels, with the fibres entangled or bundled randomly to produce a 3D network structure (Fig. 4.1). These materials are adjustable

by molecular design, since the mechanical properties are tuneable according to the desired applications [4][14][15].
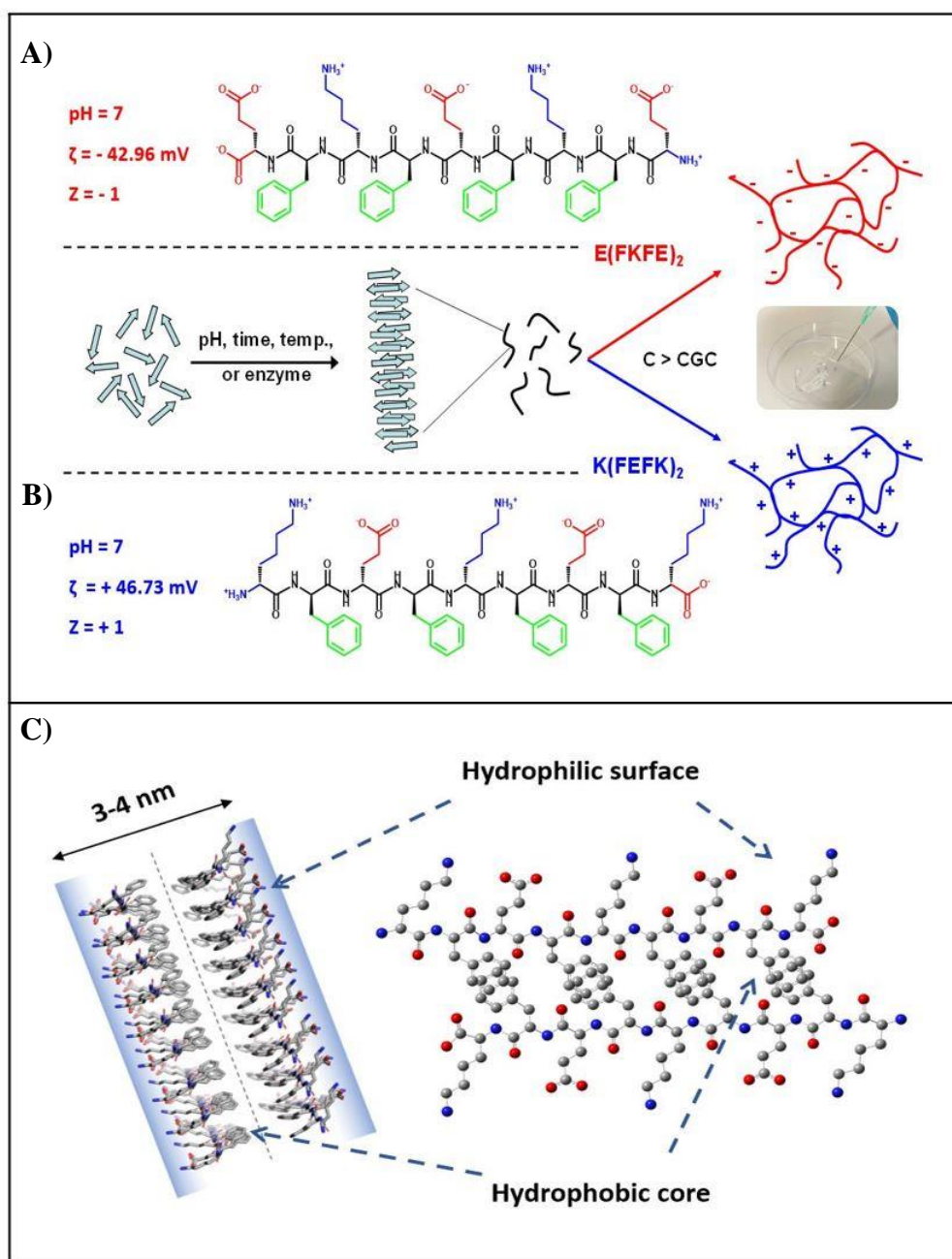
Figure 4. 1 A schematic illustrating the process of peptide self-assembly into beta sheet structure [16]. A) Chemical structure of EFKFEFKFE at pH 7. B) Chemical structure of KFEFK-FEFK at pH 7. ζ represented zeta potential, Z represented the charge of peptide at pH 7. C) The formation of antiparallel beta sheet structure. The peptide illustrated here is KFEFKFEFK.

Here, peptide sequences were designed based on the primary peptide, F8 (FEFKFEFK), studied in our group [16][17]. Phenylalanine (F) is a hydrophobic amino acid that is exposed at the fibre edge in aqueous solution. These hydrophobic contacts accelerate fibre–fibre associations to drive formation of fibre bundles, inducing a thick, fibrillose network. Previous research has shown that F8 self-assembles into a gel state at pH 3.5, with a high shear storage modulus (G') [16]. Here, we added a hydrophilic amino acid, lysine (K), to the N-terminus to cover the hydrophobic edge (KFEFKFEFK), making the peptide more soluble and leading to a cross-linked network at higher pH values. Meanwhile, EFKFEFKFE was designed by charge switching of the polar residues in the preceding peptide. These sequences will subsequently be referred to as E(FKFE)$_2$ and K(FEFK)$_2$, respectively. The theoretical relationship between pH and charge for these peptides is presented in Fig. 4.3. At pH 7, E(FKFE)$_2$ will carry -1 net charge and K(FEFK)$_2$ will carry +1 net charge. It is known from Aline Miller's work that the stability of a hydrogel depends on the charge modulus of the peptide [18]. Based on this, it was assumed that E(FKFE)$_2$ and K(FEFK)$_2$ would both enter the gel state at pH 7, permitting comparison of the charge effects on formation of the fibrillar network, mechanical properties, biocompatibility and injectability for drug delivery application.

4.2 Experimental methods

4.2.1 Reverse Phase High Performance Liquid Chromatography (RP-HPLC)

The purity of the E(FKFE)$_2$ and K(FEFK)$_2$ peptides was analysed by RP-HPLC, employing a C$_{12}$ column (Jupiter 4 µm Proteo 90 Å, 250 × 4.6 mm) for this purpose. Solvent A was HPLC grade water with 0.1% TFA, and Solvent B was ACN with 0.1% TFA. Before starting the experiment, the column was washed with solvent B until the baseline was stable. For analysis, a 2 mg/mL solution of each peptide was prepared in HPLC grade water and filtered through a 0.2 µm pore size device (Whatman Puradisc 13). Then, 50uL of peptide solution was aspirated by RP-HPLC needle, injected and analysed using UV detection at a wavelength of 214 ± 16 nm. After finishing the first run, the needle was washed by HPLC grade water to avoid cross-contamination between samples.

4.2.2 Peptide titration

To study the dependence of peptide charge on pH value, a 2 mg/mL solution of each peptide was prepared in HPLC grade water. Also, NaOH solutions were made up at 0.5 M and 0.1 M to adjust the pH value during titration. The initial pH of the peptide solution was recorded using a pH meter (Fisherbrand Hydrus 300), then the titration was started. The pH was recorded together with the addition volume of NaOH, then a curve of pH as a function of molar ratio of NaOH and peptide ($M_{NaOH}/M_{peptide}$) was plotted, which was used to evaluate the overall charge of the peptides at different pH values.

4.2.3 Peptide phase diagram

Under suitable conditions, the peptides are able to self-assemble to form a clear gel state. To find the ideal pH value and concentration for gel formation, a peptide phase diagram was constructed. Peptide solutions were prepared in HPLC grade water at a series of concentrations

of 4, 8, 12 and 16 mg/mL. Also, 0.1 M and 0.5 M NaOH solutions were made for pH adjustment. With the addition of NaOH, the peptides either precipitated, or self-assembled into different states including liquid/viscous liquid state, cloudy gel state or clear gel state.

4.2.4 Preparation of peptide hydrogel

Peptide powders were dissolved in 70% of the intended final volume of HPLC grade water, then 0.5 M NaOH was added to adjust the solution to pH 7. After this, HPLC grade water was added to the final volume to achieve the target concentration, and samples were placed in the fridge at 4 °C for formation of the gel state.

4.2.5 Dynamic oscillatory rheology

The mechanical properties of peptide hydrogels were assessed using a rheometer (Discovery HR-2, TA Instruments) equipped with a 20 mm diameter parallel plate. The gap size was set as 45,000 nm between the upper plate and sample stage at the beginning of experiment, and when the parallel plate was lowered for making measurements, the geometry gap was 500 nm. For analysis, 180 µL of sample was loaded onto the stage and equilibrated at 37 °C for 180 s before starting the run. Dynamic strain sweep was assessed by measuring the strain-dependent evolution of storage modulus (G′) and loss modulus (G″) at a fixed frequency of 1 Hz. For the shear thinning/recovery assay, samples were measured based on a dynamic time sweep at 0.2% strain for 5 min, immediately followed by 1,000% strain for 60 s, to mimic the process of administering an injection. This was followed by another 5 min dynamic time sweep to test the recovery properties at 0.2% strain. All steps were performed at a frequency of 1 Hz following equilibration for 180 s at 37 °C.

4.2.6 CD spectrum for analysing beta sheet structure

For CD analysis, peptide hydrogels at 12 mg/mL were diluted to 1.0, 0.8, 0.6, 0.4 and 0.2 mg/mL using HPLC grade water. A 40 µL aliquot of each sample was carefully dropped onto a quartz slide cell with 0.1 mm path length, avoiding bubble formation. Spectra were measured using a ChiraScan instrument (Applied Photophysics, UK). Data were collected from 260 nm - 190 nm with 3 seconds per point and 1 nm bandwidth. A background spectrum acquired using HPLC grade water, before running the samples, was subtracted from the sample spectra. The measured ellipticity values were converted to millidegrees (mdeg) and visualised in the Pro-Data Viewer software.

4.2.7 Thioflavin T (ThT) spectroscopic assay

Thioflavin T (ThT) is a dye which is commonly used to detect the β-sheet structure of amyloid fibres. Therefore, it was employed here to monitor different concentrations of peptide hydrogels [19]. A 1 mM ThT stock solution was prepared in HPLC grade water and filtered by 0.2 µm syringe filter. Then, $E(FKFE)_2$ and $K(FEFK)_2$ hydrogels were diluted from 12 mg/mL to 5.0, 2.0, 1.0, 0.5 and 0.2 mg/mL for the experiment. ThT solution (50 µL) was mixed with 1,950 µL of each diluted hydrogel sample to achieve a final volume of 2,000 µL in each case. Samples were gently vortexed and centrifuged to ensure even mixing, then transferred into a cuvette and analysed using a Fluorescence Spectrophotometer (Varian Cray Eclipse). The excitation was set at 440 nm wavelength (10 nm slit width), and data was acquired from 450–550 nm at room temperature [20].

4.2.8 Attenuated Total Reflectance Fourier Transform Infrared Spectroscopy (ATR-FTIR)

For characterisation of the secondary structure of peptide hydrogels, a Brucker Alpha-P FT-IR Spectrometer was used. The peptide hydrogel was pipetted to cover the crystal surface of the

spectrometer, and absorbance spectra were acquired from 1400–1800 cm^{-1}. For each sample, 256 scans were performed with a resolution of 4 cm^{-1}, and HPLC grade water was used to record a background spectrum prior to sample analysis.

4.2.9 Transmission Electron Microscope (TEM)

The peptide hydrogel was diluted 20-fold with HPLC grade water then vortexed to mix the sample evenly. A carbon-coated copper grid (400 mesh, Electron Microscopy Sciences, UK) was placed on the sample droplet for 1 min, moved to the water droplets to wash three times, then transferred to the 1% uranyl acetate droplet for 30 s (Fig. 4.1). Excess liquid on the grid was removed with a 70 mm filter paper (Whatman), then the grid was dried for TEM imaging. Images were acquired using an FEI Tecnai12 BioTwin at 100 keV, with a Gatan Orius SC1000A CCD camera. The fibre width of peptides was measured manually 800 times from TEM images, using the ImageJ software, and analysed by log-normal distribution.

4.2.10 Small-Angle X-ray Scattering (SAXS)

To characterise the structure of peptide hydrogels, SAXS measurements were performed at the Diamond Light Source, beamline I22 [21]. The sample–detector distance was fixed at 5.772 m resulting in a momentum transfer vector, q, in the range 0.1 < q (nm^{-1}) < 3, where $q = \frac{4\pi \sin(\frac{\theta}{2})}{\lambda}$, λ is the wavelength and θ is the scattering angle. Silver behenate powder was employed for calibration, and sample data were collected as 10×100 ms frames. Data reduction was done using the DAWN software [22]. The 2D isotropic scattering data were collected and corrected for detector response, dark current background and sample transmission, then radially averaged to obtain 1D scattering patterns.

4.2.11 2D cell culture

For 2D culture, 3T3 mouse embryonic fibroblast cells and mesenchymal stem cells (MSCs) were used, and these were also applied in 3D cell culture (as described below). The 3T3 cells were cultured in Dulbecco's Modified Eagle's Medium (Hibco) supplemented with 1% penicillin–streptomycin (Sigma–Aldrich, P0781) and 10% foetal bovine serum (Sigma–Aldrich, F9665). The MSCs were cultured in Eagle's Minimum Essential Medium (Sigma-Aldrich, M4526) containing 10% foetal calf serum (Sigma–Aldrich), 1% antibiotic/antimycotic solution (Sigma–Aldrich, A5955), 1% GlutaMAX (Life Technologies, 35050038) and 0.01% L-ascorbic acid 2-phosphate sesquimagnesium salt hydrate (Sigma–Aldrich, A8960). Growth media were warmed to 37 °C in a water bath before use.

Cells were removed from liquid nitrogen storage and transferred into a box with dry ice. Vials were then thawed in a 37 °C water bath with gentle agitation, until a small amount of ice remained floating in the middle of the vial. In order to avoid any contamination, 70–80% ethanol was used to sterilise the exterior of the vial. The vial contents were then transferred to a 75 cm^2 culture flask containing 10 mL of growth medium, and the flask was incubated at 37 °C in a 5% CO_2 atmosphere. The medium was changed the next day, and thereafter, every two days. When the cells reached 70–80% confluency and were ready to passage, the medium was removed from the flask and discarded. The cells were washed with pre-warmed Dulbecco's Phosphate Buffered Saline (DPBS; Sigma–Aldrich, D8537; 5 mL), and this wash step was repeated twice with gentle rotation of the flask. After the wash solution was aspirated out from the flask, 1× trypsin/EDTA solution (Gibco; 5 mL) was added and the flask gently rotated to ensure the solution covered the cells evenly. The flask was then incubated at 37 °C and 5% CO_2 for 5–10 min. After this step, cell detachment was confirmed under the microscope by checking that they were round and moving in suspension. Then, 10 mL of complete growth medium was added into the flask to neutralise the trypsin/EDTA, and the cells were

resuspended by pipetting up and down five times. The 15 mL of cell suspension was transferred to a 15 mL falcon tube and centrifuged at $125 \times g$ for 5 min (3T3 fibroblasts) or $400 \times g$ for 5 min (MSCs). The supernatant was discarded and the cell pellet was resuspended in 10 mL of fresh medium by gentle pipetting.

For cell counting, 0.4% trypan blue (Bio-Rad) was mixed 1:1 with an aliquot of the cell suspension, and 20 µL of the sample was quickly loaded into each side of the sample chamber of an automated cell counter (Cellometer Auto 1000, Nexcelom). Cell viability and concentration were measured, and after the cell viability reached over 80–90%, this indicated that they were ready for 3D culture.

4.2.12 Assessment of peptide hydrogel in 3D environment

To study the compatibility of the peptide hydrogels with the intended 3D cell culture conditions, their stability in the culture medium was assessed using a rheometer (Discovery HR-2, TA Instruments). First, peptide hydrogel (100 µL) was loaded into ThinCert inserts (Greiner Bio-One) in 24-well plates, and DMEM and MEME were selected to incubate with the hydrogel. The appropriate medium (250 µL) was added on the top of the hydrogel surface, and a further 750 µL was added into the well (Fig. 4.2). The cell culture plate was incubated at 37 °C in a 5% CO_2 incubator. This setup was the same as described below (Section 4.2.13), to mimic the 3D cell culture conditions. At days 3, 7 and 14, dynamic strain sweep was set up to measure the stiffness of the hydrogel. The medium was removed and the hydrogel transferred onto the rheometer stage (200 µL sample), then data acquisition was carried out using the parameters specified in Section 4.2.5.
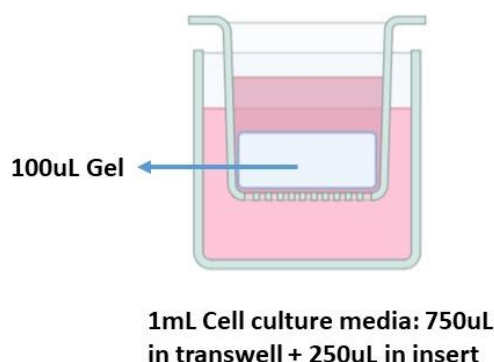
Figure 4. 2 A scheme showed the method to assess the ability of peptide hydrogel for the 3D cell culture.

4.2.13 3D cell culture in peptide hydrogel

Hydrogel samples were removed from the fridge (4 °C) and pre-warmed to 37 °C. Cells were encapsulated into the hydrogel by gentle pipetting to ensure an evenly mixed sample, at a final density of 2×10^6 cells/mL. Then, 100 µL of cell-laden hydrogel was dispensed into ThinCert inserts (Greiner Bio-One) in 24-well plates, followed by addition of cell culture medium (1 mL) into each well. Of this, 250 µL was added to the top of the hydrogel surface in the insert, and 750 µL was added to the well, as above. Cell culture plates were then incubated at 37 °C with 5% CO_2. Growth medium was changed every 20 min during the first hour of the experiment, and every two days for subsequent cell culture [23].

4.2.14 LIVE/DEAD staining

To assess cell viability in the hydrogels, the LIVE/DEAD assay (Thermo Fisher Scientific) was used. This protocol is based on the evaluation of cell membrane integrity to differentiate between live and dead cells. Cell culture medium was removed and the samples were washed 1–3 times with DPBS. A working solution of staining reagent was prepared in DPBS (2 mL

DPBS, 4 µL ethidium homodimer I, and 1 µL calcein-AM). An aliquot of this staining solution (100 µL) was added to the top of the hydrogel surface in the insert, and a further 600 µL was added into the well. The plate was incubated at 37 °C in 5% CO_2 for 1 h, then the staining reagent was removed and the sample washed 1–3 times with DPBS. The cell-laden hydrogel was then transferred onto a microscope glass slide for imaging. Samples prepared at days 0, 3, 7 and 14 were imaged by confocal laser scanning microscopy (Leica TCS SP8) with the following wavelength settings: green channel excitation/emission 494/517 nm, red channel excitation/emission 528/617 nm.

4.2.15 Pico-Green

In order to quantify the concentration of dsDNA in hydrogel, Pico-Green assay (Invitrogen, Thermo Fisher Scientific) was used. 2X Tris – EDTA buffer (TE) containing 1% Triton X – 100 and 10 mg/mL of pronase E were prepared in ultrapure water. The growth medium was discarded from each cell-laden hydrogel sample, which was transferred into a microcentrifuge tube by removing the membrane from the insert. This was done to collect all the cells which were attached to the membrane. The tube was tapped until the hydrogel sample was at the bottom of tube, then pronase E solution (400 µL) was added and the sample was mixed by vortexing. The tube was placed in a 37 °C water bath for several minutes, with agitation every 1–3 min, until the gel was hydrolysed evenly. Then, 500 µL of 2× TE buffer containing 1% Triton X-100 was added into the tube to lyse the cells. The tube was incubated at room temperature for 30 min and the membrane was taken out before freezing the sample at −20 °C [23].

For DNA quantification, a standard curve was first constructed using samples prepared with a series of cell concentrations in hydrogels. Hydrogel samples (100 µL) were prepared in microcentrifuge tubes at final cell concentrations of 1×10^7, 8×10^6, 4×10^6, 2×10^6 and $1 \times$

10^6 cells/mL, respectively. A blank hydrogel sample was also prepared as a zero reference point. For analysis, the samples were removed from the −20 °C freezer and thawed at room temperature, then agitated until homogenous. The PicoGreen reagent was diluted 200-fold in 1× TE buffer, then samples (100 uL) were added into a black 96 well plate (F-bottom) with an equal volume of diluted PicoGreen reagent. As a background control, 1× TE buffer (100 µL) was mixed with an equivalent volume of the PicoGreen solution. The assay plate was incubated at room temperature in the dark for 5 min then measured using a plate reader (CLARIOstar), using fluorescence detection with excitation at 480–512 nm and emission at 520 nm.

4.2.16 Statistical data analysis

All experiments were repeated at least three times to obtain an average value, expressed as mean ± standard deviation. The rheological results were analysed in GraphPad Prism 8 using one-way ANOVA and Student's t-test to assess the statistical significance of comparisons via P value [24]. Significance levels are represented as follows: * ($P < 0.05$), ** ($P < 0.01$), *** ($P < 0.001$), **** ($P < 0.0001$), and "ns" indicates there was no significant difference between the two groups.

4.3 Results

4.3.1 Calculation the purities of peptide

It is important to evaluate the chemical purity of peptides, as impurities might influence the experimental results. The purities of E(FKFE)$_2$ and K(FEFK)$_2$, as peptide powders, were therefore calculated based on RP-HPLC and elemental analysis results. The RP-HPLC results revealed the purity of the intact peptide sequences, referred to as P1, as shown in Fig. 4.2. The solvent peak can be seen in the first 10 min retention time, and the black arrow indicates the peak for the intact peptide sequence. Some other small peaks were observed, which based on the elution times, were presumably due to some short chains, small fractions or impurities that existed in the peptide samples.

For each powder sample, 25 mg of the peptide was taken to the Chemistry Department for elemental analysis of C, H, N and Cl content. The apparent molecular mass of peptides, referred to as M1, was calculated according to the percentage of N in the sample, as N was assumed to be only present in peptides. Thus, M1 was calculated according to Eq. 4.1:

$$M1 = \frac{N_1 \times N_2}{N_3} \tag{4.1}$$

Where, N_1 is the atomic weight of N (14.0067 u), N_2 is the number of N atoms in the chemical formula of the peptide, and N_3 is the percentage of N in the peptide powder sample. The purity of the peptide as a powder, referred to as P2, was then calculated using Eq. 4.2:

$$P2 = \frac{M1}{M2} \times 100\% \tag{4.2}$$

Where, M1 is the experimentally observed molecular mass of the peptide, and M2 is the theoretical molecular mass of the peptide. Therefore, the purity of intact peptide sequence in powders, referred to as P3, could then be obtained as per Eq. 4.3:

$$P3 = (P1 \times P2)\,/100 \qquad\qquad (4.3)$$

Different batches of peptides could have different purities, so it was important to analyse every batch before experiments. Table 4.1 presents the purities of E(FKFE)$_2$ and K(FEFK)$_2$, and it was found that the different peptide batches had similar purities according to the calculations.

Table 4. 1 The purities of E(FKFE)$_2$ and K(FEFK)$_2$ peptide.

	P1	P2	P3
E(FKFE)$_2$	84%	90.4%	76%
K(FEFK)$_2$	80%	94%	75.2%
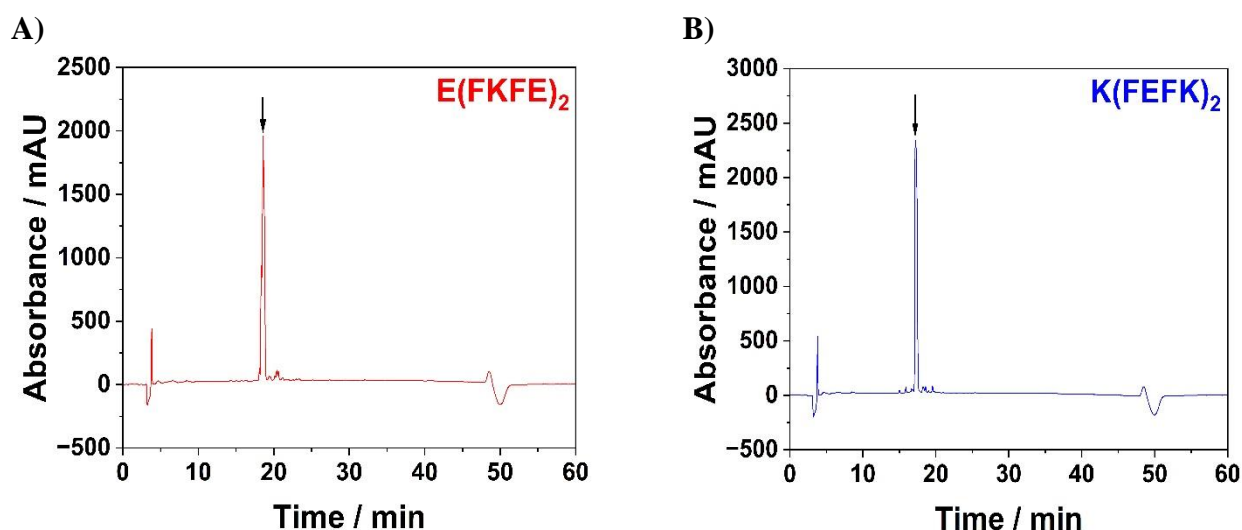
Figure 4. 3 RP-HPLC analysis of E(FKFE)$_2$ and K(FEFK)$_2$, the black arrows represented the intact peptide sequence in peptides.

4.3.2 Peptide gelation and the mechanical properties of peptide hydrogel

4.3.2.1 The relationships between charge and pH of peptide

To clearly reveal the relationship between pH value and charge, the theoretical values could be calculated using Eq. 4.4:

144

$$Z = \sum_i N_i \, \frac{10^{pKai}}{10^{pH}+10^{pKai}} - \sum_j N_j \, \frac{10^{pH}}{10^{pH}+10^{pKaj}} \qquad (4.4)$$

Where, Z is defined as the net charge of a peptide at a certain pH, N_i represents the number of amino-groups (one at the N-terminus plus the number of lysine residues in the sequence), N_j represents the number of carboxylate groups (one at the C-terminus plus the number of glutamic acid residues in the sequence), and pKai and pKaj are the pKa values of different amino acids. Using this equation, theoretical curves for pH–charge relationship were obtained (Fig. 4.4A & Fig. 4.4C).

In Fig. 4.1, the chemical structures of E(FKFE)$_2$ and K(FEFK)$_2$ are presented to explain the charge distribution. The ionic groups in these structures can be protonated or deprotonated according to variations in pH, and therefore, the charge carried by the peptides can be predicted. The ionic groups of E(FKFE)$_2$ are: carboxylic acid (COOH/COO$^-$) at the C-terminus, with pKa 2.19; glutamic acid side chains (COOH/COO$^-$), with pKa 4.25; and amino-groups (NH$_3^+$/NH$_2$) at the N-terminus and in lysine side chains, with pKa values of 9.67 and 10.53, respectively. The ionic groups of K(FEFK)$_2$ are: carboxylic acid (COOH/COO$^-$) at the C-terminus, with pKa 2.18; glutamic acid side chains (COOH/COO$^-$), with pKa 4.25; and amino-groups (NH$_3^+$/NH$_2$) at the N-terminus and in lysine side chains, with pKa values of 8.95 and 10.53, respectively. If the pH is higher than the pKa values, ionic groups will be in their deprotonated forms; i.e., COOH will be deprotonated to COO$^-$, and NH$_3^+$ to NH$_2$. These transformations determine the charge modulus of peptides.

The charge of peptides and the pKa of different ionic groups on the peptide structures are indicated in Fig. 4.4 A & Fig. 4.4 C. As these are calculated pH–charge profiles based on theoretical pKa values, peptide titrations were carried out to confirm the predictions (Fig. 4.4B & Fig. 4.4D). For this purpose, 2 mg/mL peptide solutions were prepared. For E(FKFE)$_2$, the initial pH was 3.22, so based on the pKa stated above, it was assumed that the C-terminal

carboxylic acid was already deprotonated (Fig. 4.4B). Thus, this peptide should carry a net +2 charge at the initial pH, corresponding to the theoretical results in Fig. 4.4A. Upon addition of NaOH, the first pKa-like transition was observed between pH 3.22 and 4.11, suggesting that two carboxylic acids on the glutamic acid side chains had become deprotonated, since two molar equivalents of NaOH were required (Fig. 4.4B). In that case, the net charge of the peptide should be zero at this pH (Fig. 4.4A). A second transition was observed between pH 5.6 and 6.8, interpreted as deprotonation of the third glutamic acid side chain based on the requirement for one molar equivalent of NaOH. At this point, the peptide would carry −1 net charge (Fig. 4.4A). The next transition process was observed from around pH 8.1–9.4, with the addition of one further molar equivalent of NaOH, indicating that the N-terminal amino-group was deprotonated and the net charge became −2. Finally, a transition was located at approximately pH 10.5, corresponding to deprotonation of the amino-groups of the lysine side chains and in good agreement with the theoretical pKa (Fig. 4.4A). In contrast, there was an apparent shift of about one pH unit, towards a higher value, of pKa for one of the glutamic acid side chains in E(FKFE)$_2$. This transition occurred at pH 5.6–6.8, and might be explained by the strongly acidic environment around the C-terminus of the peptide where complete deprotonation generates two negatively charged groups in close proximity.

For K(FEFK)$_2$, the initial pH was 3.4, leading to the assumption that the C-terminal carboxylic acid was deprotonated based on the theoretical pKa (Fig. 4.4D). In this case, the peptide would carry a net +3 charge, in good agreement with the predicted curve in Fig. 4.4C. The first pKa-like transition was observed from pH 3.4–4.5, indicating that the two side chain carboxylic acid groups of the glutamic acid residues were deprotonated. The NaOH added here— approximately 2.5 molar equivalents — was consistent with this double deprotonation, but the requirement for slightly more NaOH than expected (2.5 vs. 2.0 equivalents) might be due to the highly basic character (NH_3^+) of the peptide. The peptide would have a +1 overall charge

after this transition. The next transition was observed from pH 7.69–9.0, which corresponded to the deprotonation process of the N-terminal amino-group. For this process, 0.7 molar equivalents of NaOH were added, which is again interpreted in terms of the basic environment. At this point, the net charge of K(FEFK)$_2$ would be zero. The next transition began at pH ~9.9, regarded as deprotonation of the amino-groups of the lysine side chains. Considering the theoretical pKa values, two shifts of pKa value were evident in the titration curve. There was a shift of about one pH unit towards a lower value for the pKa of the N-terminal amino-group, and also a shift of ~0.5 pH units in the pKa of the lysine side chain amino-groups, again towards a lower value. This could be explained by the structure of the K(FEFK)$_2$ peptide, with the higher density of NH$_3^+$ in the region of the N-terminus probably resulting in early deprotonation of amino-groups [16].
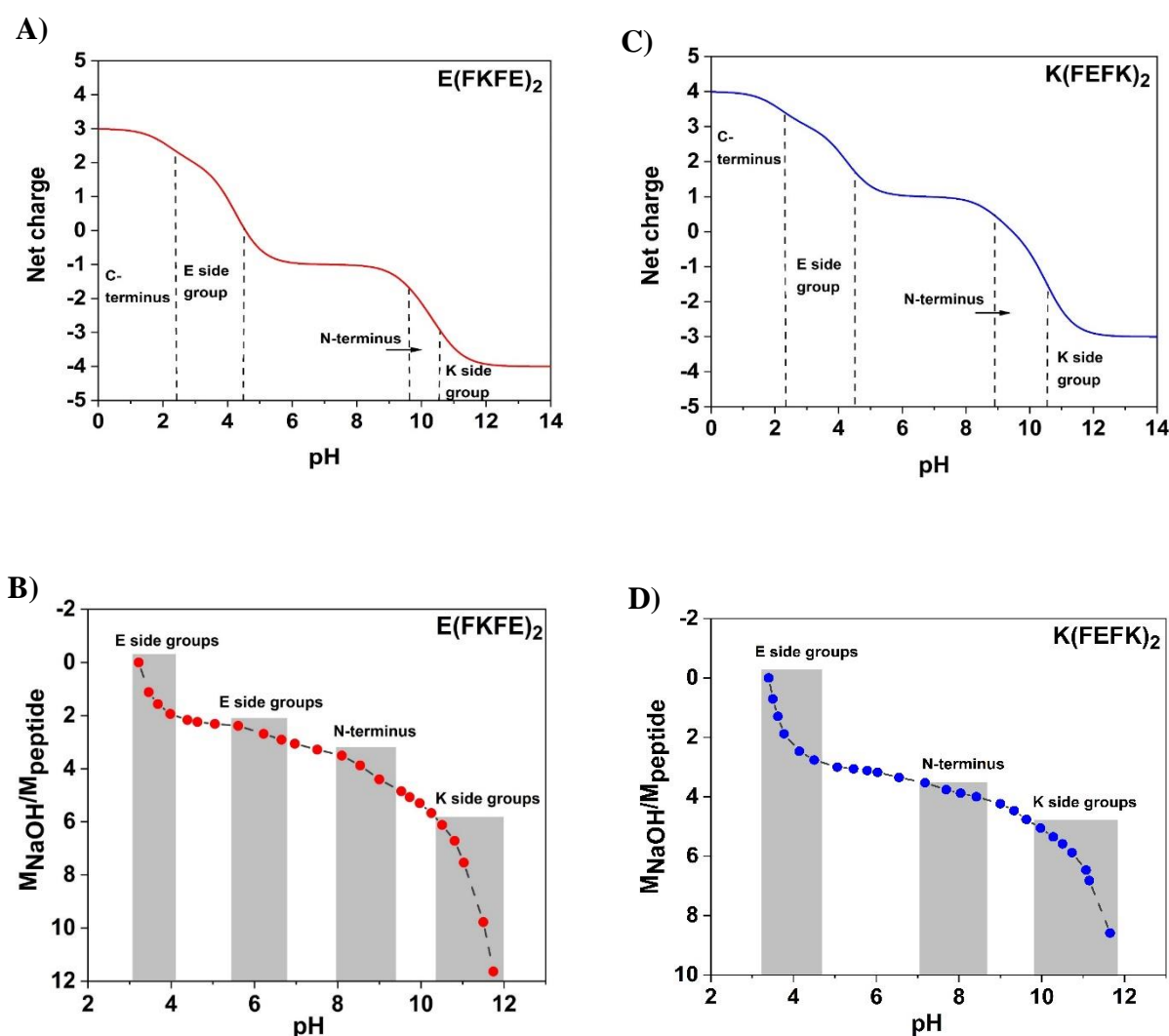
Figure 4. 4 A&C) The relationships between the pH value and the net charge of peptides (dotted lines indicate the theoretical pKa of the different ionic groups present on the peptides). B&D) Peptide titration (shadow bars were the regions indicated the deprotonation transitions of different ionic groups).

4.3.2.2 Determination of the concentration of peptide hydrogel

To investigate the relationship between net charge and gelation behaviour, peptide phase diagrams were constructed. The peptide powders were dissolved in HPLC grade water at a range of concentrations: namely, 4, 8, 12 and 16 mg/mL. Then, NaOH was added to adjust the pH of each sample. As the pH and concentration were varied, the peptides presented in various

states including clear gel, cloudy gel, precipitate or liquid/viscous liquid (Fig.4.5). The states of peptide were shown in Fig. 4.5D.

For E(FKFE)$_2$, the peptide powder dissolved in HPLC grade water to give a liquid/viscous liquid state at strongly acidic pH (~2). This changed to a clear gel state at pH ~3. After that, the peptide went through a cloudy state and subsequently precipitated, becoming a cloudy gel at pH 4–6. This transition can be explained in terms of the charge modulus of the peptide. According to the theoretical curve (Fig. 4.4A), the pH range 4–6 corresponds to a net charge close to zero. It has been shown that the charge modulus determines the state of a peptide hydrogel, and where the charge modulus is <1, the system enters a cloudy state [25][26]. Therefore, this change in charge modulus can promote formation of the cloudy gel state because some of the fibres are aggregated due to the lack of electrostatic interactions. When the peptide does not carry any charge, or has a net charge significantly below ±1, aggregation occurs leading to formation of a precipitate. In the case of E(FKFE)$_2$, it can be seen that the precipitate occurred in the region of pH 4.1–5.8, in good agreement with the theoretical curve (Fig. 4.4A), as well as the titration results. From pH 6.35–8.35, where the charge modulus is stable at around −1, the clear gel state was observed at concentrations of 8, 12 and 16 mg/mL. At higher pH, where the N-terminal amino-group is deprotonated, the charge carried by the peptide increases (Fig. 4.4A). Strong electrostatic repulsion might disrupt the self-assembly into fibres, and indeed, this peptide entered the viscous liquid state with increased pH [27]. As the pH is raised further, the amino-groups of the lysine side chains will subsequently be deprotonated, creating a higher overall negative charge (up to −4). Thus, the liquid state will form, and consistent with the titration results (Fig. 4.4B), this was observed at pH ~10.65.

For K(FEFK)$_2$, this peptide could form a clear gel in the pH range of 6–8, where it carries a +1 charge modulus. As the N-terminal amino-group is deprotonated on reaching pH ~8.4, the peptide would carry net zero charge and thus underwent the same phase change as E(FKFE)$_2$

associated with the zero-charge transition: from the cloudy gel state, to precipitate, to cloudy gel state (Fig. 4.5B). As the pH was raised to 11.3, the deprotonation of ionic groups (lysine side chains) induced a higher net charge, which influenced the peptide system, causing it to present in a liquid-like state (Fig. 4.5D).

The above results demonstrate that the charge of peptides mainly controls their self-assembly behaviour. The peptide hydrogel system can be stabilised by balancing the forces of charge repulsion to prevent fibre aggregation, and the attractive forces that drive the self-assembly process [28]. The main design concept behind the two peptide sequences in this study was based on charge and pH. For E(FKFE)$_2$, the pH range of the clear gel state increased with the peptide concentration (from pH 6–8), whereas K(FEFK)$_2$ could form the clear gel state at lower pH (~ 5) when the concentration was sufficient. These results can be explained in terms of increasing attractive forces between fibres at higher concentrations, creating a more stable hydrogel system. The E(FKFE)$_2$ and K(FEFK)$_2$ peptides formed a clear gel state in the region of pH 7, at concentrations of 8, 12 and 16 mg/mL; and under these conditions, the two peptides carried a net charge of −1 and +1, respectively. The formation of both hydrogels at physiological pH made it appropriate to further study their properties for drug delivery.
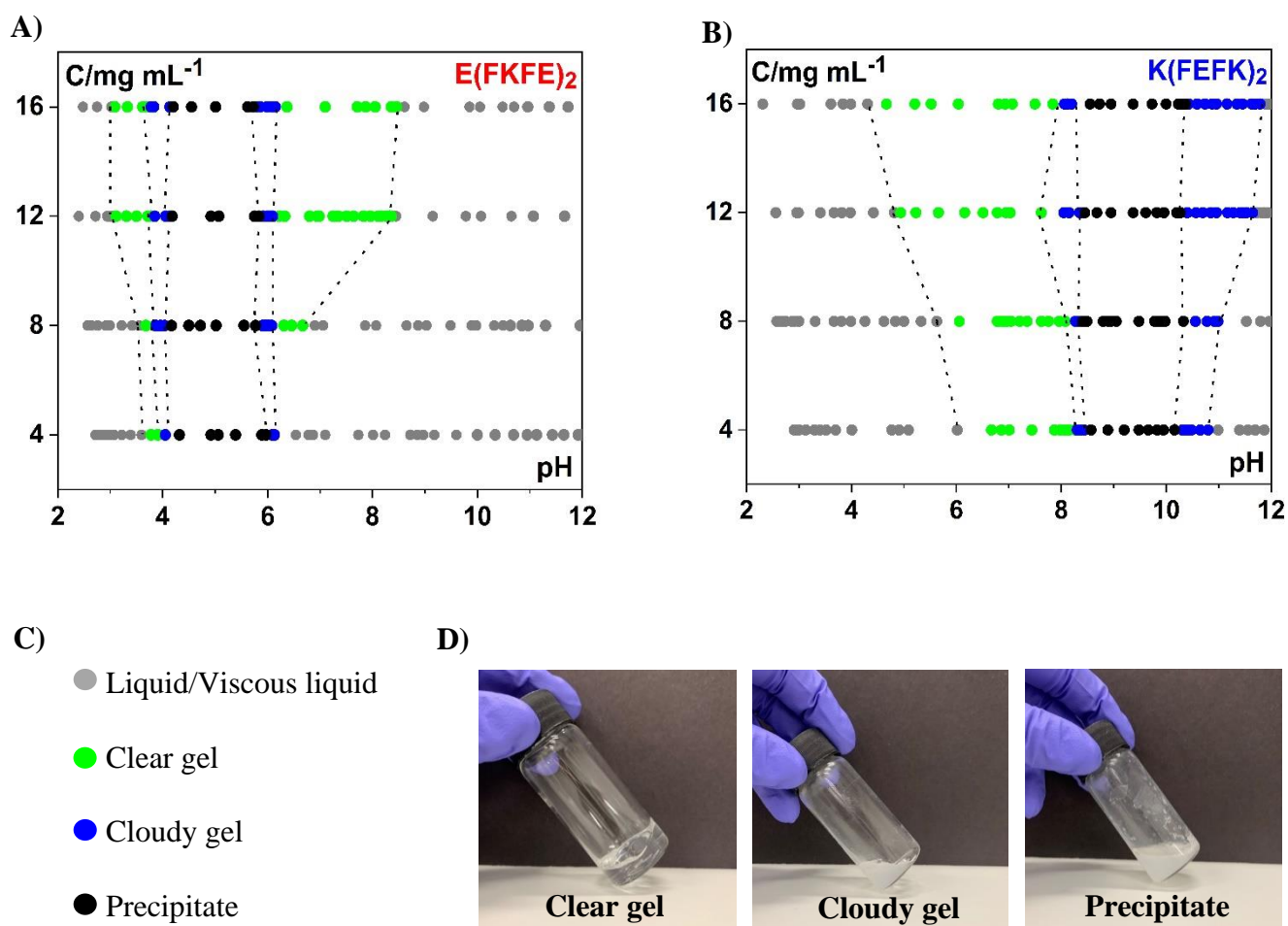
Figure 4. 5 A&B) Peptide phase diagram of E(FKFE)$_2$ and K(FEFK)$_2$. C) Symbols represented different gelation states according to different pH values. D)The states of samples at different pH value.

To compare the mechanical properties of the hydrogels at different concentrations, solutions were prepared at 8, 12, 16 and 20 mg/mL for rheological experiments at pH 7. The mechanical properties can be characterised using the shear storage modulus (G′) and loss modulus (G″) parameters. The stiffness of the gel was defined using G′, whereas the viscous liquid-like state was determined by G″. If G″ > G′, the gel was in a viscous liquid state, but if G′ > G″, the gel was in an elastic solid-like state.

In Fig. 4.6B, G′ is the storage modulus in the linear viscoelastic region (LVR), within which G′ and G″ should be parallel with each other. If G′ > G″, this means the sample is in the gel state. Thus, G′ was measured for a range of samples, and this revealed very significant differences in the mechanical properties of hydrogels prepared using the different peptides and concentrations. The storage modulus G′ showed an upward trend with increasing concentration, which was seen with hydrogels made from both peptides. Thus, G′ depended on the peptide concentration, and a higher G′ might lead to a relatively more stable hydrogel system suitable for drug or cell encapsulation. Furthermore, no difference was apparent between the E(FKFE)$_2$ and K(FEFK)$_2$ hydrogels at 12 mg/mL based on G′ values, according to the Student's t-test; a common statistical method to evaluate the difference between the means of two groups. Based on these results, 12 mg/mL was considered an ideal concentration to compare the effects of charge on hydrogel properties, including formation of β-sheet structure, morphology, fibre size and distribution. Lower G′ indicates a softer hydrogel that may be better suited to 3D cell culture and drug delivery applications.

A)

B)
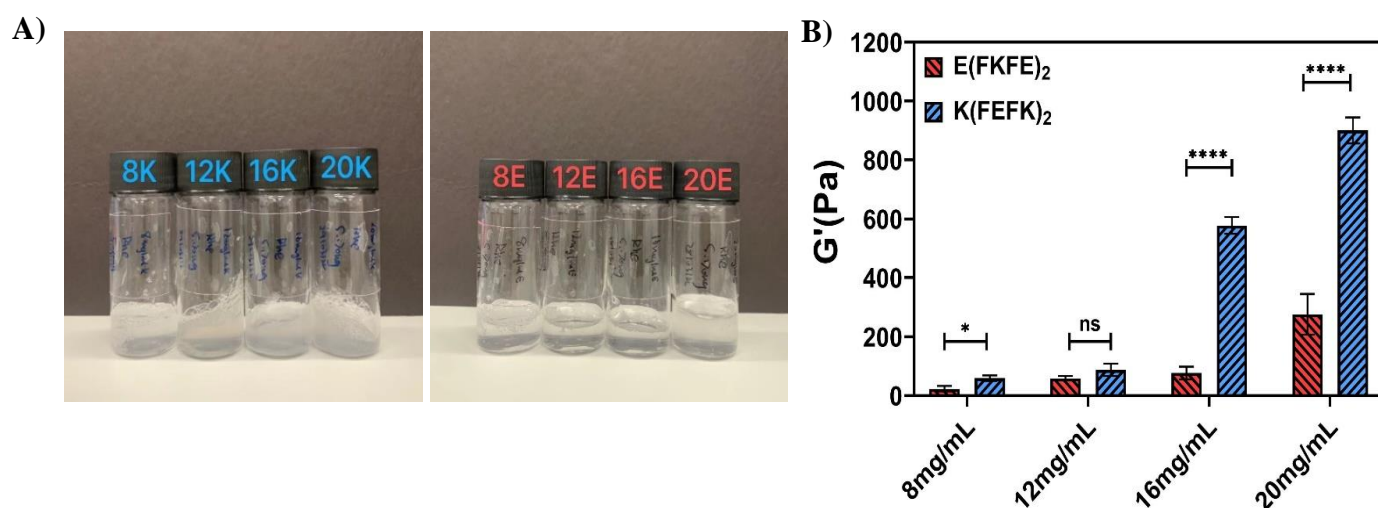
Figure 4. 6 A) Different concentration of peptide hydrogels at pH 7. The numbers represented concentrations, K represented K(FEFK)$_2$ hydrogel, E represented E(FKFE)$_2$ hydrogel. Both of

K(FEFK)$_2$ and E(FKFE)$_2$ performed relatively clear gel state at 12 mg/mL. B) Comparisons of the initial storage modulus G' of peptide hydrogels at various of concentrations (The graph was analysed by student t-test which compared G' in different charge of peptide hydrogels, p value was indicated as *$p<0.05$, **$p<0.01$, ***$p<0.001$, **** $p<0.0001$, ns represented there was no significant difference between two groups).

4.3.3 Characterization of peptide hydrogel

4.3.3.1 Confirmation of the secondary structure

Various methods were employed to characterise the secondary structure of peptide hydrogels; namely, CD spectroscopy, FTIR spectroscopy, and the Thioflavin T (ThT) binding assay. The CD spectra of both E(FKFE)$_2$ and K(FEFK)$_2$ showed a strong positive peak at around 195 nm and a relatively weak peak at approximately 216 nm, which were assigned to the antiparallel beta-sheet structure (Fig. 4.7A & Fig. 4.7B) [29]. Another peak was evident at about 201 nm in both samples, characteristic of a right-hand twisted β-strand [30]. In the CD results, the signal intensity was higher with increasing sample concentration. This might be due to the concentration affecting the secondary structure folding and fibre–fibre aggregation of the peptides.

Thioflavin T is a derivative of the benzothiazole fluorophore with a positive charge. It can bind to the surface of β-sheet fibres via hydrophobic interactions, and the observed fluorescence intensity depends on electrostatic interactions between the dye and the peptide surface [19]. In the ThT assay (Fig. 4.7C & Fig. 4.7D), E(FKFE)$_2$ presented a broad emission peak at around 488 nm, of higher intensity compared with K(FEFK)$_2$. The different results for E(FKFE)$_2$ and K(FEFK)$_2$ can be explained by the charge properties of the two peptides. Since ThT is positively charged, it will have greater affinity for the negatively charged peptide fibres through electrostatic attraction, and will therefore emit more fluorescence. In contrast, charge repulsion

between ThT and K(FEFK)$_2$ will disrupt binding to the peptide fibres, resulting in a lower fluorescence intensity. Nevertheless, the fluorescence intensity increased with concentration for both peptides (Fig. 4.7E). This supports the assumption that concentration is one factor that drives self-assembly of β-sheet fibrils.

One droplet of each 12 mg/mL sample was loaded onto the ATR-FTIR crystal for analysis. The amide I band (1700–1600 cm^{-1}) gives information on the secondary structure of proteins and peptides due to C=O stretch vibrations of peptide bonds [31]. As can be seen in Fig. 4.7F, both the E(FKFE)$_2$ and K(FEFK)$_2$ hydrogels formed β-sheet structures with a strong absorption band at around 1620 cm^{-1} and an additional, relatively weak band at around 1690 cm^{-1} [32][33]. The amide II band is located in the region 1575–1480 cm^{-1} and arises due to in-plane N–H bending and C–N stretching. Based on literature precedent [33], the observed band at 1550 cm^{-1} likely corresponds to antisymmetric stretching vibrations of carboxylate groups, and that at 1520 cm^{-1} to in-plane bending vibrations of NH$_3^+$ groups (Fig. 4.7F). There was also a small peak at around 1450 cm^{-1} that might indicate vibrations of methylene groups [32]. The findings from ATR-FTIR therefore revealed both an ordered β-sheet structure of peptide hydrogels, as well as disordered structures in the hydrogel systems.

Taken together, the above results indicate that the peptides had β-sheet structures, and were able to self-assemble into hydrogels with highly ordered β-sheet structures at high concentration.
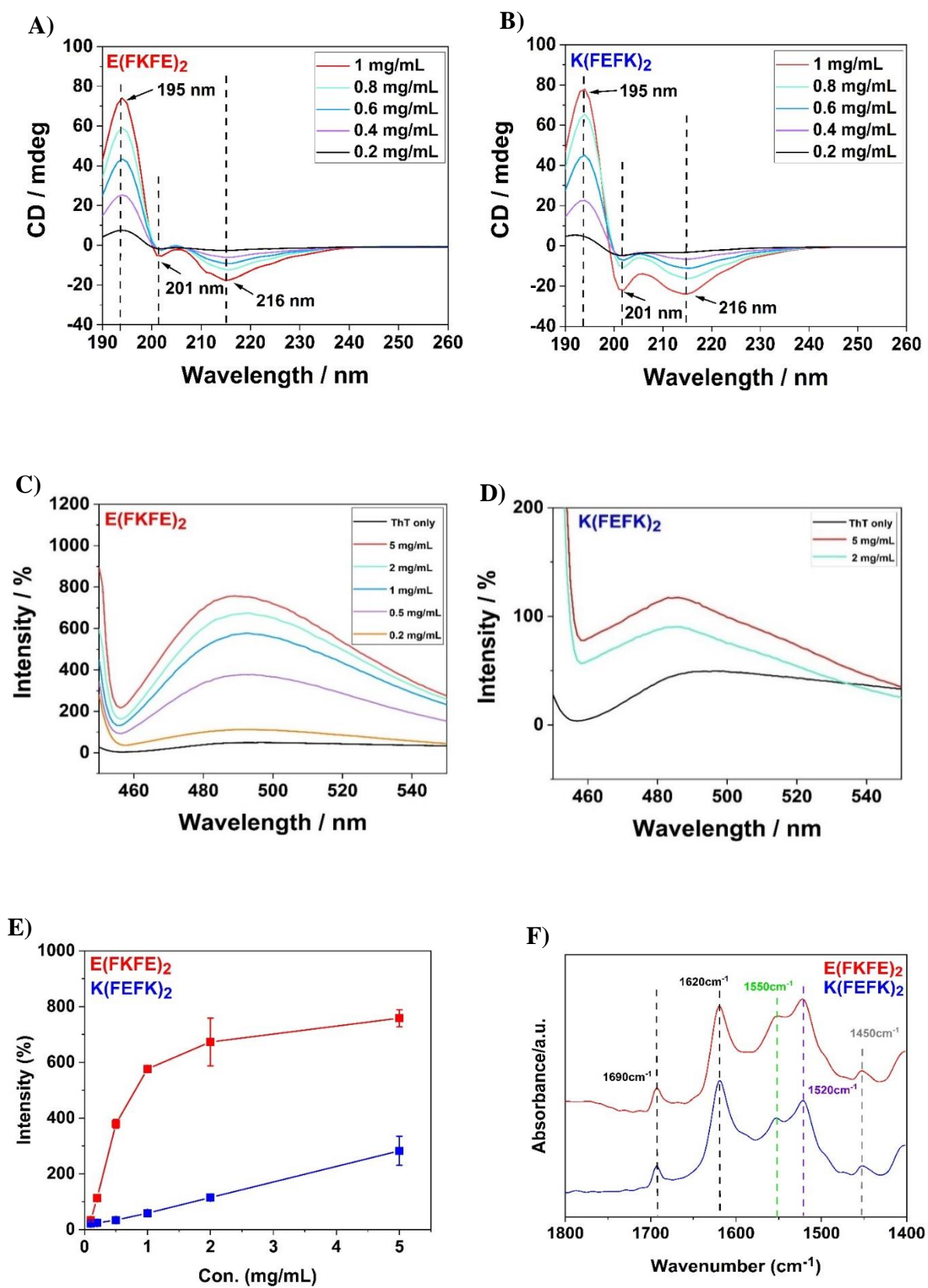
Figure 4. 7 Characterization of secondary structure. A&B) CD spectra from diluted hydrogels. C&D) Fluorescence spectra of ThT with different diluted hydrogels. E) The intensity of ThT with samples at ~ 488 nm wavelength as a function of the concentration of diluted peptide hydrogels. F) ATR-FTIR spectra of peptide hydrogels at 12 mg/mL.

4.3.3.2 Morphology of peptide hydrogel

The 12 mg/mL peptide hydrogels were diluted 20-fold for TEM imaging. At the same concentration, E(FKFE)$_2$ and K(FEFK)$_2$ hydrogels had similar morphology. They were able to form complex networks with fibres of varying diameter, as shown in Fig. 4.8. The fibre widths in these systems are presented in Fig. 4.8C, and were analysed by log-normal parameters (Table 1). Both peptides formed networks with fibres of similar width, as there were relatively high counts at 4.2 ± 1 nm (~22%) for E(FKFE)$_2$ and 4.5 ± 1 nm (~27%) for K(FEFK)$_2$. The fibres were self-assembled randomly, forming bundles or entangled together, leading to some large fibre widths as displayed in Fig. 4.8C. Furthermore, Table 4.2 shows a comparison of full width at half maximum (FWHM) between E(FKFE)$_2$ and K(FEFK)$_2$. According to this analysis, the two hydrogel networks were closely matched in terms of density, which might mean they have similar mechanical properties. This assumption was subsequently tested by rheology experiments (Fig. 4.8D).

Although both peptides formed a gel state at 12 mg/mL with similar network structure, the storage modulus for the K(FEFK)$_2$ hydrogel was higher, indicating that it was stiffer (Fig. 4.8D). This result, correlated to the morphology of the peptide hydrogels, suggests that the heterogeneous fibre distribution may disrupt the balance of the modulus of the network, in this case forming a relatively weak gel. From the dynamic strain sweep test, it can therefore be hypothesised that the network structure influenced the mechanical properties of the peptide hydrogels (Fig. 4.8D).

A)

B)

C)

D)
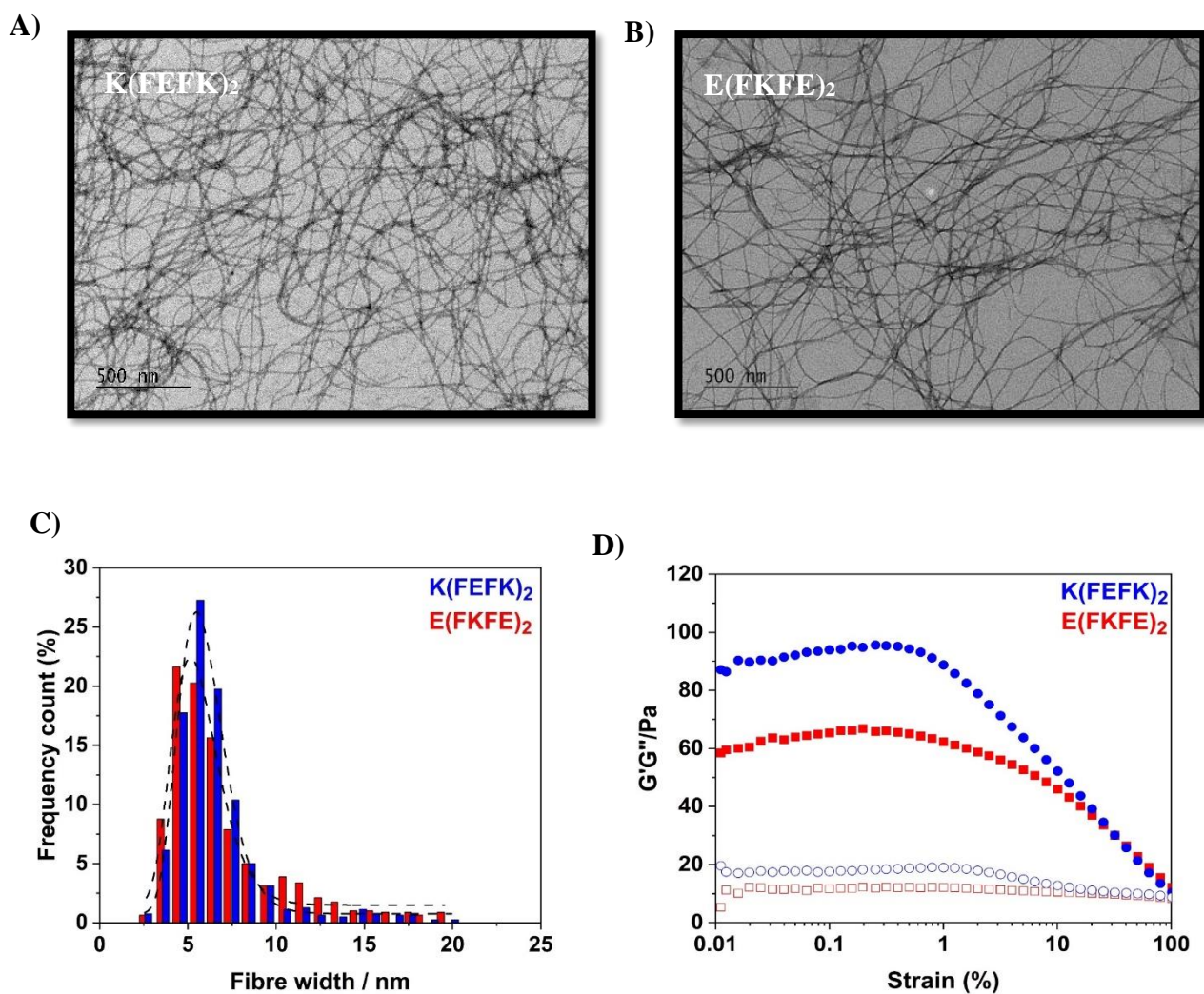
Figure 4. 8 A&B) TEM images of 20 x diluted hydrogel. C) Width of fibres measured for 800 times to create size distribution, the dash lines represent lognormal fits. D) Dynamic strain sweep of peptide hydrogel at 12mg/mL, all the experiments were repeated at least 3 times at 37℃. (The solid circles represent storage modulus G', the open circles represent loss modulus G'').

Table 4. 2 Comparison of fibre width distribution between E(FKFE)$_2$ and K(FEFK)$_2$ hydrogel.

Peptide hydrogel	charge	Fibre width half maximum (nm)/half width half max	Fibre width range (nm)
E(FKFE)$_2$	(-)	3.23	2-20
K(FEFK)$_2$	(+)	3.11	2-20

4.3.3.3 SAXS analysis of peptide hydrogel

To complement the TEM results, SAXS measurements were used to characterise the structure and fibre size of peptide hydrogels [21]. The results (Fig. 4.9) showed that the shape and single fibre diameter were obtained at a low q-value range. The shape was predicted through Eq. 4.5:

$$I_N(q) \propto q^{-\alpha} \tag{4.5}$$

Panels A and B of Fig. 4.9 were obtained by converting Eq. 4.5 into log [I$_N$(q)] vs log q, and it can be seen that both hydrogels performed as a thin, rod-like fibre with a slope of around −1. Panels C and D were generated using a modified Guinier's law, plotting $l_N [q\, I_N(q)]\; vs\; q^2$. Therefore, the cross-sectional radius of gyration of fibres, R$_{gc}$, was obtained according to Eq. 4.6:

$$qI_N(q) = KCL_M \exp(-\frac{1}{2}\, q^2 R_{gc}{}^2) \tag{4.6}$$

At a low q-values, R$_{gc}$ can be calculated from the slope of these plots (Fig. 4.9C & Fig. 4.9D). This gave values for R$_{gc}$ of approximately 1.36 nm for the E(FKFE)$_2$ hydrogel, and 1.1 nm for the K(FEFK)$_2$ hydrogel. The relationships between R$_{gc}$ and fibre diameter (d$_f$) were then estimated using Eq. 4.7 [27]:

$$R_{gc} = \sqrt{\frac{d_f{}^2}{8}}$$

(4.7)

The diameter of fibres was ~3.84 nm in the E(FKFE)$_2$ hydrogel, and ~3.10 nm in the K(FEFK)$_2$ hydrogel, which are in close agreement with the TEM values shown in Fig. 4.8C. From the TEM and SAXS analyses, it was concluded that both peptide hydrogels are able to form networks with similar fibre sizes, and their nano units make them potential biomaterials for biomedical applications.

A)

B)

C)

D)
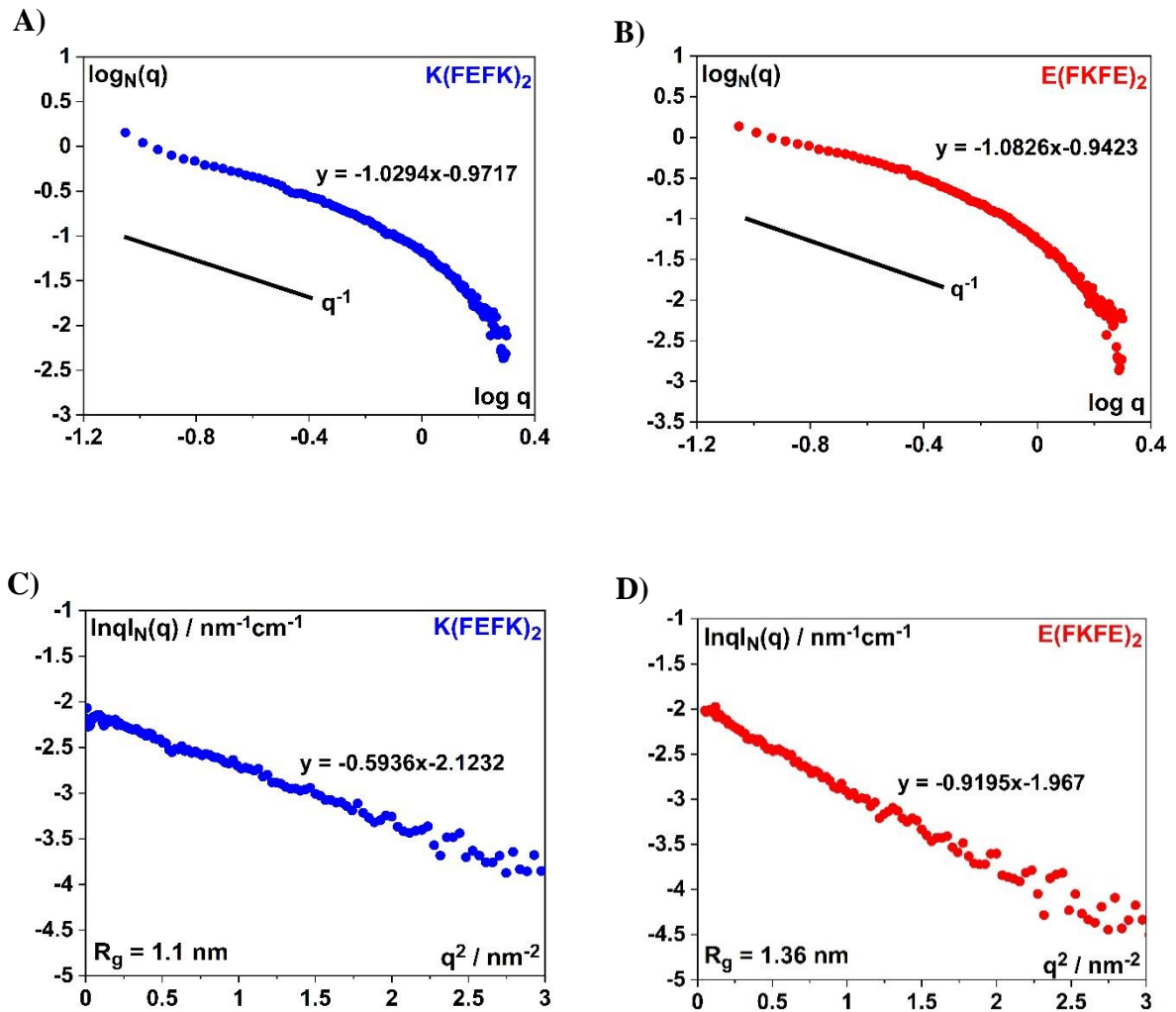
Figure 4. 9 The scattering intensity as a function of q. K(FEFK)$_2$ and E(FKFE)$_2$ hydrogels were prepared at 6 mg/mL. A&B) log [I$_N$(q)] vs log q plots to estimate the structure of hydrogels. C&D) ln[qI$_N$(q)] vs q^2 plots, the modified Guinier plot used to calculate the cross-sectional radius of gyration of fibres R_{gc}.

4.3.3.4 Injectability of peptide hydrogel

Peptide hydrogels have been used as vehicles to encapsulate drugs or cells for biomedical therapy. Among the available methods of clinical administration, injection is an efficient choice. Thus, injectability is a key factor when evaluating the specific mechanical properties of novel peptide hydrogel materials. This was assessed using a shear thinning/recovery assay, performed by rheometer. When a high shear strain of 1,000% was applied, the gel transitioned to a liquid-like state (G′ < G″), but recovered to a gel-like state (G′ > G″) at a lower shear strain of 0.2% (Fig. 4.10C). Both the E(FKFE)$_2$ and K(FEFK)$_2$ hydrogels were deformed at high strain but recovered immediately. This process mimics administration of an injection, and as is shown (Fig. 4.9A, B), both materials maintained the gel state after injection through a 21g needle. This 'self-healing' ability confirmed the present peptide hydrogels as smart injectable candidates for potential application in drug delivery, tissue engineering and 3D printing.

A)

B)

C)
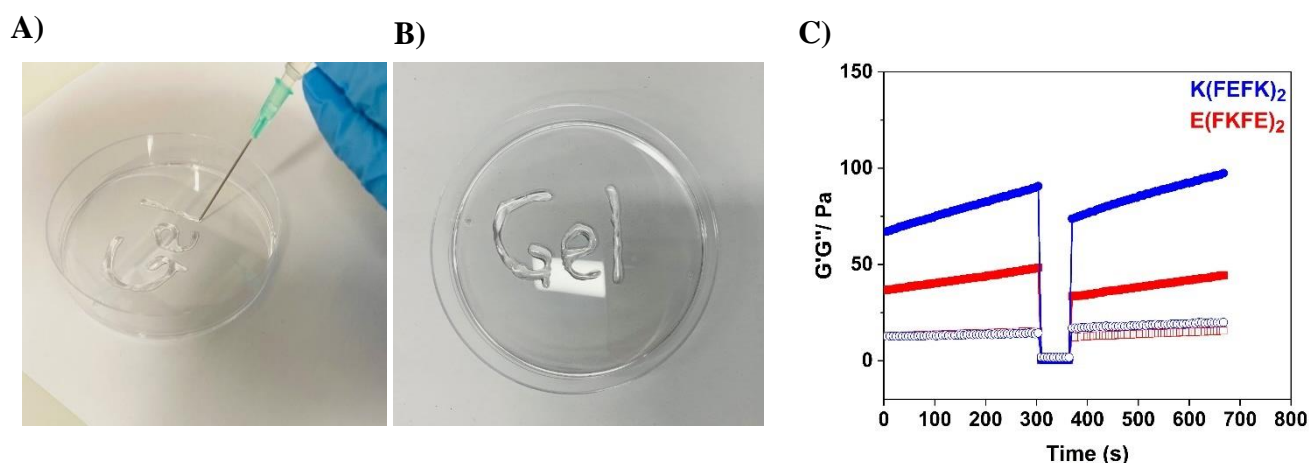
Figure 4. 10 Shear thinning/recovery assay revealed the injectability of peptide hydrogel. The hydrogels were prepared at 12 mg/mL. All the experiments were repeated at least 3 times at 37℃. (The solid circles represent storage modulus G', the open circles represent loss modulus G'').

4.3.4 3D cell culture and biocompatibility

4.3.4.1 Stability of peptide hydrogel in cell culture medium

Encapsulating cells into a hydrogel is a good method to assess the compatibility of the material with 3D cell culture, and its biocompatibility in general. However, it was essential to first evaluate the behaviour of the hydrogels under the intended 3D culture conditions, before seeding them with cells. This experiment was therefore carried out under identical conditions to subsequent 3D cell culture. Hydrogels were prepared from both peptides at 12 mg/mL and 20 mg/mL. The 12 mg/mL samples of E(FKFE)$_2$ and K(FEFK)$_2$ were named as 12E GEL and 12K GEL, respectively. Similarly, the hydrogels made using 20 mg/mL E(FKFE)$_2$ and K(FEFK)$_2$ were named as 20E GEL and 20K GEL, respectively. Hydrogel samples (100 µL) were dropped into well inserts and incubated with either DMEM or MEME at 37 °C in a 5% CO$_2$ incubator. Dynamic strain sweep measurements were made to assess the stiffness of the peptide hydrogels at days 3, 7 and 14.

The initial storage modulus (G′) of the different hydrogels was used as a baseline for this analysis (Fig. 4.11). As can be seen, the hydrogels became stiffer after incubating in cell culture medium, compared with the fresh hydrogel (no incubation). One possible explanation is the presence of salt components in the growth media. It has been reported that ions have an effect on the mechanical properties of hydrogels, due to the influence of ion valency [34]. Based on these results, it was assumed that the ions present in the cell culture media caused the observed

161

increase in G′ of the hydrogels, which provided more stable 3D culture conditions. Both the 12E GEL and 12K GEL became relatively weak in DMEM by day 14, so it might be difficult to culture cells with these hydrogels for a long period. The shape of the 12E GEL collapsed by day 14, and it could not retain the same shape as on day 3. In an attempt to improve stability, 20 mg/mL hydrogels were monitored in DMEM. Compared with the 12 mg/mL hydrogels, the initial G′ values were significantly higher. In addition, G′ was more than 2,000 Pa for the 20E GEL, and over 6,000 Pa for the 20K GEL after 14 days, which displayed the higher stiffness. This indicated that increasing the concentration of hydrogel might produce a stronger material for 3D cell culture. In contrast, the 20E GEL was more stable as the initial G′ did not change significantly over 14 days, and it maintained its shape well. Actually, the decreased G′ of this material at day 14 might be due to gradual degradation in DMEM over a long period.

As DMEM was specific to the 3T3 cells, MEME was also used for incubation to investigate whether the hydrogels were suitable for culture of MSCs. The initial G′ values of the different samples are summarised in Table 4.3. Compared with DMEM, the 20 mg/mL hydrogels displayed relatively low stiffness in MEME. At day 14, the G' of these gels in MEME was about half of that in DMEM. Thus, different types of cell culture medium variably affected the stability of the peptide hydrogels.

A)

Day 3

Day 7

Day 14

B)

Day 3

Day 7

Day 14

C)

Day 3

Day 7

Day 14

D)

E)

F)
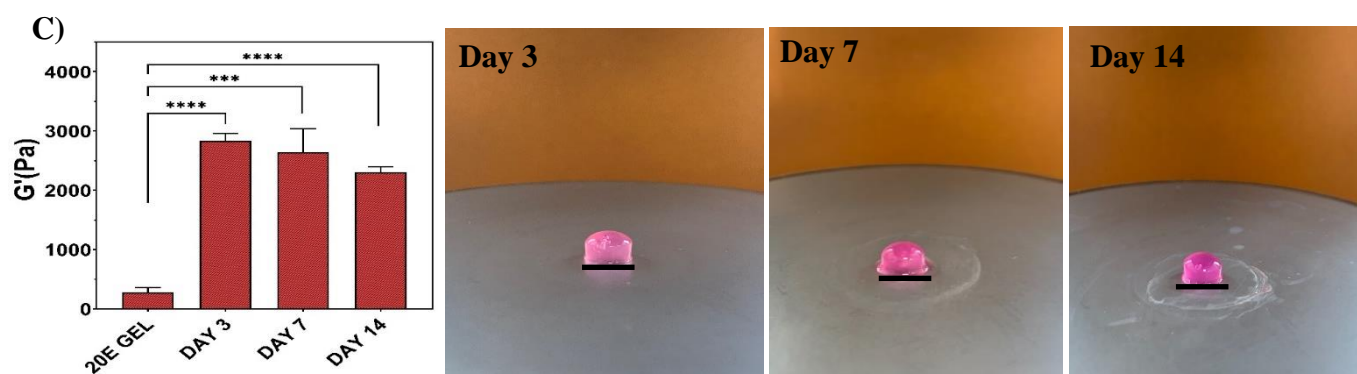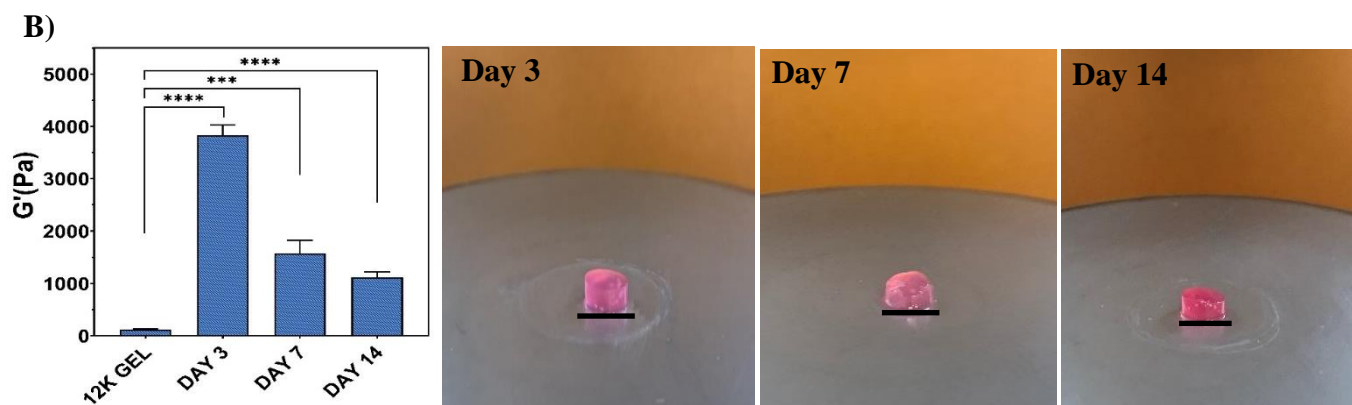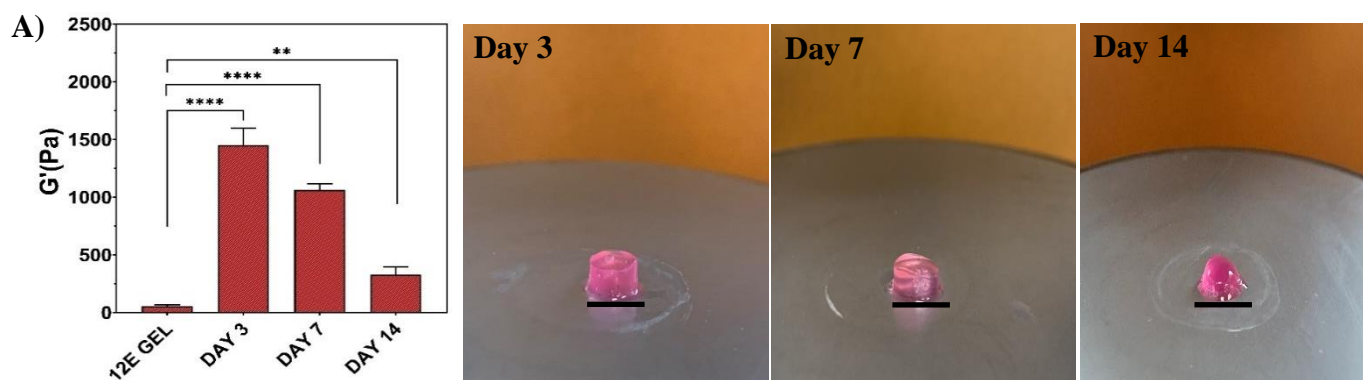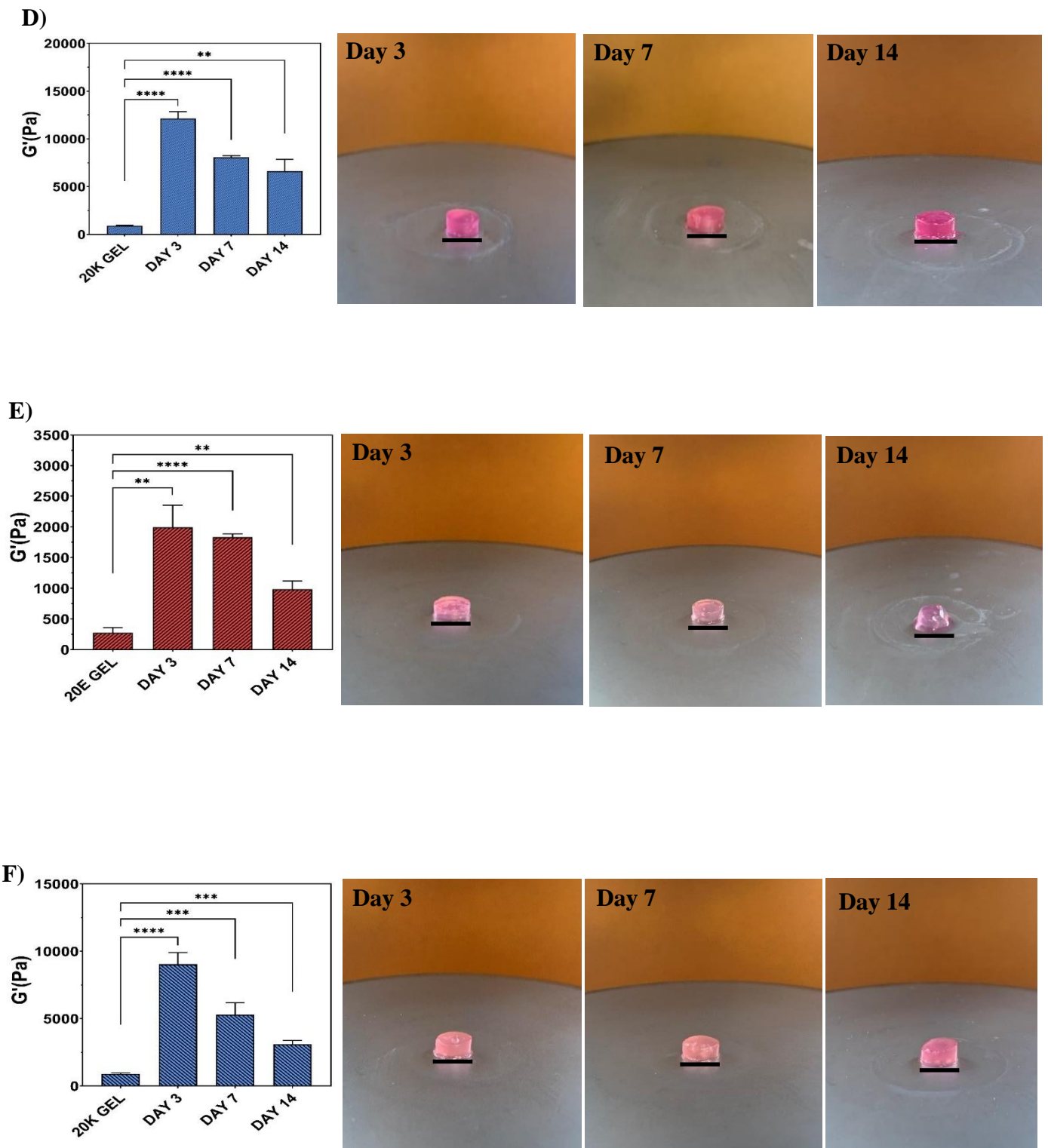
Figure 4. 11 Comparisons of initial storage modulus G' of peptide hydrogels after cell culture media incubation on day 3, 7 and 14. A-D) were the peptide hydrogels in DMEM media. E-F)

were the peptide hydrogels in MEME media. On the right side, the pictures were the gel state

after incubation in 3, 7, 14 days. The black bar represented 0.5 cm scale.

Table 4. 3 Comparison of initial storage modulus G' of different peptide hydrogels in differ-

ent cell culture medium.

	G' in Day 3/Pa	G' in Day 7/Pa	G' in Day 14/Pa
12E GEL in DMEM	1451	1062	326
12K GEL in DMEM	3832	1569	1119
20E GEL in DMEM	2803	2640	2304
20K GEL in DMEM	12150	8076	6626
20E GEL in MEME	1995	1831	982
20K GEL in MEME	9033	5298	3098

4.3.4.2 Biocompatibility of peptide hydrogel

Separately, 3T3 cells and MSCs were encapsulated in peptide hydrogels for 14 days and the

LIVE/DEAD assay was used to assess cell viability. As shown in Fig. 4.12A, a large number

of cells were viable in both the E and K hydrogels, as visualised via the green fluorescence.

For 3T3 cells, a higher density of live cells was seen in the K GEL samples compared with the

E GELs. Furthermore, at the higher hydrogel concentration, a greater cell density was observed.

In both peptide hydrogels, the cells were distributed as single cells on day 0, but had formed

clusters with a large circular shape after 3 days [22]. However, the cell number had decreased

by day 14 in the 12E GEL, due to the lower stability causing collapse of the hydrogel upon

prolonged exposure to DMEM. At relatively high concentration, the hydrogels maintained

good cell viability, which suggests they are useful to improve a 3D cell culture environment.

Since LIVE/DEAD staining is a quick method to differentiate between live and dead cells, the

PicoGreen assay was used to confirm the above results. This method quantifies cell numbers according to the concentration of dsDNA. The results showed that cell numbers followed an increasing trend over the 14 days of the experiment (Fig. 4.12B). In addition, the cells proliferated more rapidly in the 20K GEL but relatively slowly in the 12K GEL and E GELs. Thus, it appeared that the density of the hydrogel network influenced cell distribution and proliferation, with a higher density network providing a more ideal environment for aggregation of cells.

B)
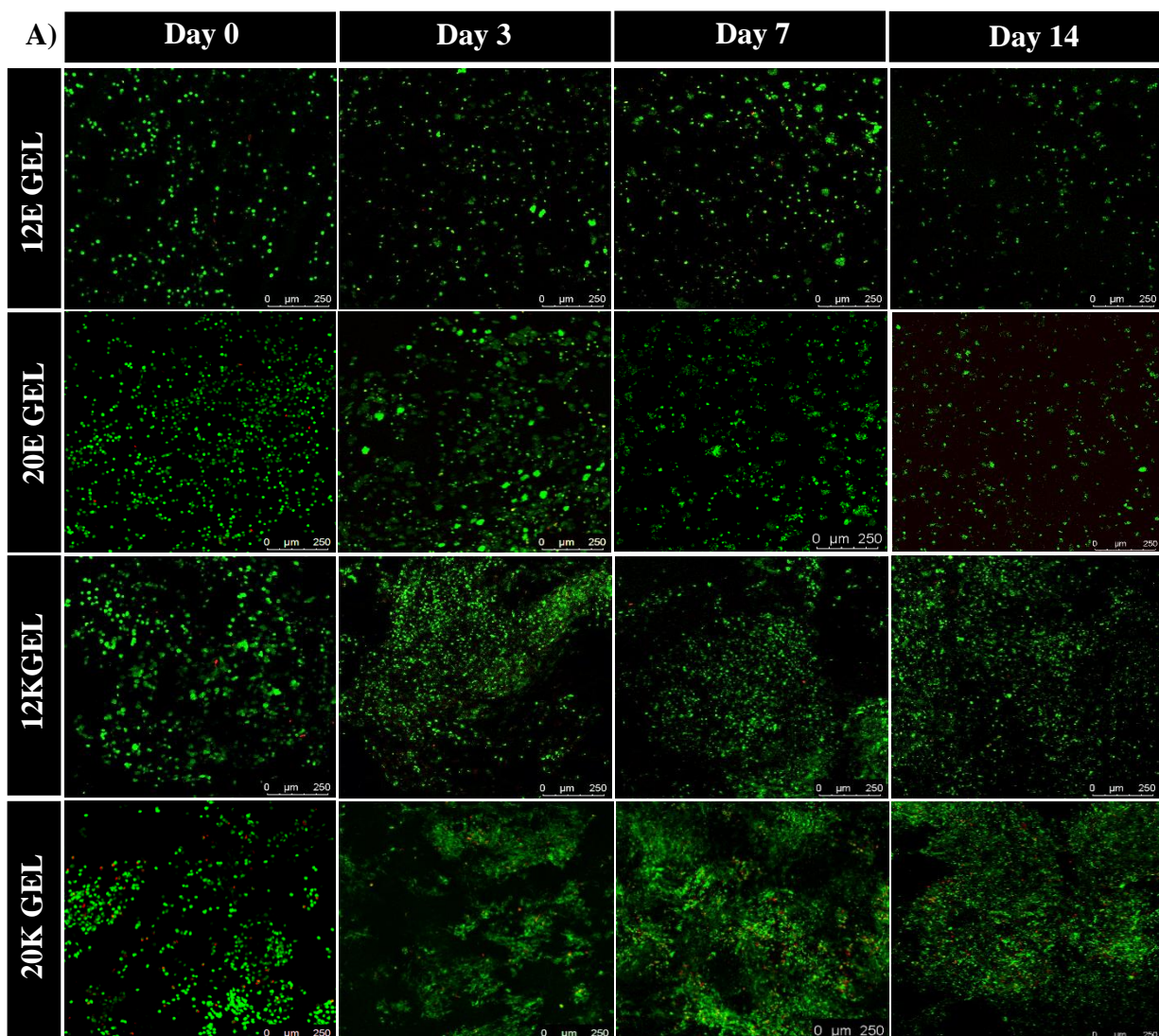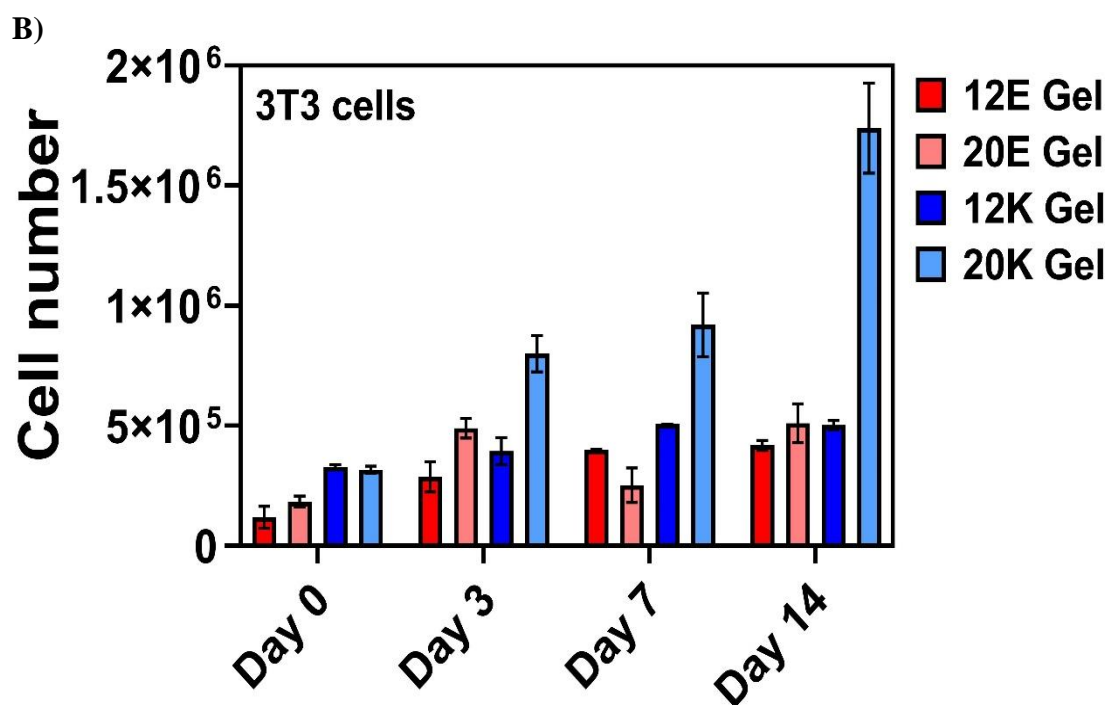
Figure 4. 12 Viability of 3T3 cells encapsulated in different peptide hydrogels. A) LIVE/DAED staining of 3T3 cells in peptide hydrogels at Day 0, 3, 7, and 14 (12E GEL means 12 mg/mL of E(FKFE)$_2$ hydrogel, 12K GEL means 12 mg/mL K(FEFK)$_2$ hydrogel, 20E GEL means 20 mg/mL E(FKFE)$_2$ hydrogel, 20K GEL means 20 mg/mL K(FEFK)$_2$ hydrogel). B) Quantity analysis of cell numbers in different peptide hydrogels using PicoGreen. All the experiments were repeated triplicate and data were presented as mean ± SD.

The MSCs encapsulated in different types of peptide hydrogel presented apparently different cell viabilities (Fig. 4.13A). On day 0, the cells were dispersed in E GELs but were aggregated in K GELs. This could perhaps be due to the different network densities of the hydrogels, given that the network density of the 20K GEL was much higher than that of the 20E GEL in the rheological analysis above (Fig. 4.6B). Additionally, although cells could be observed in the K GELs after 14 days, the E GELs had broken down and had therefore lost the 3D culture environment by this time, even at the higher concentration. The MSCs showed decreased

proliferation in both the E GELs and K GELs after 14 days. Compared to LIVE/DEAD staining, the PicoGreen analysis gave similar results (Fig. 4.13B); however, there was a significantly increased cell number in the 20E GEL on day 14. This might be because the E GEL had completely dissolved by day 14, and the cells were attached to the insert membrane. The cells were subsequently collected in a microcentrifuge tube for lysis, but such an increased cell number was not observed in the 20E GEL. Cells might have been lost during the multiple changes of medium over the 14 days.

In summary, both the E GELs and K GELs had good biocompatibility with 3T3 cells, and more so than with MSCs. Thus, the degree of biocompatibility depended on the peptide sequences and the type of cells. These hydrogels also provided an ideal 3D culture environment for specific cell lines that may be used in 3D printing applications. This was therefore a useful approach to designing 3D culture environments tailored to different cell types. In turn, this could help establish different 3D models in vitro that could potentially have a strong impact on disease diagnosis, drug screening and surgical design.
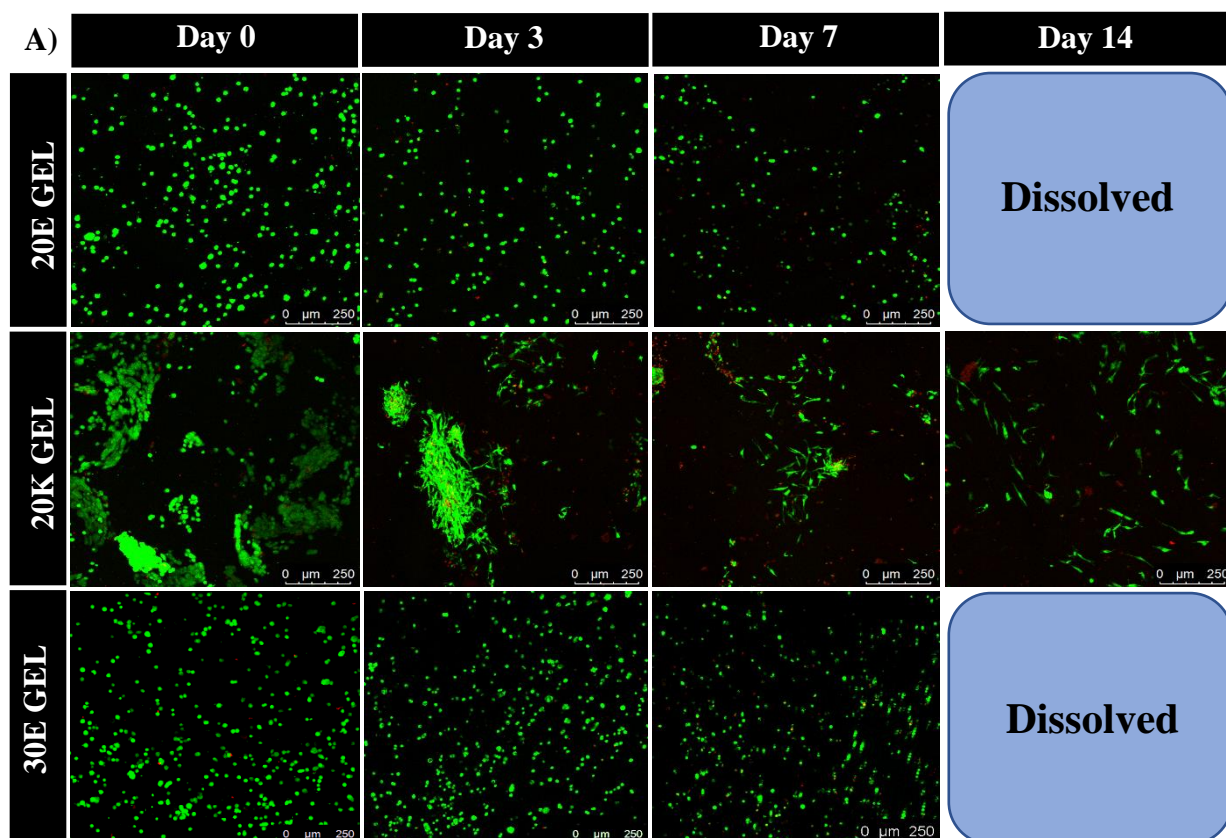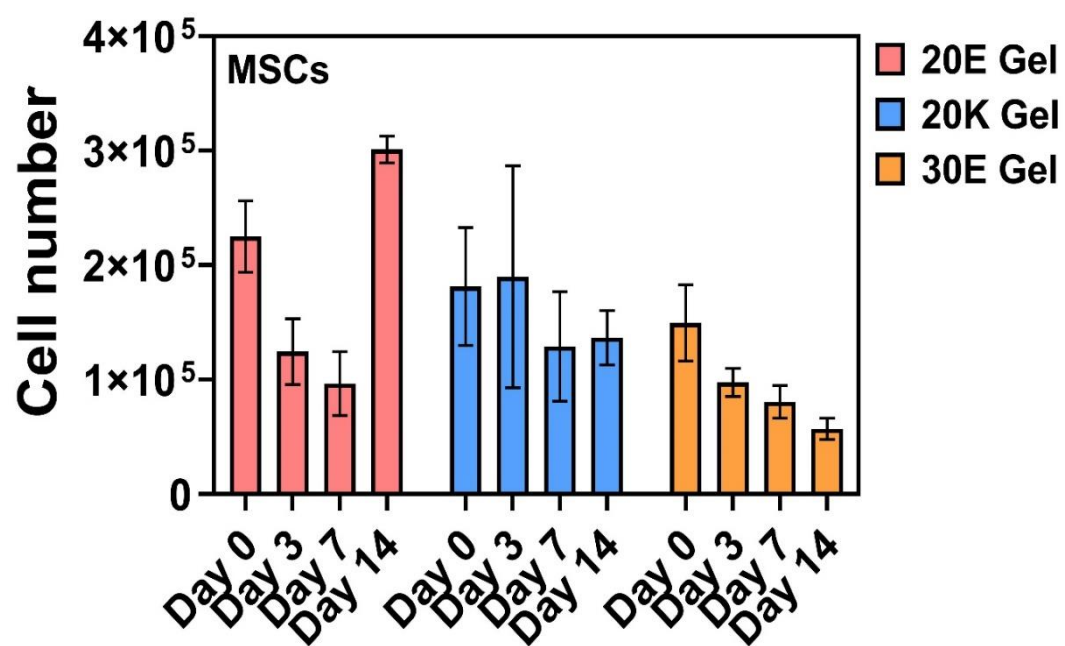
Figure 4. 13 Viability of 3T3 cells encapsulated in different peptide hydrogels. A) LIVE/DAED staining of 3T3 cells in peptide hydrogels at Day 0, 3, 7, and 14 (20E GEL means 20 mg/mL of E(FKFE)$_2$ hydrogel, 20K GEL means 20 mg/mL K(FEFK)$_2$ hydrogel, 30E GEL means 30 mg/mL E(FKFE)$_2$ hydrogel). B) Quantity analysis of cell numbers in different peptide hydrogels using PicoGreen. All the experiments were repeated in triplicate and data were presented as mean ± SD.

4.4 Conclusion

The two peptides self-assembled into hydrogels once the concentration was higher than the CGC, and different states were observed depending on the pH, which determined the charge characteristics. Therefore, hydrogels were prepared by appropriately adjusting the pH and concentration. The storage modulus (G′) relied on the concentration of peptide hydrogels, illustrating that the network structure of these materials could be controlled by concentration. Both the E(FKFE)$_2$ and K(FEFK)$_2$ hydrogels were seen to contain β-sheet structures, based on spectroscopic measurements (CD and ATR-FTIR) and ThT binding assays. They also displayed similar morphologies under TEM, and the fibre sizes were measured by SAXS, revealing them to be similar with a long, thin rod-like morphology. Both materials are potential drug delivery systems, based on their injectability as tested in shear thinning/recovery assays.

In addition, the biocompatibility and 3D cell culture properties of the peptide hydrogels were assessed using 3T3 cells and MSCs. Good biocompatibility with 3T3 cells was seen for both hydrogel types, but they were not suitable for culturing MSCs, which showed decreased proliferation in the peptide hydrogel systems after 14 days. However, they did provide a suitable 3D cell culture environment for 3T3 cells, particularly by adjusting the concentration of hydrogel to stabilise the material for prolonged use in the growth medium. The 3T3 cells formed spherical clusters, indicating suitable growth behaviour in the peptide hydrogels. Consistent with the results of LIVE/DEAD staining, PicoGreen analysis showed an increase or decrease in cell number for 3T3 cells and MSCs, respectively. Compared with the E GELs, the K GELs were more stable and thus more biocompatible with these two cell lines.

In summary, self-assembled β-sheet peptide hydrogels can be employed in biomedical research—including tissue engineering, 3D printing and drug delivery systems—by adjusting sequence, pH and concentration. Their injectability might make them useful in designing novel

drug delivery systems. Additionally, biocompatible peptide hydrogel is a promising biomaterial applied into varies studies in future.

4.5 References

[1]   A. S. Hoffman, "Hydrogels for biomedical applications," Advanced Drug Delivery Reviews. 2012. doi: 10.1016/j.addr.2012.09.010.

[2]   S. Koutsopoulos, L. D. Unsworth, Y. Nagai, and S. Zhang, "Controlled release of functional proteins through designer self-assembling peptide nanofiber hydrogel scaffold," Proc. Natl. Acad. Sci. U. S. A., 2009, doi: 10.1073/pnas.0807506106.

[3]   M. C. Branco, D. J. Pochan, N. J. Wagner, and J. P. Schneider, "Macromolecular diffusion and release from self-assembled β-hairpin peptide hydrogels," Biomaterials, 2009, doi: 10.1016/j.biomaterials.2008.11.019.

[4]   S. Koutsopoulos and S. Zhang, "Two-layered injectable self-assembling peptide scaffold hydrogels for long-term sustained release of human antibodies," J. Control. Release, 2012, doi: 10.1016/j.jconrel.2012.03.014.

[5]   L. Sun, C. Zheng, and T. J. Webster, "Self-assembled peptide nanomaterials for biomedical applications: Promises and pitfalls," International Journal of Nanomedicine. 2017. doi: 10.2147/IJN.S117501.

[6]   S. Kim, J. H. Kim, J. S. Lee, and C. B. Park, "Beta-Sheet-Forming, Self-Assembled Peptide Nanomaterials towards Optical, Energy, and Healthcare Applications," Small. 2015. doi: 10.1002/smll.201500169.

[7]   S. Zhang, T. Holmes, C. Lockshin, and A. Rich, "Spontaneous assembly of a self-complementary oligopeptide to form a stable macroscopic membrane," Proc. Natl. Acad. Sci. U. S. A., 1993, doi: 10.1073/pnas.90.8.3334.

[8]   S. Zhang, T. C. Holmes, C. M. DiPersio, R. O. Hynes, X. Su, and A. Rich, "Self-complementary oligopeptide matrices support mammalian cell attachment," Biomaterials, 1995, doi: 10.1016/0142-9612(95)96874-Y.

[9]   T. C. Holmes, S. De Lacalle, X. Su, G. Liu, A. Rich, and S. Zhang, "Extensive neurite outgrowth and active synapse formation on self-assembling peptide scaffolds," Proc. Natl. Acad. Sci. U. S. A., 2000, doi: 10.1073/pnas.97.12.6728.

[10]   S. Zhang et al., "A self-assembly pathway to aligned monodomain gels," Nat. Mater., 2010, doi: 10.1038/nmat2778.

[11]   A. Mujeeb, A. F. Miller, A. Saiani, and J. E. Gough, "Self-assembled octapeptide scaffolds for in vitro chondrocyte culture," Acta Biomater., 2013, doi: 10.1016/j.actbio.2012.08.044.

[12]   J. Gao, C. Tang, M. A. Elsawy, A. M. Smith, A. F. Miller, and A. Saiani, "Controlling Self-Assembling Peptide Hydrogel Properties through Network Topology," Biomacromolecules, 2017, doi: 10.1021/acs.biomac.6b01693.

[13]   J. B. Guilbaud et al., "Enzymatic catalyzed synthesis and triggered gelation of ionic peptides," Langmuir, 2010, doi: 10.1021/la100623y.

[14]   Y. Zhang, H. F. Chan, and K. W. Leong, "Advanced materials and processing for drug delivery: The past and the future," Advanced Drug Delivery Reviews. 2013. doi: 10.1016/j.addr.2012.10.003.

[15]   V. Delplace, A. Ortin-Martinez, E. L. S. Tsai, A. N. Amin, V. Wallace, and M. S. Shoichet, "Controlled release strategy designed for intravitreal protein delivery to the retina," J. Control. Release, 2019, doi: 10.1016/j.jconrel.2018.11.012.

[16]   J. K. Wychowaniec, A. M. Smith, C. Ligorio, O. O. Mykhaylyk, A. F. Miller, and A. Saiani, "Role of Sheet-Edge Interactions in β-sheet Self-Assembling Peptide Hydrogels," Biomacromolecules, vol. 21, no. 6, pp. 2285–2297, 2020, doi: 10.1021/acs.biomac.0c00229.

[17]   C. J. Bowerman, W. Liyanage, A. J. Federation, and B. L. Nilsson, "Tuning β-sheet peptide self-assembly and hydrogelation behavior by modification of sequence hydrophobicity and aromaticity," Biomacromolecules, 2011, doi: 10.1021/bm200510k.

[18]   D. Roberts, C. Rochas, A. Saiani, and A. F. Miller, "Effect of peptide and guest charge on the structural, mechanical and release properties of β-sheet forming peptides," Langmuir, 2012, doi: 10.1021/la303328p.

[19]   E. Arad, H. Green, R. Jelinek, and H. Rapaport, "Revisiting thioflavin T (ThT) fluorescence as a marker of protein fibrillation – The prominent role of electrostatic interactions," J. Colloid Interface Sci., 2020, doi: 10.1016/j.jcis.2020.03.075.

[20]   M. J. Krysmann, V. Castelletto, and I. W. Hamley, "Fibrillisation of hydrophobically modified amyloid peptide fragments in an organic solvent," Soft Matter, 2007, doi: 10.1039/b709889h.

[21]   J. B. Guilbaud and A. Saiani, "Using small angle scattering (SAS) to structurally characterise peptide and protein self-assembled materials," Chem. Soc. Rev., 2011, doi: 10.1039/c0cs00105h.

[22]   J. Filik et al., "Processing two-dimensional X-ray diffraction and small-angle scattering data in DAWN 2," J. Appl. Crystallogr., 2017, doi: 10.1107/S1600576717004708.

[23]   H. C. Clough, M. O'Brien, X. Zhu, A. F. Miller, A. Saiani, and O. Tsigkou, "Neutrally charged self-assembling peptide hydrogel recapitulates in vitro mechanisms of breast cancer progression," Mater. Sci. Eng. C, 2021, doi: 10.1016/j.msec.2021.112200.

[24]   F. Raza et al., "Paclitaxel-loaded pH responsive hydrogel based on self-assembled peptides for tumor targeting," Biomater. Sci., 2019, doi: 10.1039/c9bm00139e.

[25]   S. Boothroyd, A. F. Miller, and A. Saiani, "From fibres to networks using self-assembling peptides," Faraday Discussions. 2013. doi: 10.1039/c3fd00097d.

[26]   A. Aggeli et al., "pH as a trigger of peptide β-sheet self-assembly and reversible switching between nematic and isotropic phases," J. Am. Chem. Soc., 2003, doi: 10.1021/ja021047i.

[27]   D. Roberts, C. Rochas, A. Saiani, and A. F. Miller, "Effect of peptide and guest charge on the structural, mechanical and release properties of β-sheet forming peptides," Langmuir, 2012, doi: 10.1021/la303328p.

[28]   M. R. Caplan, P. N. Moore, S. Zhang, R. D. Kamm, and D. A. Lauffenburger, "Self-assembly of a β-sheet protein governed by relief of electrostatic repulsion relative to van der Waals attraction," Biomacromolecules, 2000, doi: 10.1021/bm005586w.

[29]   N. J. Greenfield, "Using circular dichroism spectra to estimate protein secondary structure," Nat. Protoc., 2007, doi: 10.1038/nprot.2006.202.

[30]   A. Micsonai et al., "Accurate secondary structure prediction and fold recognition for circular dichroism spectroscopy," Proc. Natl. Acad. Sci. U. S. A., 2015, doi: 10.1073/pnas.1500851112.

[31]   J. Kong and S. Yu, "Fourier transform infrared spectroscopic analysis of protein secondary structures," Acta Biochim. Biophys. Sin. (Shanghai)., 2007, doi: 10.1111/j.1745-7270.2007.00320.x.

[32]   A. Barth, "Infrared spectroscopy of proteins," Biochimica et Biophysica Acta - Bioenergetics. 2007. doi: 10.1016/j.bbabio.2007.06.004.

[33]   A. Barth, "The infrared absorption of amino acid side chains," Progress in Biophysics and Molecular Biology. 2000. doi: 10.1016/S0079-6107(00)00021-3.

[34]   F. Koch et al., "Mechanical characteristics of beta sheet-forming peptide hydrogels are dependent on peptide sequence, concentration and buffer composition," R. Soc. Open Sci., vol. 5, no. 3, 2018, doi: 10.1098/rsos.171562.

Chapter 5 Control release of macromolecules in self-assembled peptide hydrogel system

5.1 Introduction

According to the results described in Chapter 4, $E(FKFE)_2$ and $K(FEFK)_2$ formed hydrogels with similar stiffness at 12 mg/mL. Both materials demonstrated good injectability and were biocompatible with 3T3 cells, making them promising candidates for drug delivery systems [1][2]. These systems encompass oral, ocular, intranasal, transdermal and injection routes of administration. To optimise drug efficacy and avoid adverse effects, thereby alleviating the suffering of patients, it is necessary to design a controlled release drug delivery system and achieve localised therapy [3].

For example, peptide hydrogels have been used to establish smart drug delivery systems and encapsulate hydrophobic drug molecules used in cancer therapy. Controlled release of paclitaxel (PTX), an effective antitumour drug, was achieved using the self-assembling peptide hydrogel RADA16 to target breast cancer cells in vitro [4]. However, loading of PTX into the RADA16 hydrogel through magnetic stirring was slow. Another small hydrophobic drug, curcumin, has successfully been loaded into a hydrogel (MAX8) to induce apoptosis in medulloblastoma cells [5]. Both of these peptide hydrogel systems offered a controlled release profile at therapeutically relevant drug concentrations, and their injectability might allow localised treatment to be realised in vivo.

Whereas a variety of research has focused on designing peptide hydrogel systems to encapsulate small-molecule drugs, bio-macromolecular agents such as therapeutic antibodies have become more prevalent in cancer treatment in recent years. In this work, we designed two self-assembling, β-sheet peptide hydrogels, $E(FKFE)_2$ and $K(FEFK)_2$ with a view to

encapsulating macromolecules. As these two peptides carry opposite net charges, it is important to study the relationships between their electrostatic character and controlled release kinetics. For this purpose, a variety of polymers were selected for encapsulation, as macromolecular mimics of functional protein drugs. Negatively charged dextran (Thermo Fisher Scientific) with different molecular weights (3, 40, and 2,000 kDa), and positively charged poly-L-lysine (28 kDa; Sigma Aldrich), were used to investigate how electrostatic character and mesh size would affect the release kinetics. The chosen polymers were labelled with fluorescein to enable their detection by UV spectroscopy. To describe the release kinetics of these polymers from peptide hydrogels, the diffusion coefficient D_E was used. For comparison, D_0 was also measured, defined as the diffusion coefficient in water. The hydrodynamic radius of polymers was determined by fluorescence correlation spectroscopy (FCS) [6]. In addition, the charge of polymers and peptide hydrogels was measured by zeta potential, to verify the theoretical assumptions.

A swelling experiment was performed to assess whether the network structure of hydrogel systems can be controlled by the charge properties, and in addition, to study the influence of external molecules (H_2O) on the hydrogel network. Oscillatory shear rheology was used to study the effect of charge on the stiffness of peptide hydrogels. Furthermore, polymer-loaded hydrogel systems were characterised structurally using a range of techniques including Fourier transform infrared spectroscopy (ATR-FTIR), transmission electron microscopy (TEM) and small-angle X-ray scattering (SAXS).

5.2 Experimental methods

5.2.1 Zeta potential

To confirm the charge of peptide solutions and fluorescently labelled polymers at pH 7, a Zetasizer Nano instrument (Malvern Instruments Ltd., UK) was used. Samples were dissolved in HPLC grade water and 0.1 M NaOH was added to adjust the pH, which was measured using a pH meter. The final sample concentration was 0.2 mg/mL.

5.2.2 Preparation of polymer-loaded hydrogel

The appropriate fluorescently labelled polymer was mixed with the relevant peptide powder, then the mixture was dissolved in 70% of the final target volume of HPLC grade water, and the solution adjusted to pH 7 by addition of 0.5 M NaOH. Thereafter, the remaining volume of HPLC grade water was added to achieve a final sample with 12 mg/mL hydrogel and 0.8 mg/mL polymer. The sample was placed in the fridge at 4 °C overnight then used for subsequent experiments as required.

5.2.3 ATR-FTIR

The secondary structure of polymer-loaded hydrogels was assessed using a Bruker Alpha-P FT-IR Spectrometer. One droplet of the test sample was loaded onto the crystal surface of the spectrometer, then the absorbance spectrum was recorded from 1400–1800 cm^{-1}. For each sample, 256 scans were performed at a resolution of 4 cm^{-1}. Before running the samples, HPLC grade water was used to record a background spectrum.

5.2.4 TEM

The polymer-loaded hydrogel sample was diluted 20-fold with HPLC grade water then vortexed to ensure it was evenly mixed. A carbon-coated copper grid (400 mesh, Electron Microscopy Sciences, UK) was placed on the sample droplet for 1 min, moved to the water

droplets to wash three times, then transferred to the 1% uranyl acetate droplet for 30 s. Excess liquid on the grid was removed with a 70 mm filter paper (Whatman), then the grid was dried for TEM imaging. Images were acquired using an FEI Tecnai12 BioTwin at 100 KeV, with a Gatan Orius SC1000A CCD camera. The fibre width in the peptide hydrogels was measured 700 times manually from the TEM images, using the ImageJ software, and analysed by log-normal distribution [7].

5.2.5 SAXS

To further characterise the structure of polymer-loaded peptide hydrogels, SAXS measurements were performed at the Diamond Light Source, beamline I22 [8]. The sample–detector distance was fixed at 5.772 m resulting in a momentum transfer vector, q, in the range $0.1 < \text{q (nm}^{-1}) < 3$, where $q = \frac{4\pi \sin(\frac{\theta}{2})}{\lambda}$, λ is the wavelength and θ is the scattering angle. Silver behenate powder was used for calibration, and sample data were collected as 10×100 ms frames. Data reduction was done using the DAWN software [9]. The 2D isotropic scattering data were collected and corrected for detector response, dark current background and sample transmission, then radially averaged to obtain 1D scattering patterns.

5.2.6 Dynamic oscillatory rheology

The mechanical properties of polymer-loaded hydrogels were assessed using a rheometer (Discovery HR-2, TA Instruments) equipped with a 20 mm diameter parallel plate. The gap size was set as 45,000 nm between the upper plate and sample stage at the beginning of procedure, and when the parallel plate was lowered to make measurements, the geometry gap was 500 nm. For analysis, 180 μL of the test sample was loaded onto the stage and equilibrated at 37 °C for 180 s before starting the run. Dynamic strain sweep was assessed by measuring the strain-dependent evolution of storage modulus (G′) and loss modulus (G″) at a fixed

frequency of 1 Hz. All steps were performed using the same frequency of 1 Hz, following equilibration for 180 s at 37 °C.

5.2.7 Swelling experiment

To determine how charge affects the peptide hydrogel network, a negatively charged polymer (dextran) and a positively charged polymer (poly-L-lysine) were selected for swelling experiments. As described in Section 5.2.2, 0.8 mg/mL of polymer was mixed with the relevant peptide to form a polymer-loaded 12 mg/mL hydrogel. Then, 1 mL of this sample was transferred to a cylindrical glass tube and a marker pen was used to label the position of the gel surface on the tube. Subsequently, HPLC grade water (3 mL) was added on top of the gel. All experiments were performed in triplicate, and samples were maintained at 37 °C for 10 days. The actual volume of gels was calculated using the measured surface position and dimensions of the cylindrical tube, both before swelling (V_1) and after swelling (V_2) [10][11][12]. The swelling ratio (Q) was defined as (V_2-V_1)/V_1 and the results are expressed as mean ± standard deviation. A 12mg/mL peptide hydrogel with no polymer loading acted as the control.

5.2.8 FCS

The FCS technique was used to investigate the hydrodynamic radius and diffusion coefficient (D_0) of fluorescently labelled polymers in aqueous solution. The experimental approach has been previously described elsewhere [13]. Measurements were made using a Zeiss Confocor2 LSM 510 META (Zeiss, Germany) equipped with an Argon laser and a 40× 1.2 NA water immersion objective. The system was calibrated with 100 nM Rhodamine 6G (experimental diffusion time, τ_D, 24 ± 0.5 µs; and published D_0, 4.14 × 10^{-6} cm^2/s) to assess the laser beam waist, ω_0 [14], which was estimated using the following equation 5.1:

$$\omega_0^2 = 4D\tau_D \tag{5.1}$$

Where, τ_D is the diffusion time, ω_0 is the laser beam waist and D is the diffusion coefficient. The diffusion coefficient in water was measured for fluorescein-labelled dextrans with molecular weights of 3 kDa, 40 kDa and 2,000 kDa, and likewise for labelled 28.7 kDa poly-L-lysine. Diffusion of 3 kDa and 40 kDa dextrans was measured at 100 nM, whereas a 10 nM solution was used for 2,000 kDa dextran. All samples were analysed in eight-well Nunc Lab-Tek chamber slides (Fisher Scientific, UK). Each measurement consisted of 20 runs of 10 s each, and each sample was measured three times. Autocorrelation curves were calculated from the raw data in QuickFit 3.0, using models employing the Levenberg–Marquardt algorithm. A 3D diffusion model consisting of one fluorescent component and a non-fluorescent triplet state fraction was used, and the autocorrelation curve ($G(\tau)$) was fitted using a single-exponential model according to Eq. 5.2 below:

$$G(\tau) = 1 + \frac{1}{N}\left(1 + \frac{\tau}{\tau_D}\right)^{-1}\left(1 + \frac{\tau}{S^2 \cdot \tau_D}\right)^{-1/2} \tag{5.2}$$

Where, N is the number of particles and S is the structure parameter. The hydrodynamic radius, r_h, was determined for the dextran and peptide samples using the Stokes–Einstein equation:

$$r_h = \frac{k_b T}{6 D \mu \pi} \tag{5.3}$$

Where, k_b is the Boltzmann constant, T is the temperature in Kelvin, D is the diffusion coefficient and μ is the viscosity.

5.2.9 Release study using UV/vis spectroscopy

Fluorescein-labelled dextran (3 kDa, 40 kDa, 2,000 kDa) and poly-L-lysine (28kDa) were selected as probes for the release study, as mentioned above. Solutions were first diluted to a series of concentrations (1.0, 0.8, 0.6, 0.4 and 0.2 mg/mL) that were measured at a wavelength of 492 nm using a Jenway 6715 temperature-controlled UV/vis spectrophotometer [15], to

determine the optimum concentration. For the polymers, 0.8 mg/mL was selected as the ideal concentration for the experiment, due to the optimal absorbance within the linear region that was observed for the fluorescein dye at this concentration [15]. The E(FKFE)$_2$ and K(FEFK)$_2$ peptides were dissolved in HPLC grade water and mixed with labelled polymers to form polymer-loaded hydrogels, as outlined in Section 5.2.2, with final concentrations of peptide hydrogel and polymer of 12 mg/mL and 0.8 mg/mL, respectively. Then, 1 mL of each sample was transferred to a cylindrical glass tube and HPLC grade water (3 mL) was added slowly to the top of the hydrogel, to prevent disruption to the gel structure. Release experiments were performed for 5 days with incubation at 37 °C to mimic the environment of the human body. A 1 mL aliquot of supernatant was collected for measurement with the UV/vis spectrophotometer at 15 min, 45 min, 75 min, 2 h, 4 h, 6 h, 8 h, 12 h, and every 12 h thereafter [16].

5.2.10 Statistical data analysis

All experiments were repeated at least three times to obtain an average value, expressed as mean ± standard deviation. The rheological results were analysed in GraphPad Prism 8 using one-way ANOVA and Student's t-test to assess the statistical significance of comparisons via P value [17]. Significance levels are represented as follows: * ($P < 0.05$), ** ($p < 0.01$), *** ($P < 0.001$), **** ($P < 0.0001$), and "ns" indicates there was no significant difference between the two groups. Release graphs were made using Origin 2020b and the error bars represent standard deviations.

5.3 Results

5.3.1 Definition the charge of polymers and peptides

To study electrostatic interactions in the polymer-loaded hydrogel systems, zeta potential measurements were used to characterise the charge of polymers and peptides. The peptide and polymer samples were dissolved in HPLC grade water at 0.2 mg/mL concentration then measured at pH 7. The results, presented in Fig. 5.1, showed that the samples were in a stable state according to Table 3.1 (Chapter 3), since the zeta potential was in the range of 40–60 mV in all cases. The stability of the hydrogel networks depends on electrostatic repulsion between fibres. Strong repulsive forces cause the fibres to distribute individually in the system, thereby preventing aggregation or flocculation. However, if the attractive forces in the system outweigh the repulsive forces, the fibres will come together and the system would present in an aggregated state.

The zeta potential can be related to electrophoretic mobility, as explained by the Henry equation Eq. 5.4:

$$U_E = \frac{2\varepsilon\zeta f(\kappa a)}{3\eta} \tag{5.4}$$

Where, U_E is the electrophoretic mobility ($m^2\ s^{-1}\ V^{-1}$), ε is the dielectric constant ($kg\ mV^{-2}\ s^{-2}$), ζ is the zeta potential (mV), η is the viscosity ($kg \cdot m^{-1} \cdot s^{-1}$) and $f(\kappa a)$ is Henry's function.

In Fig. 5.1, it can be seen that E(FKFE)$_2$ carried negative charge and K(FEFK)$_2$ carried positive charge at pH 7, which is consistent with the theoretical curves in Chapter 4.3.2.1. As expected, dextran was negatively charged and poly-L-lysine was positively charged. The polymers were then loaded into differently charged peptide hydrogels to study the effect of electrostatic interactions on the structure, network and mechanical properties of the hydrogels, and to compare the release kinetics.
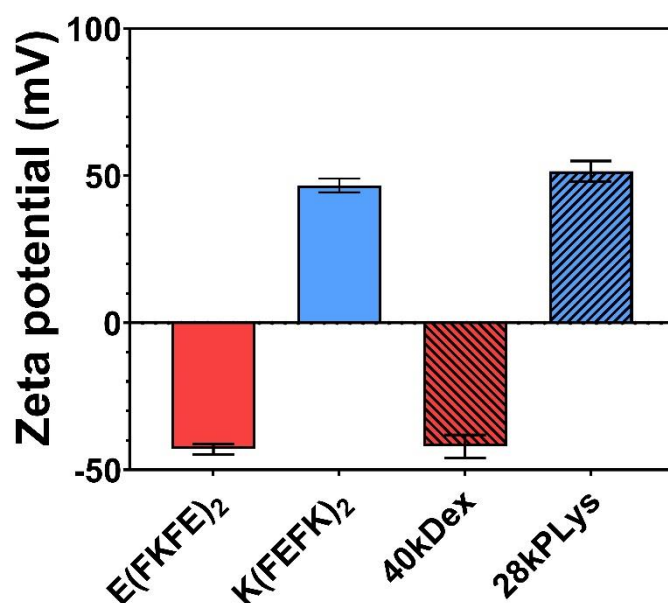
Figure 5. 1 Zeta potential of diluted peptide and polymer solutions at pH 7.

5.3.2 Characterization of polymer-loaded hydrogel

5.3.2.1 Secondary structure and morphology of polymer-loaded hydrogel

Negatively charged dextran (40 kDa) and positively charged poly-L-lysine (28 kDa) were loaded into differently charged peptide hydrogels to form 12 mg/mL hydrogels with 0.8 mg/mL of polymer. A droplet of each sample was analysed by ATR-FTIR, and the results are shown in Fig. 5.2. The β-sheet structure of the hydrogels was evidently not disrupted by polymer encapsulation, since the absorption bands at ~1620 cm^{-1} and ~1690 cm^{-1} were still present, corresponding to parallel and antiparallel β-sheet structures, respectively.
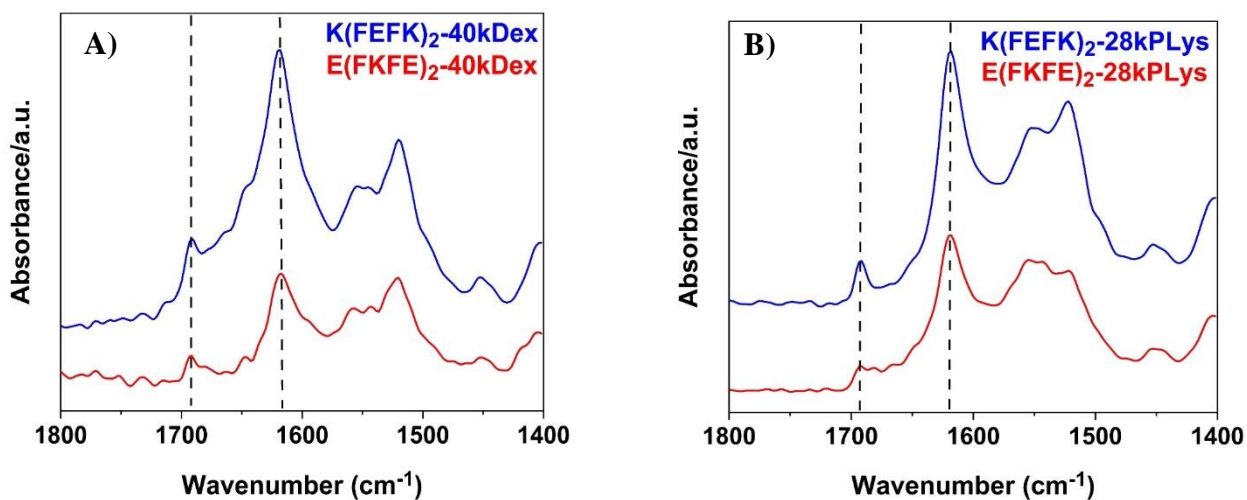
Figure 5. 2 FTIR spectroscopy of polymer-loaded hydrogels. A) 40kDa dextran-loaded peptide hydrogel. B) 28kDa Poly-L-Lysine-loaded peptide hydrogel. (The blue lines represent K hydrogel with polymers, the red lines represent E hydrogel with polymers).

At pH 7, FITC-Poly-L-Lysine (28kPLys) carried positive charge, whereas the fluorescein - dextran carried negative charge. As a result, the polymer-loaded hydrogel systems presented different morphologies under TEM (Fig. 5.3C & Fig. 5.3D). Individual fibres were clearly visible in E(FKFE)$_2$–40kDex and K(FEFK)$_2$–28kPLys, whereas the fibres were tangled together in bundles and were observed as a thick, fibrillar network in E(FKFE)$_2$–28kPLys and K(FEFK)$_2$–40kDex. It can reasonably be assumed that in the former samples, fibre aggregation was prevented via electrostatic repulsion such that individual fibres could be observed. Conversely, in the latter cases, electrostatic attraction caused the fibres to come together, driving aggregation into bundles and formation of the fibrillary network structure as described.

In addition, fibre size distribution was analysed using a log-normal model, as shown in Fig. 5.3A,B. In E(FKFE)$_2$–40kDex, measured fibre sizes ranged from 2–16 nm, with an estimated 28.2% having a width of ~3.2 ± 1 nm. This is similar to the result for the unloaded E(FKFE)$_2$

hydrogel (21.6%). In contrast, K(FEFK)$_2$–40kDex formed a more thickness network, and there was some bimodal character to the fibre size distribution (Fig. 5.3A). The individual fibres were generally more homogenous, with many in the range of 2–8 nm, and a high count (46.5%) with widths of ~3.05 ± 1 nm. However, there was another maximum (7%) in the size distribution that represented bundles of fibres (Fig. 5.3A, inset). Moreover, dextran loading of oppositely charged hydrogels induced apparently different size distributions, suggesting that the density of these peptide hydrogel networks depended on the charge interactions. This hypothesis was also applied to the 28kPLys gels. Compared with Fig. 5.3C, the network of E(FKFE)$_2$–28kPLys became more complex with entangled fibres resulting in formation of a dense, fibrillar network (Fig. 5.3D). However, K(FEFK)$_2$ loaded with poly-L-lysine showed a thinner network, and individual fibres were observed. An estimated 43.6% of fibres had a size of 3.0 ± 0.5 nm in E(FKFE)$_2$–28kPLys, and there were 21.6% of fibres with a size of 3.5 ± 0.5 nm in K(FEFK)$_2$–28kPLys. In Fig. 5.3B (inset), another maximum is evident (10%) for bundled fibres in E(FKFE)$_2$–28kPLys, corresponding to the TEM images.

Table 5.1 shows a comparison of single fibre width distributions between the peptide hydrogels and polymer-loaded hydrogels. The FWHM of E(FKFE)$_2$–40kDex (2.76 nm) was close to that of the unloaded E(FKFE)$_2$ hydrogel (3.23 nm), indicating that these peptide hydrogel systems were formed in a similar state. However, E(FKFE)$_2$–28kPLys had a smaller FWHM (1.26 nm), suggesting the differently charged E(FKFE)$_2$ hydrogel system had altered properties upon loading with positively charged poly-L-lysine. The FWHM of K(FEFK)$_2$–28kPLys was 3.76 nm, which is similar to the value for the K(FKFE)$_2$ hydrogel (3.11 nm), but an FWHM of only 1.99 nm was seen for K(FEFK)$_2$–40kDex. Thus, differently charged polymers affect the network structure of peptide hydrogels. From the above results, it can be assumed that electrostatic interactions existed in the polymer-loaded peptide hydrogels and influenced the network of these systems. In turn, this may affect the mechanical properties of these materials.
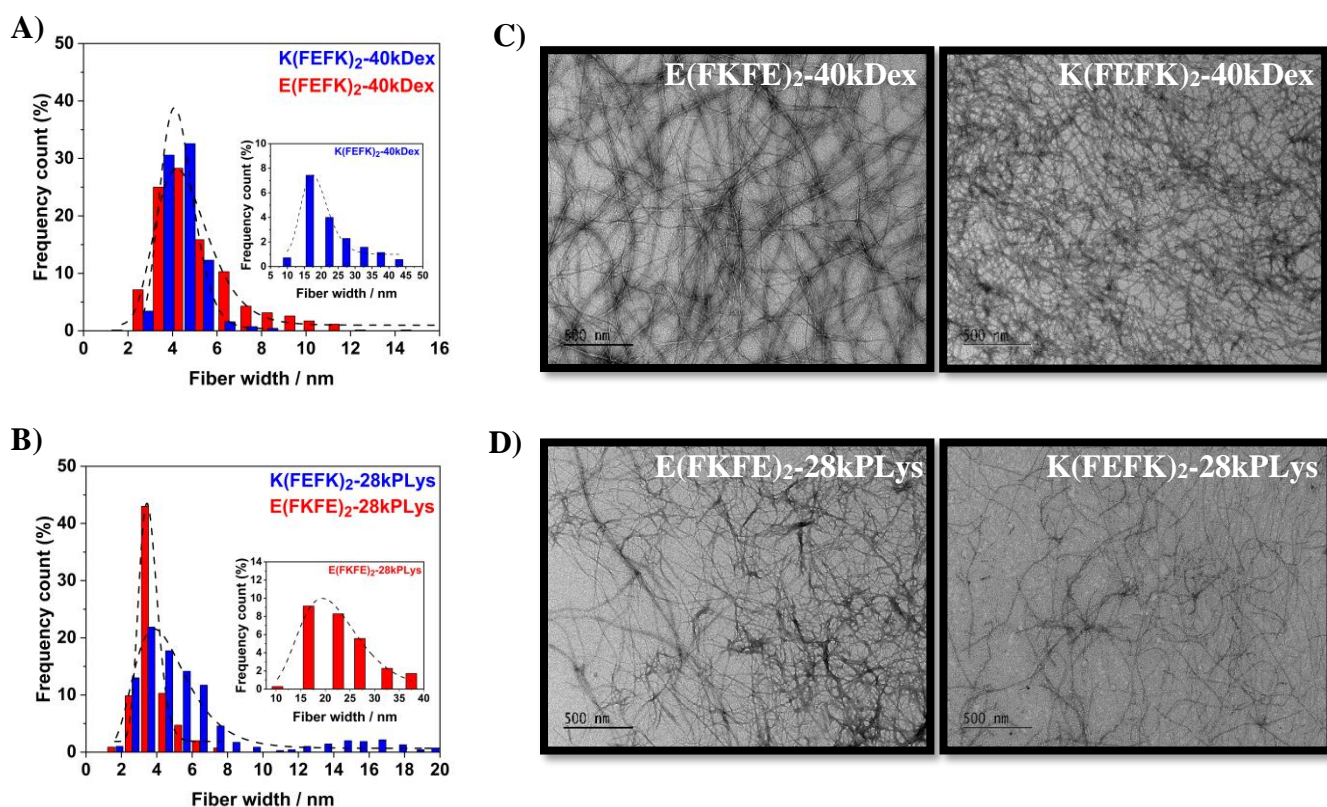
Figure 5. 3 A & B) Width of fibres measured randomly for 700 times to create single fibre size distribution, the dash lines represent lognormal fits. (insets in A & B are the bundles size distribution, the dash lines represent lognormal fits). C&D) TEM images of 20 x diluted hydrogel with polymers, 40kDex means 40kDa dextran, 28kPLys means 28kDa Poly-L-Lysine.

Table 5. 1 Comparison of single fibre width distribution.

Peptide hydrogel	charge	Fibre width (nm)	Fibre width half maximum (nm)	Fibre width range (nm)
E(FKFE)$_2$	(-)	5.2	3.23	2-20
E(FKFE)$_2$ – 40kDex	(- -)	4.2	2.76	2-16
E(FKFE)$_2$ – 28kPLys	(- +)	3.5	1.26	2-8
K(FEFK)$_2$	(+)	5.5	3.11	2-20
K(FEFK)$_2$ – 28kPLys	(+ +)	3.9	3.76	2-20
K(FEFK)$_2$ – 40kDex	(+ -)	4	1.99	2-8

5.3.2.2 SAXS analysis of polymer-loaded hydrogel

To complement the TEM results, SAXS was used to investigate the variations in structure with different charge interactions. All the samples for SAXS analysis were at 6 mg/mL, with polymers loaded at 0.4 mg/mL. The SAXS patterns are represented by l_N [q $I_N(q)$] vs q^2 (Fig. 5.4). In the low q range, it can be seen that q^{-1} is an indication of long, thin rod-like fibres in the hydrogels. There was no obvious difference between the E(FKFE)$_2$ gel and E(FKFE)$_2$–40kDex, or between the K(FEFK)$_2$ gel and K(FEFK)$_2$–28kPLys. According to the q^{-1} values, all four of these materials presented a long, thin shape, as was observed using TEM (Fig. 5.3C & Fig. 5.3D). However, an upward trend was present in E(FKFE)$_2$–28kPLys and K(FEFK)$_2$– 40kDex, indicating that the structure of these peptide hydrogels had been changed by polymer loading. The variations in the curve shown in Fig. 5.4 correspond to the fibrillar network seen in the TEM images (Fig. 5.3C & Fig. 5.3D). Thus, increased electrostatic attraction apparently changed the structure of peptide hydrogel systems; or in other words, electrostatic interactions seemed to be a driving force for variations in the hydrogel network. This might influence the mechanical properties of these gels, and could therefore play a key role in controlled release delivery.
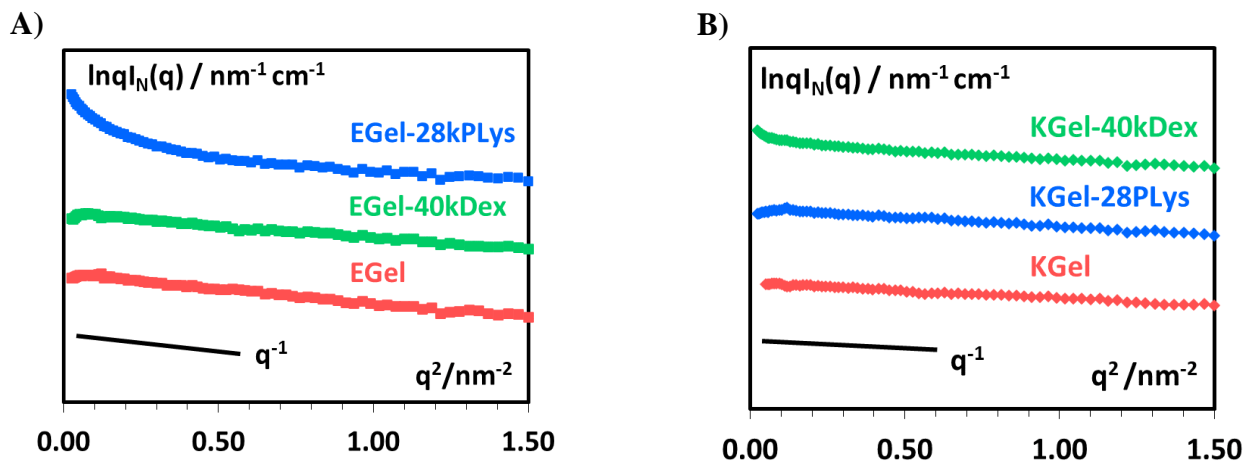
Figure 5. 4 SAXS analysis of polymer-loaded hydrogels using $l_N [q\,I_N(q)]$ vs q^2. EGel represents 6 mg/mL E(FKFE)$_2$ hydrogel, KGel represents 6 mg/mL K(FEFK)$_2$ hydrogel.

5.3.2.3 Mechanical properties analysis

To assess this effect, dynamic oscillatory rheology was performed at a frequency of 1 Hz. Unloaded E(FKFE)$_2$ and K(FEFK)$_2$ hydrogels at 12 mg/mL were employed as controls, and test samples were prepared as 12 mg/mL hydrogels loaded with 0.8 mg/mL of polymers with different sizes and charges, as described above. These measurements revealed that the differently charged polymers significantly influenced the stiffness of hydrogels, as shown in Fig. 5.5 and Fig. 5.6.

In terms of shear storage modulus (G′), there was no significant difference between the E(FKFE)$_2$ and E(FKFE)$_2$–Dex hydrogels (Fig. 5.5A). However, for the E(FKFE)$_2$–Dex samples, G′ showed a decreasing trend as the size of the encapsulated dextran increased. It can therefore be assumed that the size of loaded polymers affects the properties of the peptide hydrogel system. Peptide hydrogels form a porous network which is able to encapsulate molecules of different sizes. For 3kDex and 40kDex, these materials may form short fibres that will mostly be located within the mesh of the hydrogel network without disrupting its overall structure (Fig. 5.5B). Hence, there was no apparent change in G′. For the larger 2000kDex,

however, the negatively charged fibres might be longer and become intertwined with the peptide fibres (Fig. 5.5B). The resulting repulsive electrostatic forces would disturb the network morphology of the E(FKFE)$_2$ hydrogel, and therefore, G′ was decreased. On the contrary, increased attractive electrostatic forces were induced in the E(FKFE)$_2$–28kPLys hydrogel, resulting in a higher G′ value. According to the hydrodynamic radius of 28kPLys from FCS results, it could be assumed that 28kPLys formed short fibres that were easily accommodated within the mesh size of the hydrogel network. Thus, the positive charge of 28kPLys would attract the negatively charged peptide fibres, causing them to come together and form a more dense network (Fig. 5.5B). In this case, formation of bundles would occur leading to a thickness fibrilla network.
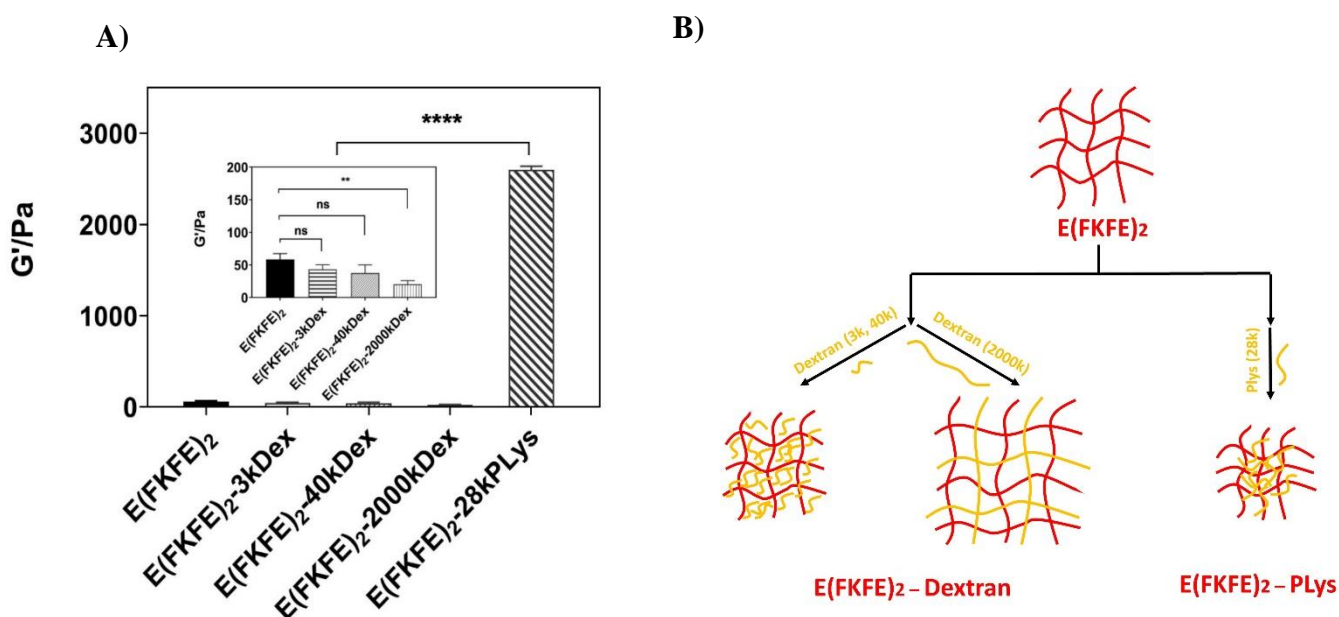
Figure 5. 5 (A) Comparisons of initial storage modulus (G') at 1Hz of between E(FKFE)$_2$ hydrogel and polymer-loaded hydrogels. All the experiments were repeated at least 3 times at 37℃. (The graphs were analysed by One-way ANOVA, student T-test was used for the comparison of peptide hydrogel and polymer-loaded hydrogels, p value was indicated as *p<0.05,

**p<0.01, ***p<0.001, **** p<0.0001, ns represented there was no significant difference between two groups.) 3kDex means 3kDa dextran, 40kDex means 40kDa dextran, 2000kDex means 2000kDa dextran, 28kPLys means 28kDa Poly-L-Lysine. (B) A schematic showed the assumptions of E(FKFE)$_2$ hydrogel network with different charge of polymers.

For the K(FEFK)$_2$ hydrogels, encapsulation of negatively charged dextran became a driving force to change their mechanical properties (Fig. 5.6A). As can be seen, G′ decreased with increasing dextran size. Since G′ was higher for the K(FEFK)$_2$ hydrogel than for the E(FKFE)$_2$ hydrogel, the network of the former should be more dense. It can therefore be hypothesised that 3kDex formed some short fibres within the mesh structure of the hydrogel, inducing a higher network density via charge attraction (Fig. 5.6B). For 40kDex, the number of fibres formed within the K(FEFK)$_2$ network might be lower, leading to fewer attractive electrostatic interactions (Fig. 5.6C). Compared with K(FEFK)$_2$–3kDex, K(FEFK)$_2$–40kDex would form a lower-density network, in which case G′ would be lower, as was observed. In the case of 2000kDex, this might form long fibres and introduce electrostatic attractive forces into the K(FEFK)$_2$ hydrogel system. However, since the molar concentration of 2000kDex was much lower than for 40kDex, the number of fibres might be lower than with 40kDex (Fig. 5.6D). Therefore, the contribution of electrostatic attractive forces would be relatively small and manifest as a decreased value of G′. As shown in Fig. 5.6A, there was no apparent increase in G′ for the K(FEFK)$_2$–40kDex hydrogel, consistent with the SAXS results for this material (Fig. 5.4B). In addition, loading with positively charged 28kPLys slightly reduced the stiffness of the K(FEFK)$_2$ hydrogel, but there was no significant difference in G′ between the K(FEFK)$_2$ and K(FEFK)$_2$–28kPLys samples (Fig. 5.6A).

Self-assembled peptide hydrogels form complex networks that might be adjustable by external factors. The above results demonstrate that electrostatic interactions affect the network structure of hydrogels, and also correspond with the TEM and SAXS results (Figs. 5.3 and 5.4).

Thus, electrostatic interactions in the peptide hydrogel systems are a key factor in modulating the mechanical properties of complementary ionic peptides.
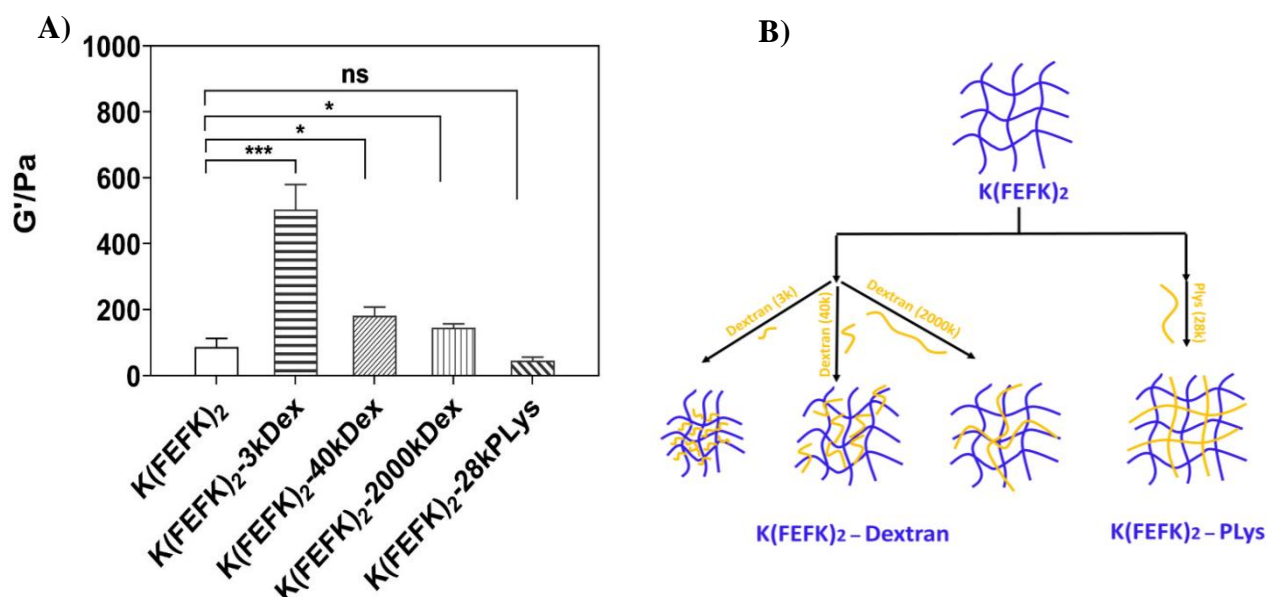
Figure 5. 6 (A) Comparisons of initial storage modulus (G') at 1Hz of between K(FEFK)$_2$ hydrogel and polymer-loaded hydrogels. All the experiments were repeated at least 3 times at 37℃. (The graphs were analysed by One-way ANOVA, student T-test was used for the comparison of peptide hydrogel and polymer-loaded hydrogels, p value was indicated as *p<0.05, **p<0.01, ***p<0.001, **** p<0.0001, ns represented there was no significant difference between two groups.) 3kDex means 3kDa dextran, 40kDex means 40kDa dextran, 2000kDex means 2000kDa dextran, 28kPLys means 28kDa Poly-L-Lysine. (B) A schematic showed the assumptions of K(FEFK)$_2$ hydrogel network with different charge of polymers.

5.3.3 Swelling experiment

To further study how the molecular size and electrostatic interactions of encapsulated polymers affect the network structure of peptide hydrogels, a swelling assay was performed. Here, 0.8

mg/mL of polymers were again loaded into 12 mg/mL hydrogels and the swelling behaviour of hydrogels was investigated after 10 days. The gels presented different swelling ratios in an aqueous environment, as shown in Fig. 5.7.

The E(FEFK)$_2$ hydrogel dissolved in water after 10 days (Fig. 5.7C), indicating that its network structure was easily disrupted. As the water on the top of the hydrogels diffused into the hydrogels, the osmotic pressure caused the network to expand which pointing toward weak network crosslinks being present. The charge repulsion forces between the fibres promoted expansion of the network, leading to the swelling behaviour. Loading negatively charged dextran into the E(FEFK)$_2$ hydrogel didn't stabilise the network structure, due to the strong repulsive forces between the negative charge dextran and negative charge hydrogel. In this case, the E(FEFK)$_2$–40kDex sample also dissolved in water. However, when adding 28kPLys a positively charged polymer, the network structure of the E(FEFK)$_2$ hydrogel was stabilised through electrostatic attraction, and a swelling ratio of only ~2% was observed for the E(FEFK)$_2$–28kPLys hydrogel. The attractive electrostatic forces led to further crosslinking of the hydrogel through 28kPLys chains' entanglement and crosslinking with the peptide fibres or the 28kPLys complexed with the peptide fibres, resulting in their negative charge being screened by the positive polymer and reducing the electrostatic repulsion between fibre and stabilising the crosslinks. In either case, the addition of 28kPLys resulted in stabilisation of the E(FEFK)$_2$ hydrogel and an increase in its stiffness (Fig. 5.5A).

The K(FEFK)$_2$ hydrogel had swelled by 31% on day 10. Since the G' of K(FEFK)$_2$ hydrogel was higher than that of E(FKFE)$_2$, the K(FEFK)$_2$ hydrogel formed a more stable network and did not dissolve. The K(FEFK)$_2$–28kPLys hydrogel swelled by 51%, which was much more than the dextran-loaded K(FEFK)$_2$ hydrogels. Furthermore, the positively charged 28kPLys generated an approximately 17% higher swelling ratio, suggesting that charge repulsion can tailor the network of peptide hydrogels. However, the electrostatic repulsion caused by loading

positive charge 28kPLys combined with osmotic pressure in K(FEFK)$_2$ hydrogel manifested as swelling behaviour. For the K(FEFK)$_2$ hydrogels containing dextran, the swelling ratios were lower than for K(FEFK)$_2$ alone. Thus, dextran loading did not create additional swelling (Fig. 5.7B). It clearly explained that the addition of negatively charged dextran reinforced the K(FEFK)$_2$ hydrogel network through charge attraction, making it more stable as seen in the rheological results (Fig. 5.6A).

One point of interest is that the different sizes of dextran caused various swelling levels. The swelling ratio for the K(FEFK)$_2$–3kDex hydrogel was larger than that for the hydrogels containing the two larger sizes of dextran. As the molar concentration of 3kDex was higher than for 40kDex and 2000kDex in these materials, there would be a stronger repulsive force in the K(FEFK)$_2$–3kDex hydrogel. The swelling behaviour thus depended on two factors: one was the charge attraction between K(FEFK)$_2$ and polymers, whilst the other was the size of the polymers.

Taken together, the above results indicate that electrostatic interactions were the major factor in controlling the variation of the peptide hydrogel networks. Different molecules tailored the network properties, and the stability of hydrogels was dependent on the charge interactions.

A)

B)

C)

| No water | Clear gel | Gel-40kDex | Gel-28kPLys |

| Day 0 | Clear gel | Gel-40kDex | Gel-28kPLys |

| Day 10 | K(FEFK)₂ | K(FEFK)₂-40kDex | K(FEFK)₂-28kPLys |

| Day 10 | E(FEFK)₂ | E(FEFK)₂-40kDex | E(FEFK)₂-28kPLys |
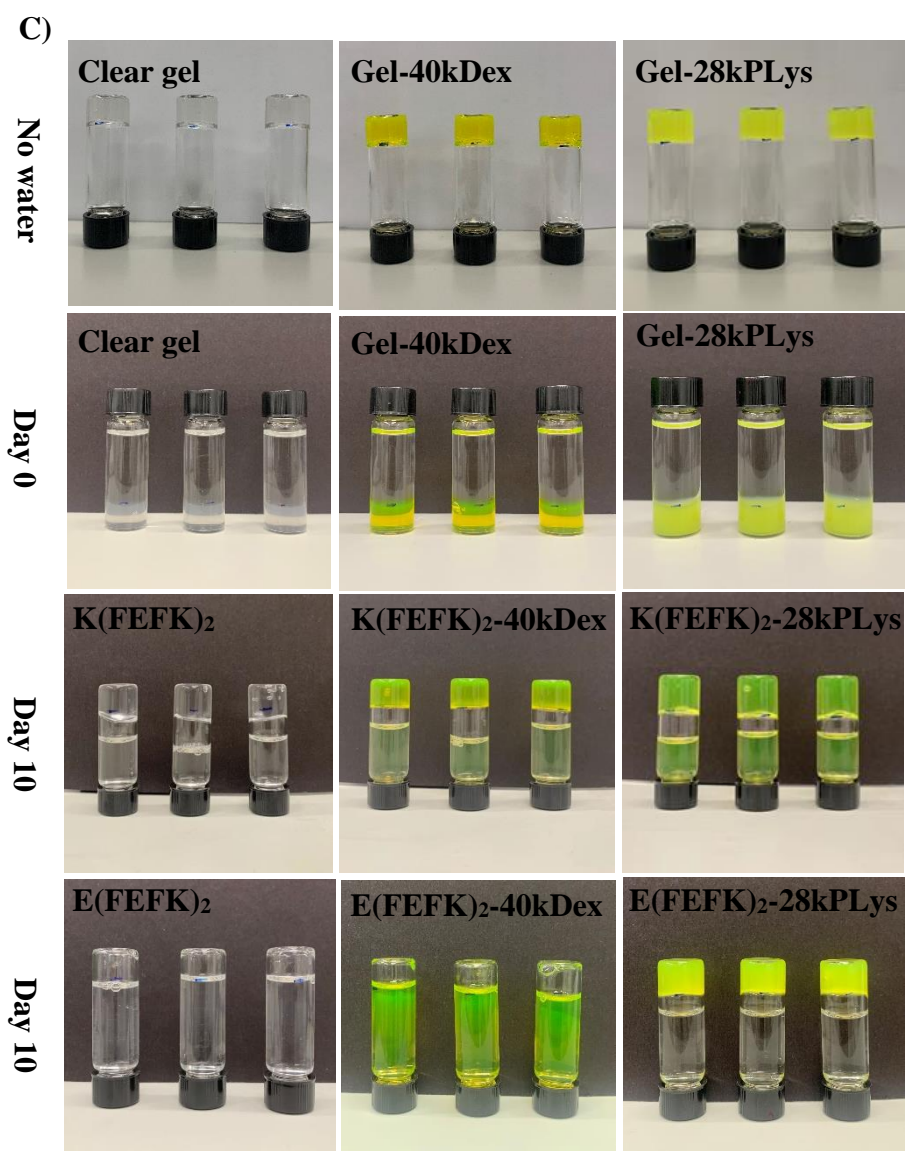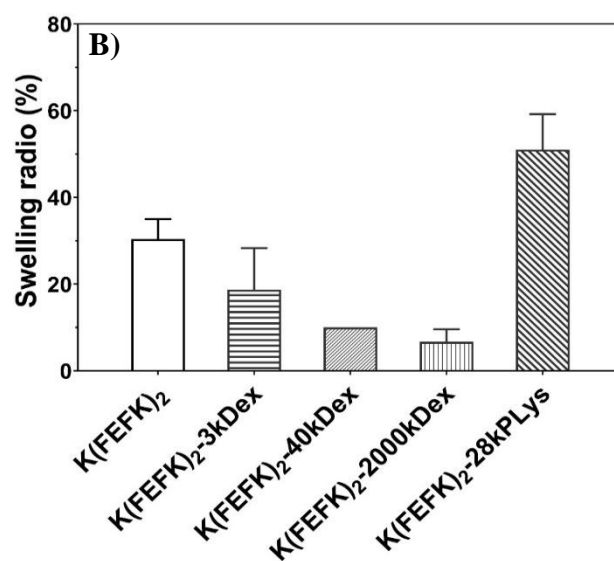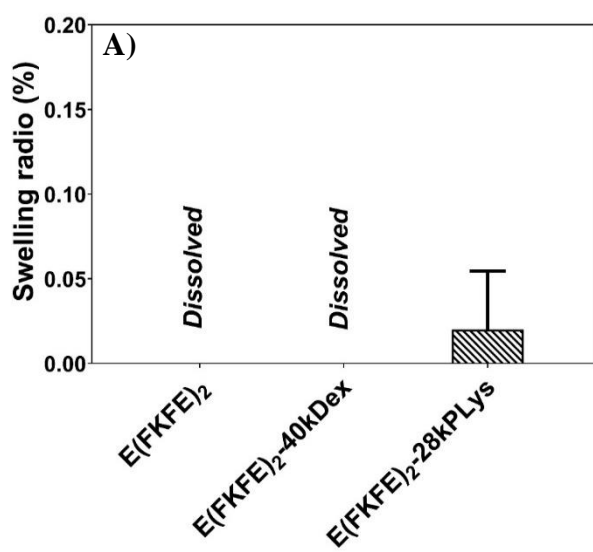
Figure 5. 7 Comparison of swelling ratios between hydrogel and dye-loaded hydrogels after 10 days. A) Swelling ratio of E(FEFK)$_2$ hydrogel and dye-loaded hydrogels. B) Swelling ratio of K(FEFK)$_2$ hydrogel and dye-loaded hydrogels. C) Swelling experiment was performed in 10 days. The first row was the gel without any disruption, the second row was the gel in HPLC grade water on the 1st day, the third row was the swelling state in K(FEFK)$_2$ gel on the 10th day, the fourth row was the swelling state in E(FKFE)$_2$ gel on the 10th day.

5.3.4 Release kinetics of polymers in peptide hydrogel

To investigate the release kinetics of peptide hydrogels, E(FKFE)$_2$ and K(FEFK)$_2$ were self-assembled into the gel state at pH 7, at a concentration of 12 mg/mL, and polymers were encapsulated into these networks as before. The final concentration of polymers in the hydrogels was 0.8 mg/mL, which was chosen according to the standard curves shown in Fig. 5.8. Dextran and poly-L-lysine were diluted to 1.0, 0.8, 0.6, 0.4 and 0.2 mg/mL in HPLC grade water and the absorbance was measured at 505 nm. The absorbance was found to be linear with respect to the concentration of both polymers, with the 0.2 and 0.8 mg/mL concentrations being closest to the line of best fit. Thus, 0.8 mg/mL was used as the encapsulation concentration due to the higher absorbance signal. Also, a higher concentration of polymers in the peptide hydrogels might improve the precision of release kinetics measurements in the early stages. Besides this, the polymers were used at 0.8 mg/mL in the above experiments and it was reasonable to keep the same conditions for this analysis.
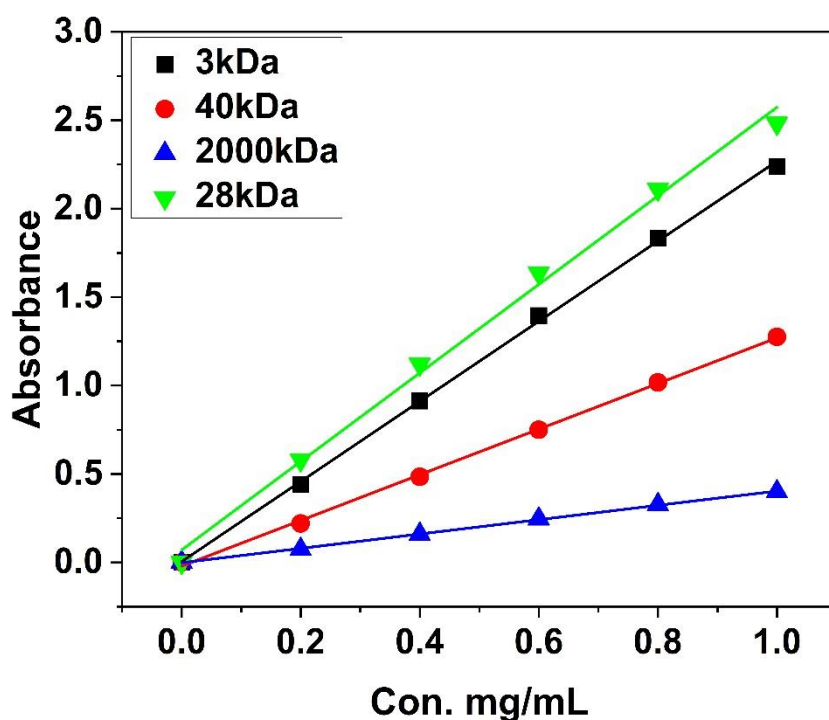
Figure 5. 8 The standard curve of different size of fluorescein dextran and FITC-Poly-L-Lysine at 505 nm. the black square symbol represents 3kDa dextran, the red circle symbol represents 40kDa dextran, the blue regular triangle symbol represents 2000kDa dextran, the green in-verted triangle symbol represents 28kDa Poly-L-Lysine.

In this experiment, the structure of the peptide hydrogel, concentration, charge and the size of polymers were taken into account as relevant factors that might affect the diffusion process. The hydrodynamic radius of each polymer was obtained using FCS, and the results are shown in Table 5.6. The release kinetics of the various polymers from the peptide hydrogels are shown in Fig. 5.9, plotting the mass fraction released (M_t/M_∞) as a function of time (t). The polymers displayed different release rates from differently charged peptide hydrogels.

For the E(FKFE)$_2$ hydrogel, on the one hand, negatively charged dextran was released faster than poly-L-lysine. This might be due to electrostatic repulsion between dextran and the E(FKFE)$_2$ hydrogel, resulting in burst release. Furthermore, the various sizes of dextran

showed apparently different release kinetics. According to Table 5.2, the hydrodynamic radius increased with molecular weight. Thus, polymer size will affect the release profile, meaning that release will be slower the larger the molecular weight of the dextran. On the other hand, positively charged poly-L-lysine was considered to be trapped in the E(FKFE)$_2$ hydrogel, as only a very small amount of polymer was released from the gel. It can be assumed that forces of electrostatic attraction controlled these release kinetics.

In the case of the K(FEFK)$_2$ hydrogel, poly-L-lysine was released more quickly than dextran, again suggesting that charge repulsion promotes faster release. On the contrary, dextran polymers were more stably embedded into the hydrogel. Among above discussions, E(FKFE)$_2$ hydrogel provided a better drug delivery system for the release of macromolecules.
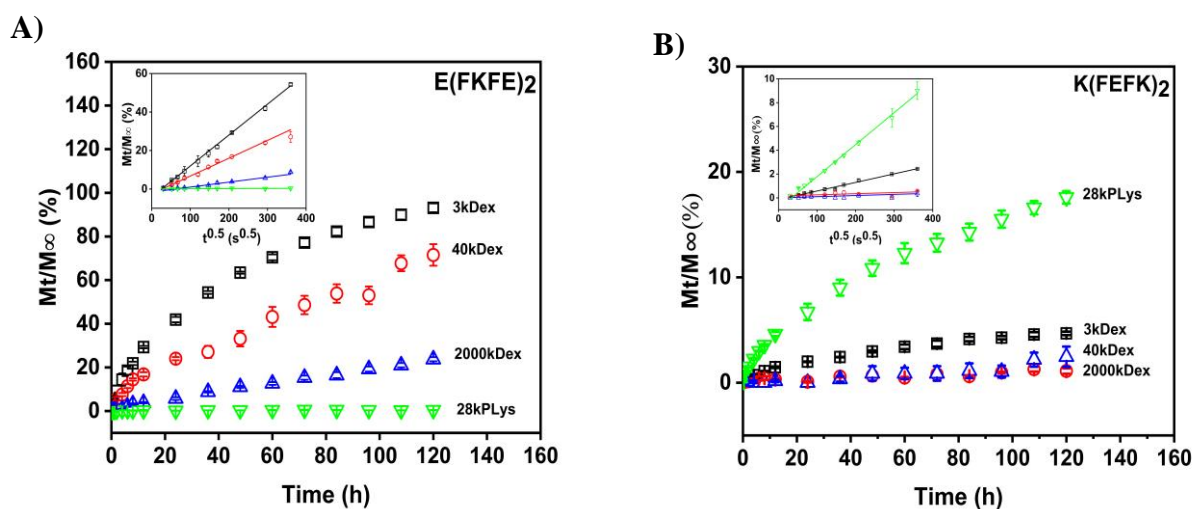
Figure 5. 9 A&B) Release kinetics of dyes from the E(FKFE)$_2$ and K(FEFK)$_2$ peptide hydrogels: the black square symbol represents 3kDa dextran, the red circle symbol represents 40kDa dextran, the blue regular triangle symbol represents 2000kDa dextran, the green inverted triangle symbol represents 28kDa Poly-L-Lysine. The plots show four different dyes release from hydrogel as a function of time. (Insets) Release kinetics of dyes at the first 36h. D$_E$ of dyes

were calculated by a plot of Mt/M∞ as a function of $t^{0.5}$. All the experiments were performed 3 times and error bars represent ± SD.

Table 5. 2 Hydrodynamic radius of polymers and comparisons of diffusion coefficients in water.

	Charge	Hydrodynamic radius (nm)	D_0 $(m^2\,s^{-1})$
3kDex	(-)	1.29	1.66×10^{-10}
40kDex	(-)	6.95	3.07×10^{-11}
2000kDex	(-)	39.48	5.41×10^{-12}
28kPLys	(+)	3.76	5.67×10^{-11}

The diffusion coefficients of the polymers in water were also obtained, denoted as D_0 (Table 5.6). To confirm the role of electrostatic interactions in controlling the kinetics of release from peptide hydrogels, it was necessary to determine the diffusion coefficients of the polymers in the peptide hydrogels. For this purpose, samples were loaded into cylindrical glass vials which served as slab-like devices for calculation. As is apparent from Fig. 5.9, the release of polymers from the hydrogels showed non-steady state diffusion behaviour, which means the concentration changed with respect to time. The release kinetics of polymers from the peptide hydrogels can be defined by the diffusion coefficient D, with D_E and D_L denoting the early-time and late-time values, respectively, obtained using Fick's second law [16][18][19]:

$$\frac{M_t}{M_\infty} = \left(\frac{16Dt}{\pi H^2}\right)^{0.5} \tag{5.5}$$

$$\frac{M_t}{M_\infty} = 1 - \left(\frac{8}{\pi^2}\right) exp\left[-\frac{(\pi^2 Dt)}{h^2}\right] \tag{5.6}$$

Where, M_t and M_∞ represent the mass of polymer released at time t and at saturation, respectively (here, M_∞ is 0.8 mg), and *H* is the thickness of peptide hydrogels in the glass vial [20][21][22]. For early-time release (<60% of total mass), Eq. 5.5 was used; i.e., where $0 < M_t/M_\infty < 0.6$ [23][16][18]. For late-time release, Eq. 5.6 was needed; i.e., where $M_t/M_\infty > 0.6$.

Drug release kinetics have been described by various mathematical models in studies of the mass transport mechanisms involved in controlled release systems. Different models are suitable for different release systems, which is a key consideration to help establish ideal formulations. Thus, optimisation of drug delivery systems can facilitate drug efficacy [24]. Empirical models for drug release kinetics include the Higuchi, Ritger–Peppas, Peppas–Sahlin and zero-order kinetic models [18][25]. Here, the Ritger–Peppas model was used for analysis (Eq. 5.7):

$$\frac{M_t}{M_\infty} = k_1 t^n \tag{5.7}$$

Where, k_1 is the rate constant, *t* is the release time and *n* is the release exponent, which is used to define the mass transport mechanism. For a thin hydrogel film, when *n* = 0.5, the system follows the Fickian diffusion model. When *n* = 1, Case II transport occurs, leading to zero-order release. When $0 < n < 1$ or $0.5 < n < 1$, the system displays non-Fickian diffusion [26]. In addition, the model is applicable when the mass fraction released is ≤60% [19].

The Ritger–Peppas model was applied to the data above to calculate D_E, assuming *n* = 0.5, to produce the insets shown in panels A and B of Fig. 5.9 [19][20][27][28]. As the peptide hydrogels were considered to experience no mass loss in 5 days, the time points collected from release experiments were fitted to Eq. 5.5 and Eq. 5.6 to derive values for D_E and D_L, respectively [18]. The results for D_E are presented in Table 5.3, and show that early-time diffusion was dependent on the size of polymer and its charge interactions with the hydrogel. Compared with D_0 (Table 5.2), measured in water, the D_E values of the polymers in peptide

hydrogels were smaller. Therefore, electrostatic interactions in the peptide hydrogel affected the release of polymers, leading to a controlled release system. Furthermore, when the polymers are retained in the peptide hydrogel through charge attraction, the goodness of fit (R^2) might not be as high, as shown for E(FKFE)$_2$–28kPLys (0.647) and K(FEFK)$_2$–40kDex (0.404).

Table 5. 3 Comparison of diffusion coefficients for different dyes in E(FKFE)$_2$ and K(FEFK)$_2$ hydrogels after 5 days.

Probe	Charge	E(FKFE)$_2$- D_E (m^2 s^{-1})	E(FKFE)$_2$- Intercept	E(FKFE)$_2$ - R^2	K(FEFK)$_2$- D_E (m^2 s^{-1})	K(FEFK)$_2$- Intercept	K(FEFK)$_2$ - R^2
3kDex	(-)	$(4.07 \pm 1.88$ E-5) $\times$ 10^{-11}	(-4.05 ± 0.23) E-2	0.999	$(7.79 \pm 2.74$ E-6) $\times 10^{-14}$	(-14.8 ± 5) E-2	0.989
40kDex	(-)	$(1.29 \pm 2.76$ E-5) $\times$ 10^{-11}	(-2.56 ± 0.32) E-2	0.993	$(1.29 \pm 3.99$ E-6) $\times$ 10^{-15}	(15.4 ± 9.92) E-2	0.292
2000kDex	(-)	$(6.36 \pm 2.25$ E-5) $\times$ 10^{-13}	(-1.56 ± 0.31) E-2	0.942	$(1.02 \pm 8.56$ E-7) $\times$ 10^{-15}	(-0.163 ± 2.01) E-2	0.977
28kPLys	(+)	$(7.79 \pm 1.9$ E-6)$\times$ 10^{-16}	(7.28 ± 3.64) E-4	0.647	$(6.35 \pm 4.85$ E-6) $\times$ 10^{-13}	(-8.99 ± 2) E-1	0.993

In addition, it was possible to derive D_L for 3kDex and 40kDex loaded into the E(FKFE)$_2$ hydrogel, since >60% of the mass was released in 5 days. The observed D_L values were 4.24×10^{-7} for 3kDex ($R^2 = 0.936$) and 1.98×10^{-7} ($R^2 = 0.863$) for 40kDex. These D_L results were obtained by plotting $\ln\left(1 - \frac{M_t}{M_\infty}\right)\left(\frac{\pi^2}{8}\right)$ versus time. For these two smaller size dextran polymers, the release rates were increased with respect to time, which might indicate that the sizes were smaller than the mesh size of the peptide hydrogel.

To probe the effect of hydrogel density on the release process, different concentrations of E(FKFE)$_2$ hydrogel were used to measure release of 40kDex. As shown in Fig. 5.10, ~72% of the dextran diffused out of the 12mg/mL gel, and ~69% from the 25 mg/mL gel. Thus, similar

release kinetics were observed for 40kDex at these gel concentrations. For the 50 mg/mL gel, the higher density of the network hindered release since only ~49% of the dextran had diffused out after 5 days; less than for the other two peptide concentrations. The corresponding D_E values were obtained from the plots in Fig. 5.10 (inset), and are included in Table 5.4.

For all of the above results, the Higuchi model was the most suitable for our peptide systems, with R^2 values tending towards 1. The release profiles relied on the electrostatic interactions, the molecular size of the polymer, and the density of the peptide hydrogel [23]. However, in the case of E(FKFE)$_2$–40kDex, the density of the network did not show a significant impact on the controlled release kinetics.
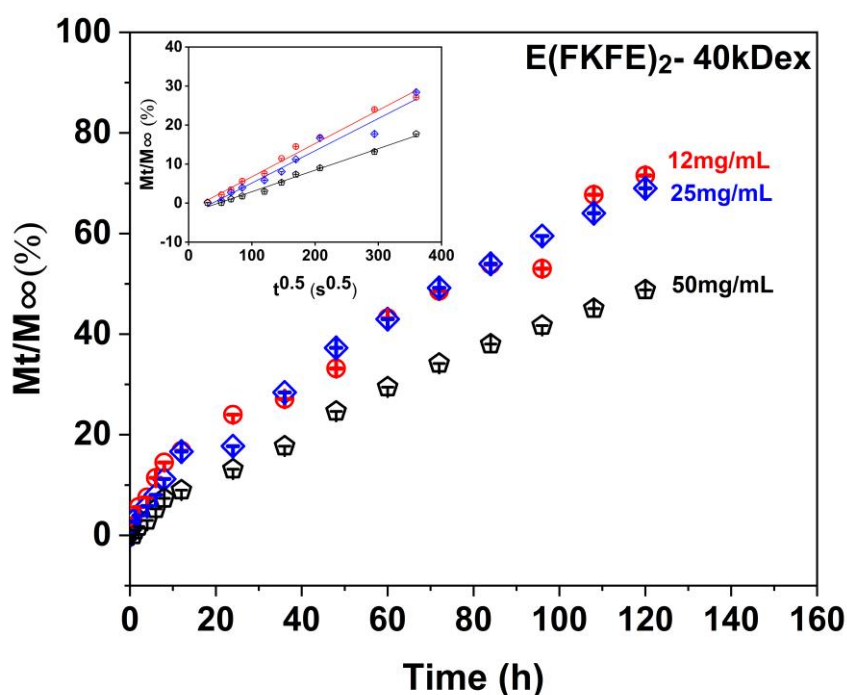
Figure 5. 10 Release kinetics of 40kDa dextran release out from different concentrations of E(FKFE)$_2$ hydrogel: the red circle symbol represents dextran release out from 12mg/mL of E(FKFE)$_2$ hydrogel, the blue rhombus symbol represents dextran release out from 25 mg/mL of E(FKFE)$_2$ hydrogel, the black pentagon symbol represents dextran release out from 50

mg/mL of E(FKFE)$_2$ hydrogel. The plots show dextran release from hydrogel as a function of time. (Insets) Release kinetics of dyes at the first 36h. D$_E$ of dyes were calculated by a plot of Mt/M∞ as a function of t$^{0.5}$. All the experiments were performed 3 times and error bars represent ± 1 SD.

Table 5. 4 Comparison of diffusion coefficients (m^2 s^{-1}) for 40kDa dextran in different concentrations of E(FKFE)$_2$ hydrogels after 5 days.

Con. (mg/mL)	D$_E$ (m^2 s^{-1})	Intercept	R^2
12	(1.29 ± 3.99 E-6) ✕ 10^{-11}	(-2.56 ± 0.32) E-2	0.993
25	(1.29 ± 3.24 E-5) ✕ 10^{-11}	(-2.61E-2 ± 0.18) E-2	0.989
50	(3.97 ± 2.93 E-5) ✕ 10^{-12}	(-1.84E-2 ± 0.27) E-2	0.975

5.4 Conclusion

In conclusion, the β-sheet structure of self-assembled peptide hydrogels was not disrupted by loading them with macromolecules. The parallel and antiparallel β-sheet bands were still detected by ATR-FTIR for polymer-loaded hydrogels. The charge of polymers and peptides was measured by zeta potential, and corresponded well with theoretical values: E(FKFE)$_2$ and dextran were negative, whereas K(FEFK)$_2$ and poly-L-lysine were positive. From the TEM results, it was seen that the hydrogel fibres were distributed randomly to produce different network densities, according to the charge interactions. A more homogenous network with smaller FWHM was seen for E(FKFE)$_2$–28kPLys and K(FEFK)$_2$–40kDex. In addition, apparently upturned curves were observed in the SAXS results for these two systems. This can be explained in terms of charge attraction and its effect on the structure of hydrogels.

In rheology experiments, the mechanical properties could be related to other characteristics of the various peptide hydrogel systems. For example, E(FKFE)$_2$–28kPLys and K(FEFK)$_2$–Dex showed higher G′, illustrating the point that the stiffness of hydrogels depends on electrostatic interactions in these systems. There was no significant difference between unloaded hydrogels and those with electrostatic repulsion between the peptide and polymer, suggesting that in these cases, the network structure was not influenced by the repulsion. This assumption was validated by SAXS, where the curves for hydrogel systems with electrostatic repulsion displayed the same trend as unloaded gels. Their networks consisted of long, thin rod-like fibres, which mirrors the results reported in Chapter 4. Furthermore, the swelling assay results showed that different molecules adjusted the network structure of hydrogels, and the stability of the hydrogel was related to the charge of these molecules. Electrostatic interactions were the main factor in controlling the variation of network morphology.

The diffusion coefficient D_0 and hydrodynamic radius were measured experimentally for the various polymers, as a precursor to the release study. Comparing the results for D_0 and D_E revealed that the peptide hydrogel systems can achieve controlled release of macromolecules through electrostatic interactions. Based on the hydrodynamic radii of these macromolecules, it can also be concluded that their size determines the release kinetics from peptide hydrogels. Thus, increasing the network density to control the release of a smaller polymer is another feasible approach when designing drug delivery systems based on peptide hydrogels. Both E(FKFE)$_2$ and K(FEFK)$_2$ hydrogels can successfully encapsulate macromolecules with controllable release kinetics by adjusting their network structures. Hence, these materials could potentially be applied to deliver peptide and protein therapeutics efficiently.

5.5 References

[1]   P. Worthington, S. Langhans, and D. Pochan, "β-hairpin peptide hydrogels for package delivery," *Advanced Drug Delivery Reviews*. 2017. doi: 10.1016/j.addr.2017.02.002.

[2]   Y. Zhu *et al.*, "Injectable pH and redox dual responsive hydrogels based on self-assembled peptides for anti-tumor drug delivery," *Biomaterials Science*, 2020, doi: 10.1039/d0bm01004a.

[3]   V. V. Ranade and M. A. Hollinger, *Drug delivery systems*. 2003. doi: 10.9774/gleaf.9781315302317-14.

[4]   J. Liu, L. Zhang, Z. Yang, and X. Zhao, "Controlled release of paclitaxel from a self-assembling peptide hydrogel formed in situ and antitumor study in vitro.," *Int J Nanomedicine*, 2011, doi: 10.2147/ijn.s24038.

[5]   A. Altunbas, S. J. Lee, S. A. Rajasekaran, J. P. Schneider, and D. J. Pochan, "Encapsulation of curcumin in self-assembling peptide hydrogels as injectable drug delivery vehicles," *Biomaterials*, 2011, doi: 10.1016/j.biomaterials.2011.04.069.

[6]   D. Wöll, "Fluorescence correlation spectroscopy in polymer science," *RSC Advances*. 2014. doi: 10.1039/c3ra44909b.

[7]   C. Ligorio *et al.*, "Graphene oxide containing self-assembling peptide hybrid hydrogels as a potential 3D injectable cell delivery platform for intervertebral disc repair applications," *Acta Biomaterialia*, 2019, doi: 10.1016/j.actbio.2019.05.004.

[8]   J. B. Guilbaud and A. Saiani, "Using small angle scattering (SAS) to structurally characterise peptide and protein self-assembled materials," *Chemical Society Reviews*. 2011. doi: 10.1039/c0cs00105h.

[9]   J. Filik *et al.*, "Processing two-dimensional X-ray diffraction and small-angle scattering data in DAWN 2," *Journal of Applied Crystallography*, 2017, doi: 10.1107/S1600576717004708.

[10]   P. Markland, Y. Zhang, G. L. Amidon, and V. C. Yang, "A pH- and ionic strength-responsive polypeptide hydrogel: Synthesis, characterization, and preliminary protein release studies," *Journal of Biomedical Materials Research*, vol. 47, no. 4, pp. 595–602, 1997, doi: 10.1002/(SICI)1097-4636(19991215)47:4<595::AID-JBM17>3.0.CO;2-I.

[11]   T. Peng, K. de Yao, C. Yuan, and M. F. A. Goosen, "Structural changes of pH-sensitive chitosan/polyether hydrogels in different pH solution," *Journal of Polymer Science Part A: Polymer Chemistry*, vol. 32, no. 3, pp. 591–596, 1994, doi: 10.1002/pola.1994.080320322.

[12]   S. Wöhl-Bruhn, A. Bertz, S. Harling, H. Menzel, and H. Bunjes, "Hydroxyethyl starch-based polymers for the controlled release of biomacromolecules from hydrogel microspheres," *European Journal of Pharmaceutics and Biopharmaceutics*, vol. 81, no. 3, pp. 573–581, 2012, doi: 10.1016/j.ejpb.2012.04.017.

[13]   Z. Hamrang, A. Pluen, E. Zindy, and D. Clarke, "Raster image correlation spectroscopy as a novel tool for the quantitative assessment of protein diffusional behaviour in solution," *Journal of Pharmaceutical Sciences*, vol. 101, no. 6, pp. 2082–2093, 2012, doi: 10.1002/jps.23105.

[14]   C. B. Müller *et al.*, "Precise measurement of diffusion by multi-color dual-focus fluorescence correlation spectroscopy," *Epl*, vol. 83, no. 4, 2008, doi: 10.1209/0295-5075/83/46001.

[15]   M. C. Branco, D. J. Pochan, N. J. Wagner, and J. P. Schneider, "Macromolecular diffusion and release from self-assembled β-hairpin peptide hydrogels," *Biomaterials*, 2009, doi: 10.1016/j.biomaterials.2008.11.019.

[16]   Y. Nagai, L. D. Unsworth, S. Koutsopoulos, and S. Zhang, "Slow release of molecules in self-assembling peptide nanofiber scaffold," *Journal of Controlled Release*, 2006, doi: 10.1016/j.jconrel.2006.06.031.

[17]   F. Raza *et al.*, "Paclitaxel-loaded pH responsive hydrogel based on self-assembled peptides for tumor targeting," *Biomaterials Science*, 2019, doi: 10.1039/c9bm00139e.

[18]   Y. Fu and W. J. Kao, "Drug release kinetics and transport mechanisms of non-degradable and degradable polymeric delivery systems," *Expert Opinion on Drug Delivery*. 2010. doi: 10.1517/17425241003602259.

[19]   L. Serra, J. Doménech, and N. A. Peppas, "Drug transport mechanisms and release kinetics from molecularly designed poly(acrylic acid-g-ethylene glycol) hydrogels," *Biomaterials*, 2006, doi: 10.1016/j.biomaterials.2006.06.011.

[20]   C. M. Hansen, "Diffusion in polymers," *Polymer Engineering & Science*, 1980, doi: 10.1002/pen.760200405.

[21]   N. Vahdat and V. D. Sullivan, "Estimation of permeation rate of chemicals through elastometric materials," *Journal of Applied Polymer Science*, 2001, doi: 10.1002/1097-4628(20010214)79:7<1265::AID-APP140>3.0.CO;2-H.

[22]   J. Siepmann, A. Ainaoui, J. M. Vergnaud, and R. Bodmeier, "Calculation of the dimensions of drug-polymer devices based on diffusion parameters," *Journal of Pharmaceutical Sciences*, 1998, doi: 10.1021/js980006a.

[23]   S. Koutsopoulos, L. D. Unsworth, Y. Nagai, and S. Zhang, "Controlled release of functional proteins through designer self-assembling peptide nanofiber hydrogel scaffold," *Proc Natl Acad Sci U S A*, 2009, doi: 10.1073/pnas.0807506106.

[24]   J. Siepmann and N. A. Peppas, "Mathematical modeling of controlled drug delivery," *Advanced Drug Delivery Reviews*. 2001. doi: 10.1016/S0169-409X(01)00111-9.

[25]   "Mathematical models of drug release," in *Strategies to Modify the Drug Release from Pharmaceutical Systems*, 2015. doi: 10.1016/b978-0-08-100092-2.00005-9.

[26]   N. A. Peppas and J. J. Sahlin, "A simple equation for the description of solute release. III. Coupling of diffusion and relaxation," *International Journal of Pharmaceutics*, 1989, doi: 10.1016/0378-5173(89)90306-2.

[27]   T. Higuchi, "Mechanism of sustained-action medication," *J Pharm Sci*, 1963, doi: 10.1002/jps.2600521210.

[28]   S. Koutsopoulos and S. Zhang, "Two-layered injectable self-assembling peptide scaffold hydrogels for long-term sustained release of human antibodies," *Journal of Controlled Release*, 2012, doi: 10.1016/j.jconrel.2012.03.014.

Chapter 6 Encapsulation of recombinant human interleukin 2/21 (rhIL-2/21) cytokine in peptide hydrogel for the activity assessment

6.1 Introduction

Peptide hydrogels are able to encapsulate macromolecules without disrupting their secondary structure. Controllable release of model macromolecules from the E(FKFE)$_2$ and K(FEFK)$_2$ hydrogels has been demonstrated, as reported in Chapter 5, and was found to depend on electrostatic interactions and network density.

This chapter describes the encapsulation of two protein drugs, recombinant human interleukin-2 and interleukin-21 (rhIL-2/21), into hydrogels for a controlled release study. Interleukin-2 (IL-2) is a protein with a four-helix bundle. It is mainly derived from activated T cells, and is therefore sometimes referred to as T-cell growth factor (TCGF), but can also be secreted from natural killer (NK) cells and dendritic cells (DC). Interleukin-2 receptors (IL2Rs) are expressed on the surface of B cells, T cells, NK cells and other lymphocyte subsets [1]. The IL-2 cytokine binds to its receptors on these cell types: B cells, NK cells, tumour-infiltrating lymphocytes (TILs), monocytes, and T cells including regulatory T cells (Tregs) to mediate their activities. It should also be noted that IL-2 modulates effector T cells and memory T cells [2]. Furthermore, there are three known subtypes of IL2R, which are classified as either low affinity (IL2Rα, K_d ~10^{-8} M), intermediate affinity (IL2Rβ, K_d ~10^{-9} M) or high affinity (IL2Rγ, K_d ~10^{-11} M) receptors. Binding of IL-2 to these various receptor subunits induces differential activation of specific signalling pathways (JAK/STAT, RAS/MAPK or PI3K/AKT). Due to the importance of these pathways in tumorigenesis, IL-2 has been successfully applied in cancer immunotherapy [1][3].

Interleukin-21 (IL-21) was discovered more recently, in 2000, and is part of the same type I cytokine family as IL-2. It also has a four-helix bundle structure, and is mainly produced by activated CD4$^+$ cells and natural killer T (NKT) cells [2][4][5]. The IL-21 receptor (IL-21R) was found to form a complex with the IL2Rγ chain, which is able to signal as a heterodimeric complex, characterising IL-21 as a γ-chain cytokine [6]. In fact, since its initial discovery, IL2Rγ has been identified as an essential subunit in the receptor complexes for a number of interleukins. Therefore, it is now known as cytokine receptor common subunit gamma.

Functionally, IL-21 is a helper cytokine that amplifies the immune response. Binding to the IL-21R/IL2Rγ receptor complex activates pathways including JAK/STAT, PI3K/AKT and MAPK signalling [7]. In this way, IL-21 is able to mediate the activities of B cells, NK cells, cytotoxic CD8$^+$ T cells, activated CD4$^+$ T cells, macrophages and dendritic cells (Fig. 6.1) [8][9][10]. In recent years, many researchers have been interested in studying activation of these immune cell types for cancer immunotherapy [11][12]. For example, Mazda and co- workers examined IL-21 in a mouse model of head and neck squamous cell carcinoma (HNSCC) to evaluate immune responses and antitumour activity [13]. After dosing with IL-21, increased production of a specific IgG against SCCVII (the murine squamous cell carcinoma cell line used in the model) demonstrated that IL-21 was specifically able to activate B cells without any side effects.

Although IL-2 and IL-21 have both shown potential as cancer immunotherapies, their efficacy as drug treatments is limited by short half-life [14]. In this work, rhIL-2 and rhIL-21 were used to evaluate the drug retention capacity of different peptide hydrogels. Both cytokines have a similar effect on the immune system, as well as a molecular weight of around 15 kDa, meaning they are similar in size to the model drug molecules (dextran and poly-L-lysine) used in Chapter 5. Compared with rhIL-2, a higher amount

of active rhIL-21 was found to remain in the gels for an extended period (3–9 days), which indicated good drug retention capacity for the peptide hydrogels. Controlled release kinetics of rhIL-21 from the E(FKFE)$_2$ hydrogel over 21 days showed the potential for this system to prolong drug exposure, promoting improved efficacy. Similarly, the Freudenberg group has established that encapsulation of cytokines in hydrogels increases their retention time, stability and efficacy [15]. The methods for encapsulation and release used in this work are described in detail below. In preliminary cellular experiments, human peripheral blood mononuclear cells (PBMCs) were used for studying cell marker (CD4, CD8, CD56) expression after dosing with rhIL-21.
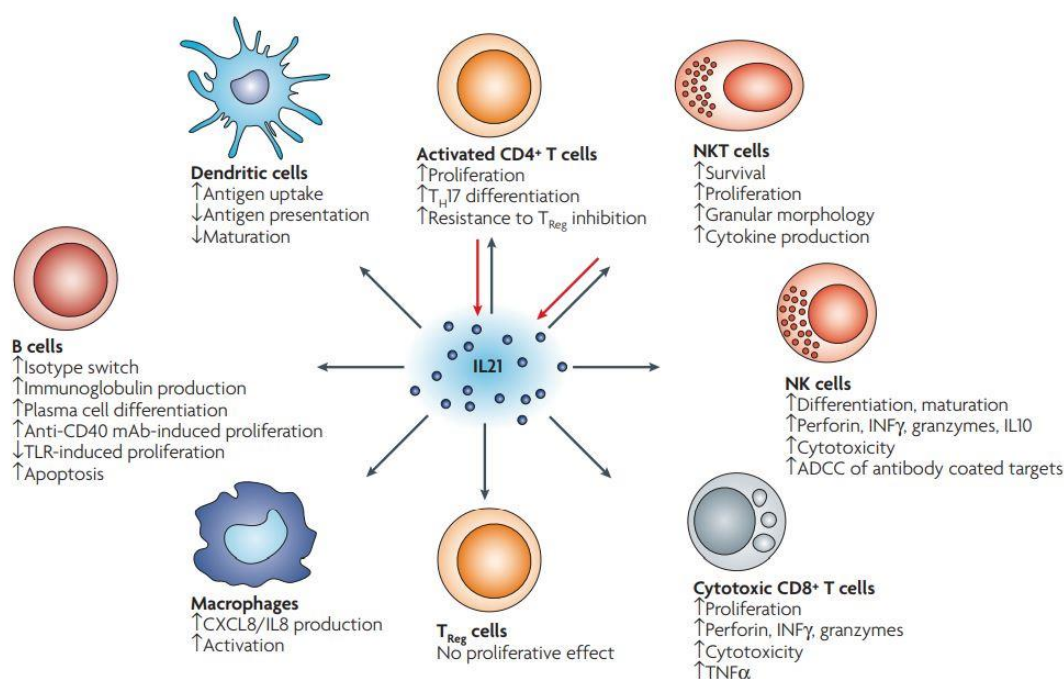
Figure 6. 1 IL-21 has pleiotropic effects on modulating immune response. It can mediate the activities of lymphocyte subsets [5].

6.2 Experimental methods

6.2.1 Encapsulation of rhIL-2/21 in peptide hydrogel

Recombinant human IL-2/21 was purchased from Bio-Techne as a lyophilised powder. It was reconstituted in PBS containing 0.1% bovine serum albumin (BSA) at a final concentration of 100 μg/mL. Peptide hydrogels were prepared at 12 mg/mL concentration and pH 7 (adjusted by addition of 0.5 M NaOH), then divided into 100 μL aliquots in microcentrifuge tubes. The reconstituted rhIL-2/21 solution was mixed into the hydrogel, then the samples were placed at 4 °C in the fridge overnight [16][17].

6.2.2 Enzyme-linked Immunosorbent Assay (ELISA) to test the activity of rhIL-2/21

A Human IL-2/21 DuoSet ELISA Kit, based on the sandwich ELISA method, was purchased from Bio-Techne. Capture antibody (4 μg/mL) was diluted in PBS and used to precoat a 96-well plate. The plate was sealed using an ELISA plate sealer (R&D Systems) then incubated at room temperature overnight. The capture antibody solution was removed from the wells, which were washed three times with 400 μL/well of wash buffer (0.05% Tween-20 in PBS, pH 7.2–7.4). The plate was then dried completely by blotting it against clean paper towels. Then, 300 μL/well of blocking buffer (1% BSA in PBS, pH 7.2–7.4, 0.2 μm filtered) was added into each well, and the plate was incubated for at least 1 h at room temperature. The liquid was aspirated from each well, and three wash steps were performed as above.

An rhIL-2/21 standard curve was also included for reference. Standard solutions were prepared at a series of concentrations (1000, 500, 250, 125, 62.5, 31.3 and 15.6 pg/mL) using dilution reagent (TBS pH 7.2–7.4 with 1% BSA and 0.05% Tween-20, 0.2 μm filtered). The TBS was prepared using 20 mM Tris base (Sigma–Aldrich) and 150 mM

NaCl (Sigma–Aldrich). Samples and standards were added to the plate in duplicate at 100 µL/well, and dilution reagent was also used as a blank group. The aim was to obtain a background reading from these two wells, to increase the accuracy of the results.

The plate was sealed using an adhesive strip, as above, and incubated for 2 h at room temperature. Then, the liquid was aspirated from each well, followed by three further wash steps. The detection antibody was made up at 100 ng/mL in dilution reagent, then added into the assay plate at 100 µL/well. The plate was again sealed by adhesive strip, then incubated for 2 h at room temperature. The liquid was aspirated from each well and three further wash steps were carried out. Next, streptavidin–HRP was diluted 40-fold from stock solution, using dilution reagent, to form a working solution that was added to the assay plate at 100 µL/well. The plate was incubated for 20 min at room temperature in the dark. Once again, the liquid was removed by aspiration followed by three additional wash steps. Substrate solution was prepared by mixing equal volumes of stabilised hydrogen peroxide (colour reagent A) and stabilised 3,3', 5,5'-tetramethylbenzidine (colour reagent B). Subsequently, 100 µL of substrate solution was added into each well, and the plate was incubated for 20 min at room temperature in the dark. Finally, 50 µL of stop solution (2 N sulfuric acid) was added directly into each well. The plate was gently shaken to ensure even mixing, then measured using a plate reader (CLARIOstar). The absorbance wavelength was set as 450 nm, and a background reading at 540 nm was used to correct for optical imperfections in the plate. This protocol was carried out in accordance with the manufacturer's instructions.

6.2.3 Stability of rhIL-2/21 in peptide hydrogel

In this experiment, rhIL-2/21 were added into different concentration of peptide hydrogels to achieve a final concentration of 2 ug/mL to study the activity. Peptide

hydrogels were prepared at 12 and 20 mg/mL. Samples were incubated at 25℃ and 37 ℃. The immunoreactivity of rhIL-2/21 was detected at days 0, 1, 3, 6, and 9 using ELISA method. All experiments were repeated at least three times, to obtain average values with standard deviations.

6.2.4 Stability of rhIL-21 in different concentration of BSA buffer

To find an ideal buffer composition as supernatant for rhIL-21 release from peptide hydrogels, samples were prepared containing different concentrations of BSA in PBS. Specifically, the 100 µg/mL stock solution of rhIL-21 was diluted to give solutions with a final concentration of 10, 5 or 2 µg/mL of rhIL-21 in PBS containing 20%, 10%, 5%, 1% or 0.1% of BSA. These different concentrations of rhIL-21 were prepared in combination with the specified concentrations of BSA, and the solutions were incubated at 37 °C to mimic the environment of the human body. The immunoreactivity of rhIL-21 was measured after 21 days, using the ELISA method described in Section 6.2.2. All experiments were repeated at least three times, to obtain average values and standard deviations.

6.2.5 Release study of rhIL-21 in peptide hydrogel

First, 100 µL aliquots of peptide hydrogel containing rhIL-21 (20 ug/mL), prepared as stated in Section 6.2.1, were dispensed into ThinCert cell culture inserts (Greiner Bio-One) in 24-well plates. Next, 10% BSA buffer (1 mL) was added into each well: 250 µL on top of the hydrogel surface, and the remaining 750 µL into the outer well. This step was the same as in the 3D cell culture protocol. Then, the 1 mL of BSA buffer was collected into a microcentrifuge tube at 15 min, 45 min, 75 min; 2, 4, 6, 8 and 12 h; and every 12 h thereafter. At each time point, after collection of the sample, fresh BSA buffer was added on top of the hydrogel surface and into the outer well, as before (250

μL and 750 μL, respectively). Release of the encapsulated cytokine was followed for 21 days to mimic a controlled release system. Samples were stored at −20 °C in the freezer until analysis, which was carried out using the sandwich ELISA method specified in Section 6.2.2 [18][19]. All experiments were performed in triplicate to obtain mean values with standard deviations.

6.2.6 2D cell culture of PBMCs and dosing with rhIL-21

Peripheral blood mononuclear cells (PBMCs), which consist of lymphocytes, were purchased from Generon to be used for analysis of cell marker (CD56, CD8, CD4) expression after the administration of rhIL-21. Cells were removed from the liquid nitrogen storage dewar and transported on dry ice. The sample was then thawed at 37 °C in a water bath, with gentle agitation, until a small amount of ice remained floating in the middle of the vial. To avoid any potential contamination, 70–80% ethanol was used to sterilise the outside of the vial. Then, 8 mL of RPMI 1640 medium (Gibco), pre-warmed to 37 °C, was added into a 15 mL Falcon tube, and the cells were gently transferred into the tube. The RPMI 1640 medium used contained D-glucose (4.5 g/L), HEPES (2.383 g/L), L-glutamine, sodium bicarbonate (1.5 g/L) and sodium pyruvate (110 mg/L). Another 1 mL of medium was added to the vial then transferred into the Falcon tube, to maximise recovery of the cells. Then, the tube was centrifuged at $400 \times g$ for 10 min. If no cell pellet was visible at the bottom of tube, centrifugation was continued for another 15 min. Once a cell pellet was obtained, the supernatant was discarded and the cells were resuspended in 10 mL of fresh medium, to ensure complete removal of the cryoprotective medium. The sample was centrifuged again at $400 \times g$ for 10 min, then the supernatant was discarded and 1 mL of cell medium was added. The cells were resuspended and counted as follows.

An aliquot of cell suspension was mixed 1:1 (v/v) with 0.4% trypan blue solution (Bio-Rad), then the solution was quickly loaded into the sample chamber of a Cellometer Auto 1000 cell counter (Nexcelom Bioscience), using 20 µL of the mixture for each side of the chamber [20]. Cell viability and concentration were then measured. A viability of around 80–90% indicated that the cells were ready for 2D culture. The PBMCs were diluted to a final concentration of 1×10^7 cells/mL, then seeded into 96-well culture plates at 100 µL/well. Since monocytes or macrophages derived from PBMCs might adhere to the plate, U-bottom 96-well plates were used for culture. The cells were then placed in a 5% CO_2 incubator at 37 °C for at least 2 h [21].

Following this step, the cells were resuspended evenly in the wells by pipetting gently. Different concentrations of rhIL-21 were then diluted into growth medium and added into the wells. Growth medium with no added rhIL-21 was used as a negative control. The plate was subsequently incubated at 37 °C with 5% CO_2 for a dosing period of 4 h [22].

6.2.7 Cell staining

The cell staining protocol used here was described by Gareth J. Howell of the Core Technology Facility, University of Manchester [23]. The fixation solution and FACS buffer were prepared first. The fixation solution consisted of 2% paraformaldehyde (PFA) in PBS, made up by adding PFA powder to $1 \times$ PBS, stirring at 60 °C on a hotplate, and adding 1 N NaOH slowly to raise the pH until a clear solution was obtained. This procedure was carried out in a fume hood. The resultant PFA solution was allowed to cool, then filtered and adjusted to pH 7 with 1 M HCl to give the final 2% PFA fixation solution. The FACS buffer was PBS containing 2.5 mM EDTA and 1% BSA.

For the staining step, all of the antibodies (BD Pharmingen) including APC mouse anti-human CD4, APC mouse IgG1 κ isotype control, FITC mouse anti-human CD8, FITC mouse IgG1 κ isotype control, BV480 mouse anti-human CD56 and BV480 mouse IgG2b κ isotype control were diluted fivefold in FACS buffer to form a working solution. Cells were collected from the 96-well assay plate and transferred into microcentrifuge tubes, then pelleted by centrifugation at 6,000 rpm for 5 min. The supernatant was carefully removed by pipette then the cells were resuspended in FACS buffer (100 μL), centrifuged at 6,000 rpm for 5 min, and the supernatant again removed by pipette. The cells were resuspended in antibody staining solution (100 μL), with gentle pipetting to ensure even mixing. The samples were then incubated on ice in the dark for around 30–60 min. After this, they were centrifuged at 6,000 rpm for 5 min to obtain cell pellets, which were each resuspended in FACS buffer (1 mL) by pipetting gently, and centrifuged as before, then the supernatant was removed. This wash step was repeated three times, and aimed to wash away unbound antibodies [24]. After the last centrifugation step, the supernatant was aspirated carefully and each cell pellet was resuspended in 2% PFA fixation solution (200 μL). Samples were incubated on ice for 15 min then centrifuged at 13,000 rpm for 5 min. The supernatant was removed gently, and finally, each sample was resuspended in 200 μL of FACS buffer. The samples were then stored at 4 °C in the dark, prior to analysis.

6.2.8 Fluorescence – activated cell sorting (FACS) for cell markers expression

Samples were vortexed to ensure efficient mixing, then analysed using a flow cytometer (LSRFortessa X-20 Cell Analyzer, BD Biosciences). For each sample, 50 μL of fixed cell suspension was transferred into a FACS tube followed by addition of a moderate amount of PBS solution. The tube was vortexed to mix the sample evenly, then placed

on the sample holder of the instrument. Cells were then sorted according to specific light scattering and fluorescence characteristics [25].

6.2.9 Statistical data analysis

All experiments were repeated at least three times to obtain an average value, expressed as mean ± standard deviation. The rheological results were analysed in GraphPad Prism 8 using one-way ANOVA and Student's t-test to assess the statistical significance of comparisons via P value [24]. Significance levels are represented as follows: * (P <0.05), ** (P <0.01), *** (P <0.001), **** (P <0.0001), and "ns" indicates there was no significant difference between the two groups.

6.3 Results

6.3.1 Activity of rhIL-2/21 in peptide hydrogel

Both rhIL-2 and rhIL-21 (2 µg/mL) were encapsulated into different concentrations of peptide hydrogel, and their immunoreactivities in the gels were evaluated by ELISA. The results are shown in Fig. 6.2, and reveal that the two cytokines apparently displayed different stabilities in the hydrogels.

At 25 °C, rhIL-2 retained its immunoreactivity in the K(FEFK)$_2$ hydrogels for nine days. However, it was not as stable in the E(FKFE)$_2$ hydrogels. After nine days, only ~50% of the initial amount of rhIL-2 could be detected after mixing into the 12 mg/mL E(FKFE)$_2$ hydrogel, indicating decreased stability in this hydrogel over the duration of the experiment. However, the higher concentration of E(FKFE)$_2$ hydrogel (20 mg/mL) possibly showed enhanced stabilisation of rhIL-2, since ~60% rhIL-2 was detected in this sample on day 9, which is closer to the result on day 0. Thus, rhIL-2 showed variable stability in the peptide hydrogels, which can be explained in terms of the

different properties of the hydrogels. In Chapter 4, the G′ of the positively charged K(FEFK)$_2$ hydrogel was higher than that for the negatively charged E(FKFE)$_2$ hydrogel, and increased concentrations also resulted in a relatively higher G′. Given this, the stability of rhIL-2 in peptide hydrogels might rely on the network density of the gels.

Compared with rhIL-2, rhIL-21 displayed relatively greater stability in E(FKFE)$_2$ hydrogels at 25 °C. The E(FKFE)$_2$ hydrogel evidently showed good encapsulation ability, because a high stability was observed for rhIL-21 in both the 12 and 20 mg/mL hydrogels over nine days. However, no immunoreactive rhIL-21 was detected in the 20 mg/mL K(FEFK)$_2$ hydrogel at day 9, leading to the assumption that it had lost all immunoreactivity.

At 37 °C, rhIL-2 quickly lost most of its activity in E(FKFE)$_2$ hydrogels, as only ~10% of rhIL-2 was detected on day 1. In the K(FEFK)$_2$ hydrogels, rhIL-2 stability exhibited a sharply decreasing trend, which means that K(FEFK)$_2$ hydrogels cannot stabilise rhIL-2 over a long period (nine days) at higher temperature.

For rhIL-21 at 37 °C, stability in the 20 mg/mL K(FEFK)$_2$ hydrogel decreased significantly over nine days. It retained ~60% of activity in the 12 mg/mL K(FEFK)$_2$ hydrogel, which was similar to the same material at 25 °C (~70%). Thus, higher concentrations of K(FEFK)$_2$ hydrogel were unable to support encapsulation of rhIL-21 for a long time. On the contrary, the activity of rhIL-21 was better preserved in E(FKFE)$_2$ hydrogels. When it was encapsulated in the higher concentration E(FKFE)$_2$ hydrogel, over 95% of rhIL-21 activity was detected after nine days.

The overall stability of rhIL-21 in the peptide hydrogels was found to be higher than for rhIL-2. This may be explained by the charge of these two cytokines. The isoelectric point (pI) of rhIL-2 is around 7, while the pI of rhIL-21 is around 9 [26][27]. Therefore,

when rhIL-2 was encapsulated into the peptide hydrogels (at pH = 7), it would be considered to carry no charges, leading to a loss of immunoreactivity. However, when rhIL-21 was encapsulated into the peptide hydrogels, since it carries a negative charge, the cytokine was not adversely affected. Apart from the charge of cytokines, higher temperature may cause the cytokines to lose their immunoreactivities, corresponding to the stability results shown in Fig. 6.2. Moreover, the different charges of the two peptide hydrogels seemingly led to different encapsulation abilities. Therefore, it can be hypothesised that the stability of cytokines in peptide hydrogels depends on the charge characteristics, pH and temperature of the system.
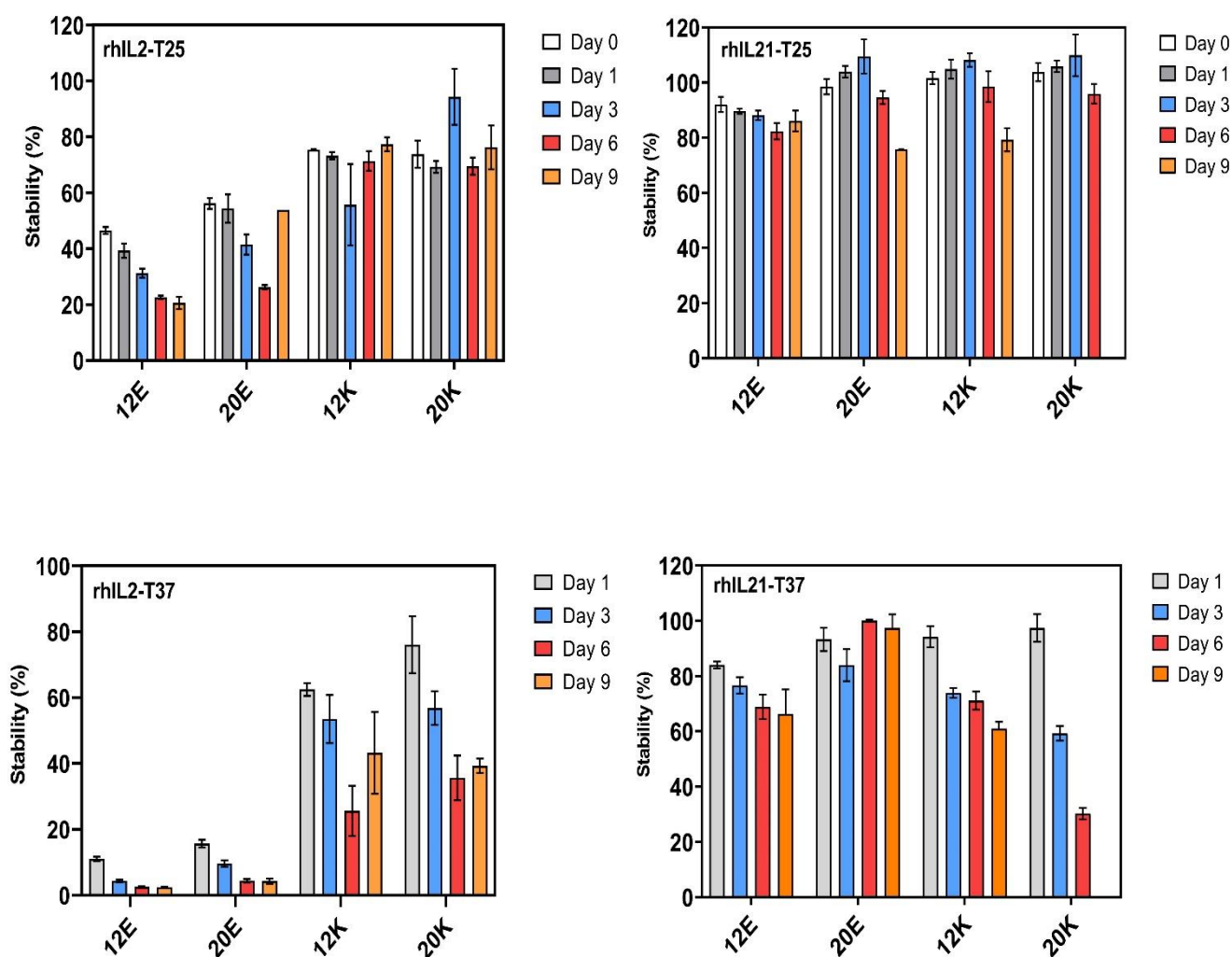
Figure 6. 2 Elisa was used for testing the stability of rhIL-2/21 in different concentration of peptide hydrogels at 25 ℃ and 37℃ incubation. The experiment was proceeded in 9 days.

6.3.2 Determination of the supernatant for the release of rhIL21 in peptide hydrogel

As rhIL-21 retained relatively high immunoreactivity in both the E(FKFE)$_2$ and K(FEFK)$_2$ hydrogels at 12 mg/mL, it was selected as a model encapsulated protein drug for a controlled release study from the peptide hydrogels. First, it was important to identify the ideal supernatant for the experiment. Thus, BSA solutions were prepared at 20%, 10%, 5%, 1% and 0.1% in PBS, and rhIL-21 was diluted into each of these solutions at final concentrations of 10, 5 and 2 µg/mL. The concentrations of rhIL-21 in the BSA solutions were measured by ELISA after incubating for 21 days at 37 ℃ (Fig. 6.3). Compared with the result at day 0, rhIL-21 retained good immunoreactivity in the higher concentrations of BSA buffer at day 21. The immunoreactivity was proportional to the concentration of rhIL-21. The higher the concentration of rhIL-21, the more stable the ELISA reactivity that was observed in BSA (Fig. 6.3D). Therefore, the concentrations of both rhIL-21 and BSA were important factors for the release experiment. Furthermore, since the peptide hydrogels will release rhIL-21 continually, it was necessary to load a higher starting concentration of rhIL-21 into the hydrogels to ensure accurate detection of the amount released during the initial stages.
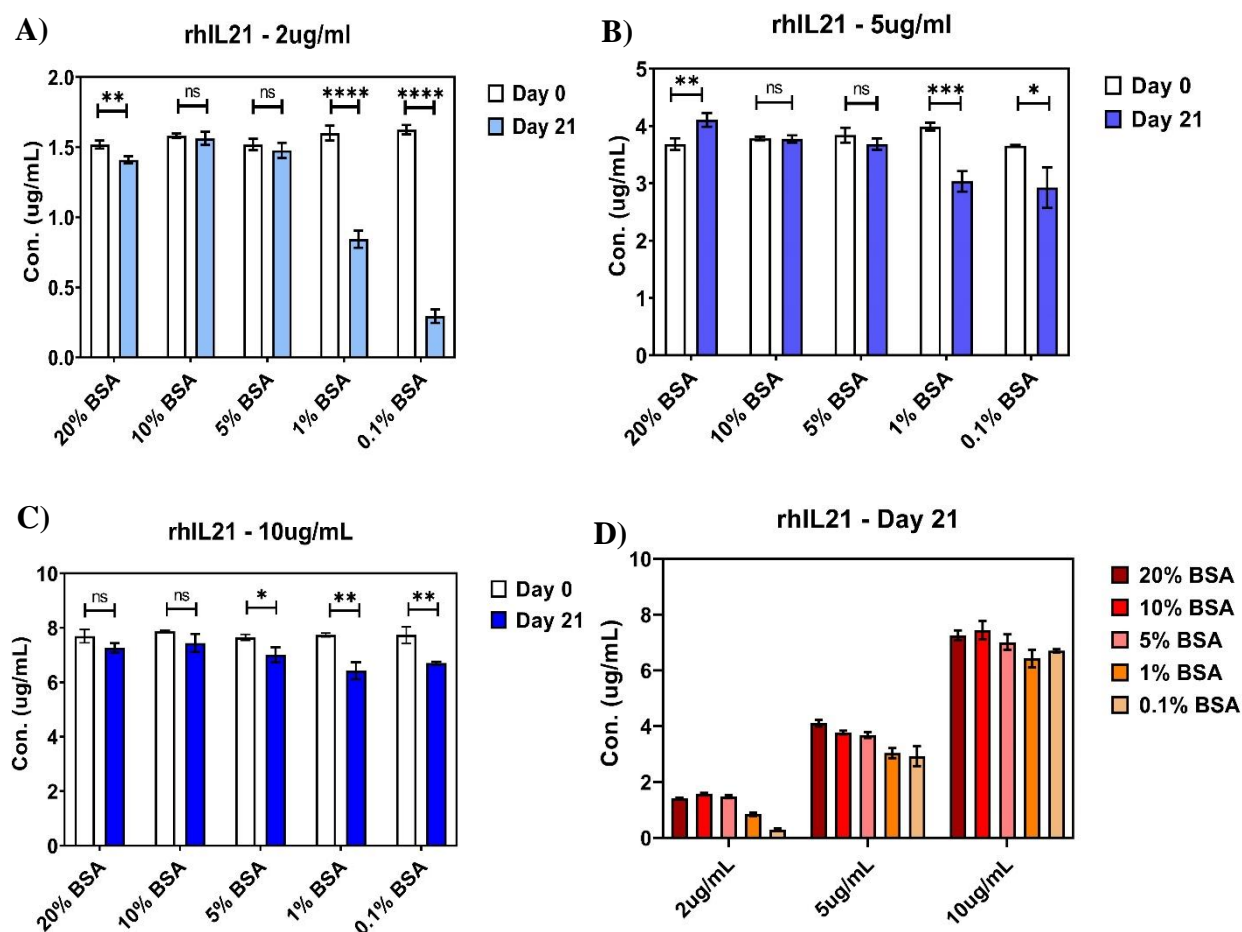
Figure 6. 3 The immunoreactivity of rhIL-21 after 21 days under 37℃ incubation. A) 10 ug/mL rhIL-21 in different concentration of BSA. B) 5 ug/mL rhIL-21 in different concentration of BSA. C) 2 ug/mL rhIL-21 in different concentration of BSA. D) Comparisons of different concentration of rhIL-21 in different concentration of BSA at day 21 (The graph was analysed by student t-test which compared activities of rhIL-21 at day 0 and day 21, p value was indicated as $*p<0.05$, $**p<0.01$, $***p<0.001$, $****$ $p<0.0001$, ns represented there was no significant difference between two groups).

6.3.3 Release kinetics of rhIL21 in peptide hydrogel

Based on the immunoreactivity assessment above, 20 µg/mL of rhIL-21 was encapsulated into 12 mg/mL peptide hydrogels, then release was monitored for 21 days

with quantification by ELISA. A schematic of the setup for this experiment is shown in Fig. 6.4A, and the results for the release kinetics are presented in Fig. 6.4B.

Over the first 40 h, rhIL-21 showed rapid release from the K(FEFK)$_2$ hydrogel, and no active rhIL-21 was subsequently detected in the supernatants. The quantity of rhIL-21 released at each time point is shown in Fig. 6.4B (inset), indicating that no active rhIL-21 was recovered beyond 60 h. This phenomenon corresponded to the results from the stability test of rhIL-21 encapsulated in hydrogels (Fig. 6.2), where the K(FKFE)$_2$ hydrogel exhibited relatively weak retention capacity. This is consistent with the fast release kinetics observed (Fig. 6.4B). Beyond 60 h, it might be that rhIL-21 was released into the supernatant without any drug efficacy, meaning that no signal could be detected by the ELISA method. On the contrary, controlled release of rhIL-21 from the E(FKFE)$_2$ hydrogel over 21 days showed detectable protein at every time point (Fig. 6.4B, inset). As time passed, the measured activity of rhIL-21 decreased, but it can nevertheless be assumed that active rhIL-21 remained in the E(FKFE)$_2$ hydrogel for a long time.

The released quantity of rhIL-21 might be adjustable by varying the original concentration loaded into the hydrogel, and the observed release kinetics from the E(FKFE)$_2$ hydrogel suggest that this material could prolong the half-life of rhIL-21 in vivo. In that case, the dosage time could be reduced to decrease the potential toxicity. The E(FKFE)$_2$ hydrogel showed better retention capacity compared with the K(FKFE)$_2$ hydrogel, according to the detectable release of rhIL-21 over an extended period, indicating that the former is an excellent candidate drug delivery system. Additionally, it can be assumed that both hydrogels are degradable, since they had reduced in volume and were floating in the BSA buffer at the end of the experiment (Fig. 6.4C & Fig.

6.4D). Therefore, these hydrogels could be applied in formulation applications for different types of drugs.
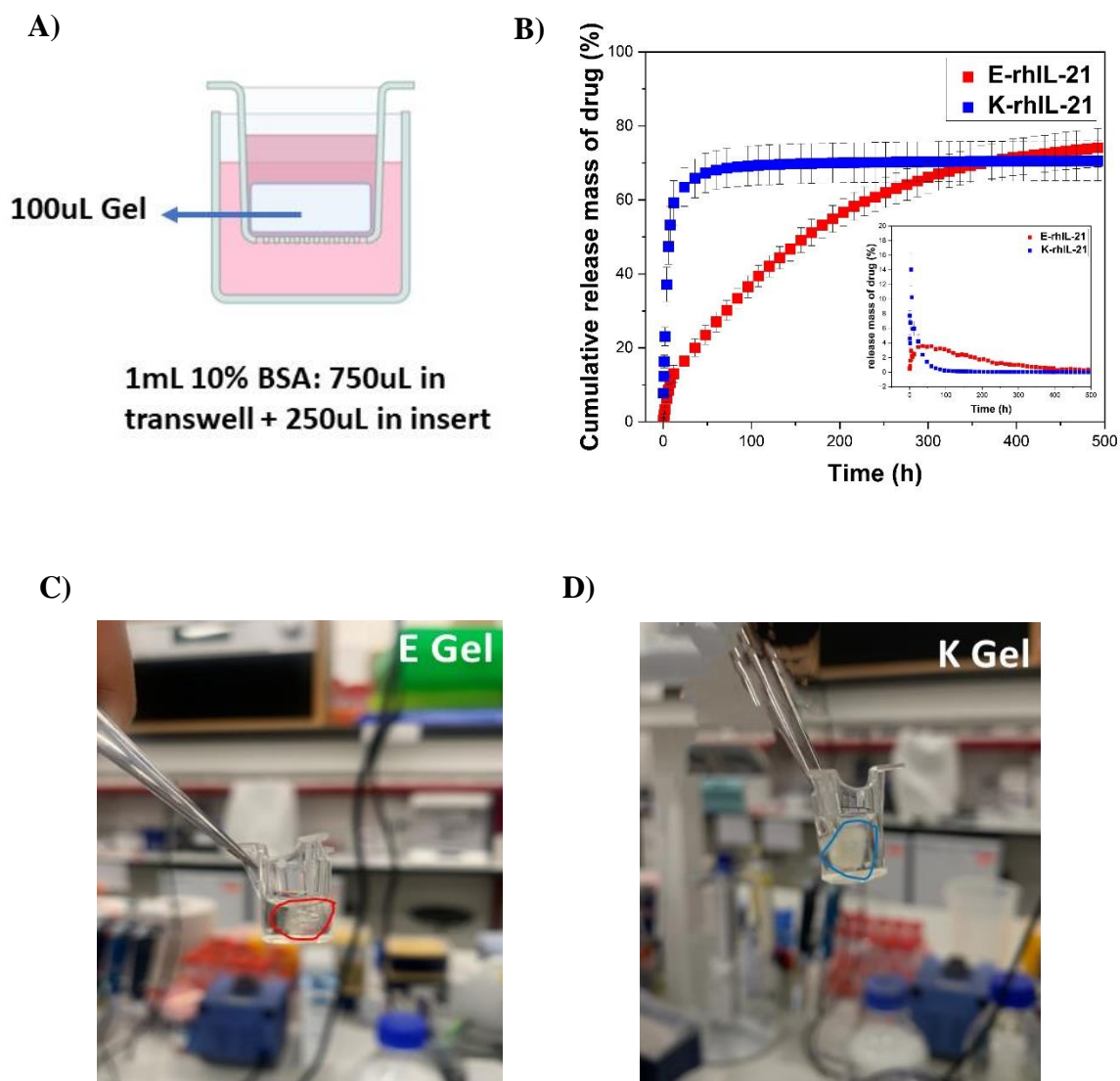
Figure 6. 4 Release of rhIL-21 from peptide hydrogels during 21 days. A) Method for release experiment. B) Release kinetics of rhIL-21 in peptide hydrogels. E-IL21 with red square represented rhIL-21 release from E(FKFE)$_2$ hydrogel, K-IL21 with blue square represented rhIL-21 release from K(FEFK)$_2$ hydrogel. (Inset figure presented the release mass of rhIL-21 at every time point). C&D) E and K gel state in BSA supernatant after 21 days.

6.3.4 Cell marker expression

Expression of cellular markers was analysed by flow cytometry. Human PBMCs were stained using specific fluorophores and sorted based on the light scattering and fluorescence properties of each subset of cells. The intensity of different fluorescence signals represented the expression of cell markers [28].

As can be seen in Fig. 6.5, an initial plot was made using forward scattering area (FSC-A) as the x-axis and side scattering area (SSC-A) as the y-axis (Fig. 6.5A). The size of cells is described by the FSC area, and the intercellular structure is described by the SSC area [29]. Then, gating was used to define different cell types for further characterisation. The gating strategy was based on reviews addressing the phenotyping of immune cell populations in flow cytometry [30][31]. On the plot of FSC-A versus SSC-A, gated lymphocytes are shown as the purple population [32][33]. According to the experiments from other researchers, after isolating the lymphocyte population, the CD4 and CD8 markers were gated and differentiated with the specific fluorophores in lymphocytes [34][35][36]. In the meantime, the total CD56 markers were differentiated and counted using the specific fluorophores. Then the number of CD56$^+$ markers was gated and counted. All the values obtained are detailed in the inset tables (Fig. 6.5). The control group results, without any rhIL-21 dosing, are shown in Fig. 6.5A, whereas Fig. 6.5B shows the results for the treatment group (20 µg/mL rhIL-21). Comparing the tables reveals an increase in the number of CD4$^+$ markers and a slight decrease in CD56$^+$ markers, whereas the number of CD8$^+$ markers was apparently reduced after dosing with rhIL-21(Fig. 6.5C). This suggested that rhIL-21 can selectively stimulate NK cells and T cells, and might potentially be able to target specific tumour cells to suppress their growth [37][38][39].

The above results therefore indicated that 20 µg/mL rhIL-21 has the ability to mediate cell populations in PBMCs. It was only run once as a preliminary validation experiment, so it is necessary to repeat it at least two more times to obtain more accurate results. However, it is feasible to use rhIL-21 loaded hydrogels with PBMCs and selected cancer cell lines to study growth inhibition, cytotoxicity and apoptosis in vitro.

A)
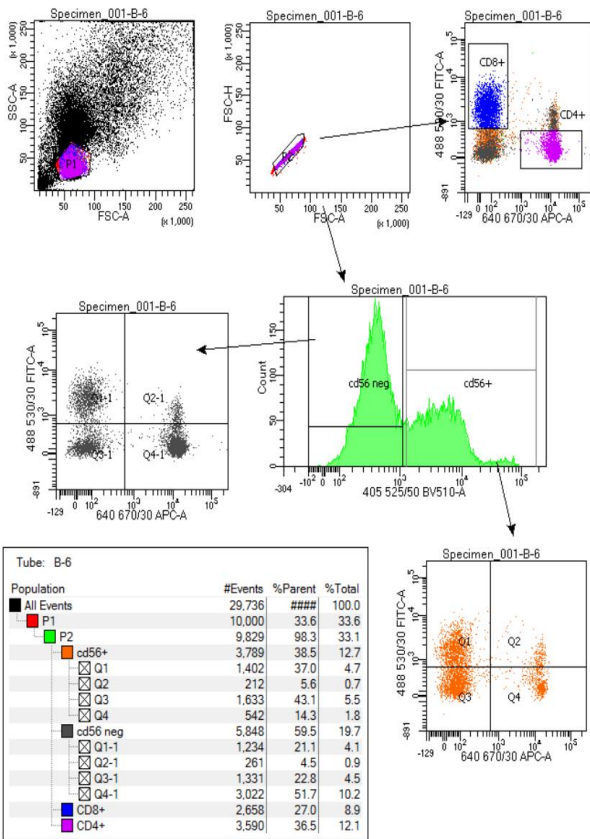
B)
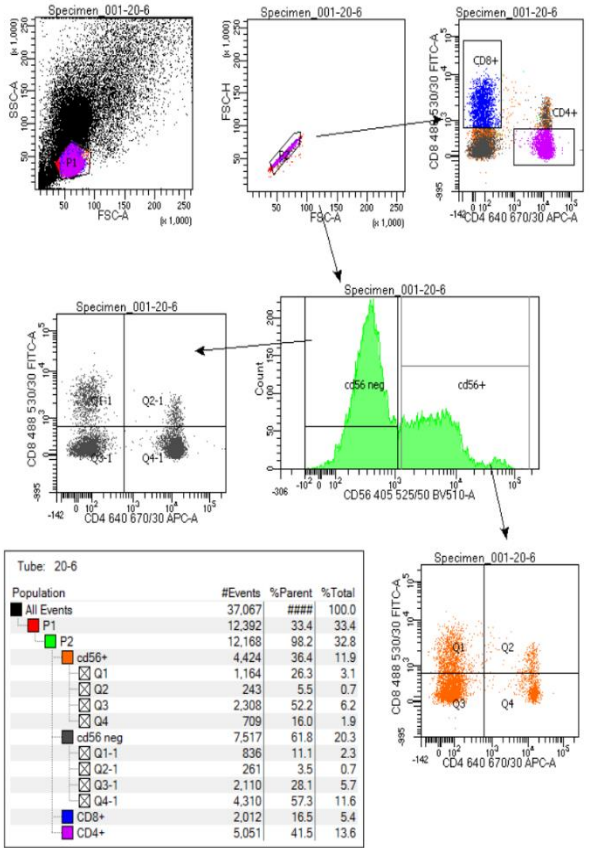
C)
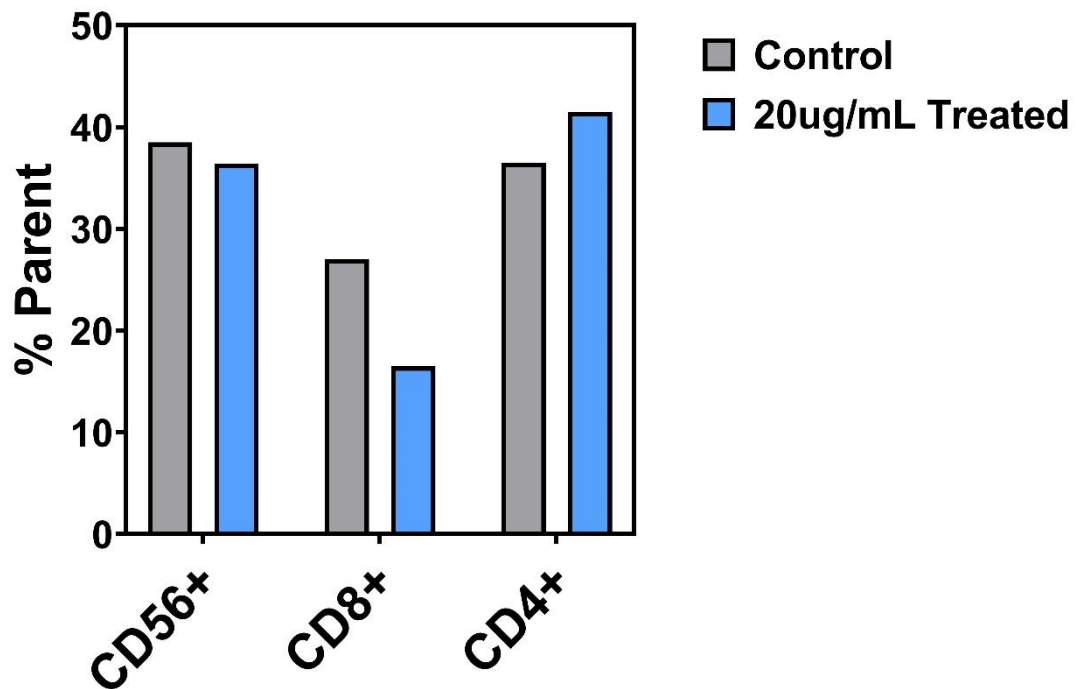
Figure 6. 5 The lymphocytes and their subsets were analysed using FACS [32]. PBMCs were stained with APC/CD4, FITC/CD8 and BV480/CD56 antibodies. The populations of CD4, CD8 and CD56 markers were identified by gating with different colours [34][35][36]. The CD56 markers were counted in a single channel based on the specific fluorophore, then the CD56⁺ markers were gated. A) Cell populations in control group without any dosing. B) Cell populations after dosing with rhIL-21 for 4 hours. C) A comparison of cell markers expression between control group and dosage group.

6.4 Conclusion

Evaluation of rhIL-2 and rhIL-21 stability in E(FKFE)$_2$ and K(FEFK)$_2$ hydrogels revealed that rhIL-21 retained better immunoreactivity over nine days at 37 °C. Furthermore, retention capacity of the peptide hydrogels was found to depend on the charge of the peptide and the particular drug. Before assessment of controlled release, the stability of rhIL-21 was first measured over 21 days, at various concentrations, in supernatant buffers containing different amounts of BSA. Based on the results of this stability study, rhIL-21 was encapsulated into 12 mg/mL peptide hydrogels at 20 µg/mL, and release kinetics were followed for 21 days.

The K(FEFK)$_2$ hydrogel, with overall positive charge, showed a burst release of active rhIL-21 compared with the negatively charged E(FKFE)$_2$ hydrogel, where release was slower. These observations corresponded with earlier results that showed higher stability in the E(FKFE)$_2$ hydrogel. The K(FEFK)$_2$ hydrogel had lower drug retention capacity for rhIL-21, leading to more rapid release of active protein. There might also be some rhIL-21 fractions released from the hydrogel without any activity, and this could be detected by RP-HPLC [40]. The release results characterise this physically cross-linked peptide hydrogel as a distinctive material for encapsulation and targeted delivery of protein drugs.

The effect of rhIL-21 on human PBMCs was assessed by flow cytometry. Cells were dosed then analysed for expression of the CD4, CD8 and CD56 markers. Compared with the control group, 20 µg/mL rhIL-21 apparently increased expression of CD4$^+$ among PBMCs. The high populations of the lymphocyte subset suggest that an appropriate dose of rhIL-21 would activate T cells. The upregulation of specific cell markers induced by rhIL-21 has the potential to promote antitumour activity [6][41].

In summary, this study has clearly demonstrated that drug retention capacity and release kinetics depend on the peptide sequence of the hydrogel, and the specific protein drug. Controlled release of immunoreactive rhIL-21 from peptide hydrogels, therefore assumed to retain its bioactivity, identified these gels as candidate drug delivery systems to prolong drug efficacy and avoid some adverse effects. For example, this approach might decrease drug toxicity due to a smaller number of doses being required [42]. Furthermore, the volume of the peptide hydrogels studied became smaller in BSA buffer, indicating that they are biodegradable materials. Therefore, these peptide hydrogels could possibly be used in injectable formulations for targeted release of rhIL-21 in vivo, to elicit therapeutic immune responses in various cancers.

6.5 References

[1]   T. Jiang, C. Zhou, and S. Ren, "Role of IL-2 in cancer immunotherapy," Oncoimmunology, vol. 5, no. 6, pp. 1–10, 2016, doi: 10.1080/2162402X.2016.1163462.

[2]   S. Mitra and W. J. Leonard, "Biology of IL-2 and its therapeutic modulation: Mechanisms and strategies," J. Leukoc. Biol., vol. 103, no. 4, pp. 643–655, 2018, doi: 10.1002/JLB.2RI0717-278R.

[3]   S. A. Rosenberg et al., "Observations on the Systemic Administration of Autologous Lymphokine-Activated Killer Cells and Recombinant Interleukin-2 to Patients with Metastatic Cancer," New England Journal of Medicine, vol. 313, no. 23. pp. 1485–1492, 1985. doi: 10.1056/nejm198512053132327.

[4]   I. D. Davis, K. Skak, M. J. Smyth, P. E. G. Kristjansen, D. M. Miller, and P. V. Sivakumar, "Interleukin-21 signaling: Functions in cancer and autoimmunity," Clin. Cancer Res., vol. 13, no. 23, pp. 6926–6932, 2007, doi: 10.1158/1078-0432.CCR-07-1238.

[5]   K. Skak, M. Kragh, D. Hausman, M. J. Smyth, and P. V. Sivakumar, "Interleukin 21: Combination strategies for cancer therapy," Nat. Rev. Drug Discov., vol. 7, no. 3, pp. 231–240, 2008, doi: 10.1038/nrd2482.

[6]   H. Søndergaard and K. Skak, "IL-21: Roles in immunopathology and cancer therapy," Tissue Antigens, vol. 74, no. 6, pp. 467–479, 2009, doi: 10.1111/j.1399-0039.2009.01382.x.

[7]   M. Croce, V. Rigo, and S. Ferrini, "IL-21: A pleiotropic cytokine with potential applications in Oncology," J. Immunol. Res., vol. 2015, 2015, doi: 10.1155/2015/696578.

[8]   W. J. Leonard and R. Spolski, "Interleukin-21: A modulator of lymphoid proliferation, apoptosis and differentiation," Nat. Rev. Immunol., vol. 5, no. 9, pp. 688–698, 2005, doi: 10.1038/nri1688.

[9]   K. Brandt, S. Bulfone-Paus, D. C. Foster, and R. Rückert, "Interleukin-21 inhibits dendritic cell activation and maturation," Blood, vol. 102, no. 12, pp. 4090–4098, 2003, doi: 10.1182/blood-2003-03-0669.

[10]   M. Pelletier, A. Bouchard, and D. Girard, "In Vivo and In Vitro Roles of IL-21 in Inflammation," J. Immunol., vol. 173, no. 12, pp. 7521–7530, 2004, doi: 10.4049/jimmunol.173.12.7521.

[11]   H. Søndergaard et al., "Interleukin 21 therapy increases the density of tumor infiltrating CD8 + T cells and inhibits the growth of syngeneic tumors," Cancer Immunol. Immunother., vol. 56, no. 9, pp. 1417–1428, 2007, doi: 10.1007/s00262-007-0285-4.

[12]   H. He et al., "Combined IL-21 and low-dose IL-2 therapy induces anti-tumor immunity and long-term curative effects in a murine melanoma tumor model," J. Transl. Med., vol. 4, pp. 1–16, 2006, doi: 10.1186/1479-5876-4-24.

[13]   H. Nakano et al., "Interleukin-21 triggers both cellular and humoral immune responses leading to therapeutic antitumor effects against head and neck squamous cell carcinoma," J. Gene Med., vol. 8, no. 1, pp. 90–99, 2006, doi: 10.1002/jgm.817.

[14]   H. Liu et al., "An engineered IL-21 with half-life extension enhances anti-tumor immunity as a monotherapy or in combination with PD-1 or TIGIT blockade," Int. Immunopharmacol., vol. 101, no. PA, p. 108307, 2021, doi: 10.1016/j.intimp.2021.108307.

[15]   L. Schirmer, P. Atallah, C. Werner, and U. Freudenberg, "StarPEG-Heparin Hydrogels to Protect and Sustainably Deliver IL-4," Adv. Healthc. Mater., vol. 5, no. 24, pp. 3157–3164, 2016, doi: 10.1002/adhm.201600797.

[16]   published Dove Press, "DDDT-109545-controlled-release-of-tgf-beta-1-from-rada-self-assembling-p," pp. 3043–3051, 2016.

[17]   C. Ligorio et al., "TGF-β3-loaded graphene oxide - self-assembling peptide hybrid hydrogels as functional 3D scaffolds for the regeneration of the nucleus pulposus," Acta Biomater., vol. 127, pp. 116–130, 2021, doi: 10.1016/j.actbio.2021.03.077.

[18]   C. Baecher-Allan, E. Wolf, and D. A. Hafler, "Functional analysis of highly defined, FACS-isolated populations of human regulatory CD4+CD25+ T cells," Clin. Immunol., vol. 115, no. 1 SPEC. ISS., pp. 10–18, 2005, doi: 10.1016/j.clim.2005.02.018.

[19]   A. Skardal, S. V. Murphy, K. Crowell, D. Mack, A. Atala, and S. Soker, "A tunable hydrogel system for long-term release of cell-secreted cytokines and bioprinted in situ wound cell delivery," J. Biomed. Mater. Res. - Part B Appl. Biomater., vol. 105, no. 7, pp. 1986–2000, 2017, doi: 10.1002/jbm.b.33736.

[20]   F. Piccinini, A. Tesei, C. Arienti, and A. Bevilacqua, "Cell Counting and Viability Assessment of 2D and 3D Cell Cultures: Expected Reliability of the Trypan Blue Assay," Biol. Proced. Online, vol. 19, no. 1, pp. 1–12, 2017, doi: 10.1186/s12575-017-0056-3.

[21]   H. Chen et al., "Functional comparison of PBMCs isolated by Cell Preparation Tubes (CPT) vs. Lymphoprep Tubes," BMC Immunol., vol. 21, no. 1, pp. 1–13, 2020, doi: 10.1186/s12865-020-00345-0.

[22]   G. Kaplanski et al., "Interleukin-1 induces interleukin-8 secretion from endothelial cells by a juxtacrine mechanism," Blood, vol. 84, no. 12, pp. 4242–4248, 1994, doi: 10.1182/blood.v84.12.4242.bloodjournal84124242.

[23]   F. R. Svedberg et al., "The lung environment controls alveolar macrophage metabolism and responsiveness in type 2 inflammation," Nat. Immunol., vol. 20, no. 5, pp. 571–580, 2019, doi: 10.1038/s41590-019-0352-y.

[24]   Y. ying Fan, B. yan Yang, and C. you Wu, "Phenotypically and functionally distinct subsets of natural killer cells in human PBMCs," Cell Biol. Int., vol. 32, no. 2, pp. 188–197, 2008, doi: 10.1016/j.cellbi.2007.08.025.

[25]   K. Huizer, D. A. M. Mustafa, J. C. Spelt, J. M. Kros, and A. Sacchetti, "Improving the characterization of endothelial progenitor cell subsets by an optimized FACS protocol," PLoS One, vol. 12, no. 9, pp. 1–18, 2017, doi: 10.1371/journal.pone.0184895.

[26]   B. K. Welte, C. Y. I. Wang, R. Mertelsmann, S. P. Feldman, and A. D. M. A. S. Moore, "PURIFICATION TO APPARENT OF HUMAN HOMOGENEITY AND ITS MOLECULAR From Memorial Sloan-Kettering Cancer Center , Department of Developmental Hematopoiesis , New York 10021 vol. 156, no. August, pp. 454–464, 1982.

[27]   D. Li et al., "Characterization of snakehead (Channa argus) interleukin-21: Involvement in immune defense against two pathogenic bacteria, in leukocyte proliferation, and in activation of JAK–STAT signaling pathway," Fish Shellfish Immunol., vol. 123, no. February, pp. 207–217, 2022, doi: 10.1016/j.fsi.2022.03.006.

[28]   Y. Cai, J. Wang, and K. Zou, "The Progresses of Spermatogonial Stem Cells Sorting Using Fluorescence-Activated Cell Sorting," Stem Cell Rev. Reports, vol. 16, no. 1, pp. 94–102, 2020, doi: 10.1007/s12015-019-09929-9.

[29]   M. Chioccioli, B. Hankamer, and I. L. Ross, "Flow cytometry pulse width data enables rapid and sensitive estimation of biomass dry weight in the microalgae Chlamydomonas reinhardtii and Chlorella vulgaris," PLoS One, vol. 9, no. 5, pp. 1–12, 2014, doi: 10.1371/journal.pone.0097269.

[30]   S. M. Barry and G. Janossy, "Optimal gating strategies for determining bronchoalveolar lavage CD4/CD8 lymphocyte ratios by flow cytometry," J. Immunol. Methods, vol. 285, no. 1, pp. 15–23, 2004, doi: 10.1016/j.jim.2003.10.016.

[31]   F. Pitoiset et al., "Deep phenotyping of immune cell populations by optimized and standardized flow cytometry analyses," Cytom. Part A, vol. 93, no. 8, pp. 793–802, 2018, doi: 10.1002/cyto.a.23570.

[32]   A. Adan, G. Alizada, Y. Kiraz, Y. Baran, and A. Nalbant, "Flow cytometry: basic principles and applications," Crit. Rev. Biotechnol., vol. 37, no. 2, pp. 163–176, 2017, doi: 10.3109/07388551.2015.1128876.

[33]   M. Faldyna, L. Levá, P. Knötigová, and M. Toman, "Lymphocyte subsets in peripheral blood of dogs - A flow cytometric study," Vet. Immunol. Immunopathol., vol. 82, no. 1–2, pp. 23–37, 2001, doi: 10.1016/S0165-2427(01)00337-3.

[34]   M. Faldyna, L. Levá, P. Knötigová, and M. Toman, "Lymphocyte subsets in peripheral blood of dogs - A flow cytometric study," Vet. Immunol. Immunopathol., vol. 82, no. 1–2, pp. 23–37, 2001, doi: 10.1016/S0165-2427(01)00337-3.

[35]   A. Adan, G. Alizada, Y. Kiraz, Y. Baran, and A. Nalbant, "Flow cytometry: basic principles and applications," Crit. Rev. Biotechnol., vol. 37, no. 2, pp. 163–176, 2017, doi: 10.3109/07388551.2015.1128876.

[36]   M. Roederer, J. G. Dubs, M. T. Anderson, P. A. Raju, L. A. Herzenberg, and L. A. Herzenberg, "CD8 naive T cell counts decrease progressively in HIV-infected adults," J. Clin. Invest., vol. 95, no. 5, pp. 2061–2066, 1995, doi: 10.1172/JCI117892.

[37]   H. Kawaida et al., "Distribution of CD4(+)CD25high regulatory T-cells in tumor-draining lymph nodes in patients with gastric cancer," J. Surg. Res., vol. 124, no. 1, pp. 151–157, 2005, doi: 10.1016/j.jss.2004.10.004.

[38]   T. Taguchi and Y. Kimoto, "LAK cells and cancer," Japanese J. Cancer Chemother., vol. 13, no. 12, pp. 3327–3333, 1986, doi: 10.4049/jimmunol.178.7.4011.

[39]   M. L. Disis, H. Bernhard, and E. M. Jaffee, "Use of tumour-responsive T cells as cancer treatment," Lancet, vol. 373, no. 9664, pp. 673–683, 2009, doi: 10.1016/S0140-6736(09)60404-9.

[40]   G. W. Bos et al., "In situ crosslinked biodegradable hydrogels loaded with IL-2 are effective tools for local IL-2 therapy," Eur. J. Pharm. Sci., vol. 21, no. 4, pp. 561–567, 2004, doi: 10.1016/j.ejps.2003.12.007.

[41]   K. S. Frederiksen et al., "IL-21 induces in vivo immune activation of NK cells and CD8+ T cells in patients with metastatic melanoma and renal cell carcinoma," Cancer Immunol. Immunother., vol. 57, no. 10, pp. 1439–1449, 2008, doi: 10.1007/s00262-008-0479-4.

[42]   R. Censi, P. Di Martino, T. Vermonden, and W. E. Hennink, "Hydrogels for protein delivery in tissue engineering," J. Control. Release, vol. 161, no. 2, pp. 680–692, 2012, doi: 10.1016/j.jconrel.2012.03.002.

Chapter 7. General conclusions and future work

7.1 General conclusions

Over the past years, hydrogels have been designed as controlled drug delivery systems for therapeutics. PEG hydrogels are a classic and common material used for drug and cell encapsulation due to their good biocompatibility under proper polymerization [1]. The chemistry properties of PEG enabled PEG-based hydrogels to encapsulate a wide sizes of drug molecules, in the case, become a versatile drug delivery system. However, the stability and bioavailability of drugs in PEG-based hydrogels still exist the obstacles. For example, PEG is high solubility. It is difficult to achieve long-term controlled release of drugs. A higher density cross-linking network of PEG-based hydrogels can be formed through chemical reactions, which may cause cytotoxicity in the human body [2][3]. In addition, the chemical initiators or crosslinkers used in the formation of PEG-based hydrogels may disrupt the structures of drug molecules, affecting drug efficiency and causing adverse effects [4][5].

This project focused on designing self-assembled physical cross-linked peptide hydrogel to establish a controlled release system for macromolecule drug delivery. Based on the electrostatic interaction between macromolecules and peptide hydrogels, we aimed to characterise the effect of charge on the structure and mechanical properties of hydrogel systems. rhIL2/rhIL21 are cytokines that were loaded into peptide hydrogels for immunoreactivity assessment and to study the release profile. The project would develop a promising drug delivery system for immune cancer therapy.

Chapter 4 presented the relationship between pH and charge of peptide, and confirm the pH of the gelation state according to the peptide phase diagram. Compared the stiffness of E(FKFE)$_2$ and K(FEFK)$_2$ hydrogels at different concentrations at pH 7.

E(FKFE)$_2$ and K(FEFK)$_2$ hydrogels with opposite charges at a concentration of 12 mg/mL were compared for their structures, morphologies, 3D cell culture abilities and biocompatibility. The properties of these hydrogels with different charges were evaluated to determine if they are suitable for a drug delivery system. The CD, ThT binding assay and ATR – FTIR confirmed the beta – sheet structure of peptide hydrogel. Both peptides were observed to contained beta – sheet structures and self – assemble into hydrogels with highly ordered beta – sheet at high concentrations. ImageJ was used to measure the diameter of an E(FKFE)$_2$ single fibre in TEM images, which was approximately 4.2 + 1 nm. The diameter of a K(FEFK)$_2$ single fibre was approximately 4.5 +1 nm. SAXS was used to complement the TEM results, which showed ~ 3.84 nm fibre size in E(FKFE)$_2$ and ~ 3.10 nm fibre size in K(FEFK)$_2$. Besides, the TEM images showed the single fibres and bundles randomly distributed. Based on the fibre distribution, the homogenous fibres in peptide hydrogel induced a more stable network. Rheology results showed a higher G' in K(FEFK)$_2$ hydrogel rather than in E(FKFE)$_2$, which corresponded to the TEM assumption. Additionally, the rheological data showed that both hydrogels were injectable.

Furthermore, 3T3 fibroblast cells and Mesenchymal stem cells (MSCs) were loaded into E(FKFE)$_2$ and K(FEFK)$_2$ hydrogels to assess their ability to 3D cell culture and their biocompatibility. The fresh peptide hydrogels were incubated in DMEM and MEME cell culture media to measure their stability. The rheological data showed that different cell culture medium influence the stability of hydrogels. This might due to the different components in the cell culture media that cause variations in the peptide hydrogels. Notably, increasing the concentration of peptide hydrogel stabilized the system. Additionally, the cell viability varied depending on the type of cells and peptide hydrogels. From the LIVE/DEAD staining images, most of 3T3 cells were live after 14

days in the peptide hydrogels. The number of cells depended on the density of the hydrogel network. K(FEFK)$_2$ hydrogel provided a more density network, in the case, 3T3 cells attached with each other and aggregated together. The PicoGreen results corresponded to the images, which showed a higher cell proliferation in 20 mg/mL K(FEFK)$_2$ hydrogel. On the contrary, MSCs showed a lower cell viability in both of peptide hydrogels, even increased the concentration of hydrogel. E(FKFE)$_2$ hydrogels were not stable for 14 days and lost most of the cells, as observed in the images. The number of cells in K(FEFK)$_2$ hydrogel significantly decreased on day 14. PicoGreen results showed a decreased in cell proliferation during 3D cell culture period. Therefore, the biocompatibility of the peptide hydrogels was dependent on the cells. The peptide hydrogels had the ability to selectively support 3D cell culture.

In **Chapter 5**, encapsulated model drug macromolecules to assess the ability of peptide hydrogel to perform control release kinetics. As established in **Chapter 4**, E(FKFE)$_2$ hydrogel was negatively charged at pH 7, while K(FEFK)$_2$ hydrogel was positively charged at pH 7. The charge of these peptides was confirmed using zeta potential in this chapter. To study the relationship between the electrostatic interaction and the controlled release profile of hydrogel, negatively charged fluorescein dextran (3k, 40k, 2000kDa) and positively charged Poly – L – Lysine (28kDa) were selected as model macromolecules to mimic protein drugs for encapsulation. These macromolecules were encapsulated in different charge peptide hydrogels and ATR – FTIR was used to characterize the structure of hydrogel system. The encapsulation process did not disrupt the beta – sheet structure of the peptide hydrogel. The parallel beta – sheet band ($\sim$ 1620 cm^{-1}) and antiparallel beta – sheet band ($\sim$ 1690 cm^{-1}) were present in ATR – FTIR results. The network of peptide hydrogel was different according to different charge effects. Electrostatic attraction induced a more density network, the fibres entangled

together in the formation of bundles. In the case, a thickness fibrilla network was presented. However, electrostatic repulsion resulted in a thinner fibrilla network, where individual fibres were visible. The SAXS results were supplemented by TEM images, which evaluated the effect of charge based on the SAXS patterns of $l_N[q\,I_N(q)]\;vs\;q^2$. Compared to the fresh peptide hydrogel, the mechanical properties of the macromolecule-loaded hydrogel were significantly increased by electrostatic attraction. However, electrostatic repulsion did not cause a significant change in the hydrogel system.

Additionally, different macromolecules in peptide hydrogels were used for swelling experiment. The network structure of the hydrogel can be adjusted according to the presence of external and internal molecules. The stability of the peptide hydrogel could be controlled by electrostatic interaction within the hydrogel. In the release study, the diffusion coefficients and hydrodynamic radius of these macromolecules were determined. The release kinetics of the macromolecules were influenced by the electrostatic interactions within the hydrogel and the size of the macromolecules, as determined by comparing the diffusion coefficients in the peptide hydrogels. Both hydrogels can perform controlled release, making them excellent candidates for delivering protein drugs.

In **Chapter 6**, cytokine rhIL2 and rhIL21 were selected to encapsulate into peptide hydrogel to assess the activity and the release profile. rhIL2 and rhIL21 had different immunoreactivities in the peptide hydrogels, rhIL21 was negatively charged and retained its immunoreactivity in hydrogels, while rhIL2 was neutral and lost its immunoreactivity in the hydrogels. This could be explained by the effect of pH on the stability of drugs in hydrogels. rhIL2 may be more stable in acidic or basic peptide hydrogels. From the release study of rhIL21, it was found that it performed controlled

release kinetics in E(FKFE)$_2$ hydrogel which might increase the half – life of rhIL21 and decrease the dosage times. In most cases, this could potentially avoid adverse effects on the human body. In order to measure the activity of rhIL21 in E(FKFE)$_2$ hydrogel, a solution of rhIL21 was used for the study in this chapter. The significant increase in the expression of CD4$^+$ in human peripheral blood mononuclear cells (PBMCs) suggested that rhIL21 can stimulate T cells, potentially making it a viable option for immune therapy in cancer treatment.

7.2 Future work

rhIL21 could be encapsulated into E(FKFE)$_2$ hydrogel and measure the activity on PBMCs. It is feasible to select cancer cell lines and culture them with rhIL21-loaded hydrogel in order to test for cell cytotoxicity. As we have assumed that the pH of drugs may affect its activity in hydrogel, rhIL2 could be encapsulated in an acidic or basic peptide hydrogel, for example, F8 peptide that self – assembled into hydrogel at pH 4 and pH 9.

In biological research, both E(FKFE)$_2$ and K(FEFK)$_2$ hydrogels have shown good biocompatibility with 3T3 cells, and these two materials are injectable. They can be applied in animal models via injection administration to study the biocompatibility, drug efficacy and any skin inflammation caused by injection process. In addition, other types of drugs can also be encapsulated in peptide hydrogels and tested in animal models in order to study whether the peptide hydrogels are promising materials a as drug delivery system.

It is clear that the peptide hydrogels can be used for a variety of purposes, including drug delivery in animal models, screening cells and drugs in vitro. The passage also

highlights that peptide hydrogels are multifunctional materials that could potentially

contribute to advances in medical research.

7.3 References

[1]   C. C. Lin and K. S. Anseth, "PEG hydrogels for the controlled release of biomolecules in regenerative medicine," Pharm. Res., vol. 26, no. 3, pp. 631–643, 2009, doi: 10.1007/s11095-008-9801-2.

[2]   C. C. Lin and A. T. Metters, "Hydrogels in controlled release formulations: Network design and mathematical modeling," Adv. Drug Deliv. Rev., vol. 58, no. 12–13, pp. 1379–1408, 2006, doi: 10.1016/j.addr.2006.09.004.

[3]   N. A. Peppas, P. Bures, W. Leobandung, and H. Ichikawa, "Hydrogels in pharmaceutical formulations," Eur. J. Pharm. Biopharm., vol. 50, no. 1, pp. 27–46, 2000, doi: 10.1016/S0939-6411(00)00090-4.

[4]   H. Soyez, E. Schacht, M. Jelinkova, and B. Rihova, "Biological evaluation of mitomycin C bound to a biodegradable polymeric carrier," J. Control. Release, vol. 47, no. 1, pp. 71–80, 1997, doi: 10.1016/S0168-3659(96)01617-3.

[5]   A. T. Metters, K. S. Anseth, and C. N. Bowman, "A statistical kinetic model for the bulk degradation of PLA-b-PEG-b-PLA hydrogel networks: Incorporating network non-idealities," J. Phys. Chem. B, vol. 105, no. 34, pp. 8069–8076, 2001, doi: 10.1021/jp004083h.